UNIVERSITY OF CALIFORNIA
Santa Barbara

Computational studies of barrier-crossing in polymer field theory

A Dissertation submitted in partial satisfaction
of the requirements for the degree of

Doctor of Philosophy

in

Physics

by

Michael Francis Carilli

Committee in Charge:

Professor Glenn H. Fredrickson, Chair

Professor Everett A. Lipman

Professor Baron Peters

Professor Philip A. Pincus

March 2016

The Dissertation of
Michael Francis Carilli is approved:

Professor Everett A. Lipman

Professor Baron Peters

Professor Philip A. Pincus

Professor Glenn H. Fredrickson, Committee Chair

December 2015

Computational studies of barrier-crossing in polymer field theory

by

Michael Francis Carilli

For my family, by blood and friendship

Acknowledgements

First of all, I would like to thank my advisor, Professor Glenn Fredrickson, for his guidance, insight, patience, and encouragement. Thanks to Glenn, I discovered a career path I am excited to embark on, high-performance parallel programming. The fact that it was possible to learn such skills in his group is a testament to its rich intellectual atmosphere. Without Glenn, I might never have discovered this passion, and I will always be grateful for the opportunity.

I am grateful to Professor Philip Pincus, Professor Everett Lipman, and Professor Baron Peters for serving on my committee. I am particularly grateful to Professor Pincus for discussions that inspired me to work in the Materials Research Lab to begin with, and to Professor Peters for his comprehensive, lucid expositions of barrier-crossing theory that made my task of understanding (some small part of) the field a great deal less daunting.

I am grateful to members of the Fredrickson group past and present with whom I have worked over the years. All have been helpful colleagues and warm friends. In particular, I would like to thank Kris Delaney, who introduced me to the fascinating world of GPUs. Reading his code was better than a textbook. I would like to thank Sean Paradiso, my officemate, who greatly aided my understanding of polymer field theory and has quite simply been a joy to have around. I would like to thank Bongkeun Kim, Nabil Laachi, Tatsuhiro Iwama, and Ken-ichi Izumi

for collaborating with me on applying the string method to SCFT, and turning my code-monkeying into something useful. Working with them was honestly the most rewarding experience of my time here, and served to influence my career aspirations more than any other aspect. I would like to thank Doug Tree, Carol Tsai, Corinne Carpenter, Jimmy Liu, Wei Li, and Jonathan Martin for their companionship and conversation, which never failed to expand my mind and lift my spirits and made going to the office something I looked forward to.

I am grateful to Coach Mateo and all my friends on the UCSB triathlon team. I can say without exaggeration that they have been the most fun, caring, and entertaining peer group I've ever had. They opened up a new world to me, and introduced me to activities I will pursue for the rest of my life. I consider the Plymires, Gary Fox, Ricky Waltman, Harjinder Singh, Tim Aikin, and my unshakably optimistic, kind, and supportive girlfriend Juli White to be part of my family.

Finally, I am grateful to Mom, Dad, Joe, John, Maria, Rose, Uncle Albert, Aunt Mayra, little Albert, little Joan, Uncle Charlie, Aunt Catherine, Sammie, Nana, Pete, and Yiayia. I love you more than anything else in the world.

Curriculum Vitæ

Michael Francis Carilli

Education

2016	Doctor of Philosophy in Physics, University of California, Santa Barbara (expected)
2010	Bachelor of Science in Physics, *magna cum laude* University of Notre Dame.

Experience

2011-2015	Graduate Student Researcher, University of California, Santa Barbara
2010-2011	Teaching Assistant, University of California, Santa Barbara
2009	Research Internship in Science and Engineering (RISE), University of Duisburg-Essen
2008	Research Assistant, University of Notre Dame
2007	NSF REU, Nat'l Radio Astronomy Observatory

Awards

2011	UCSB Physics Outstanding TA Award
2009	Notre Dame nominee for Goldwater scholarship
2006-2010	Notre Dame College of Science Dean's List, all semesters
2006	Valedictorian of Socorro High School
2002	National Spelling Bee finalist

Publications

M. Carilli, K. T. Delaney, and G. H. Fredrickson, "Nucleation of the lamellar phase from the disordered phase of the fluctuating Landau-Brazovskii model," *In preparation.*

K. Izumi, B. Kim, N. Laachi, K. T. Delaney, **M. Carilli**, and G. H. Fredrickson, "Thermodynamic and Kinetic Aspects of Barriers to Defect Melting in Lamellae-Forming Diblock Copolymer/Homopolymer Blends on Chemo-Epitaxially Patterned Substrates," *Submitted to J. Polym. Sci. B.*

M. Carilli, K. T. Delaney, and G. H. Fredrickson, "Truncation-based energy weighting string method for efficiently resolving small energy barriers," *The Journal of Chemical Physics* **143**, 054105 (2015).

T. Iwama, N. Laachi, B. Kim, **M. Carilli**, K. T. Delaney, and G. H. Fredrickson, "Computational Study of Directed Self-Assembly in Neutral Prepatterns for a Graphoepitaxial Pitch-Multiplication Application," *Macromolecules* 2015, **48**, 1256-1261.

K. Izumi, B. Kim, N. Laachi, K. T. Delaney, **M. Carilli**, and G. H. Fredrickson, "Barriers to defect melting in chemo-epitaxial directed self-assembly of lamellar-forming diblock copolymer/homopolymer blends," *Proceedings of the SPIE* **9423**, 94232C-1 (2015).

B. Kim, N. Laachi, K. T. Delaney, **M. Carilli**, E. J. Kramer, and G. H. Fredrickson, "Thermodynamic and Kinetic Aspects of Defectivity in Directed Self-Assembly of Cylinder-Forming Diblock Copolymers in Laterally Confining Thin Channels," *Journal of Applied Polymer Science* **2014**, 40790.

Selected Presentations

2015	GPU Technology Conference, San Jose, CA
2014	APS March Meeting, Denver, CO

Abstract

Computational studies of barrier-crossing in polymer field theory

Michael Francis Carilli

This dissertation is primarily a survey of the zero-temperature string method, a minimum energy path search algorithm, applied to novel barrier-crossing problems in polymer field theory. I apply the method to both self-consistent field theory (SCFT) and a phase-field model (the Landau-Brazovskii model). In the case of SCFT, the focus is on defect annealing problems in homo+copolymer melts; in the case of the Landau-Brazovskii model, the focus is on finding critical nuclei for the disorder-to-lamellar transition, which is known to be a fluctuation-induced first-order phase transition.

In SCFT, applying the string method is computationally demanding in both processing time and memory, especially for fully 3-dimensional simulations at industrially relevant system sizes. I successfully address these challenges on state-of-the-art massively parallel computing architectures (NVIDIA graphics processing units). As a result our group is able to identify free energy barriers and transition mechanisms for a wide variety of defect annealing problems relevant to industrial directed self-assembly (DSA).

Nucleation in the Landau-Brazovskii model presents its own challenges. The string method as originally formulated is inefficient for nucleation problems, since many images are wasted tracing out unphysical configurations once the nucleus grows to the edges of the simulation cell. I devise a new truncation-based energy weighting (TBEW) scheme that resolves this issue, and will prove valuable to future researchers using the string method to find critical nuclei.

Since the bare Landau-Brazovskii model predicts a second-order transition between disorder and lamellae at a mean-field level, naive application of the zero-temperature string method to this model fails to find a barrier. To circumvent this, I instead apply the string method to a renormalized model that incorporates fluctuations at a mean-field level. Using TBEW and the renormalized model, I investigate nucleation pathways for the disorder-to-lamellar transition, finding anisotropic nuclei in agreement with previous predictions and experimental observations. I also conduct a comprehensive search for experimentally observed nuclei containing various exotic defect structures.

Finally, I evaluate the validity of the nucleation pathways obtained from the renormalized model by numerically simulating the bare model with explicit fluctuations. I find that the renormalized model makes good predictions for certain quantities, including the location of the order-disorder transition. However, due to sharp dependence of critical nucleus size on proximity to the order-disorder

transition, even slight errors in the predicted ODT lead to large errors in predicted nucleus size. I conclude that the renormalized Landau-Brazovskii model is a poor tool for predicting critical nuclei in the fully fluctuating bare theory at experimentally accessible parameters, and recommend that future studies work with the fluctuating bare theory directly. I recommend several strategies to extract barriers and rates.

Contents

List of Figures

Chapter 1

Introduction

1.1 Diblock copolymers

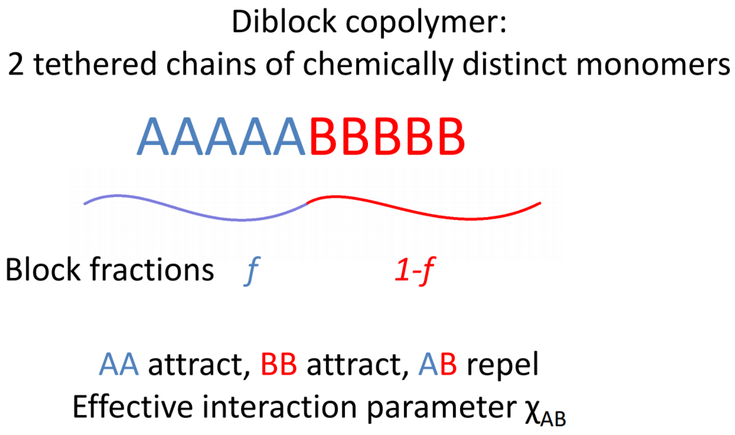

Figure 1.1: Diblock copolymer.

Diblock copolymers consist of 2 chemically bonded chains of distinct monomer species (Figure 1.1). Chains of like species act as entropic springs, thus there is an effective attraction between like monomers; however, an enthalpic contact penalty exists for contact between unlike monomers. At high temperatures entropy dom-

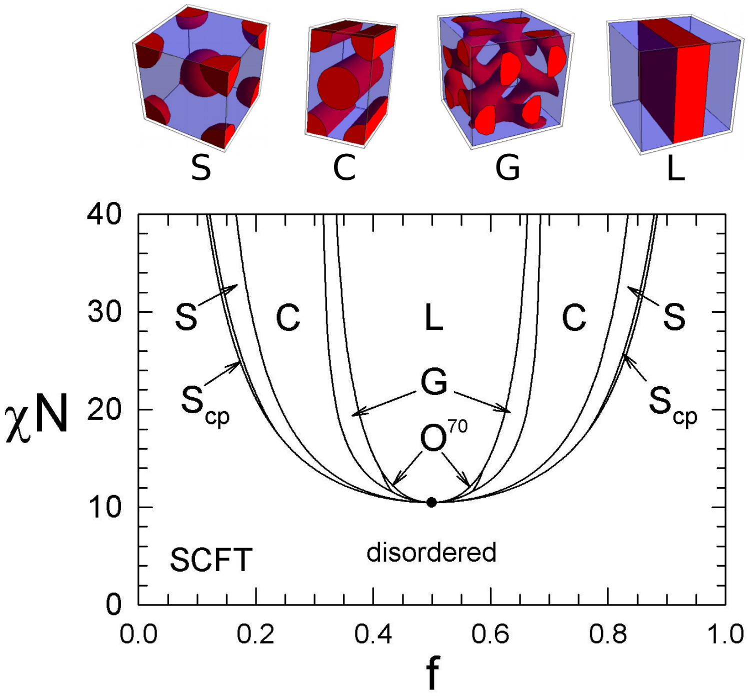

Figure 1.2: Phase diagram for diblock copolymers according to self-consistent field theory (SCFT), with several example microphases shown. Known preferred quasicrystalline structures are lamellae (L), gyroid (G), interpenetrating double-diamond with O^{70} space group, hexagonally packed cylinders (C), body-centered-cubic-packed spheres (S), and face-centered-cubic-packed spheres (S_{cp}). Images adapted from [1] and `http://chemeng.uwaterloo.ca/mwmatsen/research/mc.html`.

inates and the average composition is homogeneous in space. At low temperatures, chains of unlike species would prefer to phase separate, but cannot since the chains are chemically bonded. This frustrated repulsion leads to “microphase separation,” where the system phase-separates into a regular pattern of A-rich and B-rich domains. The A-rich and B-rich domains tend to pack according to a quasicrystalline structure. The favored structure or “microphase” depends on the block fraction f (the fraction of, *e. g.*, type A monomers in the chain) and the effective segregation strength χN, where N is the number of "statistical segments" in the chain and χ is the energy penalty for contact between segments of unlike species.[1] For example, if the diblock chains are roughly symmetric ($f \approx 1/2$) the system prefers to form A-rich lamella alternating with B-rich lamellae. Even for such a simple system as diblocks, the phase diagram of favored microphases is quite rich (Fig. 1.2). For more complicated copolymers like linear triblocks (composed of sequentially tethered chains of 3 distinct species), the set of preferred morphogies explodes into an even wider range of exotic structures [2].

1.2 Directed self-assembly and defects

This fascinating self-assembly behavior is not a mere academic curiosity. Block copolymers can form regular, patterned nanoscale structures on length scales smaller than those accessible to photolithography. This spontaneous pattern formation can be influenced by placing the copolymer on a substrate with a pre-existing topographic pattern ("graphoepitaxy") or compositional pattern where different substrate domains are more attractive to one monomer species or an-

---

[1] In a sense χN is an effective inverse temperature. High χN corresponds to low temperature, at which enthalpic effects dominate and the system orders; low χN corresponds to high temperature where entropy dominates and the system disorders. χ and N will be explained more rigorously in Chapter 2.

other (“chemoepitaxy”). Pattern formation can also be guided by the application of electric fields, shear, temperature gradients, and other external control parameters. The use of patterned substrates, electric fields, shear, etc. to influence nanoscale copolymer self-assembly into desired structures is known as “directed self-assembly” (DSA). The point is that a larger-scale prepattern can guide the formation of smaller-scale structures. Say, for example, a lamella-forming block copolymer has preferred domain spacing d. A substrate with topographic channels of width $4d$ can be prepared, *e.g.*, by optical lithography, and coated with copolymer. The copolymer then self-assembles into lamellae along the direction of the channels.[2] One monomer species or the other can then be chemically etched away, resulting in a topography with channels 4× smaller than the original prepattern; in the language of DSA we would say a “pitch multiplication” of 4 has been achieved. Self-assembling copolymer has also been shown to help rectify moderate errors in prepattern placement; in other words, if the prepattern admits some positional error, the resulting self-assembled structures will arrange themselves with improved regularity. Good introductions to DSA can be found in [3] and [4]; in Chapter 3 we present a survey of previous DSA literature relevant to this thesis.

---

[2] The use of guiding prepatterns is also important to prevent long-range bending of self-assembled structures; we will discuss this in more detail in Chapter 3.

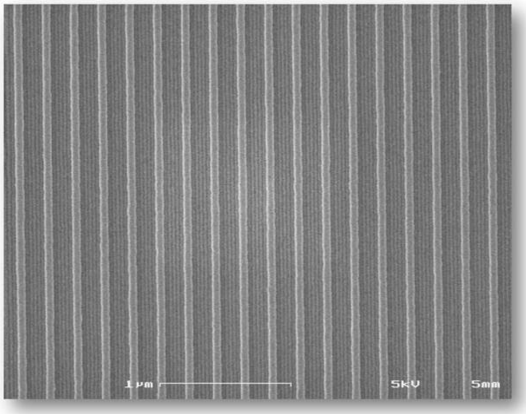

Figure 1.3: A defect-free configuration of lying-down cylinders. Image adapted from `http://on-demand.gputechconf.com/gtc/2015/posters/GTC_2015_Computational_Physics_23_P5308_WEB.pdf`.

Nanoscale lithography enabled by DSA is a promising tool for a wide range of applications, including integrated circuit patterning [6], quantum dots [7], high-density memory storage [8], photonic crystals [9], and nanofiltration membranes [10]. However, many practical applications require that copolymer reliably self-assembles into regular nanoscale structures over a macroscopically significant area (micrometers or more) or a large number of patterning attempts. When scaling up DSA to these industrially relevant system sizes, thermodynamics and the dynamics of the copolymer's structure formation often result in the copolymer becoming trapped in metastable defect-containing morphologies, even in the presence of a good guiding prepattern. An example of a defect-free self-assembled morphology can be seen in Figure 1.3. Defect structures typically observed in attempts to generate this morphology are shown in Figure 1.4. A recent review of defectivity

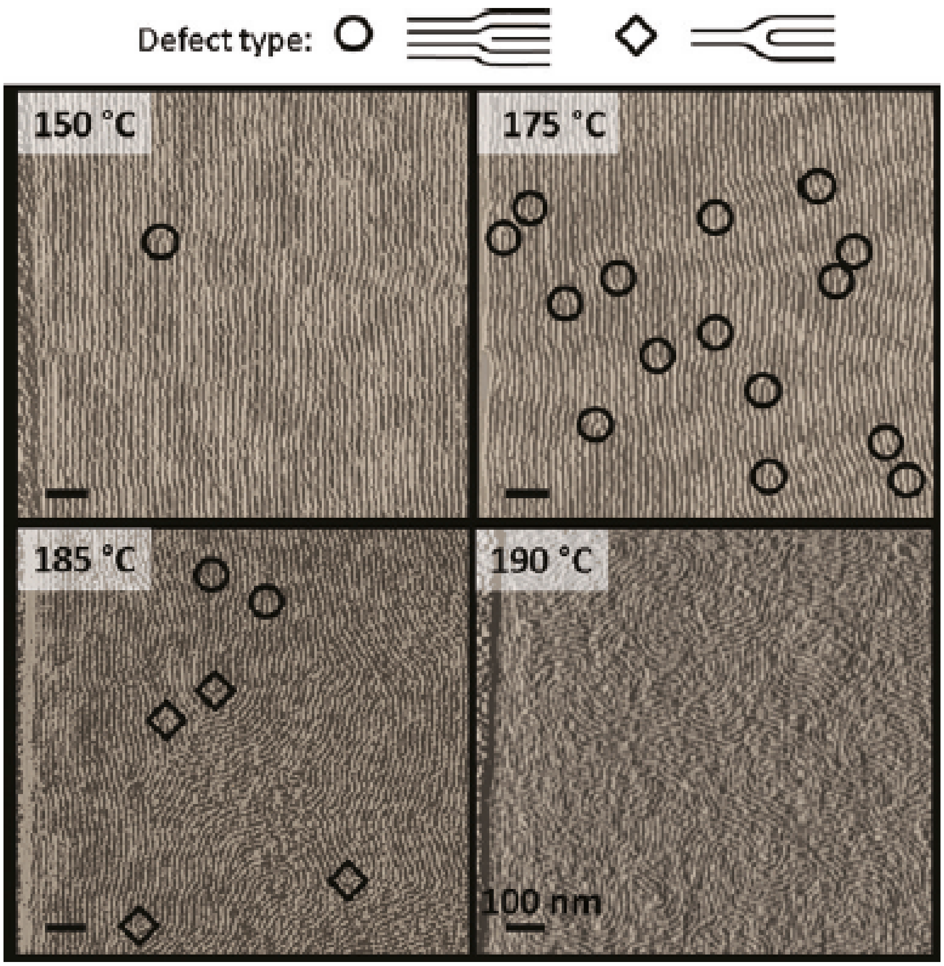

Figure 1.4: Typical defects observed during the self-assembly of lying-down cylinders. The system is less ordered at higher temperature, but even at low temperature, metastable defects remain. Image adapted from [5].

in directed self-assembly can be found in [11]. In Chapter 3 we present a survey of previous literature on defectivity in DSA as it relates to this thesis.

DSA admits a wide range of tunable experimental parameters: copolymer block fraction, monomer species segregation strength, homopolymer admixture, dimensions and regularity of topographic prepatterns, wetting affinity and placement of chemical prepatterns, and so on. From an experimental perspective, to avoid costly trial and error, it is valuable to develop computational tools capable of predicting parameters that minimize the incidence of defects and facilitate their rapid removal. In Chapter 2, I present an introduction to self-consistent field theory (SCFT), the workhorse field-theoretic model capable of predicting preferred and metastable morphologies of copolymer melts, blends, and solutions, optionally in grapho- or chemo-epitaxial confinement. SCFT can also predict the free energy of self-assembled structures at a mean-field level, enabling us to predict the energy penalty incurred by defective morphologies and thus approximate their incidence according to Boltzmann statistics. This particular use case of SCFT has been fairly standard for the last decade or more.

However, when combating defectivity in DSA, there is another aspect to consider: When metastable defective morphologies do form, how difficult are they to remove? A metastable defect, by definition, lies at a local minimum of the system's potential energy landscape, and an energy barrier must be crossed to transition to a defect-free state. This means that the system will fluctuate in the metastable state until random thermal forces cause it to diffuse across the barrier. A reasonable approximation is to assume that the transition will occur by way of the "minimum energy path" or MEP, which can be visualized as a mountain pass in the free energy landscape. The peak energy along the MEP represents the energy barrier E_B that must be crossed. Locating the MEP in the high-dimensional space of an SCFT model can be accomplished using the numerical string method; the annealing time required for defective→perfect transition can then be estimated as $\sim \exp\left(-E_B/k_BT\right)$. The string method requires simultaneously evolving multiple system configurations. When each configuration is an SCFT model, this process can become computationally demanding. Only in recent years have computers become fast enough to make string SCFT calculations feasible, especially for large 3D systems. In Chapter 2, I present an introduction to barrier-crossing theory, explain the MEP concept, and describe the string method in detail. In Chapter 3, I describe how I developed a GPU-accelerated version of the string method combined with SCFT and applied it to several industrially relevant DSA systems. Useful, practical guidance on how to minimize defectivity in these systems was obtained.

1.3 Disorder→lamellar nucleation

The disorder→lamellar (dis→lam) transition of diblock copolymers is of particular scientific interest. At a mean-field level, commonly used workhorse models for diblocks like the Leibler model [12], as well as SCFT, predict the transi-

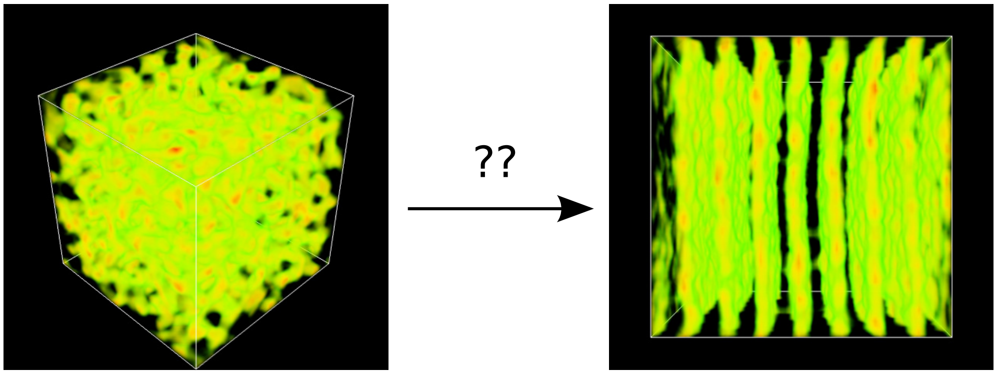

Figure 1.5: How does a fluctuating disordered morphology (left) transition to a fluctuating lamellar morphology (right)?

tion to be second-order. This second-order character does not admit a region of metastable disorder, and predicts that the transition takes place via spinodal decomposition. The experimental phase diagram for a diblock melt near the dis→lam ODT differs significantly from these predictions, however (Fig. 1.6). Interestingly, if fluctuations are explicitly included, SCFT, the Leibler model, and its derivative phase-field models do predict a first-order dis→lam transition at increased χN across a window of block fractions, in improved agreement with the experimental phase diagram. In this sense the disorder→ lamellar transition is considered a "fluctuation-induced first order phase transition," a concept that will be discussed further in Chapters 2 and 5.

An additional intriguing feature of the dis→lam transition is that disorder-lamellar interfacial surface tension is highly anisotropic, favoring interfaces normal to lamellar planes [14]. As a result, a number of authors have predicted or ob-

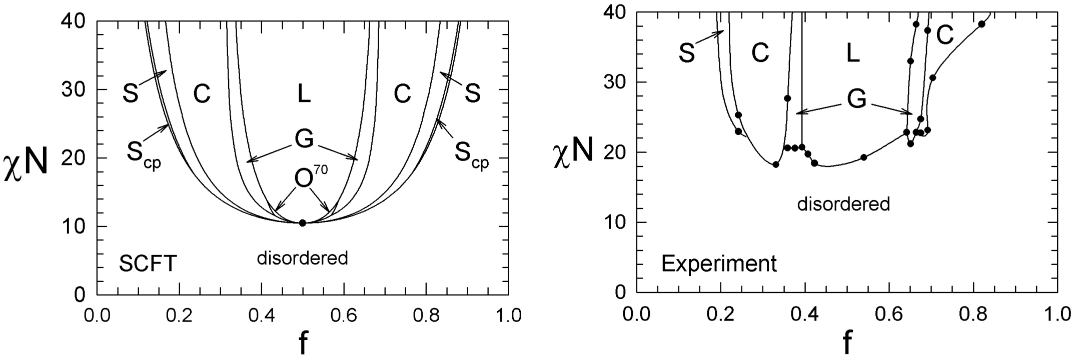

Figure 1.6: Left panel: Mean-field SCFT phase diagram for a diblock melt. Right panel: Experimental phase diagram for a diblock melt. Qualitative differences include 1. SCFT only predicts a direct dis→lam transition at f = exactly 1/2, while experimentally, a direct dis→lam transition is observed across a range of f. 2. The dis→lam transition is second-order in the mean-field SCFT diagram, while experiments show it to be weakly first-order [13]. 3. The dis→lam phase boundary occurs at a higher χN than predicted by mean-field SCFT. Images adapted from `http://chemeng.uwaterloo.ca/mwmatsen/research/mc.html`.

served exotic shapes and structures for the critical nucleus. Balsara *et al.* predict ellipsoidal grains [15], Hohenberg and Swift predict nuclei containing focal conic defects [16], and Chastek and Lodge experimentally observed needlelike, twinned, 2-fold twinned, and spherulite-shaped lamellar grains growing from a disordered diblock copolymer solution [17]. Important results are reviewed in Chapter 5. However, prior to my work no systematic computational attempt has been made to clarify the specific mechanism of the dis→lam transition.

In Chapter 2 I introduce the phase-field models used to study this problem. In Chapter 4 I introduce the truncation-based energy weighting (TBEW) string method, my own modified string method that is ideally suited to large-cell nucleation problems. In Chapter 5, I use the string method to investigate nucleation of the lamellar phase from the disordered phase of a renormalized phase-field model, at parameters connected to those of an experimentally accessible diblock melt. I find anisotropic critical nuclei in qualitative agreement with previous experimental and analytic predictions; I also find good quantitative agreement with the predictions of a single-mode approximation analysis. I then conduct a thorough search for critical nuclei containing various predicted and experimentally observed defect structures.

I evaluate the predictions of the renormalized model by simulating the bare Landau-Brazovskii model with explicit fluctuations. I find that the renormalized model makes reasonable predictions for several important quantities, including the order-disorder transition (ODT). However, the critical nucleus size depends sharply on proximity to the ODT, so even moderate errors in the ODT predicted by the renormalized model lead to large errors in predicted critical nucleus size. I conclude that the renormalized model is a poor tool to study nucleation in the fluctuating Landau-Brazovskii model, and recommend that future studies work with the fluctuating bare model directly. I recommend several strategies to extract free energy barriers and rates.

Chapter 2

Theory and Tools

2.1 A brief review of diffusive barrier-crossing

When investigating a barrier-crossing problem, three of the most important objects to discover are 1. a measure of the transition's progress, 2. an estimate of the rate at which the transition occurs, and 3. some physical intuition as to how the transition takes place. One can describe the system in terms of its fully microscopic degrees of freedom or some reduced-dimensional space of collective variables. However, one must take care that the chosen collective variables do not obscure the mechanism of the transition. A "reaction coordinate" is a single variable that quantifies the progress of a barrier-crossing event [18], for example, the size of a growing nucleus, or the arc length coordinate along the path traced out by the string method (a technique that will be discussed in Section 2.2). It should be mentioned that time is not in general a good reaction coordinate, because the system may spend a long time waiting in a metastable state before the transition occurs at random and proceeds quickly. The "committor probability," the probability that in the future the system will visit (commit to) the product well before visiting the reactant well, is considered the ideal reaction coordinate [19].

In this section, I will outline how the the committor probability can be obtained, make more precise the idea of a good reaction coordinate, show how a good reaction coordinate can be used to compute transition rates, and review some computational techniques commonly used to attack diffusive barrier-crossing problems.

2.1.1 Dynamics of probability distributions

Our starting point is a system with coordinates $\mathbf{x}$ evolving in time according to overdamped Langevin dynamics. $\mathbf{x}$ may represent either the system's microscopic coordinates or a set of coarse-grained collective variables. The equation of motion [20, 21] is the following:

$$x_i(t+\delta t) = x_i(t) + \delta t \sum_j \left(-\beta D_{ij} \frac{\partial V}{\partial x_j} + \frac{\partial D_{ij}}{\partial x_j} \right) + \sqrt{2\delta t} \sum_j \sigma_{ij}(\mathbf{x}) R_j \tag{2.1}$$

$$\equiv x_i(t) + A_i \delta t + N_i \tag{2.2}$$

where $V(\mathbf{x})$ is the energy of the system, $D_{ij}(\mathbf{x})$ is the (position-dependent) matrix of diffusion coefficients, σ is chosen such that

$$D_{ij} = \sum_k \sigma_{ik}\sigma_{jk} \tag{2.3}$$

(a choice we will justify shortly) and R_j are Gaussian random variables with $\langle R_j \rangle = 0$ and $\langle R_i R_j \rangle = \delta_{ij}$. In (2.2), $A_i \delta t \equiv \delta t \sum_j \left(-\beta D_{ij} \frac{\partial V}{\partial x_j} + \frac{\partial D_{ij}}{\partial x_j} \right)$ represents the average drift of the system and $N_i \equiv \sqrt{2\delta t} \sum_j \sigma_{ij}(\mathbf{x}) R_j$ represents the stochastic motion due to thermal fluctuations.

The dynamics (2.1) is appropriate for the systems considered in later chapters, because the collective variables typically used to describe nucleation phenomena (for example, some measure of the nucleus size, potentially coupled with some measure of its internal structure [22–25]), as well as the 1D reaction coordinate obtained by the string method, are inertialess. The microscopic field values associated with self-consistent field theory and the Landau-Brazovskii model are also inertialess coordinates.

Consider the probability density $\rho(\mathbf{x}, t)$ of a system evolving according to (2.1). Intuitively, the integral of $\rho(\mathbf{x}, t)$ over some volume V is the probability that the system is present in V at time t. We can derive an equation describing the time evolution of ρ by constructing a Chapman-Kolmogorov equation [26] and carrying out a Kramers-Moyal expansion (see, *e.g.*, Chapter 11 of Ref. [27]).[1]

The Chapman-Kolmogorov equation expresses the probability density $\rho(\mathbf{x}, t+\delta t)$ in terms of the probability density at t and the transition probability density $W(\delta\mathbf{x}, x - \delta\mathbf{x}, \delta t)$ that the system started at $\mathbf{x} - \delta\mathbf{x}$ at time t, then moved a distance $\delta\mathbf{x}$ during time interval δt to end up at $\mathbf{x}$ at time $t + \delta t$. We integrate over all possible starting positions $\mathbf{x} - \delta\mathbf{x}$ by integrating over all possible moves $\delta\mathbf{x}$ that could have taken place:

$$\rho(\mathbf{x}, t+\delta t) = \int d\delta\mathbf{x}\, W(\delta\mathbf{x}, \mathbf{x}-\delta\mathbf{x}, \delta t)\, \rho(\mathbf{x}-\delta\mathbf{x}, t) \tag{2.4}$$

then expand both sides to first order in δt and second order in $\delta\mathbf{x}$:

$$\begin{aligned}\rho(\mathbf{x}, t) + \delta t\frac{\partial\rho}{\partial t} = \int d\delta\mathbf{x} \Bigg\{ & W(\delta\mathbf{x}, \mathbf{x}, \delta t)\, \rho(\mathbf{x}, t) - \sum_i \delta x_i \frac{\partial}{\partial x_i}\Big(W(\delta\mathbf{x}, \mathbf{x}, \delta t)\, \rho(\mathbf{x}, t) \Big) \\ & + \sum_{ij} \frac{1}{2}\delta x_i \delta x_j \frac{\partial}{\partial x_i}\frac{\partial}{\partial x_j}\Big(W(\delta\mathbf{x}, \mathbf{x}, \delta t)\, \rho(\mathbf{x}, t) \Big) \Bigg\}\end{aligned} \tag{2.5}$$

$W(\delta\mathbf{x}, \mathbf{x}, \delta t)$ is the probability that the system moves a distance $\delta\mathbf{x}$ in time δt starting at $\mathbf{x}$. Therefore, using (2.2) to express δx_i as $x_i(t+\delta t) - x_i(t) = A_i + N_i$, recalling that $\langle R_j \rangle = 0$ and $\langle R_i R_j \rangle = \delta_{ij}$, and keeping terms only to first order in

---

[1] This is a fairly familiar derivation. I'm showing it here to set up later, similar derivations of the committor probability distribution and the propagator for a diblock copolymer, which use the same technique but may not be so familiar.

δt, we have

$$\begin{aligned}
&\int d\delta\mathbf{x}\, W(\delta\mathbf{x},\mathbf{x},\delta t) = 1 && (2.6)\\
&\int d\delta\mathbf{x}\, \delta x_i W(\delta\mathbf{x},\mathbf{x},\delta t) = \langle \delta x_i\rangle = \langle A_i + N_i\rangle = A_i\delta t\\
&\int d\delta\mathbf{x}\, \delta x_j \delta x_j W(\delta\mathbf{x},\mathbf{x},\delta t) = \langle \delta x_i \delta x_j\rangle = \langle (A_i\delta t + N_i)(A_j\delta t + N_j)\rangle\\
&\qquad\qquad\qquad\qquad\qquad\qquad = \langle N_i N_j\rangle = 2\delta t D_{ij} \quad .
\end{aligned}$$

Substituting these results back into (2.5) yields

$$\begin{aligned}
\rho(\mathbf{x},t) + \delta t\frac{\partial\rho}{\partial t} &= \rho(\mathbf{x},t) - \delta t\sum_i \frac{\partial}{\partial x_i}\Big(A_i\rho(\mathbf{x},t)\Big) + \delta t\sum_{ij}\frac{\partial}{\partial x_i}\frac{\partial}{\partial x_j}\Big(D_{ij}\rho(\mathbf{x},t)\Big)\\
\frac{\partial\rho}{\partial t} &= \sum_{ij} -\frac{\partial}{\partial x_i}\Big(-\beta D_{ij}\frac{\partial V}{\partial x_j}\rho + \frac{\partial D_{ij}}{\partial x_j}\rho\Big) + \frac{\partial}{\partial x_i}\frac{\partial}{\partial x_j}\Big(D_{ij}\rho\Big)\\
\frac{\partial\rho}{\partial t} &= \sum_{ij}\frac{\partial}{\partial x_i}\Big(\beta D_{ij}\frac{\partial V}{\partial x_j}\rho + D_{ij}\frac{\partial\rho}{\partial x_j}\Big) \equiv \hat{L}_+(\rho) \quad . && (2.7)
\end{aligned}$$

(2.7) is the Smoluchowski or “forward Kolmogorov” equation for overdamped Langevin dynamics, and the operator $\hat{L}_+$ is the “generator” of the forward Kolmogorov process [28]. (2.7) may be written in the suggestive form

$$\frac{\partial\rho(\mathbf{x},t)}{\partial t} = \sum_i \frac{\partial}{\partial x_i}\Big(\sum_j D_{ij}\rho_{eq}(\mathbf{x})\frac{\partial}{\partial x_j}\Big(\rho_{eq}^{-1}(\mathbf{x})\rho(\mathbf{x},t)\Big)\Big) \tag{2.8}$$

where $\rho_{eq}(\mathbf{x}) = \frac{1}{Z}\exp\left(-\beta V(\mathbf{x})\right)$ is the Boltzmann distribution. This form highlights that $\rho(\mathbf{x}, t) = \rho_{eq}(\mathbf{x})$ is a steady-state ($\partial\rho/\partial t = 0$) solution of (2.8), which can be regarded as proof that the Langevin equation (2.1) samples the physically correct stationary distribution. The fact that choosing the noise strength according to (2.3) results in correct sampling of the Boltzmann distribution is known as the fluctuation-dissipation theorem.

Additionally, (2.8) has the form of a continuity equation $\partial\rho/\partial t = -\nabla\cdot\mathbf{j}$, which allows us to identify the "probability current"

$$j_i = -\sum_i \rho_{eq}(\mathbf{x}) D_{ij} \frac{\partial}{\partial x_j}\Big(\rho_{eq}(\mathbf{x})\rho(\mathbf{x}, t)\Big) \tag{2.9}$$

Intuitively, for a volume element V bounded by surface S, the surface integral $\int_S \mathbf{j}\cdot\hat{\mathbf{n}}\, dS$ represents the rate of change of the probability that the system is present in V, in other words, the rate of escape from or entrance into V.

As previously noted, the ideal coordinate measuring the progress of a reaction in a stochastic barrier-crossing system is the committor probability. For a system evolving according to (2.1) with initial microscopic coordinates $\mathbf{x}$, we can also derive an equation governing the committor probability $q(\mathbf{x})$. Langevin dynamics are a continuous, not a discrete, Markov process. A system obeying Langevin dynamics cannot magically appear in one well or the other but must traverse a continuous trajectory of intermediate states to get there. Therefore, if the system starts at $\mathbf{x}$ and moves a (small) distance $\delta\mathbf{x}$ in time δt, the original committor probability $q(\mathbf{x})$ must be equal to the integral over "probability of each possible $\delta\mathbf{x}$" × "committor probability at the new position:"

$$q(\mathbf{x}) = \int d\mathbf{x}\, W(\delta\mathbf{x}, \mathbf{x}, \delta t)\, q(\mathbf{x} + \delta\mathbf{x}) \ . \tag{2.10}$$

(2.10) has two crucial differences from (2.4). First, the committor probability is independent of time; second, the transition probability density W is evaluated at $\mathbf{x}$ rather than $\mathbf{x} - \delta\mathbf{x}$. The solution method is identical, however. We expand the right-hand side to second order in $\delta\mathbf{x}$ to give

$$\begin{aligned} q(\mathbf{x}) = \int d\delta\mathbf{x} \Big\{ & W(\delta\mathbf{x}, \mathbf{x}, \delta t)\, q(\mathbf{x}) + \sum_i \delta x_i W(\delta\mathbf{x}, \mathbf{x}, \delta t) \frac{\partial q(\mathbf{x})}{\partial x_i} \\ & + \sum_{ij} \frac{1}{2} \delta x_i \delta x_j W(\delta\mathbf{x}, \mathbf{x}, \delta t) \frac{\partial^2 q(\mathbf{x})}{\partial x_i \partial x_j} \Big\} \ . \end{aligned} \tag{2.11}$$

Performing the moment integrals (2.6) yields

$$\begin{aligned} q(\mathbf{x}) &= q(\mathbf{x}) + \sum_i A_i \delta t \frac{\partial q(\mathbf{x})}{\partial x_i} + \sum_{ij} \delta t D_{ij} \frac{\partial^2 q(\mathbf{x})}{\partial x_i \partial x_j} \\ 0 &= \sum_i \frac{\partial q}{\partial x_i} \left(\sum_j -\beta D_{ij} \frac{\partial V}{\partial x_j} + \frac{\partial D_{ij}}{\partial x_j} \right) + \sum_{ij} D_{ij} \frac{\partial^2 q}{\partial x_i \partial x_j} \equiv \hat{L}_{-}(q) \ . \end{aligned} \tag{2.12}$$

(2.12) is also known as the "backward Kolmogorov equation" and the operator $\hat{L}_-$ is the generator of the backward Kolmogorov process [28].

In principle, the backward Kolmogorov equation can be solved to give the committor probability for all $\mathbf{x}$ (imposing boundary conditions of $q = 0$ along the border of what is deemed the reactant well and $q = 1$ along the border of the product well). In practice, this is computationally intractable for problems of high dimensionality, and simply solving the equation for all possible configurations $\mathbf{x}$ may not yield much physical insight about the mechanism of the transition. Ideally, we would like to identify a single or small number of reaction coordinates that first of all, predict monotonic increase of the committor probability, and secondly, provide a physically intuitive picture of how the transition actually takes place. For example, for nucleation problems, the size of the nucleus (or the size of the largest nucleus present in the system) is a reaction coordinate that constitutes a good rough guess (the actual means by which the size is measured may be subject to refinement [25]). The defect-annealing problems presented in Chapter 3 of this thesis provide another example: The string method obtains an effective 1D reaction coordinate. By examining how a defective self-assembled polymer configuration changes to a defect-free configuration along this coordinate, we discover how the transition physically proceeds.

2.1.2 1-dimensional barrier crossing

It is helpful to consider the consequences of (2.8) and (2.12) for a 1-dimensional system. First of all, for a 1D system with potential $V(x)$, the reactant state's border at x_R, and the product state's border at x_P, the committor equation (2.12) can be integrated explicitly with boundary conditions $q(x_R) = 0$ and $q(x_P) = 1$ to yield

$$q(x) = \frac{\int_{x_R}^{x} dx\, D(x)^{-1} \exp[\beta V(x)]}{\int_{x_R}^{x_P} dx\, D(x)^{-1} \exp[\beta V(x)]} \tag{2.13}$$

(2.13) is fully general regardless of the potential's structure.

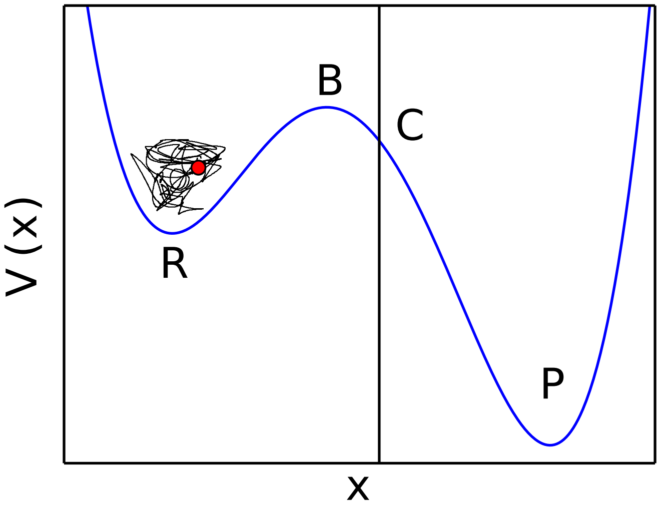

Figure 2.1: 1D potential with reactant well R, product well P, barrier B, and rescue-and-replace boundary condition imposed at C. The system fluctuates within well R; if it ever manages to reach C, it is intercepted by the ghost of Hans Kramers and thrown back into (rethermalized within) R.

Secondly, for systems with a single barrier peak higher than a few $k_B T$ where that peak is the dynamical bottleneck (a reasonable assumption unless diffusion varies very strongly with position) Kramers theory [29] yields a straightforward expression for the transition rate.[2] Consider the potential shown in Figure 2.1. For an ensemble of N systems that begin in well R, we seek a constant k such that $dN/dt = -kN$ at the moment the system is released. The Kramers argument accesses k by imposing a "rescue and replace" boundary condition: At a certain value of x past the barrier (far enough that the system's probability of return to the reactant well is small, for example, at C in Figure 2.1), we impose the condition that all trajectories reaching C are stopped and instantly returned to R (conceptually, fed back into the left-hand side of R at low x). This boundary condition, along with the system's natural Langevin dynamics (2.1), results in a quasi-steady-state distribution $\rho_{SS}(x)$ where systems within well R obey the Boltzmann distribution, but the product well P remains empty, and a constant flux (probability current) of systems attempt to cross into the product well only

---

[2] If the barrier is lower than a few $k_B T$, and therefore easily accessible by thermal fluctuations, or if the barrier is rough without a single peak that forms the dynamical bottleneck, a mean first passage time calculation [27, 30, 31] can be used to derive a general expression for the rate. However, I thought this presentation, which more closely resembles the arguments of Kramers and Langer, was more straightforward, and the Kramers result applies to the majority of systems considered in this thesis. For singly-peaked barriers higher than a few $k_B T$, the mean first passage time result is equivalent to the Kramers result.

to be intercepted at C. The constant current j_{SS} may be calculated from (2.9):

$$\begin{aligned} j_{SS} &= -\rho_{eq}(x)D(x)\frac{\partial}{\partial x}\Big(\rho_{eq}(x)\rho_{SS}(x)\Big) \\ -j_{SS}\,\frac{e^{\beta V(x)}}{D(x)} &= \frac{\partial}{\partial x}\Big(e^{\beta V(x)}\rho_{SS}(x)\Big) \\ j_{SS} &= -e^{\beta V(x)}\rho_{SS}\Big|_{x1}^{x2}\Big/\int_{x1}^{x2}\frac{e^{\beta V(x)}}{D(x)}dx \end{aligned} \tag{2.14}$$

where x_1 and x_2 are any two points we choose; for this purpose we choose $x_2 = C$ and $x_1 =$ some value less than (to the left of) R's minimum. But $\rho_{SS}(C) = 0$ by construction of the rescue-and-replace condition. Near R, $\rho_{SS}(x) = e^{-\beta V(x)}/Z_R$, since ρ_{SS} is essentially the probability distribution of particles thermalized in well R; $Z_R = \int_{\text{near R}} e^{-\beta V(x)}dx$ is the partition function of the system confined to well R. Therefore, the numerator of (2.14) becomes $-e^{\beta V(x)}\rho_{SS}|_{x1}^{C} = 0 + e^{\beta V(x_1)}e^{-\beta V(x_1)}/Z_R = 1/Z_R$. The denominator is dominated by the portion of the integral near the barrier peak B: $\int_{x1}^{x2} e^{\beta V(x)}/D(x)\,dx \approx \int_{\text{near B}} e^{\beta V(x)}/D(x)\,dx$. Putting all the pieces together, we find

$$j_{SS} = \left[\int_{\text{near R}} e^{-\beta V(x)}dx \int_{\text{near B}} \frac{e^{\beta V(x)}}{D(x)}dx\right]^{-1} . \tag{2.15}$$

This expression can be further simplified by expanding $V(x)$ in a power series about the bottom of well R and the peak of barrier B:

$$V_{\text{near R}} \approx V(x_R) + \frac{1}{2}V''(x_R)(x - x_R)^2 \ \ , \ \ V_{\text{near B}} \approx V(x_B) + \frac{1}{2}V''(x_B)(x - x_B)^2 \tag{2.16}$$

where x_R and x_B are the x-values of the minimum of well R and the peak of barrier B. Inserting these into (2.15), taking $D(x) \approx D(x_B)$ and performing the resulting Gaussian integrals (given that $V''(x_B) < 0$) yields

$$j_{SS} = \frac{\beta D(x_B)}{2\pi} \sqrt{V''(x_R)|V''(x_B)|}\, e^{-\beta[V(x_B) - V(x_R)]} \tag{2.17}$$

At the moment the rescue-and-replace condition is released, the time rate of change that the system will be present in R is $\int_C \mathbf{j} \cdot \hat{\mathbf{n}}\, dS$ which for a 1 dimensional system is simply j_{SS}. Therefore for a 1-dimensional system the current j_{SS} is exactly the desired rate constant k.

2.1.3 Generalization to higher dimensions; good and bad effective 1D coordinates

Langer [32–34] generalized the Kramers result to arbitrarily high dimensions. First, he confirmed that the transition is most likely to proceed across saddle

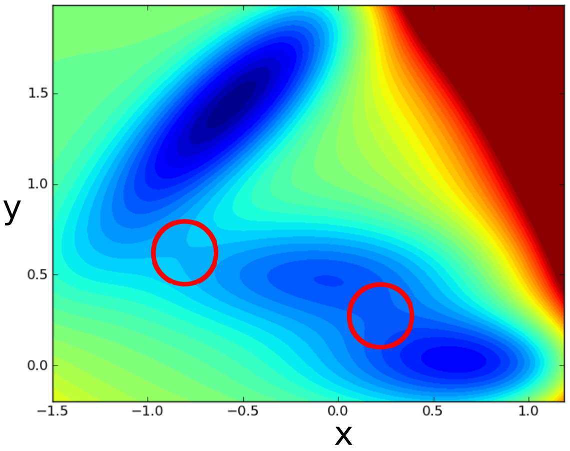

Figure 2.2: Saddle point regions on the 2D Mueller potential (Image of Mueller potential adapted from https://github.com/rmcgibbo/mullermsm.)

points regions, and that these saddle points are the dynamical bottlenecks that play the greatest role in determining the rate.[3] A saddle point is a point in the energy landscape $\mathbf{x}_{SP}$ where $\nabla \cdot V = 0$ and the Hessian matrix $H_{ij} = \frac{\partial^2 V}{\partial x_i \partial x_j}$ has a single negative eigenvalue whose corresponding eigenvector is the unstable direction. Conceptually, saddle points can be visualized as mountain passes in $V(\mathbf{x})$ (Figure 2.2). Langer's calculation proceeded in a manner similar to Kramers' 1D argument. Under the assumption that D_{ij} was position-independent, he expanded $V(\mathbf{x})$ to second order about the reactant well and saddle point in terms of the corresponding Hessians $H_{ij}(\mathbf{x}_R)$ and $H_{ij}(\mathbf{x}_{SP})$, performed the multidimensional Gaussian integrals corresponding to (2.17), and integrated the resulting

---

[3] This is usually a good assumption. For strongly anisotropic diffusion the system may exhibit saddle point avoidance [35].

expression for $\mathbf{j}$ across a surface spanning the saddle point to obtain the rate constant:

$$k = \frac{\beta}{2\pi}\left(\frac{\det H(\mathbf{x}_R)}{|\det H(\mathbf{x}_{SP})|}\right)^{1/2} \lambda_+ \exp[-\beta(V(\mathbf{x}_{SP}) - V(\mathbf{x}_R))] \tag{2.18}$$

where λ_+ is the only positive eigenvalue of the matrix $-D \cdot H(\mathbf{x}_{SP})$. He also identified the direction of the probability current at the saddle point, $\mathbf{j}_{SP}$, as pointing along the eigenvector corresponding to this eigenvalue.

The Langer result is accurate as long as D_{ij} is independent of position and the barrier is characterized by a single saddle point of height greater than a few k_BT that constitutes the dynamical bottleneck. However, we would like to describe the reaction's progress with a single reaction coordinate $c(\mathbf{x})$, an appropriate many-to-one mapping of the system's multiple microscopic or collective variables that predicts the committor. It may not be obvious why this reaction coordinate must be carefully chosen. It seems reasonable that one could project the system's multiple variables onto an arbitrary (perhaps physically guessed) reaction coordinate c, then sample the free energy $F(c)$ along that coordinate (*e.g.* by umbrella sampling or metadynamics, described shortly). The diffusion coefficient $D(c)$ can be found by exploiting the third equation of (2.6), $\langle \delta c^2 \rangle = 2\delta t\, D$ [36]: For a given value of c, say c_0, generate an ensemble of system configurations $\mathbf{x}$

such that $c(\mathbf{x}) = c_0$ and launch a swarm of short trajectories of length δt from each of these configurations. For each trajectory, compute c_{final} and the quantity $\delta c^2 = (c_{final} - c_0)^2$; average δc^2 over all tested trajectories to obtain $2\delta t\, D(c)$. Performing this procedure for a sequence of c_0 values yields the effective diffusion coefficient $D(c)$ along the reaction coordinate.[4] Once $F(c)$ and $D(c)$ have been obtained, (2.13) and (2.17) give the committor and rate (to obtain the rate alone, only $D(c)$ at the barrier peak is required), assuming the projection onto c was valid.

Unfortunately it is not that easy. A poorly chosen coordinate may not show a clear barrier. Also, the Kramers result assumes that c obeys the Smoluchowski equation. For a 1D reaction coordinate (obtained by projection of a higher-dimensional system whose dynamics obey the Smoluchowski equation) to itself obey a Smoluchowski equation, it must exhibit dynamical self-consistency [39]: For any two initial configurations $\mathbf{x}_1$ and $\mathbf{x}_2$ that map to the same value of c ($c(\mathbf{x}_1) = c(\mathbf{x}_2)$), $\rho(c,t)$ launched from $\mathbf{x}_1$ must be the same as $\rho(c,t)$ launched from $\mathbf{x}_2$.

Another pitfall is that the chosen coordinate may not be a good indicator of the committor probability (Figure 2.3). The histogram test, described in [40] and formalized in [41], can be used to evaluate how well a given reaction coordinate

---

[4] A similar procedure can be used to obtain effective diffusion tensors in higher-dimensional systems [37]. Also, a more refined procedure is outlined in [38].

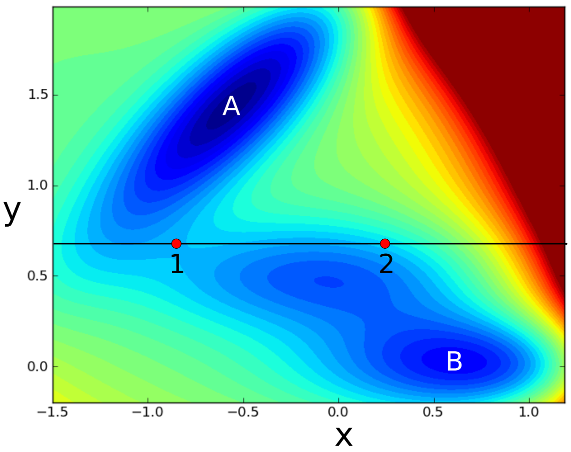

Figure 2.3: Under stochastic dynamics, a system starting at point 1 is much more likely to commit to well A, while a system starting at point 2 is much more likely to commit to well B, even though point 1 and 2 share the same y value. This indicates that y is a poor reaction coordinate to describe the transition between A and B on the 2D energy landscape.

RC corresponds to the committor. Basically, at a given isosurface of RC (say $RC = RC1$), an ensemble of $\mathbf{x}$ configurations such that $RC(\mathbf{x}) = RC1$ is chosen, and N trajectories are launched from each of those configurations. The number of trajectories N_p that reach the product well from each $\mathbf{x}$ is determined, giving an estimate of the committor probability q at each $\mathbf{x}$ as N_p/N. The estimated q values (one for each tested $\mathbf{x}$) are then histogrammed. This histogram (once normalized) approximates $\rho(q|RC1)$, the probability distribution of committor values on the isosurface $RC1$. If RC is a perfect reaction coordinate and N is very large, all $\mathbf{x}$ on the isosurface should yield the same q, and the histogram should resemble a delta function. In practice, since N is finite, the histogram is subject to sampling error, and for a perfect reaction coordinate will resemble a binomial distribution peaked about the value of q at $RC1$ (the sharpness of the distribution increases with the number of per-$\mathbf{x}$ samples N). By constructing the histogram and observing how closely it resembles a binomial distribution, one can quantify how closely the isosurface $RC1$ resembles an isosurface of q. Histograms should also be constructed at several other isosurfaces of RC, to make sure the predicted value of the committor at different values of RC varies monotonically as expected along RC (Figure 2.4). The histogram test is a stringent and reliable measure of reaction coordinate fitness, but requires constructing a new histogram for several isosurfaces of any reaction coordinate, and each histogram typically requires determining the long-time fate of tens of thousands of trajectories. It is usually impractical to test large numbers of trial reaction coordinates this way.

Berezhkovskii and Szabo [42] considered a reaction coordinate e consisting of the distance away from the saddle point along a linear vector $\mathbf{e}$ (specifically, $e(\mathbf{x}) = \hat{\mathbf{e}} \cdot (\mathbf{x} - \mathbf{x}_{SP})$, where $\mathbf{x}_{SP}$ is the location of the saddle point). They defined the free energy along this coordinate as

$$F(e) = -\frac{1}{\beta} \ln \int \delta(e - e(\mathbf{x}))\, e^{-\beta U(\mathbf{x})}\, d\mathbf{x} \tag{2.19}$$

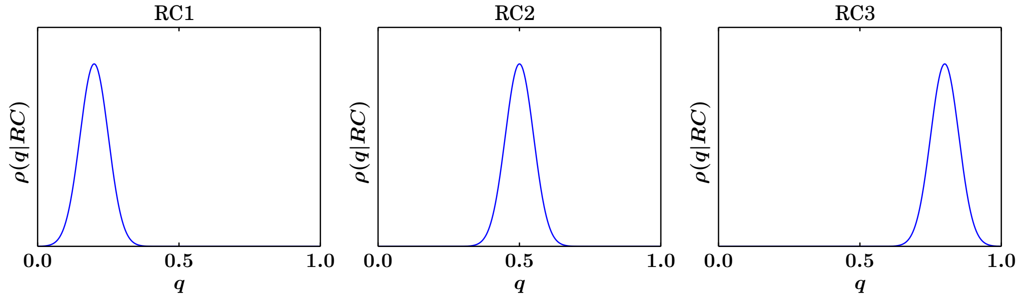

Figure 2.4: Illustration of what the committor distribution $\rho(q|RC)$ should look like at several points along a good effective 1D reaction coordinate RC. For RC=RC1 near the reactant well, the distribution of q values for the ensemble of microscopic configurations corresponding to RC = RC1 should resemble a binomial distribution peaked about a value $q < 0.5$ (left panel); for RC = RC2 "midway" between the reactant and product wells (the transition state ensemble, center panel), the q value distribution for the corresponding ensemble of microscopic configurations should be peaked about $q = 0.5$; for RC = RC3 nearer to the product well, the distribution of q values should be peaked about a value $q > 0.5$ (right panel).
A more detailed depiction of committor distributions for "good" and "bad" effective 1D coordinates is provided in Figure 9 of Ref. [40].

where $U(\mathbf{x})$ is the system's energy in terms of the dynamical variables $\mathbf{x}$ ($U(\mathbf{x})$ is a free energy if $\mathbf{x}$ are collective variables). To compute the rate according to Kramers theory, the effective 1-dimensional diffusion projected onto e at the saddle point is also required, and is given by $D_{eff} = \hat{e}_i D_{ij}(\mathbf{x}_{SP})\hat{e}_j$, which can be seen by considering a short-time displacement of the system launched from the saddle point:

$$
\begin{aligned}
&2\delta t\, D_{eff} = \langle \delta e^2 \rangle = \langle \hat{e}_i (\mathbf{x} - \mathbf{x}_{SP})_i \, \hat{e}_j (\mathbf{x} - \mathbf{x}_{SP})_j \rangle = \hat{e}_i \langle \delta x_i \delta x_j \rangle \hat{e}_j \\
&2\delta t\, D_{eff} = 2\delta t\, \hat{e}_i D_{ij}(\mathbf{x}_{SP}) \hat{e}_j \qquad (2.20)
\end{aligned}
$$

Assuming a position-independent but potentially anisotropic diffusion tensor D_{ij} as in Langer's argument, they then computed the rate constant k_{eff} along e using (2.19), (2.20), and (2.17), and compared it to the result k_{exact} of the full high-dimensional Langers theory obtained via (2.18). They showed that $k_{eff} > k_{exact}$ unless $\mathbf{e}_{opt}$ points along the single eigenvector of $-H(\mathbf{x}_{SP}) \cdot D$ whose eigenvalue is positive, in which case $k_{eff} = k_{exact}$. They also showed that this optimal direction $\mathbf{e}_{opt}$ is normal to the stochastic separatrix (isocommittor surface with $q = 0.5$) near the saddle point. Thus e along $\mathbf{e}_{opt}$is a good reaction coordinate in the twin senses that projection onto e yields an accurate rate and that isosurfaces of e are isosurfaces of q near the saddle point.[5]

These important results, which together with the Langer result are known as Kramers-Langer-Berezhkovskii-Szabo (KLBS) theory, firstly prove that a poorly or arbitrarily chosen 1D reaction coordinate overestimates the transition rate, and

---

[5] Recall that Langer identified the direction of probability current $\mathbf{j}_{SP}$ at the saddle point as the single eigenvector of $-D \cdot H(\mathbf{x}_{SP})$ whose eigenvalue is positive (as opposed to $-H \cdot D$ as is used for $\mathbf{e}_{opt}$). In general, if D is anisotropic, $\mathbf{j}_{SP}$ and $\mathbf{e}_{opt}$ do not point in the same direction, that is, the direction of maximum flux is not normal to the isocommittor surfaces.

secondly, provide an analytic expression for a good reaction coordinate when the diffusion tensor and (free) energy landscape are known.

Refs. [18, 43] describe an approach to evaluate reaction coordinates using the data-science-inspired technique of likelihood maximization. It is applicable to systems with diffusive (high-friction) and non-diffusive (low-friction/ballistic) dynamics. Likelihood maximization takes a set of trajectories (launch points $\mathbf{x}$ along with their fate, *i.e.* whether they ended up committing to the reactant or product well) and compares this data to the predictions of reaction coordinate formed by a some combination of whatever (collective) variables are deemed dynamically important. The functional form of this combination can be established as an ansatz, for example, $r(\mathbf{x}) = \alpha_0 + \sum_i \alpha_i \mathbf{x}$, where the reaction coordinate is formed as a linear combination of $\mathbf{x}$ variables with free parameters $\{\alpha\}$. Likelihood maximization can be used to optimize the free parameters of the ansatz. Alternatively, if a set of trial reaction coordinates is known, likelihood maximization can evaluate how reliably each trial coordinate predicts the fate of trajectories. A significant advantage of likelihood maximization is that the trajectories need only be harvested once; this data can then evaluate any number of trial RCs. However, for very high-dimensional systems like field theories the memory cost of saving all sampled trajectories may become prohibitive. For these types of systems one must first identify a low-dimensional set of dynamically important collective variables.

Peters *et al.* [39] showed that either dynamical self-consistency or likelihood maximization can be used to identify good reaction coordinates from a candidate set. They also showed that the reaction coordinate obtained from KLBS theory exhibits dynamical self-consistency. In other words, any of these three criteria may be used to identify good reaction coordinates, either by evaluating fitness of candidates, optimizing a variational ansatz, or analytically constructing the coordinate from a known diffusion map and free energy surface. Only then can one confidently project the system's dynamics onto the good coordinate and compute committor probabilities and rates using the 1D results (2.13) and (2.17). It should be emphasized that none of these techniques are feasible if one wishes to obtain a reaction coordinate directly in terms of a very high-dimensional set of microscopic variables.

2.1.4 Classical nucleation theory

Classical nucleation theory [44–46] uses the size of the nucleus r as the reaction coordinate, and models the extensive free energy of the nucleus as the sum of bulk and interfacial terms:

$$F(n) = -\alpha_V r^3 \Delta\mu + \alpha_S r^2 \gamma \ . \tag{2.21}$$

where $\Delta\mu = \mu_{metastable} - \mu_{stable}$ is the difference between the intensive bulk free energy densities of the metastable and stable phases, α_V is the (shape-dependent) factor relating r^3 to the nucleus volume, γ is the surface energy per unit area, and α_S is the factor relating r^2 to the surface area. For nucleation from a metastable phase, the interfacial term is energetically unfavorable (γ is positive) and the bulk term is energetically favorable ($-\Delta\mu$ is negative). For smaller nuclei, the surface term dominates, resulting in a positive free energy of formation. Within classical nucleation theory, this is the source of the barrier that must be crossed. After the nucleus reaches a critical size, the bulk term begins to take over; it becomes energetically favorable for the nucleus to grow rather than shrink. The critical nucleus size can be found by maximizing (2.21) with respect to r:

$$r_{crit} = \frac{2\alpha_S \gamma}{3\alpha_V \Delta\mu} \ . \tag{2.22}$$

The free energy barrier is $F(r_{crit})$. To obtain rates, classical nucleation theory models the growth process in terms of the rate at which (discrete) free particles in solution attach and detach themselves to a growing nucleus (details can be found in [46]). This particular analysis is irrelevant for present purposes, because all reaction coordinates we consider are inertialess and continuous and can therefore be treated using Kramers-Langer theory. However, in Chapter 5 we will draw on (2.21) and (2.22) to predict the size of critical nuclei for the disorder-to-lamellar transition of the Brazovskii model.

2.1.5 Methods for determining rates and free energy barriers

Systems in which an energy barrier must be crossed to transition from one state to another are difficult to tackle with brute-force simulations due to separation of timescales. The system may wait in a metastable configuration for a long time before a barrier-crossing event occurs due to thermal fluctuations. It is often more effective to use numerical techniques that bias or force the system to cross the barrier in some way. One useful family of techniques is the string method and its derivatives, which will be explained in detail in the next subsection. Only the string method is used in this thesis, but for completeness I mention several other important approaches often used for diffusive barrier-crossing problems.

The nudged elastic band (NEB) method [47] is a saddle-point-finding algorithm that operates (like the string method) by evolving a discrete chain of configurations that connects two locally stable states. To ensure that the configurations remain roughly evenly spaced, an artificial stretching force (*e.g.*, a Hookian spring force with adjustable spring constant) is imposed that penalizes distance between consecutive configurations. To avoid the elastic band "cutting corners" in the energy landscape due to its tension, the component of the stretching force normal to the string and the component of the physical force parallel to the string are both projected out. The resulting motion of the chain converges to a minimum energy path (MEP, described in detail in the next section) that crosses a saddle point.

Umbrella sampling [23, 24, 48, 49] and metadynamics [50–52] are two popular techniques to map out free energy surfaces for a a low- (1-, 2-, perhaps 3-)dimensional set of collective variables. In umbrella sampling, a restraining potential V is imposed to confine the system to a particular region of collective variable space. The probability distribution of the collective variables within this confining window under the influence of V is then sampled. This procedure is performed for a grid of windows in the collective variable space; the system's full free energy surface in the absence of V can be analytically reconstructed as described in [49]. Metadynamics begins by letting the system evolve freely, but adds a small biasing potential in the space of collective variables at each point the system visits, thus encouraging the system to explore elsewhere in the free energy landscape. Once the system's motion has continued long enough, the (biased) free energy surface in collective variable space is effectively flat (the biasing potential has exactly "filled in" the topography of the underlying physical free energy surface). The physical free energy surface can then be obtained as the negative of the accumulated biasing potential.

Transition path sampling [40, 53, 54] is a Monte Carlo technique to sample reactive trajectories (the ensemble of trajectories that start in the reactant basin R and end in the product basin P). In contrast to metadynamics and umbrella sampling, it requires no *a priori* identification of a few important collective variables. Typically, transition path sampling is accomplished via the shooting algorithm, which begins by launching a single trajectory from a microscopic configuration m_0 estimated to lie near the transition ($q = 0.5$) surface. Two short trajectories (one forward-time, one backward-time) are launched from m_0; if the forward-time trajectory reaches P and the backward-time trajectory reaches R, the trajectory as a whole (forward + backward, which I will denote fbm_0) is considered reactive. A new configuration m_0' is selected at some timeslice along fbm_0. m_0' is perturbed slightly to generate a new shooting point m_1, and new forward+backward trajectories are launched from m_1 to generate a new trajectory fbm_1. If fbm_1 is reactive, it is accepted with some probability based on detailed balance (see [53]), in which case a point m_0' is picked from a timeslice of fbm_1, perturbed slightly to generate the next shooting point m_2, and the process continues. If

fbm_1 was rejected, m_2 is picked from a perturbed point along the most recently accepted trajectory (in this case fbm_0) instead. The ensemble of shooting points $\{m\}$ collected this way characterizes the probability of reactive paths to visit different microscopic configurations. Many different methods of perturbing points along old reactive trajectories to generate new shooting points have been proposed, and prove more or less efficient for different physical systems. For diffusive barrier-crossing problems aimless shooting, in which the perturbation consists of freshly randomizing the microscopic momenta according to the Boltzmann distribution, has proven particularly efficient at generating new trajectories with high acceptance rates while injecting sufficient randomness to thoroughly sample the reactive trajectories [25, 54]. By itself, transition path sampling does not supply physical insight about the transition mechanism, or a single important reaction coordinate, but the transition path ensemble can be used to compute the transition rate as described in [53]. Also, the set of sampled shooting points $\{m\}$ along with their fates can supply the data for a likelihood maximization analysis to evaluate candidate reaction coordinates or construct optimal coordinates from a set of collective variables, as described in Section 2.1.3.

Transition interface sampling (TIS) [53, 55], forward flux sampling (FFS) [53, 56, 57], and milestoning [53, 58] are three techniques for computing rates that begin by dividing configuration space between R and P into n consecutive bins

B_i with interfaces λ_i defined by monotonically increasing values of an assumed 1D reaction coordinate. TIS estimates the reaction rate as

$$k = \Phi_0 P_R(\lambda_n|\lambda_1) \tag{2.23}$$

where Φ_0 is the flux of trajectories leaving R (bounded by λ_0) and $P_R(\lambda_n|\lambda_1)$ is the probability that a trajectory leaving R will reach λ_n (which forms the border of P). $P_R(\lambda_n|\lambda_1)$ can be decomposed into a sequence of discrete interface-crossing probabilities:

$$P_R(\lambda_n|\lambda_1) = \prod_{i=1}^{n-1} P_R(\lambda_{i+1}|\lambda_i) \tag{2.24}$$

where $P_R(\lambda_{i+1}|\lambda_i)$ is the probability that a trajectory coming from R and crossing λ_i will cross λ_{i+1} before returning to R. For a given i, TIS uses a shooting procedure similar to transition path sampling to sample the ensemble of trajectories that start in R and cross λ_i, taking note of whether each such trajectory reaches λ_{i+1} or returns to R to obtain $P_R(\lambda_{i+1}|\lambda_i)$. $P_R(\lambda_{i+1}|\lambda_i)$ is determined this way for each i and $P_R(\lambda_n|\lambda_1)$ is reconstructed from (2.24). FFS also estimates k using (2.23), but instead of a shooting procedure, FFS computes $P_R(\lambda_{i+1}|\lambda_i)$ by first launching a set of trajectories from R to see where they impact λ_1, then launching a set of trajectories from the recorded λ_1 impact points to see how many impact λ_2 rather than return to λ_0 (recording λ_2 impact points in the process), then launching a set of trajectories from the recorded λ_2 impact points to see what fraction manage to impact λ_3, and so forth. Milestoning does not use (2.23) and (2.24); rather, it prepares a constrained equilibrium ensemble confined to each λ_i and launches trajectories from a large number of configurations in this ensemble to determine the distribution of times required for systems beginning at λ_i to reach λ_{i+1} or λ_{i-1}. The distribution of times for each i can be used to reconstruct the overall transition rate. Note that since TIS, FFS, and milestoning measure fluxes directly from a sampled set of microscopic trajectories, without making any attempts to collapse the system's evolution to a 1D Smoluchowski equation, accurate rates can be obtained even if the assumed reaction coordinate used to defined the interfaces is not optimal.

2.2 The String Method

2.2.1 The MEP and the zero-temperature string method

The zero-temperature string method [59, 60] is an algorithm designed to find the minimum energy path (MEP) connecting two locally stable wells in a high-dimensional energy (or free energy) landscape. For the case of isotropic diffusion, and if the effective width [61] of a transition pathway is neglected, the MEP represents the most probable transition path according to the Freidlin-Wentzell theory of large deviations [62], and the peak of the MEP represents the critical barrier state. The MEP peak also corresponds to the saddle point used by Kramers-Langer-type theories of barrier-crossing problems [29, 34]. Also, if diffusion is isotropic and the energy landscape is not rough on a scale smaller than a few $k_B T$, arc length travelled along the MEP is a good reaction coordinate in the sense of Section 2.1.3, and the direction of the MEP across the saddle point is both the direction of probability current and the direction normal to the isocommittor surface $q = 0.5$.

For clarity we repeat the exposition of the string method found in Refs. [59, 60].

Let ϕ represent a configuration of a system's degrees of freedom, and $V(\phi)$ represent the potential energy corresponding to that configuration. Also let $V(\phi)$ have at least two local minima, labelled A and B, separated by a barrier, and let $\phi(\alpha)$ represent a continuous path between A and B parametrized by some distance measure α. Minimum energy paths connecting A and B are defined as follows: The path $\phi(\alpha)$ is an MEP if the force is parallel to the path along the path's entire length, in other words if

$$(\nabla V)^{\perp}(\phi(\alpha)) = 0 \tag{2.25}$$

where $(\nabla V)^{\perp}$ denotes the component of the force ∇V normal to the path $\phi(\alpha)$.

The string method is an algorithm designed to take a path ("string") between A and B, discretize it into a sequence of N system configurations ("images") $\phi_1 \ldots \phi_N$, and converge this sequence to a path satisfying (2.25). The full, smooth (non-discretized) path, $\phi(\alpha)$, can be recovered by assigning each image ϕ_i a distance coordinate α_i, then using cubic splines or some similar interpolation method to define a smooth parametric curve connecting them. The distance measure α, conventionally normalized to vary between 0 and 1 from ϕ_1 to ϕ_N, can be defined as the absolute (2.26a) or energy weighted (2.26b) arc length between the images:

$$\alpha_{i+1} = \alpha_i + \frac{|\phi_{i+1} - \phi_i|}{T} \tag{2.26a}$$

$$\alpha_{i+1} = \alpha_i + W\left(V(\phi_{i+1}), V(\phi_i)\right)\frac{|\phi_{i+1} - \phi_i|}{T}\,, \tag{2.26b}$$

where $|\phi|$ represents the L2 norm of ϕ, W is a positive definite weighting function, and T is a constant that enforces normalization of α. T is the total non-normalized arc length, e.g., $T = \sum_{i=1}^{N-1} |\phi_{i+1} - \phi_i|$ for (2.26a). To maintain resolution along the string, and ensure that images do not simply evolve to the lowest-lying state of their respective basins of attraction, images are forced to maintain equal spacing along the distance coordinate: $\alpha_i = \frac{i-1}{N-1}$.

Energy weighting causes points to cluster more strongly in regions of higher energy, improving resolution of barrier peaks (placing more images in a region increases the string's accuracy in that region; see Fig. 1 of Ref. [60]). Typically, W is a continuous, positive, monotonically increasing function of its arguments, which provides weighted coverage of the entire MEP from A to B. An example is the choice $W(E_i) = E_i$, where

$$E_i = \frac{(V(\phi_{i+1}) - V_{min}) + (V(\phi_i) - V_{min})}{2}\,, \tag{2.27}$$

and V_{min} is some low energy value such that $V(\phi_i) - V_{min}$ is positive for all i. This choice weights each arc length interval by the (averaged) energy of its nearest images relative to V_{min}; more aggressive schemes like $W(E_i) = E_i^2$ can also be employed. In the following text we will refer to schemes for which W is a continuous, positive, monotonically increasing function of its arguments as "conventional energy weighting" (conventional EW).

2.2.2 Algorithm

To calculate the MEP between A and B, the string is initialized such that ϕ_1 lies within A's basin of attraction and ϕ_N lies within B's basin of attraction. The intervening images are initialized according some scheme that gradually makes them less similar to ϕ_1 and more similar to ϕ_N (this scheme could be simple linear interpolation between ϕ_1 and ϕ_N, or it could be motivated by some physical intuition as to how the converged MEP will eventually appear). The initialization scheme should loosely, but need not stringently, satisfy the requirement of spacing the images equally along α; this criterion will soon be enforced by the evolution algorithm.

Once initialized, the string is evolved according to the following dynamics:

$$\dot{\phi}(\alpha) = -[\nabla V(\phi(\alpha))]^{\perp} + \lambda \hat{t}(\alpha) \tag{2.28}$$

where $[\nabla V(\phi(\alpha))]^{\perp}$ denotes the force projected into the plane normal to the path:

$$[\nabla V]^{\perp} = \nabla V - (\hat{t}(\alpha) \cdot \nabla V)\hat{t}(\alpha) \tag{2.29}$$

and $\hat{t}(\alpha) = \frac{\partial\phi(\alpha)/\partial\alpha}{|\partial\phi(\alpha)/\partial\alpha|}$ is the unit tangent to the path at α. This dynamics becomes

$$\dot{\phi}_i = -[\nabla V(\phi_i)]^{\perp} + \lambda \hat{t}_i \tag{2.30}$$

for the discretized string. The λ term is a Langrange multiplier designed to ensure equal-α spacing by forcing each image tangentially along the string in one direction or the other. It is clear that a string corresponding to a steady state of (2.28) will satisfy (2.25), as desired.

In practice, the terms on the right-hand side of (2.30) are time-split into 2 half-steps, which are repeated until convergence (stationarity).

Step 1: Independently evolve each image.

Each image is independently evolved according to $\dot{\phi}_i = -[\nabla V(\phi_i)]^\perp$ for a single discrete timestep. This can be done using any desired ODE or PDE integrator.

It was shown in Ref. [60] that projecting the force into the transverse plane is actually unnecessary, since any motion along $\hat{t}$ can be incorporated into the second term in (2.30). Therefore, it is equally suitable and usually more computationally convenient to evolve each image according to the full force, $\dot{\phi}_i = -\nabla V(\phi_i)$.

Step 2: Interpolate and reparametrize.

During Step 1, images on each side of the barrier will evolve away from the barrier, in the direction of their respective basins of attraction. To compensate and maintain resolution along the string, the images are repositioned to enforce equal spacing along α. This operation encodes the action of the $\lambda\hat{t}$ term in (5).

First, an arc length coordinate α_i is assigned to each image ϕ_i according to the chosen definition of α, e.g., (2.26a) or (2.26b). Then, a smooth, non-discretized

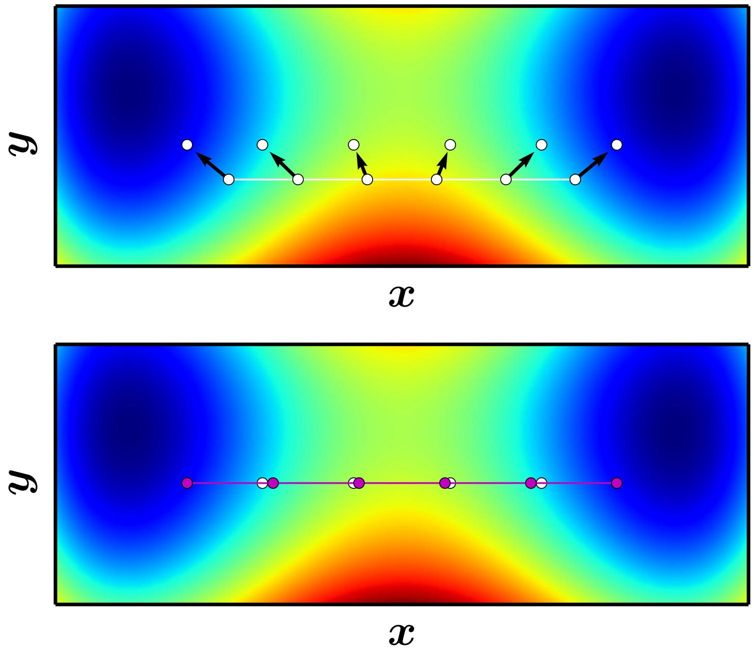

Figure 2.5: Upper panel: Step 1 of the string algorithm. Beads represent images. The white beads with a line through them represent the state of the string at the beginning of the timestep. Each image is evolved independently according to the full force (simplified string method). After this step, images are no longer evenly spaced across the barrier, resulting in nonuniform resolution of the MEP.
Lower panel: Step 2 of the string method. An interpolation (magenta line) is drawn between the recently evolved images (white beads) and the images at the end of the full timestep (magenta beads) are created by spacing them evenly along this interpolation, ensuring that coverage of the barrier region remains uniform as the string evolves.

path $\phi(\alpha)$ is recovered by interpolation. Finally, the discrete images are repositioned at uniform α-intervals along the smooth path. Note that for conventional energy weighting the endpoints ϕ_1 and ϕ_N are unaffected by the reparametrization, and eventually evolve to stationary configurations corresponding to A and B respectively.

Steps 1 and 2 are illustrated in Figure 2.5 for a 2D energy landscape. Figure 2.6 illustrates a converged MEP found by the string method for a 2D energy landscape with a twisting barrier region. The endpoints of the string naturally seek local minima, since they are unaffected by the interpolation and reparametrization step. Figure 2.6 also demonstrates how energy weighting helps to concentrate images near the barrier peak.

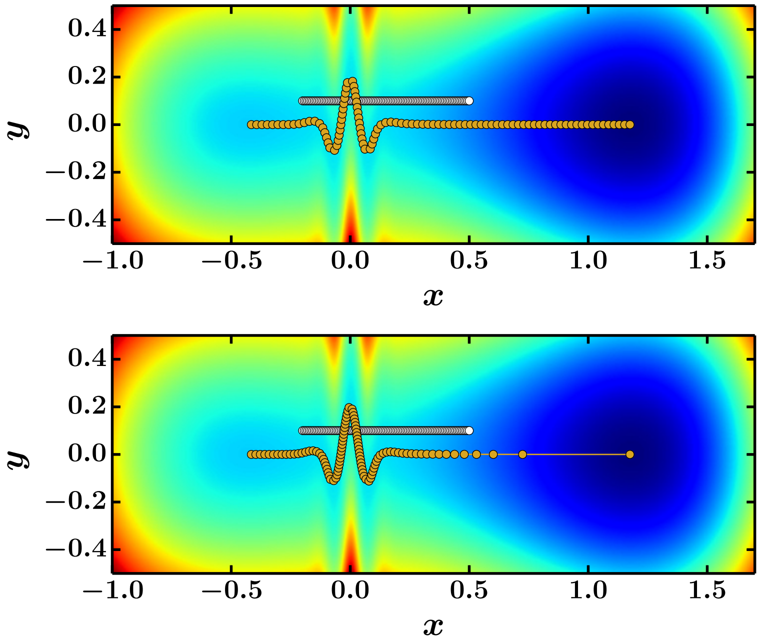

Figure 2.6: Initialized (white) and converged (gold) strings on an example 2D energy landscape with a twisting barrier region. Upper panel: energy weighting not used.
Lower panel: using energy weighting with $W(E) = \exp(4E)$.

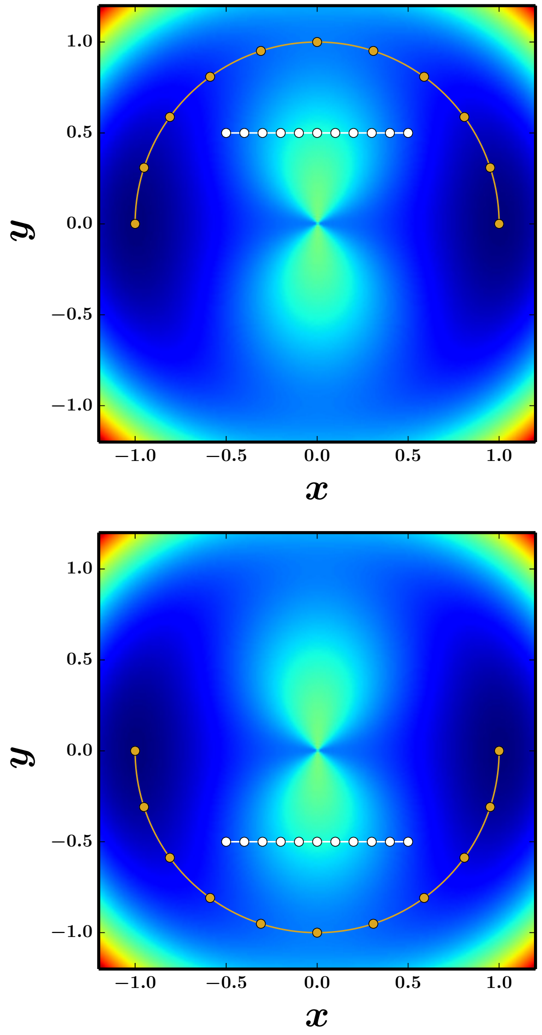

Figure 2.7: Upper panel: Initialized (white) and converged (gold) string for images initialized at $y = 0.5$ on a 2D free energy surface that offers multiple local MEPs.
Lower panel: Initialized (white) and converged (gold) string for images initialized at $y = -0.5$.

2.2.3 Initialization dependence

One important feature of the string method is that the converged MEP is a local MEP, and is not necessary unique. If the free energy landscape offers multiple MEPs between two locally stable wells, the MEP to which the string converges will depend on how it is initialized (Figure 2.7). We exploit this property in Chapters 3 and 5 to search for multiple MEPs. For example, in Chapter 3 we find that if the string is initialized in a spatially symmetric way, the returned MEP is also spatially symmetric, but if the MEP is initialized in a spatially asymmetric way, the returned MEP is spatially asymmetric with different qualitative and quantitative features. In Chapter 5, we search for critical nuclei that are expected to contain certain defect structures by seeding images with the anticipated defects.

2.2.4 Image climbing

The converged string traces out a discretized minimum energy path. Due to discretization error, simply taking the highest-energy image to give the barrier peak is likely to give an approximate, but inexact, estimate of the actual critical barrier state. A computationally efficient means to obtain a more precise estimate of the critical barrier state starting from an already-converged string is presented in [60]. The algorithm proceeds as follows:

First, use the initial converged string to estimate the string's tangent vector in the vicinity of the peak. This could be done, for example, by setting the tangent vector near the peak $\hat{t}^*$ according to

$$\hat{t}^* = \frac{\phi_{b+1} - \phi_b}{|\phi_{b+1} - \phi_b|} \tag{2.31}$$

where ϕ_b and ϕ_{b+1} are the two images along the initial converged string that immediately straddle the barrier.

Next, create a test image ϕ_t and initialize it near the barrier peak estimated by the initial converged string. This can easily be done by setting, *e.g.*, $\phi_t = \phi_b$ or $\phi_t = \phi_{b+1}$. ϕ_t is then evolved according to the following dynamics:

$$\dot{\phi}_t = -\nabla V(\phi_t) + 2\left(\nabla V(\phi_t) \cdot \hat{t}^*\right)\hat{t}^* \tag{2.32}$$

The $2\left(\nabla V(\phi_t) \cdot \hat{t}^*\right)\hat{t}^*$ term reverses the component of the force $-\nabla V(\phi_t)$ that is tangent to the MEP near the saddle point. Conceptually, what this dynamics accomplishes is to force ϕ_t to remain within the MEP valley but climb up the MEP instead of relaxing down along it.

If $\hat{t}^*$ provides a good estimate for the MEP tangent vector in the vicinity of the peak (that is, if the initial string used to obtain $\hat{t}^*$ is sufficiently well-resolved) the test image will converge to a state where it undergoes infinitesimal oscillations about the exact barrier peak.

This technique is known as image climbing. It is computationally inexpensive once the initial converged string has been obtained, because it only involves updating a single image and requires no further interpolation or reparametrization steps.

Although image climbing is a helpful technique for users of the string method to keep in mind, in practice we usually find that for well-resolved strings, using image climbing does not significantly change the estimated barrier state or the barrier's energy. For the simulations presented in Chapters 3, 4, and 5, we do not employ image climbing, and take the highest-energy image found by the discrete string across a given barrier to represent the barrier state and energy height of that barrier.

2.2.5 Variants of the zero-temperature string method

As previously mentioned, since its original formulation the string method has been applied to a wide variety of physical systems. Many variants of the zero-temperature string method have been introduced that enhance its utility for different types of problems.

In [60] the authors note that projecting the force into the tangent hyperplanes is unncessary. Simply evolving images according to the full force yields the same converged MEP, and in fact demonstrates superior convergence characterstics in addition to favorable computational simplicity.

In [63], Peters *et al.* introduces the growing string method, which begins with endpoints in two separate wells (reactant or product states) then successively adds images further into the interior as the string evolves, enabling efficient blind exploration of a energy landscape where only the reactant and product states are known. The growing string method has received a good deal of attention as a tool for exploring unknown energy landscapes, and numerous incremental improvements have been devised [64–70].

Ren and Vanden-Eijnden [71] introduce a climbing string method that starts entirely within a single metastable well; the force on one endpoint is reversed in a manner similar to that of image climbing, which causes that endpoint to climb to the nearest (initialization-dependent) saddle point, while the remainder of the string traces out the path back down to the well. This method is useful for exploring saddle points around a known minimum without needing to compute the full path to a different well.

Behn *et al.* [72] introduce a freezing string method that grows into the interior of an unknown energy landscape in a manner similar to the growing string method, except that images are fixed in place and no longer evolved once they have been used to compute the growth directions. Chaffey-Millar *et al.* [73] introduce the searching string method, which progressively adds images into the region of the string estimated to bracket the barrier state. Du and Zhang [74] introduce a string method to handle Hamiltonians with constraints.

Backofen and Voigt [75] introduce a fixed arc length string method to study nucleation in phase-field crystals. Their method begins by running a coarse string method calculation of the full MEP between the metastable and stable states. They use this calculation to estimate the arc length necessary to resolve the barrier region, then run a fine calculation where one endpoint is fixed in the metastable well and the remaining images are draped across the barrier, but constrained to trace out an arc length equal to the estimated arc length from the prior coarse calculation. This procedure successfully focuses all images within the barrier region.

In Chapter 4, I describe “truncation-based energy weighting,” (TBEW) my own contribution to this literature. Truncation-based energy weighting actively truncates the string as it evolves, forcing all images to remain within and cover uniformly a desired barrier region. TBEW is ideally suited to problems with small energy barriers, and nucleation problems in particular. It is more convenient than the fixed arc length string method proposed in [75], because the fixed arc length method requires a preliminary coarse string calculation to estimate the arc length required to resolve the nucleation barrier, while a TBEW calculation can proceed in one step.

2.2.6 The string method beyond mean-field theory

The string method as described above determines a minimum energy path purely at a mean-field level. It does not take into account the influence of anisotropic or position-dependent diffusion on system's motion, nor does it account for fluctuations about the minimum energy path (the "width" of the transition pathway). The physical behavior of a system in the presence of fluctuations may exhibit significant qualitative differences from its behavior predicted by mean-field theory; for example, the system may prefer to fluctuate its way across a high, broad saddle point in the free energy landscape rather than a lower but narrower saddle point. Also, if the mean-field energy landscape contains roughness on the scale of thermal fluctuations, a zero-temperature string calculation may easily find its endpoints trapped in spurious small wells, and the barriers it traces out will be affected by small rough features that in reality do not have a significant impact on the system's dynamics (see *e.g.*, Figure 1 of Ref. [76]).

Numerous extensions of the string method have been devised to quantify the influence of fluctuations and anisotropic diffusion, as well as to allow operation of the string method in reduced-dimensional spaces of collective variables (although to my knowledge, a string method that simultaneously accounts for both diffusive and fluctuation effects has not been devised).

Hyperplane sampling to obtain free energy along a converged zero-temperature string

The simplest such extension is the observation of E and coworkers [59] that by starting with a converged zero-temperature string and sampling a certain quantity in the hyperplanes normal to the string at each image, the free energy in these hyperplanes can be determined, giving the free energy barrier (not just the mean-field energy barrier) along the string's arc length and thus a measure of the effective width of the transition pathway. The procedure is briefly explained but not explicitly derived. I rederive it here since it involves some tricks the authors do not mention.

E and coworkers begin by defining the free energy difference between a given arc length coordinate α and the start of the string $\alpha = 0$ as

$$F(\alpha) - F(0) = -\frac{1}{\beta}\ln[Z(\alpha)/Z(0)] \tag{2.33}$$

where $H(x)$ is the Hamiltonian as a function of the microscopic coordinates x (x here represents a large set of microscopic variables, not a single variable). $Z(\alpha)$ is the system's partition function constrained to the hyperplane normal to the string at point α, and is given by

$$Z(\alpha) = \int_{S^*(\alpha)} e^{-\beta H(x)} dx \tag{2.34}$$

in which $S^*(\alpha)$ represents the normal hyperplane. (2.34) may equivalently be written as

$$Z(\alpha) = \int e^{-\beta H(x)} \delta\left(\hat{t}(\alpha) \cdot (x - \phi)\right) dx \tag{2.35}$$

where the integral is now carried out over all space and the hyperplane constraint is supplied by the delta function. ϕ represents the microscopic coordinates $x(\alpha)$ along the string, and as before, $\hat{t}(\alpha)$ represents the unit tangent vector $\frac{\partial\phi}{\partial\alpha}/|\frac{\partial\phi}{\partial\alpha}|$. To streamline notation, as in Ref. [59] we will occasionally write derivatives with respect to α as a subscripted α, *e. g.*, $\frac{\partial\phi}{\partial\alpha}$ is ϕ_α.

To determine the free energy difference along the string, a thermodynamic-integration-like procedure may be employed starting from the identity $F(\alpha) - F(0) = \int_0^\alpha \frac{\partial F}{\partial\alpha} d\alpha$. From 2.35, we have

$$\frac{\partial F}{\partial\alpha} = -\frac{1}{\beta}\frac{1}{Z(\alpha)} \int e^{-\beta H(x)} \frac{\partial}{\partial\alpha} \left(\delta\left(\hat{t}(\alpha) \cdot (x - \phi)\right)\right) dx \tag{2.36}$$

or equivalently, defining $u \equiv \hat{t}(\alpha) \cdot (x - \phi)$ and using the chain rule,

$$\frac{\partial F}{\partial \alpha} = -\frac{1}{\beta} \frac{1}{Z(\alpha)} \int e^{-\beta H(x)} \frac{\partial \delta(u)}{\partial u} u_\alpha \, dx \; . \tag{2.37}$$

To deal with the $\frac{\partial \delta(u)}{\partial u}$ term, we note that

$$\frac{\partial \delta(u)}{\partial x_i} = \frac{\partial \delta(u)}{\partial u} \frac{\partial u}{\partial x_i} = \hat{t}_i \frac{\partial \delta(u)}{\partial u} \tag{2.38}$$

in which x_i represents the ith microscopic coordinate and $\hat{t}_i$ represents the ith component of $\hat{t}$. We then take the dot product of both sides of (2.38) with $\hat{t}$:

$$\sum_i \hat{t}_i \frac{\partial \delta(u)}{\partial x_i} = \frac{\partial \delta(u)}{\partial u} \sum_i \hat{t}_i^2 = \frac{\partial \delta(u)}{\partial u} \tag{2.39}$$

in other words

$$\hat{t} \cdot \nabla \delta(u) = \frac{\partial \delta(u)}{\partial u} \tag{2.40}$$

where ∇ is the gradient in the space of x, *i.e.*, $\nabla_i = \frac{\partial}{\partial x_i}$. Meanwhile, the u_α term of (2.37) is simply

$$u_\alpha = \hat{t}_\alpha \cdot x - (\hat{t} \cdot \phi)_\alpha \; . \tag{2.41}$$

Substituting (2.40) and (2.41) back into (2.37), we obtain

$$\frac{\partial F}{\partial \alpha} = -\frac{1}{\beta}\frac{1}{Z(\alpha)} \int e^{-\beta H(x)}\, \hat{t} \cdot \nabla \delta(u) \left[\hat{t}_\alpha \cdot x - (\hat{t} \cdot \phi)_\alpha\right] dx\ . \tag{2.42}$$

Integrating by parts on each $\frac{\partial}{\partial x_i}$ of the ∇ yields

$$\begin{aligned}\frac{\partial F}{\partial \alpha} = -\frac{1}{\beta}\frac{1}{Z(\alpha)} \int dx \Big\{ &\beta\, (\hat{t} \cdot \nabla H(x))\, e^{-\beta H(x)}\, \delta(u)\ \left[\hat{t}_\alpha \cdot x - (\hat{t} \cdot \phi)_\alpha\right] \\ &- e^{-\beta H(x)}\, \delta(u)\, \hat{t}_\alpha \cdot \hat{t} \Big\}\ .\end{aligned} \tag{2.43}$$

This expression can be simplified by noting that since $\hat{t} \cdot \hat{t} = 1$, $(\hat{t} \cdot \hat{t})_\alpha = 2\hat{t}_a \cdot \hat{t} = 0 \implies \hat{t_\alpha} \cdot \hat{t} = 0$, so the term on the second line of (2.43) drops out, giving

$$\frac{\partial F}{\partial \alpha} = \frac{1}{Z(\alpha)} \int (\hat{t} \cdot \nabla H(x))\, e^{-\beta H(x)}\ \left[(\hat{t} \cdot \phi)_\alpha - \hat{t}_\alpha \cdot x\right] \delta(u)\, dx\ . \tag{2.44}$$

Recalling that $\delta(u) = \delta\left(\hat{t}(\alpha) \cdot (x - \phi)\right)$ serves to confine the system to the hyperplane normal to the string at α, we recognize that the right-hand side of (2.44) is simply the thermal average of the quantity $(\hat{t} \cdot \nabla H(x)) \left[(\hat{t} \cdot \phi)_\alpha - \hat{t}_\alpha \cdot x\right]$ in that hyperplane:

$$\frac{\partial F(\alpha)}{\partial \alpha} = \Big\langle \left(\hat{t} \cdot \nabla H(x)\right) \left[(\hat{t} \cdot \phi)_\alpha - \hat{t}_\alpha \cdot x\right] \Big\rangle_{S^*(\alpha)} \tag{2.45}$$

in agreement with Eq. (9) of Ref. [59].[6] By sampling this quantity in the tangent hyperplane at each discrete image along the string (through a constrained Langevin dynamics, for example), $\frac{\partial F}{\partial \alpha}$ at that image can be computed. The free energy difference between the beginning of the string and a given image i at arc length coordinate α_i can be approximated according to

$$F(\alpha_i) - F(0) = \int_0^{\alpha_i} d\alpha' \, \frac{\partial F(\alpha')}{\partial \alpha'} \approx \sum_{j=2}^{i} (\alpha_j - \alpha_{j-1}) \left. \frac{\partial F}{\partial \alpha} \right|_{\text{at image j}} \tag{2.46}$$

where images are indexed from 1 and α_i is the arc length coordinate of image i (the integral is approximated as a Riemann sum along the images).

Finite-temperature string method

As mentioned in Section 2.1, the ideal reaction coordinate is the committor probability. It would be helpful to have a string method that yielded a reaction coordinate corresponding to the committor probability, taking into account the width of the transition path as well as any roughness that might exist on the scale of thermal fluctuations. In Refs. [61, 76–78] Vanden-Eijnden, E, Ren and coworkers outline a method to find a string whose normal hyperplanes are isocommittor surfaces (to within a planar approximation near the string, at least). This

---

[6] If you happen to look up equation (9) of Ref. [59], in their presentation one of the α subscripts is primed while the other is unprimed. This is a typo on their part; both *alpha* subscripts should be primed. Eq. (10) of Ref. [77] displays a correct version.

means that the committor probability increases monotonically along the string's arc length α, and the committor probability for a system configuration ϕ on or near the string can be determined by identifying the arc length coordinate of the normal hyperplane in which ϕ resides (this is accomplished by simply picking out the point on the string nearest to ϕ in configuration space).

Vanden-Eijnden and coworkers show that the string whose normal hyperplanes are isocommittor surfaces is a "principle curve," a curve that is everywhere equal to the equilibrium thermal average of the system's position in the curve's tangent hyperplanes (in other words, if the system is confined to one of those hyperplanes and allowed to fluctuate, its resulting thermally averaged position will be exactly the spot at which the principle curve intersects the plane). They propose several algorithms to find this curve in a space of high-dimensional variables. The hyperplane formulation [77] fixes the string at timestep t, initializes a test system confined to the tangent hyperplane at each image, allows each of those test systems to fluctuate until the approximate thermal average position in each tangent hyperplane is obtained, then moves each image to the thermally averaged position in its corresponding tangent hyperplane to generate the string at $t + 1$. The Voronoi cell formulation [76] is similar, but instead of confining the test systems to hyperplanes, it confines the test system for image n to the Voronoi cell region of configuration space closest to image n, and the test system finds the thermal averaged position within the Voronoi cell. The replicas formulation [61] takes a collection of M replica strings and evolves each of their images according to $\nabla V +$ noise, and defines the nth image of the "finite temperature string," $\phi_n^{(FT)}$ as the average of the nth images of the replicas, $\phi_n^{(FT)} = \frac{1}{M}\sum_{i=1}^{M} \phi_n^{(i)}$.

Once the principle curve has been obtained, the free energy along the curve can be computed using (2.45) and (2.46). In the case of the Voronoi cell formulation, free energy differences between consecutive cells can also be obtained by counting fluxes across cell boundaries (the number of times each test system attempts to cross the boundaries of its cell during the confined thermal average). As long as diffusion is isotropic and position-independent, arc length along a converged finite temperature string is guaranteed to be a good reaction coordinate in the sense of Section 2.1.3, even if the energy landscape is rough on the scale of $k_B T$.

A weakness of the finite-temperature string algorithm is that since its evolution is dictated by thermal averages, diffusive effects are washed out, and do not affect the string's motion or the converged pathway. In fact, the math shown in [78] indicating that the principle curves' normal hyperplanes are also (approximately) isocommittor surfaces is only guaranteed to work in the case of isotropic, position-independent diffusion.

String method in collective variables

Another variant is the string method in collective variables [79, 80], which treats images as points in a reduced-dimensional space of CVs. Images are evolved according to a potential of mean force multiplied by a mobility tensor arising from the curvilinear nature of the CVs (see [79] for details). The string method in collective variables converges to a local minimum free energy path (MFEP) in the space of the chosen CVs. The method can feasibly treat large numbers of CVs (unlike metadynamics or umbrella sampling, which become computationally intractable for more than 2 or 3). This gives researchers flexibility in choosing what CVs to use, and to what extent the system's microscopic degrees of freedom should be coarse-grained. As a result, the method has found popularity in exploring free energy barriers for a variety of problems, including conformational changes in myosin [81], hydrophobic collapse of a hydrated chain [82], self-assembly of block copolymers into a network morphology [83], and membrane fusion [84].

String method with swarms of trajectories

The string method in collective variables and the finite-temperature string method succeed in capturing free-energy barriers, but fail to account for anisotropic diffusion. The string method with swarms of trajectories, introduced by Pan *et al.* [85], takes the opposite approach, emphasizing diffusion over free energy. At each timestep, it launches a swarm of short trajectories from each image to determine the average diffusive drift, then moves the images in the direction of the drift (reinterpolating as usual after each move to maintain equal spacing of images). The algorithm eventually converges to a pathway that is everywhere parallel to the average diffusion current; this is also the pathway of maximum reactive flux or “most probable transition path” (MPTP). Like the finite temperature string method, in principle the string method with swarms of trajectories can operate either in a space of collective variables or in the full Cartesian space of a system’s microscopic coordinates. Pan *et al.* showed that the MPTP constituted a good reaction coordinate for two model systems, provided suitably chosen collective variables (or a suitably high number of collective variables) were used.

The swarms-of-trajectories method and the finite-temperature string method can in a sense be considered complementary approaches, because the former accounts for diffusion but not path width while the latter accounts for path width but not diffusion.

2.3 Self-consistent field theory

The interesting length scales one would like to capture in simulations of (co)polymer melts and solutions are typically those associated with copolymer microphase domains (10s to 100s of nanometers). Particle-based modeling of polymer melts and solutions on these length scales is difficult [86]. Direct atomistic molecular dynamics simulations are computationally infeasible. Even if a coarse-grained particle-based model is used, a number of challenges remain, *e.g.*, the lack of access to an explicit free energy functional, and slow kinetics associated with self-assembly processes.

Self-consistent field theory (SCFT) [87, 88] is a *field*-based model of polymer fluids capable of simulating polymer melts and solutions on the interesting mesoscopic length scales mentioned above. SCFT has established itself as a powerful tool to study both directed and non-directed self-assembly. SCFT offers a number of advantages over particle-based models, for example, the field-based model transparently handles issues like chain crossing, and actually becomes more accurate with increasing polymer molecular weight and chain density. Additionally, SCFT offers explicit access to an analytic Hamiltonian. Within the saddle point approximation (*i.e*, if one assumes that the dominant contribution to the partition function $Z = \int \mathcal{D}\phi \exp\left(-\beta H[\phi]\right)$ comes from some field configuration ϕ^* that minimizes H), the partition function may be approximated as $Z \approx \exp\left(-\beta H[\phi^*]\right)$ and the free energy may be accessed directly as $F \approx H[\phi^*]$.

SCFT is based on the *Hubbard-Stratonovich transformation.* This procedure begins with a partition function whose Hamiltonian is expressed in terms of explicit microscopic particle coordinates $\{\mathbf{r}_j\}$, and reexpresses that partition function as a functional integral over a set of density fields $\rho_K(\mathbf{r})$ and conjugate auxiliary fields $w_K(\mathbf{r})$. K is an index running from 1 to i, where i is the number of monomer and solvent molecule species present in the fluid. The transformation from a particle-based to a field-based representation of the partition function is mathematically exact, and yields a Hamiltonian expressed as a functional of $\rho_K(\mathbf{r}), w_K(\mathbf{r})$. In many cases of practical interest, the functional integrals over the set of one or more density fields ρ_K may be performed analytically, leaving a Hamiltonian that is a functional of the auxiliary fields $w_K(\mathbf{r})$ alone.

2.3.1 The diblock copolymer + homopolymer melt

To illustrate the Hubbard-Stratonovich transformation more explicitly, and to set up future discussions of the computational challenges associated with SCFT as well as the subtleties associated with applying the string method to SCFT, I derive the SCFT Hamiltonian for an AB+A+B diblock copolymer+homopolymer melt starting from the microscopic Hamiltonian for a Gaussian chain, as expressed in [87].

All subsequent SCFT calculations (presented in Chapter 4) use the Hamiltonian derived here, either with or without the inclusion of added A- and B-homopolymer.

Single-chain machinery

The microscopic Gaussian chain Hamiltonian describes a single polymer chain as a sequence of N statistical segments. Each statistical segment is assumed to consist of a sufficient number of monomer repeat units such that the segment as a whole acts like an entropic spring, with a harmonic penalty for stretching. Therefore, the polymer can be thought of as a discrete sequence of beads connected by springs ("discrete Gaussian chain model"), and its Hamiltonian can be written as

$$U_0 = \sum_{i=1}^{N} \frac{3k_BT}{2b_i^2}\mathbf{b}^2 \tag{2.47}$$

where the bond vector $\mathbf{b}$ is the distance between bead i and bead $i-1$ (beads are indexed from 0). b is the *statistical segment length* or *Kuhn length* associated with our choice of statistical segment size. A useful quantity based on U_0 is the transition probability density $\mathbf{\Phi}(\mathbf{r}_i - \mathbf{r}_{i-1}; \mathbf{r}_{i-1})$, the normalized conditional probability density that bead i lies at position $\mathbf{r}_i$ given that bead $i-1$ lies at position $\mathbf{r}_{i-1}$:

$$\mathbf{\Phi}(\mathbf{r}_i - \mathbf{r}_{i-1}; \mathbf{r}_{i-1}) = \left(\frac{3}{2\pi b^2}\right)^{3/2} \exp\left[\frac{-3|\mathbf{r}_i - \mathbf{r}_{i-1}|^2}{2b^2}\right] = \left(\frac{3}{2\pi b^2}\right)^{3/2} \exp\left[\frac{-3|\mathbf{b}|^2}{2b^2}\right] \tag{2.48}$$

Similarly, if the chain is considered to be continuous, its Hamiltonian can be written as

$$U_0[\mathbf{r}(s)] = \frac{3k_BT}{2b^2}\int_0^N ds \left|\frac{d\mathbf{r}(s)}{ds}\right|^2 \tag{2.49}$$

where the contour variable s can be thought of as a "mass distance" along the chain that is linearly proportional to the number of statistical segments (or monomer repeat units) contained in the interval 0 to s. U_0 is now a *functional* of the continuous function $\mathbf{r}(s)$. (2.49) is known as the Edwards Hamiltonian. For the Edwards Hamiltonian, the transition probability density that a contour point s lies at position $\mathbf{r}$ given that point $s - \Delta s$ lies at position $\mathbf{r} - \Delta\mathbf{r}$ is given by

$$\mathbf{\Phi}(\Delta\mathbf{r};\mathbf{r}-\Delta\mathbf{r}) = \left(\frac{3}{2\pi b^2\Delta s}\right)^{3/2}\exp\left(-\frac{3|\Delta\mathbf{r}|^2}{2b^2\Delta s}\right) \tag{2.50}$$

Since (2.50) is a transition probability, we may build up the probability density $p_0(\mathbf{r}, s)$ that the contour point s lies at position r using a Chapman-Kolmogorov prescription [26, 27]:

$$p_0(\mathbf{r}, s+\Delta s) = \int d(\Delta\mathbf{r})\,\mathbf{\Phi}(\Delta\mathbf{r};\mathbf{r}-\Delta\mathbf{r})p_0(\mathbf{r}-\Delta\mathbf{r}, s) \tag{2.51}$$

The transition probability for a short jump depends only on the jump distance $\Delta\mathbf{r}$ and not on the initial position $\mathbf{r}$, so is straightforward to expand (2.51) to first order in Δs and second order in $\Delta\mathbf{r}$:

$$\begin{aligned} p_0(\mathbf{r},s)+\Delta s\frac{\partial}{\partial s}p_0(\mathbf{r},s) &= \int d(\Delta\mathbf{r})\,\mathbf{\Phi}(\Delta\mathbf{r})p_0(\mathbf{r},s) \\ &\quad-\int d(\Delta\mathbf{r})\,\mathbf{\Phi}(\Delta\mathbf{r})\,\Delta r_a\frac{\partial}{\partial r_a}p_0(\mathbf{r},s) \\ &\quad+\int d(\Delta\mathbf{r})\,\mathbf{\Phi}(\Delta\mathbf{r})\,\Delta r_a\Delta r_b\frac{\partial}{\partial r_a}\frac{\partial}{\partial r_b}\nabla p_0(\mathbf{r},s) \end{aligned} \tag{2.52}$$

a and b run over the Cartesian indices x,y,z. The $\Delta\mathbf{r}$ integrals are now Gaussian integrals that may be performed explicitly, yielding

$$\begin{gathered} \int d(\Delta\mathbf{r})\,\mathbf{\Phi}(\Delta\mathbf{r})=1\;,\;\int d(\Delta\mathbf{r})\,\mathbf{\Phi}(\Delta\mathbf{r})\,\Delta r_{x,y,z}=0\;, \\ \int d(\Delta\mathbf{r})\,\mathbf{\Phi}(\Delta\mathbf{r})\,\Delta r_a\Delta r_b=\frac{b^2\Delta s}{3}\delta_{ab} \end{gathered} \tag{2.53}$$

Substituting eqs. 2.53 into eq. 2.52, we find the Fokker-Planck equation associated with the Chapman-Kolmogorov equation:

$$\frac{\partial}{\partial s}p_0(\mathbf{r},s)=\frac{b^2}{6}\nabla^2 p_0(\mathbf{r},s)\;. \tag{2.54}$$

which can be solved to find the desired probability density subject to a given initial condition (the spatial probability distribution $p_0(\mathbf{r},s=0)$ associated with the beginning of the chain).

To proceed from these concepts to a full SCFT model of a melt of interacting chains, we must first consider the behavior of a single Gaussian chain in an external field $w(\mathbf{r})$. This field, and the form in which it is imposed, can be considered artificial for the moment; it anticipates terms that will arise when evaluating the partition function for an interacting melt, as we will see later. Specifically, for a continuous Gaussian chain we consider the Hamiltonian

$$U = U_0 + U_{ext} = \frac{3k_BT}{2b^2}\int_0^N ds \left|\frac{d\mathbf{r}(s)}{ds}\right|^2 + k_BT\int d\mathbf{r}\, w(r)\hat{\rho}(\mathbf{r})\ , \tag{2.55}$$

where

$$\hat{\rho}(r) = \int_0^N ds\, \delta(\mathbf{r} - \mathbf{r}(s)) \tag{2.56}$$

is the segment density. A useful quantity to compute (again, because it will become important later) is the normalized single-chain partition function

$$Q[w] = \frac{Z[w]}{Z_0} = \frac{\int \mathcal{D}\mathbf{r}\ \exp(-\beta U_0 - \beta U_{ext})}{\int \mathcal{D}\mathbf{r}\ \exp(-\beta U_0)} \tag{2.57}$$

Q is a functional of the imposed field $w(\mathbf{r})$. If the continuous chain is discretized into $N_s + 1$ beads and N_s springs of length Δs, (2.57) can be written as

$$\begin{aligned} Q[w] = \frac{1}{V} \int d\mathbf{r}^{N_s+1} \Big\{ & \exp[-\Delta s\, w(\mathbf{r}_{N_s})]\, \boldsymbol{\Phi}(\mathbf{r}_{N_s} - \mathbf{r}_{N_s-1})\, \exp[-\Delta s\, w(\mathbf{r}_{N_s} - 1)] \\ & \times\ \boldsymbol{\Phi}(\mathbf{r}_{N_s-1} - \mathbf{r}_{N_s-2}) \ldots \exp[-\Delta s\, w(\mathbf{r}_2)] \\ & \times\ \boldsymbol{\Phi}(\mathbf{r}_2 - \mathbf{r}_1)\, \exp[-\Delta s\, w(\mathbf{r}_1)]\, \boldsymbol{\Phi}(\mathbf{r}_1 - \mathbf{r}_0)\, \exp[-\Delta s\, w(\mathbf{r}_0)] \Big\} \end{aligned} \tag{2.58}$$

If we define the quantities

$$q(\mathbf{r}, 0; [w]) = \exp[-\Delta s\, w(\mathbf{r})] \tag{2.59}$$

and

$$q(\mathbf{r}, s + \Delta s; [w]) = \exp[-\Delta s\, w(\mathbf{r})] \int d\mathbf{r}'\, \boldsymbol{\Phi}(\mathbf{r} - \mathbf{r}') q(\mathbf{r}', s; [w]) \ , \tag{2.60}$$

then (2.58) can alternatively be written as

$$Q[w] = \frac{1}{V} \int d\mathbf{r}\, q(\mathbf{r}, N; [w]) \ . \tag{2.61}$$

(2.60) is a Chapman-Kolmogorov equation, therefore we can derive a Fokker-Planck equation for $q(\mathbf{r}, N; [w])$, Expanding (2.60) to first order in Δs and second order in $\Delta\mathbf{r}$, and following the same sequence of steps used to obtain (2.54), we find

$$\frac{\partial}{\partial s} q(\mathbf{r}, s; [w]) = \frac{b^2}{6} \nabla^2 q(\mathbf{r}, s; [w]) - w(\mathbf{r}) q(\mathbf{r}, s; [w]) \tag{2.62}$$

which can be solved to give $q(\mathbf{r}, s; [w])$ subject to the initial condition $q(\mathbf{r}, 0; [w]) = \exp[-\delta s\, w(\mathbf{r})] = 0$ in the continuous-chain ($\Delta s \to 0$) limit. $q(\mathbf{r}, s; [w])$ is called the *propagator*. Intuitively, it can be interpreted as the probability that the end of the chain $s = N$ lies at position $\mathbf{r}$.

The only remaining quantity we will later need is the average single-chain monomer density in the presence of w, $\rho(\mathbf{r}; [w]) = \langle \hat{\rho}(\mathbf{r}) \rangle_w$, given by

$$\rho(\mathbf{r}; [w]) = \frac{\int \mathcal{D}\mathbf{r}\, \hat{\rho}(\mathbf{r}) \, \exp(-\beta U_0 - \beta U_{ext})}{\int \mathcal{D}\mathbf{r} \, \exp(-\beta U_0)} \tag{2.63}$$

From the form of (2.55), we see that $\frac{\delta}{\delta w(\mathbf{r})}(U_0 + U_{ext}) = k_B T \hat{\rho}(\mathbf{r})$; using $Q[w]$ from (2.57) we can write

$$\frac{\delta \ln Q[w]}{\delta w(\mathbf{r})} = \frac{1}{Q[w]} \frac{\delta Q[w]}{\delta w(\mathbf{r})} = \frac{\int \mathcal{D}\mathbf{r}\, \rho\hat{(\mathbf{r})} \, \exp(-\beta U_0 - \beta U_{ext})}{\int \mathcal{D}\mathbf{r} \, \exp(-\beta U_0)} = -\rho(\mathbf{r}; [w]) \ . \tag{2.64}$$

It is shown in [87] that

$$-\frac{\delta \ln Q[w]}{\delta w(\mathbf{r})} = \rho(\mathbf{r}; [w]) = \frac{1}{V Q[w]} \int_0^N ds\, q(\mathbf{r}, N - s; [w]) q(\mathbf{r}, s; [w]) \tag{2.65}$$

From (2.65) and (2.61) we see that both the average single-chain density $\rho(\mathbf{r};[w]$ and $Q[w]$ can be obtained by appropriately integrating the propagator $q(\mathbf{r},s;[w])$. This highlights the importance of computing q via the propagator equation (2.62). It turns out that solving the propagator equation is the most computationally costly step of the SCFT method.

Up to this point, the results we obtained apply to a homopolymer chain of a single monomer species (say A). The only difference when considering a chain composed of multiple monomer species is that different species may be acted upon by a different realization of the external field, *i.e.*, w_A acts on monomer species A and w_B acts on monomer species B. For a diblock chain of length N and block fraction f, where $0 \leq s \leq fN$ consists of species A and $fN < s \leq N$ consists of species B, the microscopic single-chain densities and Hamiltonian become

$$\hat{\rho}_A(\mathbf{r}) = \int_0^{fN} ds\, \delta(\mathbf{r}-\mathbf{r}(s)) \;\; , \;\; \hat{\rho}_B(\mathbf{r}) = \int_{fN}^{N} ds\, \delta(\mathbf{r}-\mathbf{r}(s)) \tag{2.66}$$

and

$$\begin{aligned} U &= U_0 + U_{ext} \qquad\qquad (2.67)\\ &= \frac{3k_BT}{2b^2}\int_0^N ds \left|\frac{d\mathbf{r}(s)}{ds}\right|^2 + k_BT\int d\mathbf{r}\, w_A(r)\hat{\rho}_A(\mathbf{r}) + k_BT\int d\mathbf{r}\, w_B(r)\hat{\rho}_B(\mathbf{r}) \;\; . \end{aligned}$$

The potential U is now a functional of both w_A and w_B. The propagator equation becomes

$$\begin{aligned}\frac{\partial}{\partial s} q(\mathbf{r}, s; [w_A, w_B]) = \frac{[b(s)]^2}{6} \nabla^2 q(\mathbf{r}, s; [w_A, w_B]) \\ -w(\mathbf{r}, s) q(\mathbf{r}, s; [w_A, w_B])\end{aligned} \tag{2.68}$$

where

$$w(\mathbf{r}, s) = \begin{cases} w_A(\mathbf{r}), & 0 \leq s \leq fN \\ w_B(\mathbf{r}), & fN < s \leq N \end{cases} \tag{2.69}$$

$b(s)$ represents the Kuhn length along the chain, which may change as we pass from species A to species B; in practice it is often assumed to be the same for both monomer species: $b(s) = b = const.$

To compute the densities ρ_A and ρ_B, it is also convenient to define the complementary propagator $q^\dagger(\mathbf{r}, s; [w_A, w_B])$, whose $s = 0$ point is defined to start at the B-species end instead of the A-species end:

$$\begin{aligned}\frac{\partial}{\partial s} q^\dagger(\mathbf{r}, s; [w_A, w_B]) = \frac{b^2}{6} \nabla^2 q^\dagger(\mathbf{r}, s; [w_A, w_B]) \\ -w^\dagger(\mathbf{r}, s) q^\dagger(\mathbf{r}, s; [w_A, w_B])\end{aligned} \tag{2.70}$$

where

$$w^{\dagger}(\mathbf{r}, s) = \begin{cases} w_B(\mathbf{r}), & 0 \leq s \leq (1-f)N \\ w_A(\mathbf{r}), & (1-f)N < s \leq N \end{cases} \tag{2.71}$$

(2.70) is solved subject to the same initial condition as (2.68): $q^{\dagger}(\mathbf{r}, 0; [w_A, w_B]) = 1$. The single-chain partition function may be computed from either the q or $q^{\dagger}$:

$$\begin{aligned} Q[w_A, w_B] &= \frac{1}{V} \int d\mathbf{r}\, q(\mathbf{r}, N; [w_A, w_B]) \\ &= \frac{1}{V} \int d\mathbf{r}\, q^{\dagger}(\mathbf{r}, N; [w_A, w_B]) \end{aligned} \tag{2.72}$$

and the densities may be expressed in terms of q and $q^{\dagger}$ as

$$\begin{aligned} \rho_A &= -\frac{\delta \ln Q[w_A, w_B]}{\delta w_A(\mathbf{r})} \\ &= \frac{1}{VQ[w_A, w_B]} \int_0^{fN} ds\, q^{\dagger}(\mathbf{r}, N-s; [w_A, w_B])\, q(\mathbf{r}, s; [w_A, w_B]) \\ \rho_B &= -\frac{\delta \ln Q[w_A, w_B]}{\delta w_B(\mathbf{r})} \\ &= \frac{1}{VQ[w_A, w_B]} \int_{fN}^{N} ds\, q^{\dagger}(\mathbf{r}, N-s; [w_A, w_B])\, q(\mathbf{r}, s; [w_A, w_B]) \end{aligned} \tag{2.73}$$

as described in [87].

From single chains to an interacting melt

With the above single-chain results in hand we can derive the SCFT Hamiltonian of an AB+A+B diblock plus homopolymer melt. Assume that the melt contains n_{AB} diblock chains of length N_{AB} with A-block fraction f, n_A A-homopolymer chains of length N_A, and n_B B-homopolymer chains of length N_B. The microscopic densities of the two species are given as a sum over chains by

$$\begin{aligned}\hat{\rho}_A(\mathbf{r}) &= \sum_{i=1}^{n_{AB}} \int_0^{fN_{AB}} ds\, \delta(\mathbf{r} - \mathbf{r}_{AB,i}(s)) + \sum_{j=1}^{n_A} \int_0^{N_A} ds\, \delta(\mathbf{r} - \mathbf{r}_{A,j}(s)) \\ \hat{\rho}_B(\mathbf{r}) &= \sum_{i=1}^{n_{AB}} \int_{fN_{AB}}^{N_{AB}} ds\, \delta(\mathbf{r} - \mathbf{r}_{AB,i}(s)) + \sum_{k=1}^{n_B} \int_0^{N_B} ds\, \delta(\mathbf{r} - \mathbf{r}_{B,k}(s))\end{aligned} \tag{2.74}$$

and the contribution to the total Hamiltonian stemming from chain stretching is given by

$$\begin{aligned}U_0[\{\mathbf{r}_{AB}(s)\},\{\mathbf{r}_A(s)\},\{\mathbf{r}_B(s)\}] &= \sum_{i=1}^{n_{AB}} U_{0AB}[\mathbf{r}_{AB,i}(s)] + \sum_{j=1}^{n_A} U_{0A}[\mathbf{r}_{A,j}(s)] \\ &\quad + \sum_{k=1}^{n_B} U_{0B}[\mathbf{r}_{B,k}(s)] \\ &= \sum_{i=1}^{n_{AB}} \frac{3k_BT}{2b^2} \int_0^{N_{AB}} ds \left|\frac{d\mathbf{r}_i(s)}{ds}\right|^2 + \sum_{j=1}^{n_A} \frac{3k_BT}{2b^2} \int_0^{N_A} ds \left|\frac{d\mathbf{r}_j(s)}{ds}\right|^2 \\ &\quad + \sum_{k=1}^{n_B} \frac{3k_BT}{2b^2} \int_0^{N_B} ds \left|\frac{d\mathbf{r}_k(s)}{ds}\right|^2\end{aligned} \tag{2.75}$$

(in which chains of different species are assumed to have identical Kuhn lengths). $\mathbf{r}_{AB,i}(s)$ denotes, *e.g.*, the position at contour variable s along the ith AB diblock chain; U_0 is a functional of the set $\{\mathbf{r}_{AB}(s)\}, \{\mathbf{r}_A(s)\}, \{\mathbf{r}_B(s)\}$ of these configurations for all the individual chains present in the melt.

The Hamiltonian must also account for the interaction between different monomer species. Typically, this interaction is modeled using a repulsive local (Flory-Huggins [89]) contact potential of the form

$$\beta U_1 = v_0 \chi_{AB} \int d\mathbf{r}\, \hat{\rho}_A(\mathbf{r}) \hat{\rho}_B(\mathbf{r}) \tag{2.76}$$

where v_0 is the volume occupied by a single statistical segment.

Finally, the melt is assumed to be incompressible everywhere, *i.e.*, $\hat{\rho}_A(\mathbf{r}) + \hat{\rho}_B(\mathbf{r}) = \rho_0 \equiv 1/v_0$.

Including both U_0 and U_1, the partition function for the AB+A+B melt can be written as

$$Z = \tag{2.77}$$

$$\frac{1}{n_{AB}! n_A! n_B! (\lambda_T^3)^{n_{AB} N_{AB} + n_A N_A + n_B N_B}} \prod_{i=1}^{n_{AB}} \int \mathcal{D}\mathbf{r}_{AB,i} \prod_{j=1}^{n_A} \int \mathcal{D}\mathbf{r}_{A,j} \prod_{k=1}^{n_B} \int \mathcal{D}\mathbf{r}_{B,j}$$
$$\Big(\exp\left(-\beta U_0 - \beta U_1\right) \times \delta(\hat{\rho}_A(\mathbf{r}) + \hat{\rho}_B(\mathbf{r}) - \rho_0) \Big)$$

The anterior constants account for the identical nature of the chains and the thermal de Broglie wavelength λ_T of individual segments; however, they are unimportant, since we are only interested in finding the Hamiltonian that appears in the exponential. Also, from a general statistical mechanics perspective, quantities of physical interest (*e.g.*, the thermal average of some operator O over the system's degrees of freedom ϕ) are expressed as a ratio:

$$\langle O \rangle = \frac{\int d\phi \, O \, e^{-\beta H[\phi]}}{Z} \tag{2.78}$$

in which any multiplicative constants will cancel. Subsequently, these and other multiplicative constants attached to the partition function will be ignored.

The Hubbard-Stratonovich transformation introduces an auxiliary field that serves to decouple the $\hat{\rho}_A(\mathbf{r})\hat{\rho}_B(\mathbf{r})$ interaction contained in U_1. It is carried out as follows.

First, for convenience, we define two linear combinations of the microscopic density fields

$$\hat{\rho}_+(\mathbf{r}) = \hat{\rho}_A(\mathbf{r}) + \hat{\rho}_B(\mathbf{r}) \ \ , \ \ \hat{\rho}_-(\mathbf{r}) = \hat{\rho}_A(\mathbf{r}) - \hat{\rho}_B(\mathbf{r}) \ . \tag{2.79}$$

In terms of $\hat{\rho}_+$ and $\hat{\rho}_-$, the incompressibility condition becomes $\delta(\hat{\rho}_+ + \rho_0)$, and, noting that $4\hat{\rho}_A\hat{\rho}_B = \hat{\rho}_+^2 - \hat{\rho}_-^2 = \rho_0^2 - \hat{\rho}_-^2$, we can rewrite U_1 as

$$\beta U_1 = \frac{1}{4} v_0 \chi_{AB} \int d\mathbf{r} \, \left(\rho_0^2 - \hat{\rho}_-^2(\mathbf{r})\right) = \frac{1}{4}\chi_{AB} N - \frac{1}{4} v_0 \chi_{AB} \int d\mathbf{r} \, \hat{\rho}_-^2(\mathbf{r}) \tag{2.80}$$

where $N = n_{AB}N_{AB} + n_A N_A + n_B N_B$ is the total number of statistical segments present in the system. Then

$$e^{-\beta U_1} = const \cdot \exp\left(\frac{1}{4} v_0 \chi_{AB} \int d\mathbf{r} \, \hat{\rho}_-^2(\mathbf{r})\right) \tag{2.81}$$

To introduce the auxiliary field, consider the Gaussian functional integral identity

$$\begin{aligned} &\frac{\int \mathcal{D}f \, \exp\left[-(1/2)\int dx \, \int dx' \, f(x)A(x,x')f(x') + \int dx \, J(x)f(x)\right]}{\int \mathcal{D}f \, \exp\left[-(1/2)\int dx \, \int dx' \, f(x)A(x,x')f(x')\right]} \\ &\qquad = \exp\left(\frac{1}{2}\int dx \, \int dx' \, J(x)A^{-1}(x,x')J(x')\right) \end{aligned} \tag{2.82}$$

from Appendix C of [87]. Comparing (2.81) with the right-hand side of (2.82), we can identify $A^{-1}(x,x')$ with $(1/2)v_0\chi_{AB}\delta(\mathbf{r}-\mathbf{r}')$. Since the functional inverse A^{-1} of A is defined via

$$\int dx' \, A(x-x')A^{-1}(x'-x'') = \delta(x-x'') \tag{2.83}$$

we can also identify $A(x, x')$ with $\frac{2}{v_0 \chi_{AB}} \delta(\mathbf{r} - \mathbf{r}') = \frac{2\rho_0}{\chi_{AB}} \delta(\mathbf{r} - \mathbf{r}')$, and substitute into the left-hand side of (2.82) to write (2.81) as

$$e^{-\beta U_1} = const \cdot \int \mathcal{D}w_- \, \exp\left(\hat{\rho}_- w_- - \frac{\rho}{\chi_{AB}} w_-^2\right) \tag{2.84}$$

where w_- is the newly introduced auxiliary field (the denominator of (2.82) is a constant). Since w_- is conjugate to $\hat{\rho}_-$, the difference between the densities of the two species, w_- is conventionally referred to as the *exchange field*. Note that the remaining microscopic density term in (2.84) is linear; in other words, the contact interaction has been decoupled.

We may also write the delta-functional incompressibility condition as a functional integral over another auxiliary field:

$$\delta(\hat{\rho}_+(\mathbf{r}) - \rho_0) = const \cdot \int \mathcal{D}w_+ \exp\left(-i \int d\mathbf{r} \, w_+ (\hat{\rho}_+(\mathbf{r}) - \rho_0)\right) \tag{2.85}$$

The second newly introduced auxiliary field w_+ is conjugate to the sum of the microscopic densities of the two species and enforces incompressibility; it is conventionally referred to as the *pressure field*.

These steps may seem to have complicated rather than clarified the partition function, but we will find that everything collapses in a clean and satisfying way. Substituting (2.74), (2.75), (2.84), and (2.85) into (2.77), we find that the sums over individual chains yield independent terms in the Hamiltonian that factor:

$$
\begin{aligned}
&Z = const \cdot \int \mathcal{D}w_- \int \mathcal{D}w_+ \Bigg\{ \\
&\prod_{i=1}^{n_{AB}} \int \mathcal{D}\mathbf{r}_{AB,i} \, \exp\Bigg(- \beta U_{0AB}[\mathbf{r}_{AB,i}(s)] - \\
&\int d\mathbf{r} \int_0^{fN_{AB}} ds \, w_A(\mathbf{r}) \delta(\mathbf{r} - \mathbf{r}_{AB,i}(s)) - \int d\mathbf{r} \int_{fN_{AB}}^{N_{AB}} ds \, w_B(\mathbf{r}) \delta(\mathbf{r} - \mathbf{r}_{AB,i}(s)) \Bigg) \\
&\prod_{j=1}^{n_A} \int \mathcal{D}\mathbf{r}_{A,j} \, \exp\Bigg(- \beta U_{0A}[\mathbf{r}_{A,j}(s)] - \int d\mathbf{r} \int_0^{N_A} ds \, w_A(\mathbf{r}) \delta(\mathbf{r} - \mathbf{r}_{A,j}(s)) \Bigg) \\
&\prod_{k=1}^{n_B} \int \mathcal{D}\mathbf{r}_{B,k} \, \exp\Bigg(- \beta U_{0B}[\mathbf{r}_{B,k}(s)] - \int d\mathbf{r} \int_0^{N_B} ds \, w_B(\mathbf{r}) \delta(\mathbf{r} - \mathbf{r}_{B,k}(s)) \Bigg) \\
&\exp\Bigg(- \int d\mathbf{r} \, \frac{\rho_0}{\chi_{AB}} w_-^2(\mathbf{r}) - i\omega_+(\mathbf{r}) \rho_0 \Bigg) \Bigg\} \\
&= const \cdot \int \mathcal{D}w_- \int \mathcal{D}w_+ \Bigg\{ \\
&\prod_{i=1}^{n_{AB}} \int \mathcal{D}\mathbf{r}_{AB,i} \, \exp\Bigg(- \beta U_{0AB}[\mathbf{r}_{AB,i}(s)] - \\
&\int_0^{fN_{AB}} ds \, w_A(\mathbf{r}_{AB,i}(s)) - \int_{fN_{AB}}^{N_{AB}} ds \, w_B(\mathbf{r}_{AB,i}(s)) \Bigg) \\
&\prod_{j=1}^{n_A} \int \mathcal{D}\mathbf{r}_{A,j} \, \exp\Bigg(- \beta U_{0A}[\mathbf{r}_{A,j}(s)] - \int_0^{N_A} ds \, w_A(\mathbf{r}_{A,j}(s)) \Bigg) \\
&\prod_{k=1}^{n_B} \int \mathcal{D}\mathbf{r}_{B,k} \, \exp\Bigg(- \beta U_{0B}[\mathbf{r}_{B,k}(s)] - \int_0^{N_B} ds \, w_B(\mathbf{r}_{B,k}(s)) \Bigg) \\
&\exp\Bigg(- \int d\mathbf{r} \, \frac{\rho_0}{\chi_{AB}} w_-^2(\mathbf{r}) - i\omega_+(\mathbf{r}) \rho_0 \Bigg) \Bigg\}
\end{aligned}
\tag{2.86}
$$

where we have defined $w_A = iw_+ - w_-$ and $w_B = iw_+ + w_-$. Comparing with the expression for the partition functions of *single* chains in external fields (2.57), we see that the three products are simply $(Z_{0AB}Q_{AB}[w_A, w_B])^{n_{AB}}$, $(Z_{0A}Q_A[w_A])^{n_A}$, and $(Z_{0B}Q_B[w_B])^{n_B}$ respectively, leading to the following compact expression for the partition function:

$$\begin{aligned} Z &= const \cdot \int \mathcal{D}w_+ \int \mathcal{D}w_- \, e^{-H[w_+,w_-]} \qquad (2.87) \\ H[w_+, w_-] &= \rho_0 \int d\mathbf{r} \left(\frac{1}{\chi_{AB}} w_-(\mathbf{r}) - iw_+ \right) \qquad (2.88) \\ &\quad - n_{AB} \ln Q_{AB}[w_A, w_B] - n_A \ln Q_A[w_A] - n_B \ln Q[w_B] \end{aligned}$$

$w_-(\mathbf{r})$ and $w_+(\mathbf{r})$ are fields that can be discretized on a lattice of computationally tractable dimensionality. In practice, roughly 10 discretization points per characteristic microphase domain length is sufficient. For example, simulating a system of size $8 \times 8 \times 8$ lamellar periods would require $80 \times 80 \times 80 = 512,000$ grid points. Q_A, Q_B, and Q_{AB} can be found by solving the single-chain propagator diffusion equations for a homopolymer (2.62) or diblock (2.70) to obtain $q_A(\mathbf{r}, s; [w_A])$, $q_B(\mathbf{r}, s; [w_B])$ and $q_{AB}(\mathbf{r}, s; [w_A, w_B])$, then plugging those into (2.72) and (2.61).

To compute the average value of the density of a given monomer species, say ρ_A, we add to the Hamiltonian of (2.77) a source term $S = (1/\beta)\left(\int d\mathbf{r}\, J_A(\mathbf{r})\hat{\rho}_A(\mathbf{r})\right)$ with an artificial field $J_A(\mathbf{r})$ conjugate to the microscopic density of the desired species (such that $\exp(\beta U_0 - \beta U_1)$ becomes $\exp(\beta U_0 - \beta U_1 - \beta S)$). Next, we note that

$$\langle \hat{\rho}_A(\mathbf{r}) \rangle = -\frac{1}{Z[J_A]} \cdot const \cdot \int \mathcal{D}w_+ \int \mathcal{D}w_- \left\{ \frac{\delta H[w_+, w_-, J_A]}{\delta J_A(\mathbf{r})} e^{-H[w_+,w_-]} \right\} \Bigg|_{J_A=0} \tag{2.89}$$

If we retrace the steps that led from (2.77) to (2.87), but this time with S present in the Hamiltonian, we find that J_A ultimately appears in the Hamiltonian as follows:

$$\begin{aligned} H[w_+, w_-, J_A] = {} & \rho_0 \int d\mathbf{r} \left(\frac{1}{\chi_{AB}} w_-(\mathbf{r}) - i w_+ \right) \qquad (2.90) \\ & - n_{AB} \ln Q_{AB}[w_A + J_A, w_B] - n_A \ln Q_A[w_A + J_A] - n_B \ln Q[w_B] \end{aligned}$$

so that

$$\begin{aligned} \frac{\delta H[w_+, w_-, J]}{\delta J(\mathbf{r})} \bigg|_{J_A=0} &= \frac{\delta H[w_+, w_-, 0]}{\delta w_A(\mathbf{r})} \qquad (2.91) \\ &= -n_{AB} \frac{\delta \ln Q_{AB}[w_A, w_B]}{\delta w_A(\mathbf{r})} - n_A \frac{\delta \ln Q_A[w_A]}{\delta w_A(\mathbf{r})} \\ &\equiv \tilde{\rho}_A \left(\mathbf{r}; [w_A, w_B] \right) \qquad (2.92) \end{aligned}$$

Therefore, to find the thermally averaged averaged value of the microscopic A-segment density $\hat{\rho}_A$, dealing with an artificial source term is unnecessary; we can simply compute the thermal average of the *segment density operator* $\tilde{\rho}_A(\mathbf{r}; [w_A, w_B])$. To compute the instantaneous value of $\tilde{\rho}_A(\mathbf{r}; [w_A, w_B])$, the second term of (2.91) can be constructed by solving the propagator equation (2.62) for the A-homopolymer to obtain $q_A(\mathbf{r}, s; w_A)$, then plugging into (2.65). The first term can be constructed by solving the forward and backward propagator equations (2.68), (2.70) for the AB-diblock to obtain $q_{AB}(\mathbf{r}, s; [w_A])$ and $q^{\dagger}_{AB}(\mathbf{r}, s; [w_A, w_B])$, then plugging into (2.73).

To model graphoepitaxy, as presented in Chapter 3, the polymer melt can be simulated in the presence of confining sidewalls. Walls are implemented by considering an additional polymer-excluding "wall density" field ρ_W that is fixed in space, and rises rapidly from zero to ρ_0 wherever a wall is present. To model a combination of grapho- and chemoepitaxy, it is also necessary to make the wall locally attractive to one species or another. This is implemented in the Hamiltonian by including contains contact terms for interactions between the wall density field and the microscopic polymer density fields $\hat{\rho}_A$ and $\hat{\rho}_B$.

The use of an artificial wall density field to simulate confinement was originally proposed by Matsen [90]. Further details can be found in [91, 92].

2.3.2 SCFT relaxation equations

SCFT makes use of the saddle point approximation mentioned earlier; in other words, it attempts to find configurations w_+^*, w_-^* that (locally) dominate the path integral (2.87). It then assumes $Z \approx \exp -H[w_+^*, w_-^*]$, such that the free energy is given by $F \approx H[w_+, w_-]$ and the thermally averaged microscopic density of species K is given by $\langle \hat{\rho}_K \rangle \approx \tilde{\rho}_K \left(\mathbf{r}; [w_A^*, w_B^*]\right)$.

For a real-valued Hamiltonian $H[\phi]$, finding field configurations that give locally dominant contributions to the Hamiltonian is straightforward. One must simply find local minima of H with respect to ϕ. In SCFT, finding configurations that give locally dominant contributions to the Hamiltonian is more subtle because the Hamiltonian is complex-valued; specifically, the pressure field enters H through the purely imaginary term iw_+. We can account for this by appealing to the method of steepest descent and stationary phase [93]. Ostensibly, the functional integrals over w_+ and w_- in (2.87) are along the real axes between $\pm\infty$ for each $w(\mathbf{r})$; however, since e^{-H} is analytic, in principle we may deform these integration paths (individually, as desired) to any contours in the complex plane whose endpoints are at $\pm\infty$ on the real axis. The method of steepest descent considers integration along a contour where the imaginary part of the Hamiltonian H_I (the "phase") is constant, and uses the fact that the integrals along such contours are dominated by "saddle points" where the real part of the Hamiltonian

H_R along the constant-phase contour is minimized. Due to certain analytic properties of complex-valued functions, detailed in [93], two constant-phase contours intersect at each saddle point, and both of these contours are also paths along which the real component of H is changing most rapidly; thus, a constant-phase contour in the vicinity of a saddle point S is also a contour of *steepest ascent* or *steepest descent* as one moves away from S. Along one of these two contours, H_R at S is a local minimum; along the other contour, H_R at S is a local maximum.

We can combine these general insights about complex-valued functions with intuition about the specific analytic structure of $H[w_+, w_-]$, to come up with a set of relaxation equations to search for the saddle point. First of all, the Hamiltonian at the saddle point $H[w_+^*, w_-^*]$ should be real-valued. Since w_+ enters the Hamiltonian only through iw_+, we anticipate that w_+^* is purely complex; similarly, since w_- enters the Hamiltonian without factors of i attached, we anticipate that w_-^* is purely real.

We compute the purely real saddle point by a simple gradient descent scheme that minimizes H_R:

$$\begin{aligned}\frac{\partial w_-(\mathbf{r})}{\partial t} &= -\lambda_- \frac{\delta H[w_+, w_-]}{\delta w_-(\mathbf{r})} \qquad (2.93)\\ &= -\lambda_- \left[\frac{2\rho_0}{\chi_{AB}} w_-(\mathbf{r}) - \tilde{\rho}_A\left(\mathbf{r}; [w_A, w_B]\right) + \tilde{\rho}_B\left(\mathbf{r}; [w_A, w_B]\right)\right]\end{aligned}$$

where as usual $w_A = iw_+ - w_-$ and $w_B = iw_+ + w_-$ and we have recognized, for example, that $-n_{AB}\frac{\delta \ln Q_{AB}}{\delta w_-} - n_A \frac{\delta \ln Q_A}{\delta w_-} = n_{AB}\frac{\delta \ln Q_{AB}}{\delta w_A} + n_A \frac{\delta \ln Q_A}{\delta w_A} = \tilde{\rho}_A$. λ_+ controls the size of the effective relaxation timestep, and should be made as large as possible while maintaining stability of whatever scheme is used to discretize (2.93) in time. The "time" here is fictitious and has no connection to physical dynamics of the polymers. To find the purely imaginary saddle point, we relax w_+ along the imaginary axis:

$$\begin{aligned} \frac{\partial(iw_+(\mathbf{r}))}{\partial t} &= +\lambda_+ \frac{\delta H[w_+, w_-]}{\delta(iw_+(\mathbf{r}))} \\ &= +\lambda_+ \left[-\rho_0 + \tilde{\rho}_A\left(\mathbf{r}; [w_A, w_B]\right) + \tilde{\rho}_B\left(\mathbf{r}; [w_A, w_B]\right)\right] \end{aligned} \tag{2.94}$$

It turns out that along this search axis, H_R is a local *maximum* at the saddle point w_+^*. Therefore, while (2.93) represents a gradient descent scheme, (2.94) represents a gradient ascent scheme.

Equations (2.93) and (2.94) can be integrated forward in fictitious time using any desired discretized algorithm. The simplest choice is forward Euler; however, a number of methods have been proposed that offer improved accuracy and stability (details of several useful examples can be found in [87, 94–97]).

Because the density operators $\tilde{\rho}_A$ and $\tilde{\rho}_B$ must be constructed using the propagators for each chain type, and the propagators themselves depend on the fields

w_+ and w_- at a given timestep, in order to advance w_+ and w_- the propagators must be recomputed at each timestep. This is accomplished by solving the propagator diffusion equations for each chain type present in the melt (AB diblock, A homopolymer, and B homopolymer; for the diblock, the complementary propagator equation (2.70) must also be solved). Solving these diffusion equations is by far the most expensive step of the SCFT relaxation prescription, since the propagator is an $M \times N_S$ dimensional object, where M is the number of spatial grid points and N_s is the number of contour steps used to discretize the propagator. N_s depends on chain length; for the systems we study later it is typically around ~ 100 for the longest chain type present.

Again, a number of methods have been proposed to solve the diffusion equations [87, 98]. The simulations presented in Chapter 3 use a pseudo-spectral method described in [87, 99, 100] to integrate $q_0(\mathbf{r}, s)$ forward from 0 to N along the contour variable s, which proceeds as follows:

The diffusion equation for a generic propagator is

$$\frac{\partial}{\partial s} q(r, s) = \frac{b^2}{6} \nabla^2 q(\mathbf{r}, s) - w(\mathbf{r}, s) q(\mathbf{r}) \tag{2.95}$$

which may be discretized in Δs as

$$q(\mathbf{r}, s + \Delta s) = \exp(\mathcal{L}\Delta s) q(\mathbf{r}, s) \tag{2.96}$$

where $\mathcal{L} = (b^2/6)\partial^2/\partial\mathbf{r}^2 - w(\mathbf{r}, s)^2$. $\mathcal{L}$ as a whole is not diagonal in either real space or Fourier space, but the first term $\mathcal{L}^D = (b^2/6)\partial^2/\partial\mathbf{r}^2$ is diagonal in Fourier space and the second term $\mathcal{L}^W = -w(\mathbf{r}, s)$ is diagonal in real space. The basic idea behind the pseudospectral method is to apply $\mathcal{L}^D$ and $\mathcal{L}^W$ separately using a combination of Fourier transforms and elementwise operations. First, we apply Strang splitting [101] to the operators, expressing $\exp(\mathcal{L}\Delta s)$ as

$$\exp(\mathcal{L}\Delta s) = \exp(\mathcal{L}^W \Delta s/2) \exp(\mathcal{L}^D \Delta s) \exp(\mathcal{L}^W \Delta s/2) + O(\Delta s^3) , \tag{2.97}$$

an identity that can be shown by Taylor expansion. Next, beginning with $q(\mathbf{r}, s)$ in real space at contour point s, we determine $q(\mathbf{r}, s + \delta s)$ via a three-step procedure:

1. Compute $q(\mathbf{r}, s + \Delta s/3) \equiv \exp(\mathcal{L}^W \Delta s/2) q(\mathbf{r}, s)$. Since $\mathcal{L}^W$ is diagonal in real space, this involves a simple elementwise multiplication.
2. Take the Fourier transform of $q(\mathbf{r}, s + \Delta s/3)$ and compute $q(\mathbf{k}, s + 2\Delta s/3 \equiv \exp(\mathcal{L}^D \Delta s) q(\mathbf{k}, s + \Delta s/3)$. Again, since $\mathcal{L}^D$ is diagonal in Fourier space,

applying $\exp(\mathcal{L}^D \Delta s)$ to $q(\mathbf{k}, s + \Delta s/3)$ involves only elementwise multiplication.

3. Third and finally, perform an inverse Fourier transform on $q(\mathbf{k}, s + 2\Delta s/3$ and compute $q(\mathbf{r}, s + \Delta s) = \exp(\mathcal{L}^W \Delta s/2) q(\mathbf{r}, s + 2\Delta s/3)$.

The algorithm may be summarized as

$$q(\mathbf{r}, s + \Delta s) = \exp(\mathcal{L}^W \Delta s/2)\, FT^{-1}\Big[\exp(\mathcal{L}^D \Delta s) FT\Big[\exp(\mathcal{L}^W \Delta s/2) q(\mathbf{r}, s + \Delta s)\Big]\Big] \tag{2.98}$$

where FT and FT^{-1}, respectively, represent forward and inverse Fourier transforms. The initial condition is $q(\mathbf{r}, 0) = 1$.

Overall, the pseudo-spectral algorithm requires one forward and inverse Fourier transform pair per contour step; computationally, the corresponding fast Fourier transforms (FFTs) consume most of the algorithm's required wall time. The computational order of the FFTs is $M \log M$, where M is the number of grid points; for N_s contour steps, the overall computational order of the pseudospectral method is then $N_s M \log M$.

Computing propagators is also the most memory-intensive step of the SCFT procedure. The propagator's dimensionality $N_s \times M$, for a typical calculation, might come out to $100 \times 128 \times 48 \times 48 = 29{,}491{,}200$ complex double-precision values. Each complex double-precision value requires 16 bytes of storage, meaning that such a propagator would consume $16 \times 29,491,200$ bytes $= 0.472GB$ of memory. Furthermore, a separate propagator must be computed for each chain type present in the melt (in our case AB diblock, A homopolymer, and B homopolymer). Finally, the string method requires $\sim 20 - 30$ separate images to be effective, and each image is a fully independent SCFT model. When attempting to pair the string method with SCFT calculations on GPUs, the memory requirements can become challenging, as discussed in Chapter 3.

2.3.3 The string method and the partial saddle point approximation

SCFT is effective at modeling the mean-field behavior of polymer melts, and the string method is effective at finding minimum energy paths in high-dimensional systems. To explore annealing pathways for defect-containing or otherwise metastable configurations of polymer melts, combining the two methods is a natural choice. In principle, since the evolution step and reparametrization step of the zero-temperature string method are carried out independently, any field-based model with a well-defined force and Hamiltonian can be made to work with the string method. However, SCFT presents the unique difficulty that the configurations of its evolving fields (w_+ and w_-) away from saddle points are not guaranteed to produce real-valued, physical Hamiltonians. When performing

SCFT on a single model this is not a problem, because the relaxation equations are specifically intended to reach equilibrium at a saddle point. In the string method, by contrast, the string reaches an equilibrium configuration where only the two endpoints are guaranteed to lie at saddle points, while the interior images trace out a sequence of configurations along the minimum energy path between them (in the context of a complex-valued Hamiltonian, even the concept of "mininum energy path" is not physically relevant).

To deal with this issue, we make use of the partial saddle point approximation, described in [87, 102, 103]. We noted earlier that since the pressure field w_+ enters the Hamiltonian only through iw_+, the saddle point configuration of the pressure field w_+^* is purely imaginary; similarly, since the exchange field w_- enters the Hamiltonian without any factors of i attached, the saddle point configuration of the exhange field w_-^* is purely real. In the partial saddle point approximation, the pressure field is slaved to the exchange field, and is considered to lie at its (w_--dependent) saddle point configuration w_+^* for whatever realization of the exhange field is currently being considered. Within the partial saddle point approximation, the partition function (2.87) becomes

$$Z \approx const \cdot \int \mathcal{D}w_- \, \exp\left(-H_p[w_-]\right) \tag{2.99}$$

$$H_p[w_-] \equiv H[w_+^*, w_-] \tag{2.100}$$

Note that Z now involves a functional integral over the w_- fields only. The w_+ fields are constrained to lie at their partial saddle point $w_+(\mathbf{r},[w_-])$, which for a given realization of $w_-(\mathbf{r})$ is defined via

$$\left.\frac{\delta H[w_+,w_-]}{\delta w_+(\mathbf{r})}\right|_{w_+=w_+^*}=0 \tag{2.101}$$

through which w_+^* is a functional of w_-. In practice, the partial saddle point is found by fixing w_- and integrating w_+ in fictitious time according to using Eqn. (2.94) until (2.101) is satisfied.

From the perspective of the string method, the key point is that w_+^* found through (2.101) is purely imaginary, which means that $H[w_+^*,w_-]=H_p[w_-]$ is purely real. If we impose the partial saddle point approximation on all interior images at each timestep, the string will trace out a sequence of real-valued energies. Therefore, we apply the string method to SCFT using the following sequence of steps:

1. For each image, relax the w_+ field by integrating (2.94) (holding w_- fixed) until a partial saddle point is reached.
2. For each image, relax the w_- field by integrating (2.93) for one timestep.
3. Perform the interpolate and reparametrize step on the w_- fields only.

The restring operations should only be performed on the exchange field because the pressure field is slaved to the exchange field through (2.101).

2.4 Phase-field models for the diblock melt

SCFT is a powerful tool that reproduces much of the qualitative phase diagram and sequence of phase transitions observed in experiments. However, constructing the propagator is computationally costly. To study the dis→lam transition in Chapter 5, we only require a model that is accurate near the dis→lam ODT. Near the ODT the melt may be considered weakly segregated; that is, the local overdensity of a given monomer species is relatively small. In this section we introduce several phase-field models that express the Hamiltonian of a diblock melt directly in powers of local monomer concentration variations. These models are valid in the weak-segregation limit, and demonstrate the expected fluctuation-induced first-order character. In sections 2.4.2 and 2.4.3 we introduce the models that will be used in Chapter 5. In many of the expressions below χ serves as shorthand for the unlike-segment enthalpic contact penalty χ_{AB} defined in Section 2.3.

2.4.1 The Leibler model

The Leibler model [12] is the canonical model for a diblock melt in the weak-segregation limit. It is expressed in terms of the local concentration fluctuation (local overdensity of, say, A-type monomers) $\psi(\mathbf{r}) = \frac{\rho_A(\mathbf{r})}{\rho} - f$, where $\rho_A(\mathbf{r})$ is the number density of A monomers at position $\mathbf{r}$, $\rho = N_p N/V$ is the total monomer density in the melt (N_p = number of chains, N = number of monomers per chain, V = system volume) and f is the block fraction. The average value of ψ over the entire system is zero. The Hamiltonian for this model (as written in [104]) in Fourier space is the following:

$$\begin{aligned} H[\psi] = {} & \frac{1}{2!}\int_{\mathbf{k}} \gamma_2(\mathbf{k},-\mathbf{k})\psi(\mathbf{k})\psi(-\mathbf{k}) \\ & + \frac{1}{3!}\int_{\mathbf{k}_1}\int_{\mathbf{k}_2} \gamma_3(\mathbf{k}_1,\mathbf{k}_2,-\mathbf{k}_1-\mathbf{k}_2)\psi(\mathbf{k}_1)\psi(\mathbf{k}_2)\psi(-\mathbf{k}_1-\mathbf{k}_2) \\ & + \frac{1}{4!}\int_{\mathbf{k}_1}\int_{\mathbf{k}_2}\int_{\mathbf{k}_3} \gamma_4(\mathbf{k}_1,\mathbf{k}_2,\mathbf{k}_3,-\mathbf{k}_1-\mathbf{k}_2-\mathbf{k}_3)\psi(\mathbf{k}_1)\psi(\mathbf{k}_2)\psi(\mathbf{k}_3)\psi(-\mathbf{k}_1-\mathbf{k}_2-\mathbf{k}_3) \end{aligned} \tag{2.102}$$

where $\int_{\mathbf{k}} = \int \frac{d\mathbf{k}}{(2\pi)^3}$ and $\psi(\mathbf{k}) = \int d\mathbf{x}\, \exp(i\mathbf{k}\cdot\mathbf{x})\, \psi(\mathbf{x})$. The vertex γ_2, γ_3, and γ_4 can be found in [12] or [104]. Ref. [87] describes how γ_2 can be derived by applying a weak inhomogeneity expansion (also called a random phase approximation or RPA) to the SCFT model for a diblock. An important qualitative feature is that $\gamma_2(\mathbf{k})$ is minimized for $|\mathbf{k}|$ = some specific magnitude q^*. This indicates that the system's ordered phases prefer composition fluctuations with some particular wavelength q^*, *i.e.*, quasicrystalline mesophases similar to those found in the SCFT phase diagram (Figure 2.8).

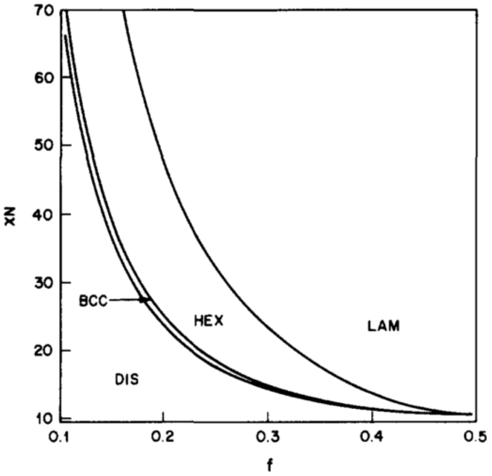

Figure 2.8: Phase diagram of the Leibler model. DIS = disorder, BCC = body-centered cubic spheres, HEX = hexagonally packed cylinders, LAM = lamellae. Note that the only direct transition between disorder and lamellae occurs across the critical point at $f = 0.5, \chi N = 10.495$. This transition is second-order. Figure adapted from [104].

2.4.2 The Brazovskii model

Brazovskii [105] considered a mean-field Hamiltonian of the form

$$H[\phi(\mathbf{r})] = \int d\mathbf{r}\, a[(\nabla^2 + q_0^2)\phi]^2 + b\phi^2 + c\phi^3 + d\phi^4 \tag{2.103}$$

with $a > 0$. The a term is positive definite, and zero if ϕ contains only modes of magnitude q_0, so the model prefers periodic ordered phases with wavelength

q_0. The preferred amplitude of the periodic spatial variation of ϕ in the ordered phases is set by b, c, and d. Brazovskii showed on the basis of a one-loop Hartree approximation (see, *e.g.*, [106] or Chapters 3-5 of [107]) that this model exhibits a fluctuation-induced first-order phase transition between the disordered phase and a periodic lamellar phase. The parameter c introduces asymmetry between negative and positive values of ϕ. The system will only form BCC and hexagonally packed cylinders if $c \neq 0$. If $c = 0$, the system will form either disorder or lamellae.

Fredrickson and Helfand (FRH) showed that by considering $\gamma_3 \approx const$ and $\gamma_4 \approx const$ (approximations they justify), and expanding γ_2 about the preferred wavenumber q^*, the Leibler model could be written as a mean-field Brazovskii model.[7] Applying Brazovskii's fluctuation analysis to this model, they showed that the dis→lam transition became first-order in the presence of fluctuations, and that the system showed a direct first-order dis→lam transition across a range of f values, in improved agreement with the experimental phase diagram. They also showed that fluctuation corrections acted to stabilize the disordered phase, causing the dis→lam ODT to shift to a higher value of χN, given by $\chi N_{ODT} = 10.495 + 41.0\bar{N}^{-1/3}$, where 10.495 is the mean-field ODT and $\bar{N}$ is a dimensionless parameter related to chain density that will be explained shortly.

---

[7] The Brazovskii model has also been shown to describe weakly anisotropic ferromagnets [105], fluids near the Rayleigh-Bénard instability [108, 109], and liquid crystals near the nematic-smectic C transition [109, 110].

In this thesis we are only concerned with the dis→lam transition for symmetric diblocks, for which the coefficient of the ψ^3 term is zero. Fredrickson and Binder (FRB) restate the mapped mean-field Brazovskii model for symmetric diblocks as follows:

$$\beta H[\psi(\mathbf{x})] = \int d\mathbf{x} \left(\frac{e_0}{2}[(\nabla^2 + (q^*)^2)\psi]^2 + \frac{\tau_0}{2}\psi^2 + \frac{u_0}{4!}\psi^4 \right) \ , \quad \int \psi \, d\mathbf{x} = 0$$

$$\tau_0 = 2\rho_c[\chi_s N - \chi N] \ , \quad e_0 = (3c^2/2x^*)\rho_c R_g^4 \ , \quad u_0 = \rho_c N \Gamma_4(0,0) \qquad (2.104)$$

Physically, τ_0 functions as an effective temperature: for $\tau_0 < 0$, a stable ordered phase will exist, while for $\tau_0 > 0$, disorder is favored. u_0 is > 0 and provides an amplitude cutoff for the ordered phase. q^* is the wavenumber that minimizes the Leibler structure factor $\gamma_2(\mathbf{k})$. R_g, the "radius of gyration," is the root-mean-square distance of statistical segments from the chain's center of mass; for a Gaussian chain, $R_g^2 = Nb^2/6$. $x \equiv (q^*)^2 R_g^2$, and c and $N\Gamma_4(0,0)$ are O(1) functions of the block fraction f, given in [104], evaluated at $f = 1/2$ (relevant numerical values will be given shortly). $\chi_s N = 10.495$ is the mean-field value of the dis→lam ODT, and ρ_c = (num chains)/(system volume) is the chain density. The constraint $\int \psi \, d\mathbf{x} = 0$ enforces global conservation of volume fraction f; the same constraint exists on the order parameters of (2.105), (2.106), and (2.107) presented subsequently.

To expose the dimensionless parameter $\bar{N}$ that dictates the significance of fluctuations, FRB define $\bar{N} \equiv 6^3(R_g^3\rho_c)^2$ and perform the rescalings $\mathbf{r} \equiv 6^{-1/2}R_g^{-1}\mathbf{x}$, $\phi(\mathbf{r}) \equiv c\bar{N}^{1/4}\psi(\mathbf{r})$ to express (2.104) as

$$\beta H[\phi(\mathbf{r})] = \int d\mathbf{r} \left(\frac{e}{2}[(\nabla^2 + q_0^2)\phi]^2 + \frac{\tau}{2}\phi^2 + \frac{u}{4!}\phi^4 \right) \tag{2.105}$$

$$\tau = 2(\chi_s N - \chi N] \ \ , \ \ e = 1/(24x^*) \ \ , \ \ q_0^2 = 6x^* \ \ , \ \ u = \frac{N\Gamma_4(0,0)}{c^4\bar{N}^{1/2}} \equiv \lambda\bar{N}^{-1/2}$$

For a symmetric ($f = 1/2$) diblock, $c = 1.1019$, $x^* = 3.7852$, $\chi_s N = 10.495$, and $\lambda = 106.18$. To make the role of $\bar{N}$ explicit, we can define a further rescaled field $\phi_s \equiv \phi/\bar{N}^{1/4}$ and write

$$\beta H(\phi_s(\mathbf{r})) = \bar{N}^{1/2} \int d\mathbf{r} \left(\frac{e}{2}[(\nabla^2 + q_0^2)\phi_s]^2 + \frac{\tau}{2}\phi_s^2 + \frac{\lambda}{4!}\phi_s^4 \right) \tag{2.106}$$

In this form it is clear that $\bar{N}$ dictates the strength of the overall Hamiltonian relative to thermal fluctuations; the greater $\bar{N}$ is, the closer to mean-field theory the fully fluctuating phase diagram will appear. Since $\bar{N}$ increases with increasing R_g and ρ_c, the physical interpretation is that mean-field theory becomes more accurate for denser melts of longer chains. $\bar{N}$ also dictates the accuracy of the FRH one-loop Hartree corrections to the Leibler phase diagram, which are rigorously valid for $\bar{N} >\approx 10^{10}$. Realistic diblock melts typically have $\bar{N}$ in the range 200-

20,000, so 10^{10} is highly unrealistic. However, the FRH analysis has been shown to predict the fluctuation-induced shift of the dis→lam ODT with reasonable accuracy for values of $\bar{N}$ down to $\approx 10^4$ [111], which is experimentally accessible. (2.106) is the form we use in Chapter 5 for Langevin trajectories with explicit fluctuations.

2.4.3 The renormalized Brazovskii model

We would like to use the zero-temperature string method to investigate dis→lam nucleation. However, the z.-t. string method is only applicable when an metastable region of dis and a stable region of lam, separated by an energy barrier, are accessible on a mean-field level. Therefore (2.105) is unsuitable. We would like to derive an effective free energy functional H_{eff} that folds in fluctuations such that a mean-field treatment of H_{eff} implicitly captures the influence of fluctuations. One method to derive H_{eff} for a Landau-type field theory is detailed in Chapter 4 of [107]. Fredrickson and Binder [112], using a one-loop Hartree approximation for the propagator, derive H_{eff} for (2.105) as follows:

$$\beta H_{eff}[\bar{\phi}(\mathbf{r})] = \int d\mathbf{r} \left(\frac{e}{2}[(\nabla^2 + (q_0)^2)\bar{\phi}]^2 + \frac{\tau_R}{2}\bar{\phi}^2 + \frac{u_R}{4!}\bar{\phi}^4 + \frac{w_R}{6!}\bar{\phi}^6 \right) \tag{2.107}$$

with τ_R, u_R, w_R given by

$$\tau_R = \tau + du\,\tau_R^{-1/2}\ ,\ u_R = u\left(\frac{1-\frac{1}{2}\,du\,\tau_R^{-3/2}}{1+\frac{1}{2}\,du\,\tau_R^{-3/2}}\right)\ ,\ w_R = \frac{9\,du^3}{2\tau_R^{5/2}\left(1+\frac{1}{2}\,du\,\tau_R^{-3/2}\right)^3}$$

where $d \equiv 3x^*/2\pi$. The renormalized parameters τ_R, u_R, w_R all depend on temperature (through τ) and $\bar{N}$. The field configuration is written as $\bar{\phi}$ instead of ϕ because the field configurations $\bar{\phi}^*(\mathbf{r})$ that minimize H_{eff} are the anticipated *thermally averaged* field configurations, $\bar{\phi}^* = \langle\phi\rangle$, while the field configurations $\phi^*(\mathbf{r})$ that minimize (2.105) are mean-field solutions.

The fluctuation-induced first-order character of the dis→lam transition can be verified by considering a single-mode approximation to a lamellar morphology, a sinusoidal concentration variation along, say, the z axis with preferred wavenumber q_0[8]:

$$\phi(\mathbf{r})\ (\text{or}\ \bar{\phi}(\mathbf{r})) = 2A\cos(\hat{\mathbf{z}}\cdot\mathbf{r}) \tag{2.108}$$

---

[8] In the high χN/low τ regime where A- and B-type monomers are strongly segregated, concentration fluctuations will be sharper and higher harmonics would be needed to accurately capture the morphology; however; in the weak-segregation regime near the ODT, which is our current region of interest, the single-mode approximation is reasonable.

Substituting 2.108 into (2.105) and (2.107) and averaging over 1 lamellar period yields

$$\beta H(A) = V\left(\tau\, A^2 + \frac{u}{4}\, A^4\right) \quad , \quad \beta H_{eff}(A) = V\left(\tau_R\, A^2 + \frac{u_R}{4}\, A^4 + \frac{w_R}{36}\, A^6\right) \tag{2.109}$$

Minimizing $H(A)$ with respect to A yields the predicted mean-field amplitude of a (single-mode) lamellar configuration; minimizing $H_{eff}(A)$ with respect to A yields the predicted thermally averaged amplitude of a fluctuating lamellar configuration. If $A = 0$ minimizes H or H_{eff}, disorder is favored by that model; if $A \neq 0$ minimizes H or H_{eff}, lamellae are favored. Figure 2.9 shows $H(A)$ and $H_{eff}(A)$ for several ranges of the (bare) effective temperature parameter τ, showing that $H_{eff}(A)$ admits a region of metastable disorder while $H(A)$ does not. For the renormalized model, when lamellae are stable or metastable their optimal amplitude (within the single mode approximation) is given by

$$A_{opt}^2 = -3\bar{u}_R + \sqrt{9\bar{u}_R^2 - 12\bar{\tau}_R} \tag{2.110}$$

where $\bar{\tau}_R, \bar{u}_R \equiv \tau_R/w_R, u_R/w_R$ and their predicted free energy is $\beta H_{eff}(A_{opt})$. The dis→lam ODT for H_{eff} is determined by $H_{eff}(A_{opt}) = H_{eff}(0) = 0$; this occurs at $\bar{\tau}_R = (9/16)\bar{u}_R^2$, or equivalently at $\chi N_{ODT} = 10.495 + 37.823\bar{N}^{-1/3}$, similar to the FRH prediction of $\chi N_{ODT} = 10.495 + 41.0\bar{N}^{-1/3}$.

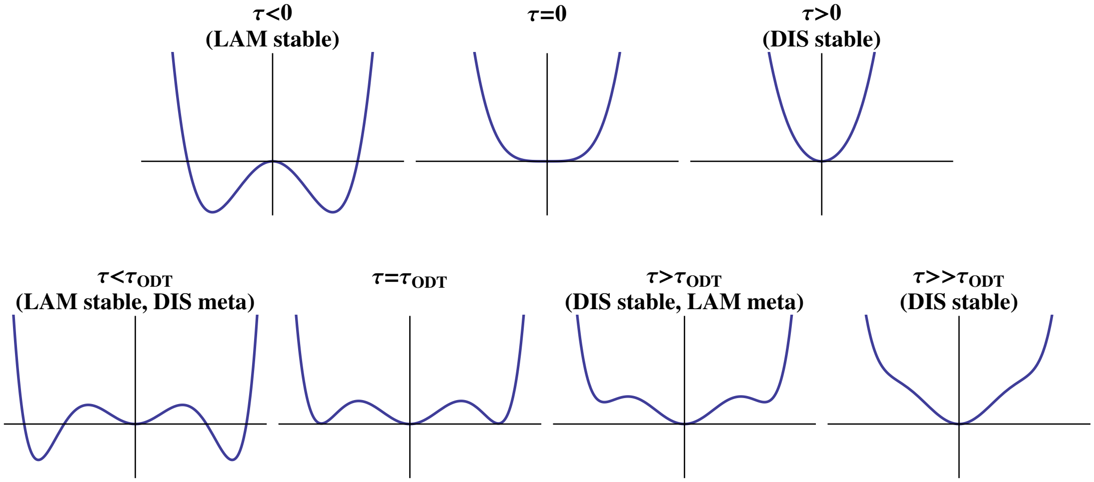

Figure 2.9: Upper row: $H(A) \propto \tau\, A^2 + (u/4)\, A^4$ for three distinct regimes of bare τ. u is always > 0. At $\tau < 0$ (low temperature) H is minimized at $A_{opt} \neq 0$, indicating stable lamellae. However, A_{opt} goes smoothly to zero as $\tau \to 0$, indicating a second-order transition. Above $\tau = 0$, disorder is stable. Lower row: $H_{eff}(A) \propto \tau_R\, A^2 + (u_R/4)\, A^4 + (w_R/36)\, A^6$ for four distinct regimes of bare τ. τ_R and w_R are always > 0, but in the regime near the renormalized ODT u_R may be < 0, allowing lamellae with free energy $H_{eff}(A_{opt})$ and disorder with free energy $H_{eff}(0)$ to be relatively metastable.

2.4.4 Numerical methods: mean-field and Langevin

In Chapter 5 we treat 1. mean-field dynamics of the renormalized model (2.107) and 2. Langevin dynamics of the bare model (2.106). ϕ and $\bar{\phi}$ are discretized on Cartesian grids with periodic boundary conditions. Several different grid resolutions are tested, as described in Chap. 5.

The mean-field dynamics of (2.107) are given by

$$\begin{aligned}
\frac{\partial\bar{\phi}(\mathbf{r})}{\partial t} &= \nabla^2 \frac{\delta H}{\delta\bar{\phi}(\mathbf{r})} \\
\bar{\phi}_{t+\Delta t}(\mathbf{r}) &= \bar{\phi}_t + \Delta t\, \nabla^2 \left(e(\nabla^2 + q_0^2)^2 \bar{\phi}_t + \tau_R \bar{\phi}_t + \frac{u}{6}\bar{\phi}_t^3 + \frac{w_R}{5!}\bar{\phi}_t^5 \right)
\end{aligned} \tag{2.111}$$

For the mean-field dynamics, we only care about the final converged solution, so timestepping accuracy is not as important as stability. For this reason, we employ a semi-implicit evolution in Fourier space:

$$\begin{aligned}
&\bar{\phi}_{t+\Delta t}(\mathbf{k}) = \\
&\bar{\phi}_t(\mathbf{k}) - k^2 \Delta t \left(e(-k^2 + q_0^2)^2 \bar{\phi}_{t+\Delta t}(\mathbf{k}) + \tau_R \bar{\phi}_{t+\Delta t}(\mathbf{k}) + FT \left[\frac{u}{6}\bar{\phi}(\mathbf{r})^3 + \frac{w_R}{5!}\bar{\phi}_t(\mathbf{r})^5 \right] \right)
\end{aligned} \tag{2.112}$$

where “FT” represents a Fourier transform. The “semi-implicit” nature is due to the fact that the linear e and τ_R terms are treated at timestep $t + \Delta t$. Solving for $\phi(\mathbf{k})_{t+\Delta t}$, we find

$$\begin{aligned}
&\bar{\phi}_{t+\Delta t}(\mathbf{k}) = \\
&\frac{1}{1 + k^2 \Delta t \left[e(-k^2 + q_0^2)^2 + \tau_R \right]} \left(\bar{\phi}_t(\mathbf{k}) - k^2 \Delta t\, FT \left[\frac{u_R}{6}\bar{\phi}(\mathbf{r})^3 + \frac{w_R}{5!}\bar{\phi}_t(\mathbf{r})^5 \right] \right)
\end{aligned} \tag{2.113}$$

This scheme has the advantage of unconditional stability, allowing us to choose large timestep sizes. The Fourier transform convention in our code is

$$\begin{aligned}\phi(\mathbf{k}) &= \frac{1}{V}\int d\mathbf{r}\, e^{-i\mathbf{k}\cdot\mathbf{x}}\,\phi(\mathbf{r}) = \frac{1}{N}\sum_{\mathbf{r}} e^{-i\mathbf{k}\cdot\mathbf{x}}\,\phi(\mathbf{r}) \equiv \text{“}FT[\phi(\mathbf{r})]\text{”}\\ \phi(\mathbf{r}) &= \int d\mathbf{k}\, e^{i\mathbf{k}\cdot\mathbf{x}}\,\phi(\mathbf{k}) = \sum_{\mathbf{r}} e^{i\mathbf{k}\cdot\mathbf{x}}\,\phi(\mathbf{k}) \equiv \text{“}FT^{-1}[\phi(\mathbf{k})]\text{”} \quad . \end{aligned} \tag{2.114}$$

According to (2.1), the Langevin dynamics for (2.106) are given by

$$\frac{\partial\phi_s(\mathbf{r})}{\partial t} = -M\frac{\delta\,\beta H}{\delta\phi_s(\mathbf{r})} + \xi \tag{2.115}$$

where ξ is the thermal noise and M is a mobility; we take $M = 1$ for simplicity as in [106]. Here we do not use a Laplacian to conserve ϕ as in (2.111) because it introduces too much stiffness; instead, we enforce $\int \phi\, d\mathbf{r} = 0$ by zeroing the $\mathbf{k} = 0$ mode at each timestep (this is found not affect the evolution of other modes).

Writing the discretized version of (2.115) with the correct noise strength is slightly subtle. The fluctuation-dissipation theorem expects that $\frac{\delta\,\beta H}{\delta\phi(\mathbf{r})}$ represents the *physical* change in energy associated with a change in $\phi(\mathbf{r})$ for a single grid point. That physical change in energy is actually $\frac{\delta\,\beta H}{\delta\phi(\mathbf{r})}\Delta V$, where $\Delta V = \Delta r_x \Delta r_y \Delta r_z$ is the volume associated with a single grid point. Therefore a lattice-discretized version of (2.115) that satisfies the fluctuation-dissipation theorem, and thus samples the Boltzmann distribution of H, is

$$\phi_{s,t+\delta t}(\mathbf{r}) = \Delta V\, \delta t\, \bar{N}^{1/2}\left(e[\nabla^2 + q_0^2]^2\phi_{s,t} + \tau\, \phi_{s,t} + \frac{u}{6}\phi_{s,t}^3\right) + \sqrt{2\delta t}\,\eta(\mathbf{r},t) \quad (2.116)$$

$\eta(\mathbf{r},t)$ is Gaussian random noise with $\langle \eta(\mathbf{r},t)\eta(\mathbf{r}',t')\rangle = \delta_{\mathbf{r},\mathbf{r}'}\delta_{t,t'}$ where δ is the Kronecker delta, $\mathbf{r}, \mathbf{r}'$ are discrete grid sites, and t, t' are discrete timesteps. We may also define a rescaled timestep $\Delta t = V\delta t$ and write

$$\phi_{s,t+\Delta t}(\mathbf{r}) = \Delta t\, \bar{N}^{1/2}\left(e[\nabla^2 + q_0^2]^2\phi_{s,t} + \tau\, \phi_{s,t} + \frac{u}{6}\phi_{s,t}^3\right) + \sqrt{\frac{2\Delta t}{\Delta V}}\eta(\mathbf{r},t) \quad (2.117)$$

2.117 is the version used in our code.

For Langevin dynamics, timestepping accuracy and stability are both important, since thermal averages are computed as time averages over long trajectories. Using a timestep that is too large may cause the simulation to diverge or, at best, result in inaccurate thermal averages. A range of timesteps must be explored by examining the time average of some test quantity $f(\phi)$, and finding Δt_{max} such that $\langle f(\phi)\rangle$ does not change significantly for $\Delta t < \Delta t_{max}$. Δt_{max} should then be used as the simulation timestep size. To evolve (2.117), we use the Fourier-space exponential time differencing scheme described in [98], which provides second-order accuracy in time.

Because the noise strength in (2.117) depends on ΔV, the largest acceptable timestep depends on the resolution. Finer resolutions tend to require smaller timesteps. In Chapter 5, for example, we find that at $\bar{N} = 10^4$, 7 grid points/lamellar period requires $\Delta t = 0.00005$ while 10 grid points/lamellar period requires $\Delta t = 0.00002$.

2.4.5 Invariance of physical control parameters

Concerning the SCFT and phase-field models' control parameters, one subtle point deserves clarification. Physically, a polymer chain consists of a well-defined number of monomer repeat units N_m. However, in constructing the above models, we lumped sections of monomer repeat units into N "statistical segments," each of which consists of enough monomer repeat units to act as an entropic spring, then used this value of N to derive Hamiltonians. Thus N for a given physical diblock is essentially arbitrary, and depends on our choice of statistical segment length. However, we also considered the enthalpic penalty χ_{AB} for contact between statistical segments of unlike monomers. For a physical chain with fixed N_m, choosing to lump, *e. g.*, a larger number of monomers into our definition of a single statistical segment will reduce N but increase χ_{AB}, so that the combination $\chi_{AB}N$ does not depend on our (arbitrary) choice of statistical segment length. For our Hamiltonians to make physical sense, then, we anticipate they will depend on χ_{AB} only through the combination $\chi_{AB}N$, which fortunately is the case. (The other control parameter, the block fraction f, has a direct physical interpretation.)

A similar situation occurs with the control parameter $\bar{N} = 6^3(R_g^3\rho_c)^2$. $R_g = \sqrt{Nb^2/6}$ is physically well-defined because for a given N_m, choosing smaller statistical segments will increase N but decrease the statistical segment length b^2 to compensate, and $\rho_c =$ num chains/volume is also physically well-defined for a given melt. Therefore, $\bar{N}$ is physically well-defined.

Chapter 3

Application of the string method to SCFT

Reproduced in part with permission from B. Kim, N. Laachi, K. T. Delaney, M. Carilli, E. J. Kramer, and G. H. Fredrickson, “Thermodynamic and Kinetic Aspects of Defectivity in Directed Self-Assembly of Cylinder-Forming Diblock Copolymers in Laterally Confining Thin Channels,” *Journal of Applied Polymer Science* **2014**, 40790. Copyright 2014 Wiley Periodicals, Inc.

Reproduced in part with permission from K. Izumi. B. Kim, N. Laachi, K. T. Delaney, M. Carilli, and G. H. Fredrickson, “Barriers to defect melting in chemo-epitaxial directed self-assembly of lamellar-forming diblock copolymer/homopolymer blends,” *Proceedings of the SPIE* **9423**, 94232C. Copyright 2015 Society of Photo-Optical Instrumentation Engineers.

Reproduced in part with permission from K. Izumi, B. Kim, N. Laachi, K. T. Delaney, M. Carilli, and G. H. Fredrickson, “Thermodynamic and kinetic aspects of barriers to defect melting in lamellae-forming diblock copolymer/homopolymer blends on chemo-epitaxially patterned substrates.” *Submitted to the Journal of Polymer Science Part B.*

3.1 Implementation of the string method on NVIDIA GPUs

As mentioned in the Introduction, metastable defects present a major obstacle against scaling up directed self-assembly to the system sizes and production volumes required for industrial semiconductor patterning. The International Technology Roadmap for Semiconductors (ITRS) has established a desired target defect density of < 0.01 defects/cm^2 [113, 114]. Theoretical tools capable of predicting the incidence of defects, as well as the kinetic barriers and annealing times associated with their removal, are a valuable asset. Such tools can be used to evaluate the qualitative and quantitative effects of experimentally controllable parameters like χN, trench width in grapho-epitaxy, sidewall/substrate wetting conditions, polydispersity, and the presence of added homopolymer, and suggest parameters that suppress the formation of defects and facilitate their removal. Self-consistent field theory by itself is an effective tool to investigate the formation energy of defects, and predict their incidence; the string method used in conjuction with SCFT can find minimum energy paths that provide an estimate of the kinetic barriers for transitions between metastable defect states and stable defect-free states.

Because of the computational horsepower required to relax multiple SCFT models (images), especially in 3 dimensions, and the relatively recent development of the string method itself, it is only within the last several years that the string method in conjuction with SCFT has become practical. It was first used by Cheng *et al.* to calculate minimum energy paths for lamellar-to-cylinder, lamellar-to-gyroid, cylinder-to-gyroid, and gyroid-to-cylinder transitions in an AB diblock melt [115]. Takahashi *et al.* [116, 117] performed an SCFT study of defect formation energies for diblock melts in confining channels. His study explored the effects of sidewall wetting, substrate wetting, and polydispersity in both 2 and 3 dimensions. He also used the string method to calculate minimum energy paths for defect annealing in the 2D case. He did not extend the string calculations to 3 dimensions, citing high computational cost. However, his 3D SCFT calculations for individual models revealed that substrate wetting caused significant quantitative changes in the energies of defects as well as qualitative changes in the types of defects that most readily formed. These effects could not be captured by a purely 2D model. Therefore, for realistic studies of defect annealing in confined polymer melts, the capability to perform fully 3-dimensional string method SCFT simulations is highly desirable, provided a sufficiently powerful computing platform can be found.

Figure 3.1: Block diagram of an Nvidia GF100 GPU, whose Fermi architecture is similar to the GPUs present on Knot and Braid. The device is organized into 16 “streaming multiprocessors” or SMs, each of which contains 32 cores for standard arithmetic instructions. Figure adapted from http://images.anandtech.com/reviews/video/NVIDIA/GF100/GF100.png .

Graphics processing units (GPUs) are one platform with the necessary attributes. Modern GPUs contain hundreds to thousands of lightweight cores capable of processing data in parallel (Figure 3.1), allowing the GPU overall to achieve high throughput of arithmetic instructions. For example, the recently released NVIDIA Titan X contains 3,072 cores, with an arithmetic throughput of up to 7 trillion single-precision or 200 billion double-precision floating-point operations (FLOPS) per second [118]. In addition to their high throughput, modern GPUs also possess a sizeable amount of onboard dedicated RAM (“device memory") which the cores can access at relatively high bandwidth (336 gigabytes/sec for the Titan X; bandwidth for earlier-generation boards also tends to be in the range of hundreds of GB/s). These characteristics make GPUs an ideal choice for problems where a significant amount of data must be processed, as long as an algorithm can be chosen that allows different data elements to be processed in parallel (choosing such an algorithm is known as "exposing parallelism"). Additionally, since the primary market for GPUs is gaming PCs, GPUs are designed with a relatively small form factor and power requirements. Individual GPUs can be installed on a single workstation, conveniently delivering "cluster-on-a-desktop" performance. Finally, in 2007 Nvidia released the Compute Unified Device Architecture (CUDA) framework [119], an API for C, C++, and Fortran that allows researchers to write general-purpose GPU code without needing to package their calculations in the language of graphics processing, as was necessary earlier [120]. Other APIs that facilitate general-purpose GPU computing, like OpenACC [121] and OpenCL [122], are also easily accessible to researchers. These combined factors have led to an explosion in the use of GPUs for scientific computation over the last decade. In 2008 roughly 4,000 academic papers had been written with the the aid of GPUs; by 2015 that figure had risen to 60,000 [118]. Current scientific applications for GPUs include molecular dynamics [123], computational fluid dynamics [124], combustion [125], protein folding [126], quantum chemistry [127], and many others, including polymer field theory [128, 129].

Over the past several years, our group has developed a comprehensive software suite (PolyFTS) capable of performing SCFT calculations for a variety of different polymer chain architectures, blends, and solutions. PolyFTS can impose arbitrary confinements and sidewall wetting conditions in 1, 2 and 3 dimensions. As mentioned in Chapter 2, the most memory- and processing-time-intensive aspect of SCFT is solving the propagator equations via the pseudo-spectral algorithm (2.98), in which the most expensive component is the sequence of forward and backward FFTs required to advance $q(\mathbf{r}, s)$ along the contour variable s. To offset this computational cost, PolyFTS can be compiled to run on multiple nodes and multiple cores per node using the MPI and OpenMP libraries, or compiled to run on individual Nvidia GPUs using CUDA. The MPI-OpenMP configuration makes use of FFTW, a highly optimized, (optionally) parallel open-source FFT library [130, 131]. The GPU configuration makes use of cuFFT, an optimized library provided by Nvidia [132]. In the MPI-OpenMP configuration of PolyFTS, field data is distributed across multiple nodes, meaning that internode data transfer is necessary to perform certain global operations (tranposes, etc) required by the FFTs. By contrast, in the GPU configuration of PolyFTS, all the data required for a single model resides in the global memory of a single GPU, and no internode communication is required. In practice we find that the global communications required by the FFTs scales poorly across multiple nodes in the MPI-OpenMP configuration of PolyFTS [133]. In typical tested cases, increasing the number of MPI cores from 8 to 64 reduces the wall time only a factor of approximately 2. By comparison, for systems with a large ($>\sim 200,000$) number of plane waves, SCFT calculations on a single GPU run roughly twice as fast as equivalent calculations on 64 MPI cores. Also, as system size increases, the performance of the single-GPU configuration is observed to improve relative to the multinode MPI configuration: the bigger the system, the more favorable it becomes to run on a GPU. All these factors indicate that GPUs are an advantageous platform for large-cell 3-dimensional SCFT calculations.

Although the FFTs typically dominate the wall time of our SCFT code, we note that other operations frequently appearing in the SCFT equations are highly amenable to the massively parallel architecture of GPUs. Elementwise field arithmetic like adding, subtracting, or multiplying two fields parallelizes trivially, and reduction operations like summing a particular value across a field or taking the L2 norm of two fields can be implemented using well-known, efficient parallel algorithms [134].

I set out to write a GPU-accelerated string method into PolyFTS capable of interfacing with the existing AB+A+B copolymer+homopolymer melt model (this was the system of greatest interest to my colleagues and our industrial partners). From an algorithmic perspective, the task was straightforward.

The update step of the string method is performed independently for each image. The w_+ field is iterated to a partial saddle point and the w_- field is advanced for one timestep using the standard SCFT relaxation equations. Therefore, in my code, this step trivially makes use of functionality already present in PolyFTS, and allows the user to choose any desired timestepping scheme already present in the code. Although the updates for each image are serialized, each image's update step is a full SCFT iteration which internally takes advantage of the large amount of parallelism over grid points inherent to SCFT, and thus makes efficient use of the GPU.

The interpolation and reparametrization step, as described in Chapter 2, consists of considering each grid point individually, constructing a spline through the values at that grid point possessed by the sequence of images, and redistributing the values associated with that grid point at even arc length values along the spline. To construct the spline, first we must calculate the L2 norm of the difference between each image (and possibly the energy of each image as well, if energy weighting is being used) to obtain the images' initial arc length coordinates. For each pair of consecutive images, the L2 norm can be computed using an efficient parallel reduction operation. However, the same initial arc length coordinates are

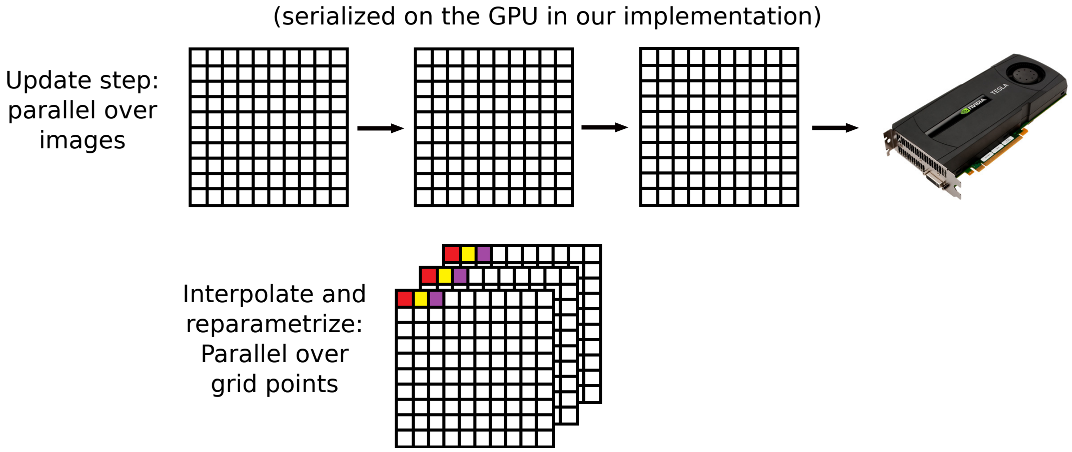

Figure 3.2: Parallelism exposed by the string method. The update step is performed independently for (is parallel over) different images; however, we choose to perform this step in serial for each image on the GPU, taking advantage of the internal parallelism exposed by individual SCFT updates to make efficient use of the GPU's many-core architecture.
The interpolation and reparametrization step is parallel over grid points.

Figure 3.3: To perform the interpolation and reparametrization steps of the string method, each grid point is assigned to a single thread, and each thread runs on a single GPU core.

used to construct the splines for each grid point, meaning that once the initial arc length coordinates have been obtained, the remaining operations required to construct the spline for each grid point, as well as the reinterpolation of that grid point's values for each image along the spline, are completely parallel over grid points (Figure 3.2). I wrote a kernel in which each thread handles a single grid point (Figure 3.3). Each thread accepts an array of initial arc length values and grid point values, then performs the remaining steps of spline construction and reinterpolation independently, using a cubic spline and spline interpolation routine from Numerical Recipes in C [135].

The most significant challenge associated with integrating an efficient GPU-accelerated string method SCFT code into PolyFTS was the high memory demand of placing multiple models on the GPU. In order for the string method to accurately trace out minimum energy paths between locally stable states, typically at least 20 images are required. However, PolyFTS was originally written to simulate individual models in isolation. A given model allocation includes memory for its propagator, w_+ and w_- fields, and a significant number of internal utility fields. Each model also contains forces and an associated field updater, and each of these in turn allocates additional utility fields. All these fields are complex-valued double precision, with dimensionality equal to the number of grid points. Many of the fields must be FFTable, and the cuFFT API requires that a unique "cuFFTplan" object be assigned to each of these. The cuFFTplans themselves require a significant amount of memory to allow out-of-place operations. As an example, the model for a single image used in the simulations of lying-down cylinders presented in Section 3.2 requires 231 internal field allocations for a total of 2.4 GB per model. Our available GPUs contain at most 6.14 GB of onboard device memory, meaning that if PolyFTS' original memory allocation strategy is used, only 2 images can fit in onboard memory for that particular model and grid size. Needless to say, this is insufficient for string method calculations.

In principle, for a given model, the memory demands of the propagator can be alleviated by transferring each field along the contour from device (GPU) to host (CPU) RAM as the propagator is computed, then, once the finished propagator resides on the CPU, computing the density fields purely on the CPU. However, the bandwidth of the PCI-Express bus, through which the GPU accesses CPU RAM, is roughly a factor of 10 less than the bandwidth at which GPU is able to access its onboard device memory. Overall, swapping out the propagator from device to host memory increases wall time by roughly a factor of 2 for individual SCFT models, as described in [133]. I decided on a more elegant approach, inspired by four points:

1. The field updates for each image are performed independently.

2. The underlying parameters of each image (plane wave grid, system size and composition, wall configuration, etc.) are identical.

3. The w_+ field is recomputed from the w_- field at each timestep using the partial saddle point approximation, and the propagators in turn are recomputed from the w_- and w_+ fields at each timestep.

4. At each timestep, once computed, the propagator is used only to obtain the density fields and timestep the w_- fields.

Points 3 and 4 indicate that, since all quantities relevant to the SCFT relaxation equations are recomputed from the w_- fields timestep to timestep, within the partial saddle point approximation the w_- field contains all information associated with a given model (aside from external parameters like the wall density). Thus, in principle, for a given image only the w_- field needs to be stored persistently. The w_+ field, density fields, and most importantly, the propagator can be computed in a scratch space, then ignored or overwritten once they have been used to advance the w_- fields. The w_- field is a relatively lightweight object, and for complex-valued double-precision fields requires only $M \times 16$ bytes of storage, where M is the number of plane waves, in contrast to the $N_s \times M \times 16$ bytes required by the propagator. For a system size of $128 \times 128 \times 40$ grid points with $N_s = 100$

contour points, for example, the w_- field consumes only 10.5 MB of GPU global memory, while the propagator consumes 1.05 GB.

Points 1 and 2 indicate that, since the plane wave grid is identical for each image, different images can use the same scratch space.

With these points in mind, a obviously beneficial strategy is to allocate scratch memory for the propagator computation and any other quantities that are recomputed at each timestep, and allow all images to share this memory. For convenience, I accomplished this by writing two constructors for the AB+A+B model class in our code, one of which built the model normally, allocating memory for all internal objects including the propagator, and one of which accepted scratch memory from another model, storing references to this external memory instead of making new internal allocations. The first image along the string (“image 0”) is built using the former constructor; the other images are built using the latter constructor and references to the internal memory of the first image. In this way the memory of the first image devoted to the propagator and other overwriteable objects becomes the scratch space used by all images. The propagators are by far the most important object for which to implement a shared scratch space; however, I also reuse memory for as many of the AB+A+B model’s internal utility fields as is convenient. Figure 3.4 shows the conceptual implementation of the memory-sharing scheme. During the update step of the string method, images

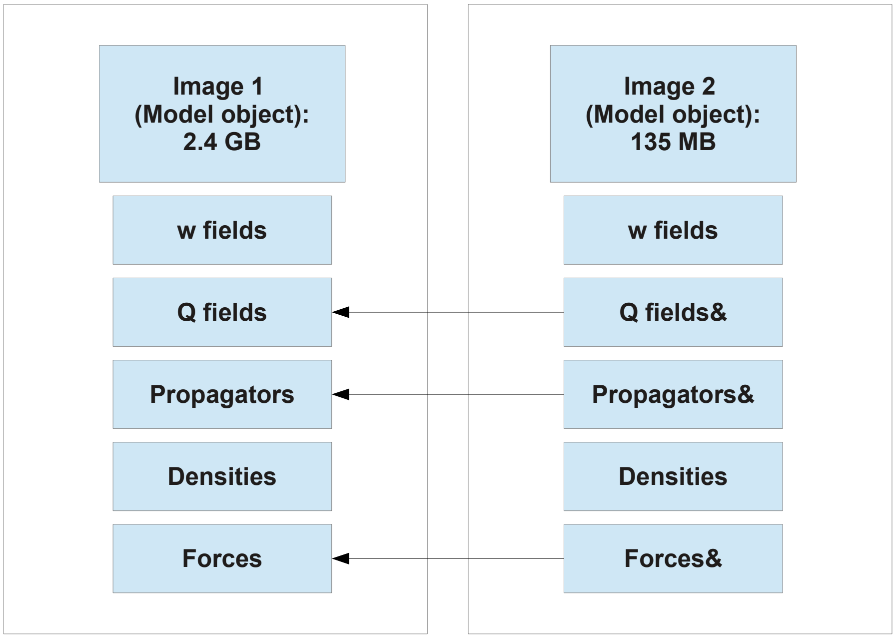

Figure 3.4: Memory sharing scheme implemented for the system considered in Section 3.2, with grid dimensionality 128 × 128 × 40. The first image allocates memory for all internal fields, including the propagator, and consumes 2.4 GB. The second image, and all subsequent images, accept references to first images' memory for many fields that are overwritten at each timestep (*e.g.*, the propagator, forces, and utility fields used for internal calculation like the "Q fields"). These later images consume only 135 MB apiece. The density fields (ρ_A, ρ_B) and the w_+ fields are retained as independent allocations because, even though they are overwritten based on the w_- fields, storing them persistently is helpful when writing the string's data to files.

are updated individually, one after the other. Their propagators are recomputed in the scratch space, which overwrites the propagator of the previous image, but this is not a problem.

The results of my memory-sharing strategy are dramatic: The first model (unavoidably) consumes a relatively large amount of memory, but each additional image requires roughly 95% less memory than the first, allowing enough images to fit in GPU global memory to make the string method feasible without resorting to costly CPU-GPU transfers. For the system studied in Section 3.2, the first image consumes 2.4 GB while subsequent images consume only 135 MB. This means that we can fit up to 27 images in the 6.14 GB of onboard memory possessed by our available GPUs. In addition, since I take care to share the memory only for quantities that had to be recomputed at each timestep, there is no computational penalty for this memory optimization.

My implementation of the string method is capable of either advancing the w_{-} field for each image according to the full force or projecting the force into the hyperplane tangent to the string; it can also perform the interpolation and reparametrization step in either real or Fourier space. In practice, we find that these choices do not significantly affect the converged barrier states; however, restringing in real space appears to offer improved stability over restringing in Fourier space. My implementation is also capable of image climbing, as described in Chapter 2. For well-resolved strings, we typically find that image climbing is unnecessary, and using the highest-energy image directly to estimate the barrier peak is sufficiently accurate to establish qualitative and quantitative trends.

Colleagues in the Fredrickson group applied my GPU string method code to several industrially relevant systems. The following three sections present an overview of three such studies, which resulted in four published papers. In all cases, I added functionality to the code as requested and supplied technical guidance; in the case of [136, 137] I also co-wrote and extensively edited the manuscripts.

3.2 Application to cylinder-forming diblocks in graphoepitaxial channels

For linear one-dimensional structures like lamellae or cylinders, long-range phonon (bending) modes require negligibly low energy to excite, meaning that creating such structures with long-range (millimeters to centimeters) order is difficult. In previous experimental work, electric fields [138], shear application [139], flow [140], and guiding chemical or lithographic templates [3, 141, 142] have all been shown to help overcome this difficulty and facilitate long-range order. In this section, we review a recent publication [143] in which SCFT is used to explore the formation energies of dislocation and disclination (Fig. 3.5) defects appearing in lying-down cylinder morphologies in a grapho-epitaxial guiding channel. The string method is then used to find the minimum energy paths by which these defects anneal out. The polymer system under consideration is a neat AB diblock melt, which can be simulated within the scope of PolyFTS' AB+A+B model. In an attempt to find the most favorable conditions for defect-free lying-down cylinders, we explore a variety of segregation strengths, channel widths, and A-monomer volume fractions. Both neutral and preferentially wetting sidewalls, substrates, and top surfaces are considered, although each surface's attractiveness to one monomer species or the other is taken to be spatially homogeneous (not chemo-epitaxially patterned). For the purpose of determining free energies, the χ value for repulsion of statistical segments of differing monomer species is assumed to be that of polystyrene-b-methymethacrylate (PS-b-PMMA). This particular composition is commonly used in experiments [142] and is consistent with our group's previous theoretical studies [116].

3.2.1 Commensurability windows for A-attractive sidewalls, neutral top and bottom surfaces

First, we consider confinements where the top and bottom surfaces are neutral while the sidewalls are attractive to PMMA (which I will also refer to as monomer species "A"). Here and subsequently in this section, PMMA is the minority-block, cylinder-forming species. This wetting configuration has been experimentally shown to favor the formation of lying-down cylinders with long-

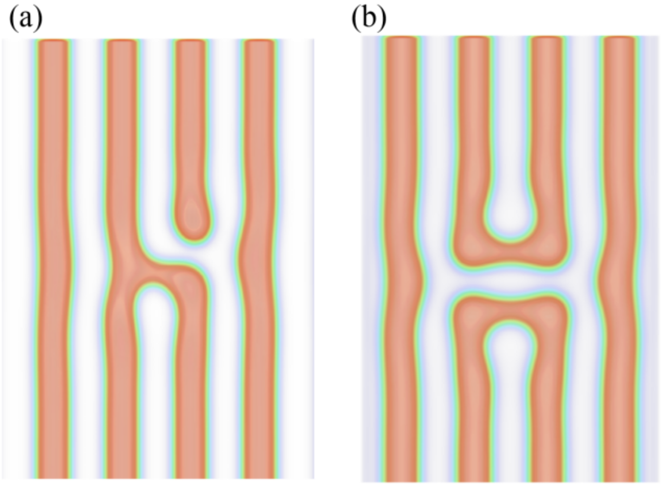

Figure 3.5: Top view of a dislocation defect (a) and a disclination defect (b) as they appear in lying-down cylinders. Initially, these dislocation and disclination defects are obtained by relaxation from random seeds.

range order [144], and theoretically shown to favor the formation of standing-up lamellae [116]; therefore, it is a logical starting point when attempting to stabilize horizontal cylinder morphologies.

We sweep the height L_z of the channel to determine optimal thickness for a monolayer of lying-down cylinders, then sweep the width, establishing that morphologies with different numbers of adjacent lying-down cylinders each have distinct favorable channel widths (Figure 3.6) at which their elastic stress is minimized. If the channel width is increased (decreased) too significantly relative to the favorable channel width for a given number of cylinders, a morphology with one cylinder added (removed) becomes energetically favorable. The free energies in Figure 3.6 are reported relative to the free energies of corresponding stress-free

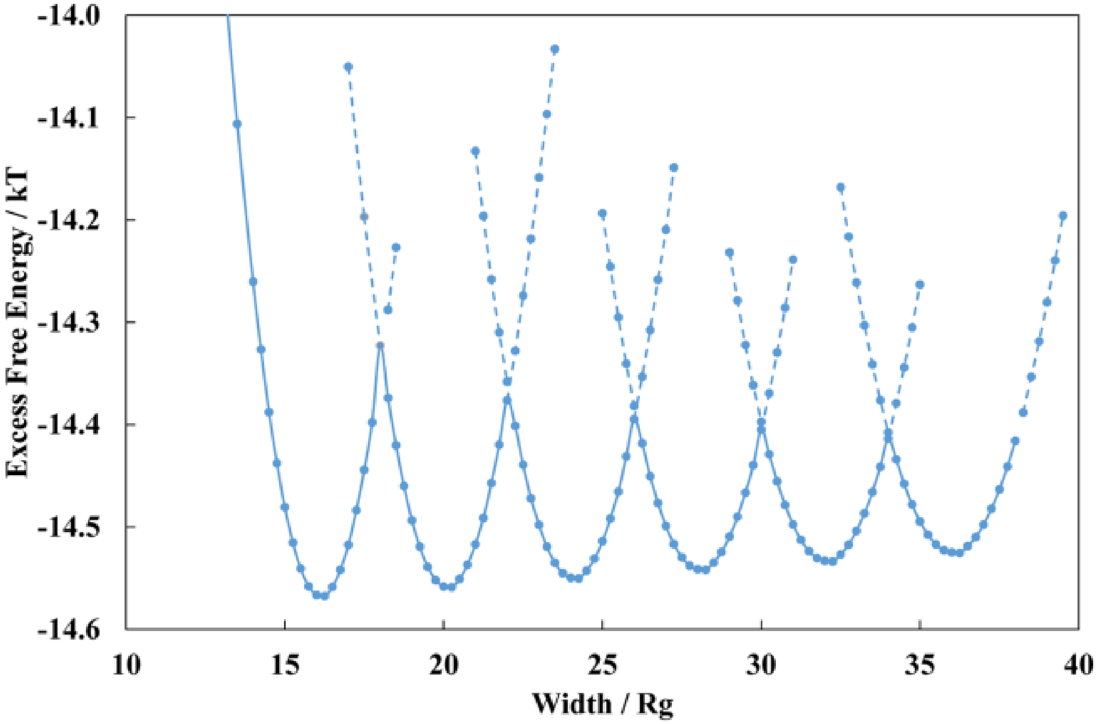

Figure 3.6: Commensurability windows for morphologies with 3 to 8 (from left to right) defect-free lying-down cylinders at $\chi N = 25$, $f_A = 0.3$. The sidewalls are A-attractive with $\chi w_A = -32$. Note that each morphology has a well-defined favorable channel width window. The "excess free energy" is defined relative to a bulk (unconfined) configuration with the same number of cylinders.

bulk morphologies; the difference between the free energies of bulk and confined stress-free configurations is due to the surface tension in confinement.

Since our emphasis is on the elimination of defects, we investigate the formation energy of dislocation and disclination defects as a function of channel width at several different block fractions at the optimal monolayer height $L_z = 3.75R_g$. Here and subsequently, we focus on the range of channel widths in which a mor-

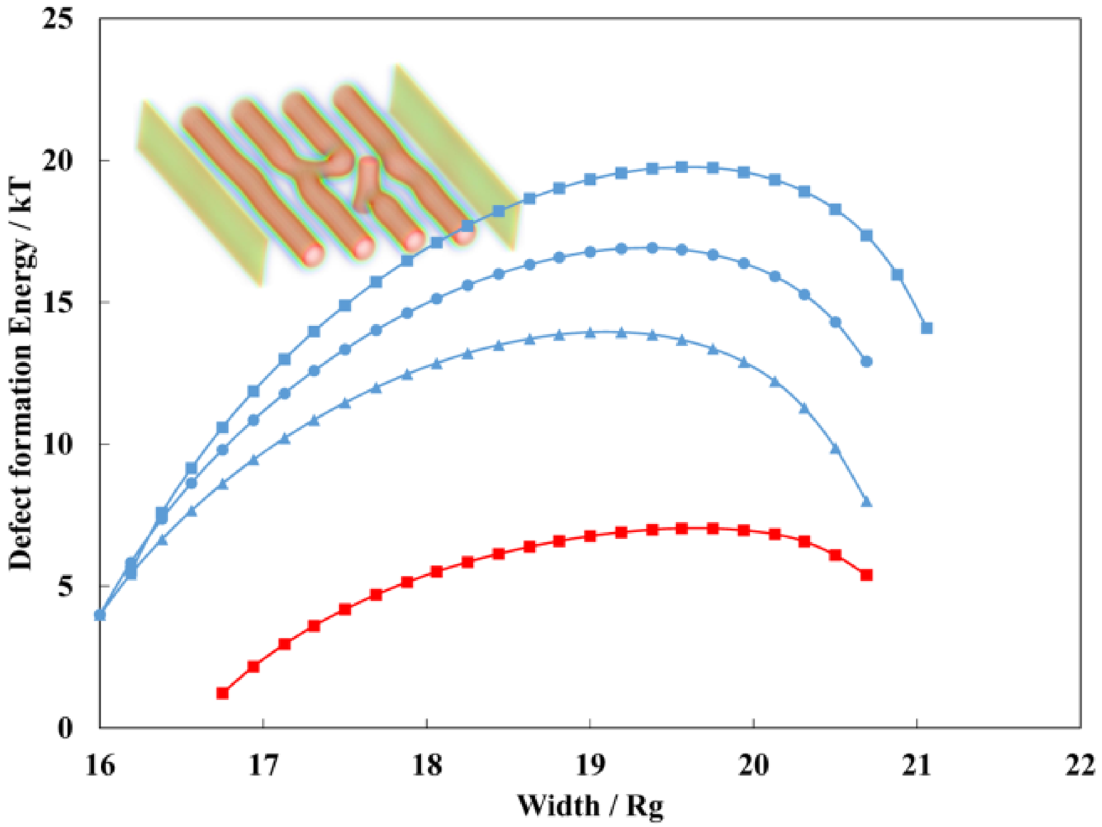

Figure 3.7: Excess free energy (relative to defect-free morphologies) of dislocation defects (red) and disclination defects (blue) in a confining geometry with A-wetting sidewalls, a neutral top surface, and a neutral bottom surface (substrate) for $\chi N = 25$, $L_z = 3.75R_g$, and $\chi_{wA} = -32$. Triangles denote $f_A = 0.23$, circles denote $f_A = 0.24$, and squares denote $f_A = 0.25$. Note that the dislocation defect is only observed to be metastable for $f_A = 0.25$. Important trends to note are 1. there clearly exists a commensurability width that maximizes the formation energy of defects and 2. the formation energy of defects increases with increasing f_A.
The inset shows an interesting effect for the dislocation: the terminus of the unconnected cylinder "tongue" branches out to the neutral top and bottom surfaces.

phology containing 4 adjacent lying-down cylinders is favored. This width is sufficient to contain the two defect types under investigation and capture their excess free energy relative to a defect-free 4-cylinder morphology. Results are summarized in Figure 3.7. It happens that the dislocation defect is only stable for one of the tested block fractions, $f_A = 0.25$. One interesting effect we observe is that the terminus of the unconnected cylinder "tongue" in the dislocation branches out to the neutral top and bottom surfaces (inset of Fig. 3.7). In general, the observed disclination defects have higher excess free energies than the dislocation defects at the same channel widths. This is because the four right-angle bends required to form disclinations incur a higher energy penalty than the bending required to form dislocations.

Importantly, the energies for both types of defects exhibit clear maxima at specific channel widths. Also, for $f_A = 0.25$, where both disclinations and dislocations are observed, this width is roughly the same for both types of defects. We conclude that there is a specific commensurable channel width that maximizes the free energy of defects relative to the free energy of perfect cylinders. The commensurable channel width depends noticeably on the minor-block fraction, ranging from $\sim 19\ R_g$ for $f_A = 0.23$ to $\sim 20\ R_g$ for $f_A = 0.25$. The range of defect excess free energies, $2-7$ kT for the dislocation and $\approx 5-20$ kT for the disclinations, is significantly smaller than the range of excess defect free energies for similar defects occuring in lamellae at similar system sizes. Dislocations appearing in lamellae had excess free energies in the range of $55-90$ kT and disclinations appearing in lamellae had excess free energies in the range of $95-120$ kT [116]. This could be because those defects in lamellae extend all the way from the top to the bottom of the channels; for the dislocation it could also be because the branches coming out of the disconnected cylinder act to stabilize the defect, as observed in [145]. Another observed trend is that the formation energy of dislocation defects increases with increasing minor block fraction f_A.

3.2.2 Commensurability windows for A-attractive sidewalls and bottom surfaces, B-attractive top surfaces

We repeat the commensurable width analysis for confinements with a B-attractive top surface and A-attractive sidewalls and substrate. This setup is expected to remove the stabilizing branches protruding from the disconnected cylinder of the dislocation; it also corresponds to the setup used in [5]. The A-attractive sidewalls and substrate (bottom surface) are taken to have $\chi_{wA}N = -32$, and the B-attractive top surface is taken to have $\chi_{wB}N = -32$.

First, to extract the trends associated with changing the minor block fraction, we fix the AB interaction at $\chi N = 30$ and sweep through $f_A = 0.23, 0.24, 0.25, 0.27$ (Figure 3.8). Formation energies of defects are plotted in terms of the strain percentage $100 \times \frac{width-width_{optimal}}{width_{optimal}}$, where $width_{optimal}$ is the commensurable width that maximizes the free energy associated with that particular defect type. Also,

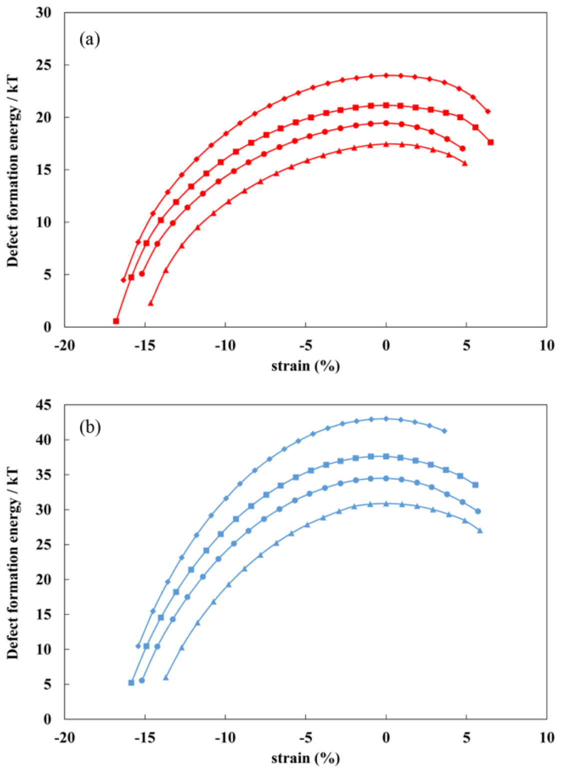

Figure 3.8: Excess free energy (relative to defect-free morphologies) of dislocation defects (a) and disclination defects (b) in a confining geometry with A-wetting ($\chi_{wA}N = -32$) sidewalls and substrate and a B-wetting ($\chi_{wB}N = -32$) top surface. χN is fixed at 30, and $L_z = 5.6\ R_g$. Triangles denote $f_A = 0.23$, circles denote $f_A = 0.24$, squares $f_A = 0.25$, and diamonds denote $f_A = 0.27$. As in 3.7, there is a clear commensurability width, and also, the formation energy of both types of defects increases with increasing f_A.

the wetting condition (B-attractive top surface and A-attractive sidewalls and substrate) successfully removes the branches coming out of the dislocation's disconnected cylinder. As in Subsection 3.2.1, the disclination defects demonstrate higher formation energy than the dislocation defects at all widths, and the trend of increasing defect formation energy with increasing minor block fraction continues to hold. However, comparing Figures 3.7 and 3.8, we see that the defect formation energies for this setup are significantly higher than those observed in neutral top and bottom surfaces, indicating that the wetting conditions considered here represent a more promising setup for producing defect-free morphologies in experiments.

In Figure 3.7, for the neutral top surface and substrate, the commensurable width changes with block fraction. This effect also occurs in the presence of an A-wetting substrate and B-wetting top surface, but it is obscured in Figure 3.8 because we plot energy as a function of the strain percentage instead of the absolute width. The commensurable width varies from ≈ 19 R_G to ≈ 21 R_g as f_A is increased from 0.23 to 0.25.

Second, to extract the trends associated with changing χN, we fix f_A at 0.25 and sweep through $\chi N = 25, 27, 30, 33$ (Figure 3.9). Again, clear commensurable widths are observed, and the disclinations generally possess higher formation energies than dislocations at the same conditions. The observed trend is that defect formation energy increases with increasing χN.

Changes in commensurable width with χN are once more not displayed by 3.9 because formation energies are plotted as a function of relative strain; however, there is a mild change (from ≈ 20 R_G to ≈ 20.7 R_g) in the observed width that maximizes the free energy of disclination defects as χN increases from 25 to 33.

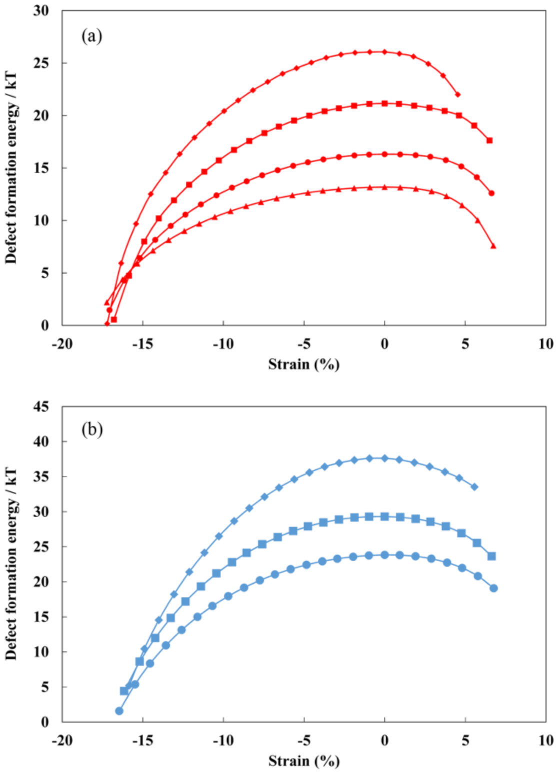

Figure 3.9: Excess free energy (relative to defect-free morphologies) of dislocation defects (a) and disclination defects (b) in a confining geometry with A-wetting ($\chi_{wA}N = -32$) sidewalls and substrate and a B-wetting ($\chi_{wB}N = -32$) top surface. f_A is fixed at 0.25, and $L_z = 5.6\ R_g$. Triangles denote $\chi N = 25$, circles denote $\chi N = 27$, squares denote $\chi N = 30$, and diamonds denote $\chi N = 33$. A clear commensurability width exists in all cases. The formation energy of both types of defects increases monotonically with increasing χN; however, the disclination defects are not stable for $\chi N = 25$.

3.2.3 Sweeps over χN and f_A for various wetting conditions

Having established that channel width, χ_N, minor block fraction f_A, and wetting conditions all play an important role in the formation energy of defects, we conduct a comprehensive set of sweeps over the former three parameters at four different wetting conditions:

1. Top A-attractive, sides+bottom B attractive
2. Sides+bottom A-attractive, top B attractive
3. Sides, bottom, and top all A-attractive
4. Sides A-attractive, bottom+top neutral

For brevity, at each tested value χ_N and f_A, we report only the maximum value of the defect's formation energy found at the commensurable channel width; that is, for each value of χ_N and f_A we sweep the width to determine where the formation energy of the defect is maximized and report that maximal value. Results are summarized in Figures 3.10 and 3.11.

The general trends we extract are as follows:

From Figure 3.10, we see that higher χN values tend to increase the formation energy of defects and thus should reduce their incidence. In experimental applications, χN can be increased either by using longer chains (larger N), or by using a diblock whose monomer species are more strongly repulsive (larger χ). Using longer chains is not ideal because first of all, the increased number of entanglements results in slow annealing kinetics, and secondly, longer chains

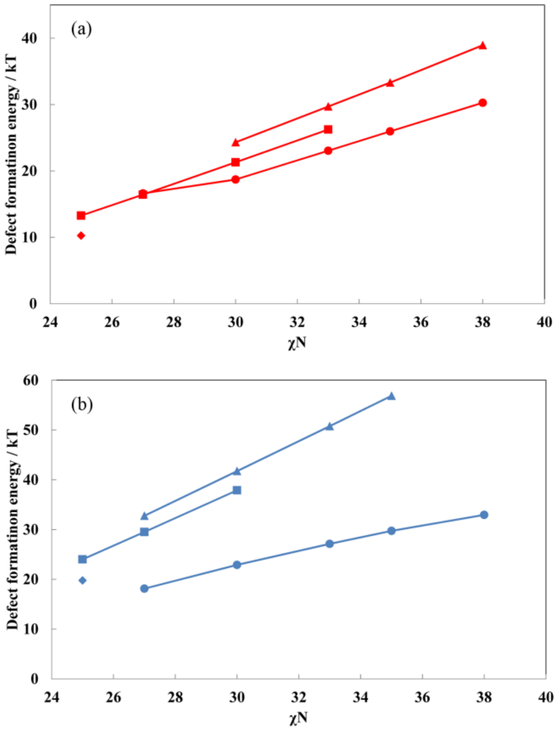

Figure 3.10: Formation energies of dislocations (a) and disclinations (b) at commensurable widths for several different wetting conditions, as a function of χN. f_A is fixed at 0.25. Triangles, squares, circles, and diamonds correspond to wetting conditions 1, 2, 3, and 4 respectively. Wetting condition 1 (triangles, Top A-attractive, sides+bottom B attractive) produces the highest observed defect formation energies for both defect types.

result in larger domain spacings, which runs counter to the intention of DSA (creating regular patterns on length scales as small as possible). A better strategy is to use a diblock with a higher χ value, like polystyrene-b-2-polyvinylpyridine (PS-b-P2VP) as in [5, 144] or polystyrene-b-polydimethylsiloxane (PS-b-PDMS) [8, 146].

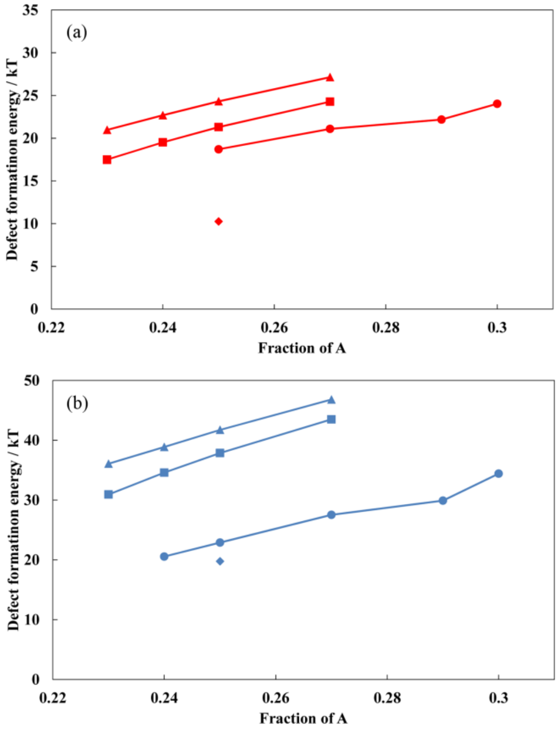

Figure 3.11: Formation energies of dislocations (a) and disclinations (b) at commensurable widths for several different wetting conditions, as a function of f_A. χ_N is fixed at 30. Triangles, squares, circles, and diamonds correspond to wetting conditions 1, 2, 3, and 4 respectively. As for the sweeps over χN in Fig. 3.10, wetting condition 1 (triangles, Top A-attractive, sides+bottom B attractive) produces the highest observed defect formation energies for both defect types.

From Figure 3.11, we see that increasing the block fraction of the minority species tends to increase the formation energy of both defect types. Since this does not change the overall length of the chains, it should not slow the defect annealing kinetics or significantly increase domain spacing. However, if f_A is increased above 0.33, the cylindrical phase will no longer be favored, and the system will form lamellae instead [147].

3.2.4 The string method: Annealing pathways and mechanisms

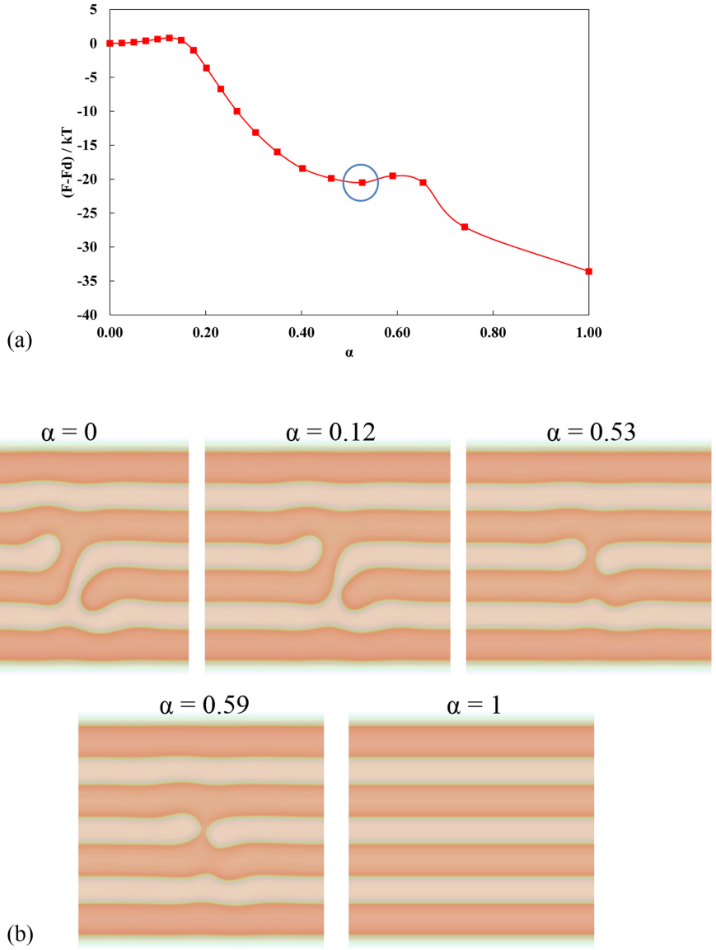

Figure 3.12: (a) Converged MEP for the dislocation-to-perfect-cylinders transition at $\chi_N = 30$, $f_A = -0.3$ in a channel of width 18 R_g and height 6 R_g. The MEP passes through an intermediate metastable state. (b) Polymer density profiles corresponding to each of the metastable and barrier states along the MEP. The barrier at $\alpha = 0.12$ corresponds to disconnected cylinder attempting to connect; the intermediate metastable state at $\alpha = 0.53$ corresponds to connected cylinders with a single bridge (single-bridge-double contact or SBDC); the barrier at $\alpha = 0.59$ corresponds to the pinching off of this bridge.

When choosing experimental parameters that are optimal for DSA, it is desirable not only to maximize the free energy of defects, but also to minimize the estimated time required for defects to anneal out if they happen to form. According to Kramers-like theories of barrier crossing [29], the rate of escape from a metastable well corresponding in this case to a defective morphology is proportional to $\exp[-E_b/kT]$, where E_b is the free energy difference between the metastable state and the peak of the nearest kinetic barrier. To estimate these barriers we use the string method to find the MEP(s) by which disclinations and dislocations may anneal to perfect structures. We concentrate on wetting condition 1 (top surface A-attractive, sidewalls+bottom surface B-attractive) because this condition was shown in the previous section to maximize the formation energy of defects across a range of block fractions and χ_N values. The surfaces' A and B affinities are taken to be $\chi_{wA} = -32$ and $\chi_{wB} = -32$.

First, we run several example string calculations to clarify the qualitative means by which the two defect types may anneal. Figure 3.12 shows the result for a dislocation defect at $\chi_N = 30$, $f_A = -0.3$ in a channel of width 18 R_g and height 6 R_g. Images were initialized as a linear interpolation between the dislocation and the perfect structure (more specifically, the w_- fields of interior images were initialized along a linear interpolation between the w_- field of the dislocation and the w_- field of the defect-free cylinders). An interesting feature to note is that the annealing pathway is two-step, proceeding through an intermediate metastable state. For the purposes of later discussion, we refer to this intermediate metastable configuration of two adjacent lying-down cylinders connected by a single bridge as a "single-bridge-double-contact" (SBDC) defect.

Figure 3.13 shows the result for a disclination defect at $\chi_N = 30$, $f_A = -0.3$ in a channel of width 18 R_g and height 6 R_g. Images (w_- fields) were again initialized along a linear interpolation between the disclination structure and the perfect structure. Again, the annealing pathway proceeds through an intermediate metastable configuration, this time with two bridges between adjacent cylinders instead of one. For the purposes of later discussion, we refer to this intermediate metastable configuration as a "double-bridge-double-contact" (DBDC) defect. Another important feature to note about this pathway is that it is symmetric about the defect core.

In [116], the authors discovered two MEPs associated with the annealing of disclination defects in standing-up lamellae: a symmetric pathway proceeding through a DBDC defect similar to that of Figure 3.13 and an asymmetric pathway proceeding through an intermediate dislocation defect. It is sensible to expect that an asymmetric MEP may exist for our system of lying-down cylinders as well. To search for this pathway, we initialized a string according to a two-step linear interpolation that passed through a dislocation defect. This was accomplished

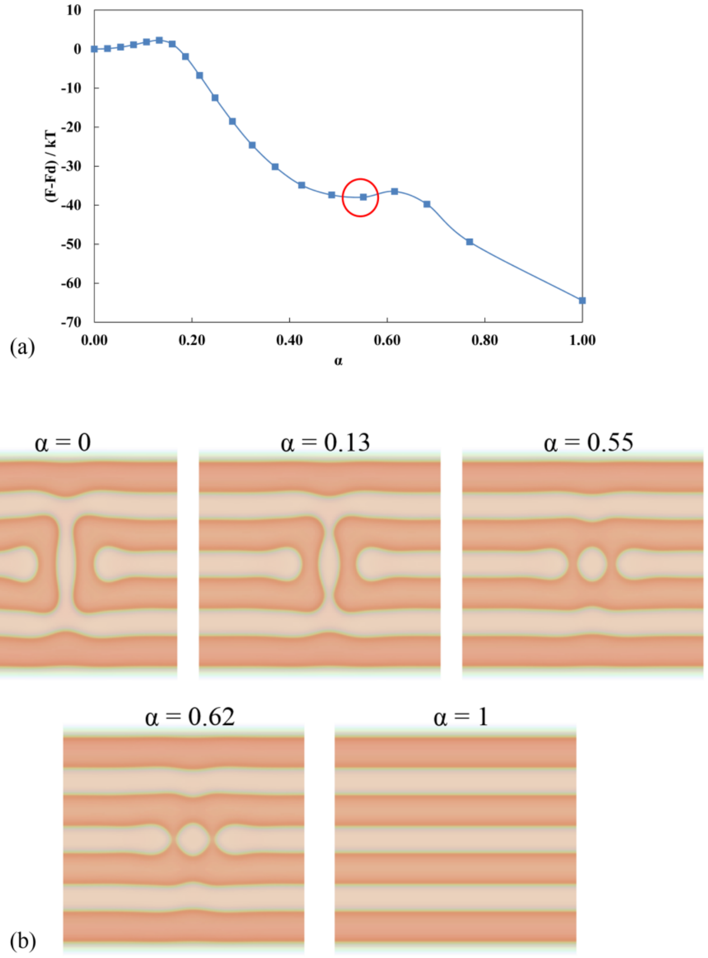

Figure 3.13: (a) Converged symmetric MEP for the disclination-to-perfect-cylinders transition at $\chi_N = 30$, $f_A = -0.3$ in a channel of width 18 R_g and height 6 R_g. The MEP passes through an intermediate metastable state. (b) Polymer density profiles corresponding to each of the metastable and barrier states along the MEP. The barrier at $\alpha = 0.13$ corresponds to the two disconnected cylinders attempting to connect; the intermediate metastable state at $\alpha = 0.55$ corresponds to connected cylinders with two bridges (double-bridge-double contact or DBDC); the barrier at $\alpha = 0.62$ corresponds to the pinching off of these bridges.

by setting the w_- field of one interior image to the w_- field of a dislocation defect. Images preceding the dislocation image were initialized according to a linear

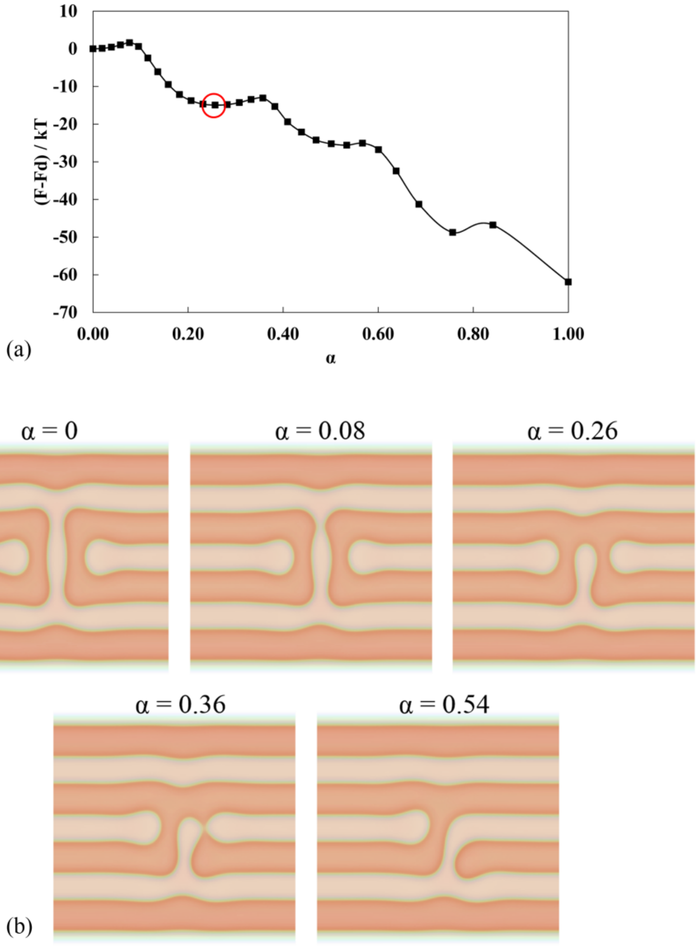

Figure 3.14: (a) Converged asymmetric MEP for the disclination-to-perfect-cylinders transition at $\chi_N = 30$, $f_A = -0.3$ in a channel of width 18 R_g and height 6 R_g. The MEP passes through several intermediate metastable states, including a dislocation. (b) Polymer density profiles corresponding to each of the metastable and barrier states along the MEP up to the dislocation. The barrier at $\alpha = 0.08$ corresponds to one disconnect cylinder attempting to connect; the intermediate metastable state at $\alpha = 0.26$ corresponds to one connected cylinder with two bridges (double-bridge-single-contact or DBSC); the barrier at $\alpha = 0.36$ corresponds to the pinching off of one of these bridges, resulting in a dislocation defect ($\alpha = 0.54$). Once the dislocation defect is reached, the remainder of the MEP is identical to the dislocation-annealing pathway shown in Figure 3.12.

interpolation between the disclination and the dislocation; images following the dislocation image were initialized according to a linear interpolation between the dislocation and the perfect structure. The converged MEP resulting from this initialization is shown in Figure 3.14. As expected, the MEP is an asymmetric pathway proceeding through a dislocation. Before the MEP reaches the dislocation, it first encounters an intermediate defect with one connected cylinder and two bridges (double-bridge-single-contact or DBSC). Once the MEP reaches the dislocation defect, the remainder of the MEP is identical to that of Figure 3.12. While all barriers along the asymmetric and symmetric paths for annealing of the disclination are relatively low, the first encountered barrier is lower for the symmetric pathway, indicating the the physical system is more likely to anneal by way of the asymmetric path at these conditions.

3.2.5 The string method: Effect of commensurability on barrier heights

Since commensurability has been shown to affect the formation energy of defects, it is reasonable to expect that the kinetic barriers will also change with channel width. To quantify these effects, we compute MEPs for both the symmetric and asymmetric pathways at a range of different channel widths while holding χ_N and f_A fixed. There are six barriers in total to examine, two for the symmetric pathway and four for the asymmetric pathway. For the symmetric pathway, the first barrier corresponds to the transition between the disclination (DISC) and DBDC; the second barrier corresponds to the transition between DBDC and the perfect structure (P). For the asymmetric pathway, the first barrier corresponds to the transition between DISC and DBSC, the second corresponds to the transition between DBSC and the dislocation (DISL), the third corresponds to the transition between DISL and SBDC, and the fourth corresponds to the transition between SBDC and P.

Note that the annealing pathway for the dislocation is a subset of the asymmetric annealing pathway of the disclination.

The heights of the six barriers as a function of channel width are summarized in Figure 3.15. For reference, the commensurable width that maximizes the free energy of disclination defects at these conditions is 17.9 R_g. All barriers are observed to be minimized at a certain channel width, but that optimal width is different for each barrier; that is to say, there appears not to be an overall ideal channel width that minimizes all barriers.

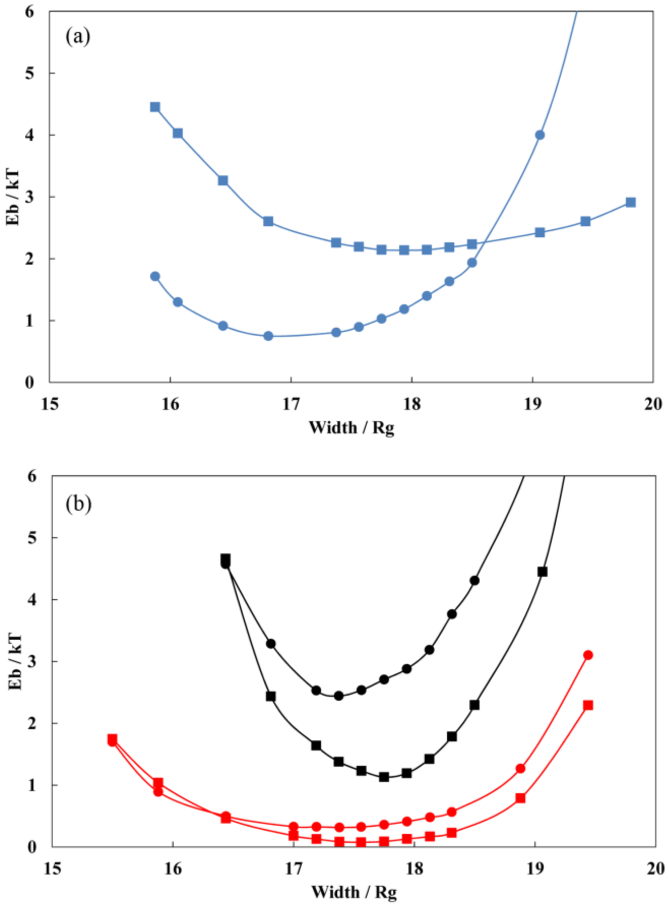

Figure 3.15: Barrier heights as a function of channel width. Commensurable width at these conditions is 17.9 R_g. (a) shows barrier heights for the symmetric pathway. Squares correspond to the first barrier (DISC→DBDC); circles correspond to the second barrier (DBDC→P). (b) shows barrier heights for the asymmetric pathway. Black squares correspond to the first barrier (DISC→DBSC), black circles correspond to the second barrier (DBSC→DISL), red squares correspond to the third barrier (DISL→SBDC), and red circles correspond to the fourth barrier (SBDC→P). The red barriers are also those associated with annealing of dislocations. Neither (a) nor (b) exhibits an "ideal" width that minimizes all barriers.

3.2.6 Barrier-crossing: Time evolution of defect populations

Since there is no ideal channel width that minimizes the height for all barriers, when attempting to choose a channel width that will minimize the overall annealing time of a certain defect structure, there are tradeoffs that must be considered. Different barriers become more or less important at different widths. To illustrate these tradeoffs, we use a simple reaction-rate kinetic model to estimate the total annealing time for a disclination defect at three different channel widths (16.4 R_g, 18 R_g, and 19.4 R_g). 18 R_g is relatively close to the commensurate channel width of 17.9 R_g. We choose to investigate the disclination defect specifically because the barriers associated with annealing of dislocations (Figure 3.15, lower panel, red) are generally lower than the other barriers required to anneal disclinations; therefore, dislocations are expected to anneal out more quickly than disclinations at all tested conditions. Additionally, dislocations appear along the asymmetric path for annealing disclinations; therefore, information on the lifetime of dislocations will also be obtained by modeling the lifetime of disclinations.

We assume the system begins containing a single disclination, and at any later time has either annealed to a perfect structure (P) or contains an isolated defect, whose type is one of the five defect types (DISC, DBDC, DBSC, DISL, or SBDC) identified along the disclinations' symmetric and asymmetric paths. The following reactions must be considered:

$$DISC \Longleftrightarrow DBDC \Longleftrightarrow P \tag{3.1}$$

$$DISC \Longleftrightarrow DBSC \Longleftrightarrow DISL \Longleftrightarrow SBDC \Longleftrightarrow P \tag{3.2}$$

(3.1) corresponds to the symmetric path, and (3.2) corresponds to the asymmetric path. The time evolution of the population of each defect type in an ensemble of systems (or equivalently, the time evolution of the probability that a system contains a given defect type) obeys a set of coupled differential equations; for example, if P_{DISC} represents the probability that the system contains the disclination, then

$$\begin{aligned}\frac{dP_{DISC}}{dt} = & -k_{DISC \to DBDC} P_{DISC} - k_{DISC \to DBSC} P_{DISC} \\ & + k_{DBDC \to DISC} P_{DBDC} + k_{DBSC \to DISC} P_{DBSC}\end{aligned} \tag{3.3}$$

where $k_{DISC \to DBDC}$, represents the the transition rate from DISC to DBDC, and so forth. The estimated rate of each transition is modeled using a 1-dimensional Kramers-like approach [29], given by

$$k = \tau_0^{-1} \exp\left[-E_b/kT\right] \tag{3.4}$$

where E_b is the energy of the barrier that must be overcome and τ_0^{-1} is a kinetic prefactor. The kinetic prefactors are not immediately accessible because SCFT obscures information about physical dynamics of the polymers (for finding saddle points, that is a feature of SCFT, not a bug; SCFT does not suffer from the slow kinetics associated with entangled chains that bog down other methods [86]). Determining the proper kinetic prefactor would require calculating the diffusion coefficient along the string's arc length at the barrier peak, using a model known to capture the polymer melt's physical dynamics; candidates include dynamical self-consistent field theory [148–150], dynamical density functional theory [151], and molecular dynamics [152]. For a diblock melt of the size, chain density, and chain length considered here, this would be a state-of-the-art calculation in its own right, and is an intriguing direction for future work. For present purposes, following [116], we estimate τ_0 as the time necessary for a single chain to diffuse over a distance comparable to the defect size in a direction parallel to a microdomain interface. For PS-PMMA at $\chi N = 25$, $\tau_0 \approx 9$ sec. This same value of τ_0 is used for all barriers.

Figure 3.16 shows results for the three different tested widths. Estimated annealing times are presented in units of τ_0. For a channel width of 16.4 R_g, we see from Figure 3.15 that the first barrier along the asymmetric path (black squares) is roughly equal to the first barrier along the symmetric path (blue squares),

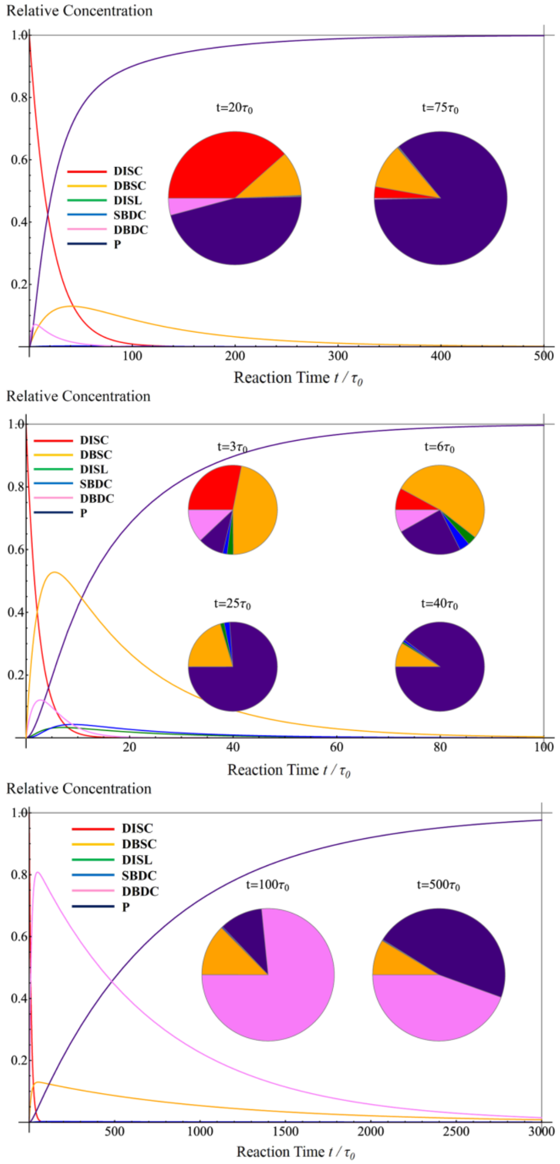

Figure 3.16: Estimated time evolution of defect populations during the annealing of a disclination. Pie chart insets show relative defect populations (or probabilities) at given times. Upper panel: channel width = 16.4 R_g. Middle panel: channel width = 18 R_g, near commensurability. Lower panel: channel width = 19.4 R_g.

meaning that the system will take either path with roughly equal probability. The second barrier along the symmetric path (blue squares) is relatively low, so in Figure 3.16 we see that the initial population spike and lifetime of DBDC defects on the symmetric path is lower than the initial spike and lifetime of DBSC defects along the asymmetric path. The total time for a disclination to anneal with 99% probability is $\approx 500\tau_0$.

For a channel width of 18 R_g, close to the commensurability width of 17.9 R_g, we see from Figure 3.15 that the first barrier along the asymmetric path (black squares) is lower than the first barrier along the symmetric path (blue squares). Therefore, the asymmetric path is favored, and in Figure 3.16 we see an initial spike in the population of DBSC defects. This population gradually anneals because the second barrier along the asymmetric path (black circles) is relatively high. The total time required for a disclination to anneal with 99% probability is $\approx 100\tau_0$.

For a channel width of 19.4 R_g, the first barrier along the symmetric path is significantly lower than the first barrier along the asymmetric path, meaning that the asymmetric path is favored. Correspondingly, in Figure 3.16 we see an initial spike in the population of DBDC defects. This population anneals relatively slowly because the second barrier along the symmetric path (Fig. 3.15, blue circles) is relatively high. The total time required for a disclination to anneal with 99% probability is $3000\tau_0$.

In all three cases, the rates appear to be governed by the first and second barriers along both paths. The dislocation defect, and subsequent SBDC defect, anneal relatively quickly and their populations/probabilities remain low.

The overall lessons are first of all, that channel width has a significant effect not only on the free energy of defect formation, but also on the kinetics of defect annealing, and secondly, that using a channel width close to commensurability appears to minimize the annealing time for disclination defects.

3.2.7 The string method: Effect of χN on barrier heights

Finally, we study the effects of changing χN on barrier heights while holding f_A and channel width fixed. Results are summarized in Figure 3.17. Once again, there appears not to be an ideal χN that minimizes all barriers, and the tradeoff of different barriers heights increasing or decreasing will cause populations of different defect types to become more or less important at different values of χN. We do not carry out a systematic study of defect population evolution at different values of χN, but it would be straightforward to implement in a similar manner to that of Section 3.2.6.

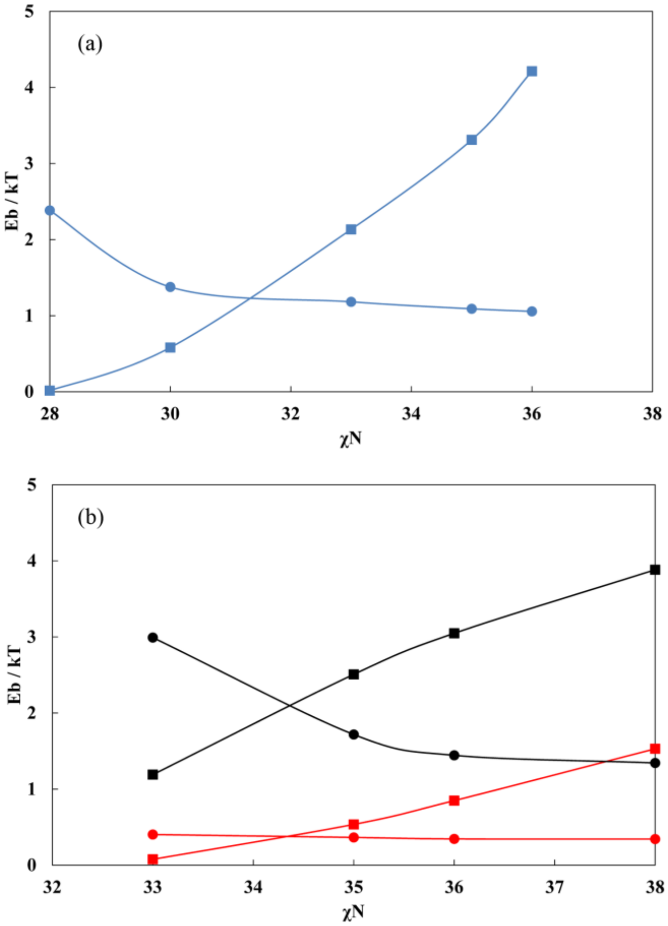

Figure 3.17: Barrier heights as a function of χN with width fixed at 18 R_g. (a) shows barrier heights for the symmetric pathway. Squares correspond to the first barrier (DISC→DBDC); circles correspond to the second barrier (DBDC→P). (b) shows barrier heights for the asymmetric pathway. Black squares correspond to the first barrier (DISC→DBSC), black circles correspond to the second barrier (DBSC→DISL), red squares correspond to the third barrier (DISL→SBDC), and red circles correspond to the fourth barrier (SBDC→P). The red barriers are also those associated with annealing of dislocations. Neither (a) nor (b) exhibits an "ideal" χN that minimizes all barriers.

3.3 Application to chemo-epitaxial prepatterns

In the previous section we reported the results of study quantifying defect formation energies and channel confinement corresponding to a grapho-epitaxial experimental setup. Chemo-epitaxy, the use of substrates prepatterned with domains attractive to one monomer species or the other, is another approach that has been experimentally shown to facilitate the formation of long-range order in self-assembling block copolymer systems [6, 11, 114, 153–160]. Chemo-epitaxial prepatterns can guide copolymer to self-assemble into regular structures several times smaller than the prepattern itself ("pitch multiplication"). The copolymer can rectify roughness and placement errors present in the prepattern, up to a point; when attempting to form defect-free self-assembled structures, matching the prepattern spacing to a multiple of the copolymer domains' commensurability width remains desirable.

As with grapho-epitaxy, the formation of metastable defects in chemo-epitaxy remains a significant challenge, especially when scaling the method up for industrial lithographic applications (the defect density level set by ITRS for commercial production is < 0.01 defects/cm^2 [113, 114]; for a defect of size ≈ 30 nm, this corresponds to defect energies $>\approx 30$ kT [161]). One source of defects is gel particles in the block copolymer solutions; these can in some instances be removed by filtration [162]. However, even when filtration is used during the manufacturing process, dislocation-pair (DP, see Figure 3.18) and single dislocation (SD) defects are still observed in attempts to generate line-and-space morphologies via self-assembly [163], likely as a result of the system's natural annealing kinetics.

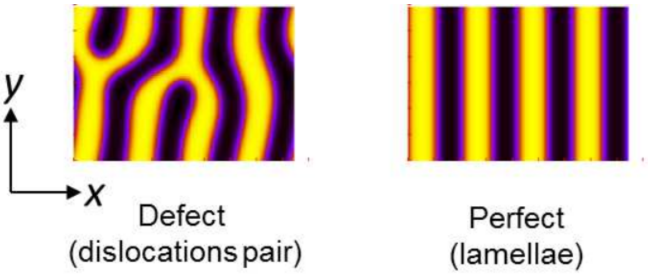

Figure 3.18: Top view of a dislocation-pair defect and perfect lamellae.

The large amount of experimental attention received by chemo-epitaxial directed self-assembly in recent years has been supplemented by several computational studies, many of which use the theoretically informed coarse grained (TICG) Monte Carlo method developed by Detcheverry *et al.* [164]. Nagpal *et al.* [165] use this framework to investigate free energies of defects in standing-up lamellae on a chemically patterned substrate and find jog, 1/2 disclination, and single dislocation defects with extraordinarily high formation energies (hundreds of kT). Liu *et al.* [159] and Detcheverry *et al.* [166] observe that for a PS-b-PMMA diblock melt self-assembling on a surface with PS-attractive stripes, defect-free standing-up lamellae with long range order form more reliably if the substrate background ("background" meaning the relatively wide regions between PS-attractive guiding domains) is made weakly attractive to the opposite monomer species (PMMA). Ruiz *et al.* [157] reach a similar conclusion for self-assembling vertical cylinders. Detcheverry *et al.* [167], demonstrate that self-assembling cylinder-forming diblock copolymer can rectify placement defects in a substrate patterned with a hexagonal lattice of minor block-attractive spots. In all of these studies, it is observed that at suboptimal substrate conditions, complicated defect structures can form in the bulk of the system even if the top surface (free surface) appears defect-free from above; this highlights the importance of 3D modeling.

To date we are aware of relatively few computational studies of defectivity in these system using SCFT. Ginzburg *et al.* [168, 169] use 2-dimensional SCFT to investigate "registration defects" in which a PMMA-rich domain, rather than a PS domain, overlays a PS-attractive stripe on the substrate. They find that at higher attempted pitch multiplication, the PS domains neighboring the attractive strip will tilt rather than exchange places with the PMMA domains. At an attempted pitch multiplication of 1 (1 PS-attractive stripe per lamellar period), they obtain an estimated registration defect density of $\approx 1 \times 10^{-4}$ defects/cm^2; at an attempted pitch multiplication of 5 (1 attractive stripe for every 5 lamellar periods), they obtain an estimated registration defect density of to ≈ 5000

defects/cm^2. Izumi *et al.* [161] conduct 3D SCFT simulations, finding metastable dislocation-pair defects with formation energies up to 110 kT near commensurability.

To our knowledge only a single prior computational study (external to our group) has investigated kinetic pathways for defect annealing on a chemo-epitaxially patterned surface. Li *et al.* [170] apply the string method in conjuction with SCFT to a lamellae-forming diblock melt containing disclination-pair (DP) defects (Figure 3.18) similar to the dislocation-dipole defects observed in experiments [156]. They find a melting mechanism (minimum energy path) along which the bridges forming dislocations initially break near the wetting surface, and the break "zippers" upwards (this mechanism will be illustrated in further detail later in this section). Furthermore, they report a region of χN close to the ODT (but still within the lamellar ordered phase) where kinetic barriers are predicted to vanish entirely but defect formation energies remain high, suggesting a useful temperature regime for thermal annealing of defects.

The study of Li *et al.*, however, focused on a neat diblock melt. In experimental synthesis of PS-b-PMMA diblock copolymer by living anionic polymerization, some living A-block (PS) ends are terminated prior to initiating polymerization of the B-block (PMMA), leaving residual PS homopolymer in the melt [171]. This residual homopolymer can affect both the spacing (pitch) of self-assembled line-and-and-space structures as well as the energy and stability of defect morphologies. Hashimoto *et al.* [172, 173] investigate bulk (unconfined) self-assembly of lamellae on a non-patterned substrate, finding that the distribution of homopolystyrene within the PS-rich domains depends on the molecular weight and volume fraction of added PS. This inhomogeneous distribution of homopolystyrene produces variations in domain size and spacing of lamellae. Matsen [174] investigates the phase behavior and domain spacing of an AB+A diblock+homopolymer melt, finding that high-molecular-weight A-homopolymer tends to localize n the central region of A-rich domains, while lower-molecular-weight A homopolymer distributes itself more homogeneously within A-rich domains. As in Hashimoto's experiments, this behavior affects the preferred domain spacing. Stoykovich *et al.* [154] add homopolymer to an AB-diblock melt to facilitate self-assembly of a periodic array of bent lamellae. Homopolymer aggregates at the corners of the bent periodic pattern, which mitigates the free energy cost of forming the desired frustrated structure. This example demonstrates that introducing homopolymer can stabilize unusual morphologies that may not be observed in pure AB-diblock melts; therefore, when attempting to form lamellar structures using DSA, we should determine if blended homopolymer acts to stabilize defect structures. Williamson *et al.* [175] report that adding 2.5% PS homopolymer to an AB-diblock melt on a chemo-epitaxially patterned substrate causes commensurability widths to increase relative to the pure diblock case. In a recent SCFT study of directed self-assembly of vertical cylinders in confinement [176], our group shows that the presence of added homopolymer in a diblock melt acted to reduce the free energy of defects and increase the process window for probable formation of perfect self-assembled cylinders. All these results indicate that the presence of residual homopolymer is important to consider when designing industrial DSA processes.

In this section we review a pair of recent publications [136, 137] in which PolyFTS is used to explore the formation energies of dislocation-pair (DP) defects for an AB-diblock+homopolymer melt on a chemo-epitaxially pattered substrate. For brevity I focus on reporting the results of [137]; [136] studies essentially the same system A comprehensive study of the kinetic annealing pathways, and how various barriers are influenced by the presence of homopolymer, is carried out using my string method SCFT code. Finally, we estimate total annealing times using the method of Section 3.2.6.

3.3.1 Simulation geometry

We consider a lamellae-forming symmetric ($f_A = 0.5$) AB-diblock copolymer with AB segregation strength $\chi N = 0.5$. This corresponds to a symmetric PS-b-PMMA diblock with a molecular weight of 70,000, a radius of gyration

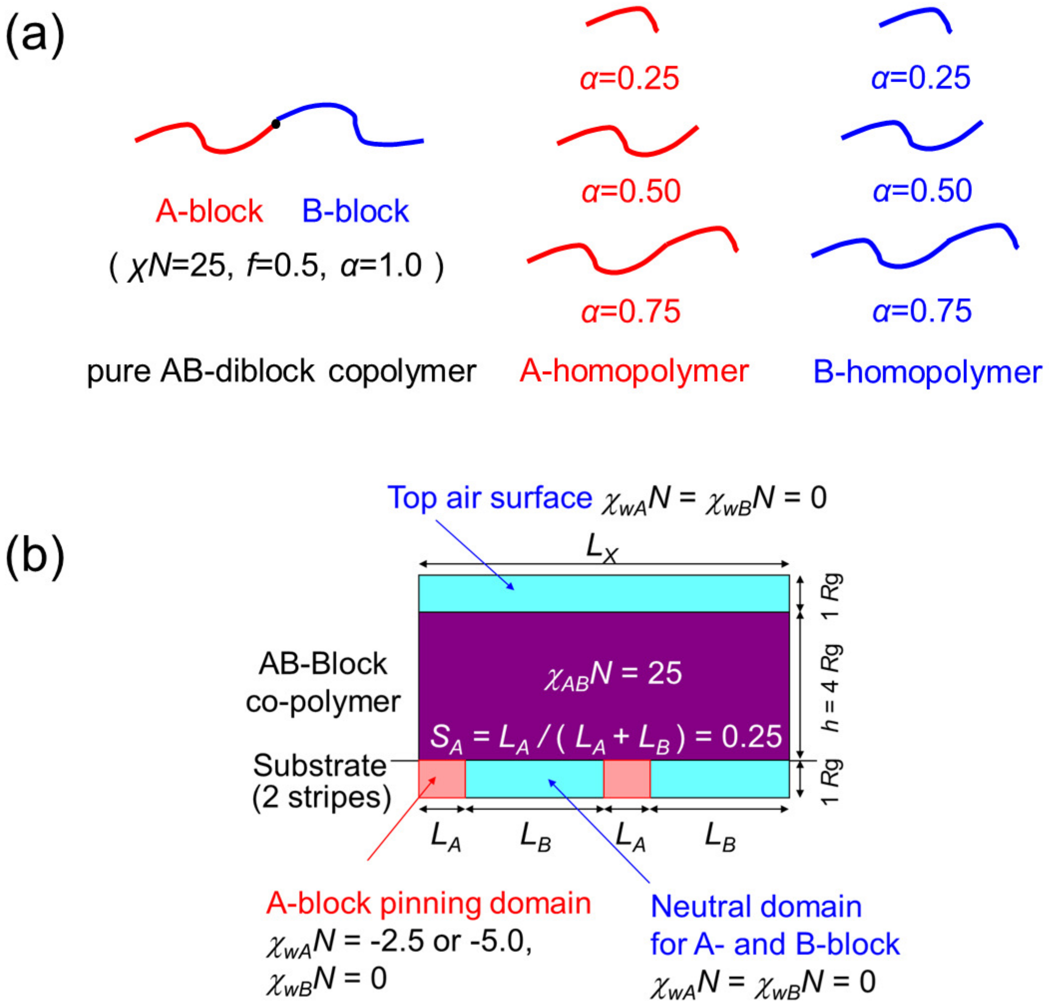

Figure 3.19: (a) Schematic of diblock copolymer + homopolymer melt. (b) Simulation cell geometry for 3D simulations.

$R_g \approx 7.2$ nm, and preferred (in the absence of confinement) lamellar domain spacing $l_0 \approx 4.2R_g$. To describe the blend composition, α denotes the ratio of molecular weight (chain length) of the homopolymer to that of the copolymer (*e. g.*, $\alpha = 0.5$ denotes a system where the homopolymers chains are half as long as the diblock chains), and ϕ denotes the volume fraction of each species of added homopolymer (*e.g.*, for $\phi = 0.1$, when A- or B-homopolymer alone is added, the total homopolymer volume percentage is 10%, but when A and B are both added, the total homopolymer volume percentage is 20%).

In Section 3.3.2 we present 2D bulk simulations. In addition to pure diblock, we consider three different molecular weight ratios, $\alpha = 0.25$, 0.50, and 0.75, as shown schematically in Figure 1a, at volume fraction $\phi = 0.1$ for each homopolymer species. In Section 3.3.3, we present 3D simulations in confinement with chemo-epitaxial stripes. The physical system consists of polymer forming a thin film of width L_X and height h above a chemically-modified bottom surface (substrate) composed of A-attractive bands alternating with neutral stripes. L_A and L_B denote the width of individual A-attractive stripes and neutral stripes, respectively, and we define the ratio $S_A = L_A/(L_A + L_B)$. Two repeats of A-attractive and neutral stripes are contained in the simulation cell so that $L_X = 2(L_A + L_B)$. The top layer of the polymer film is assumed to be in contact with air. To implement a simulation cell corresponding to this physical system, we apply a polymer-excluding mask at the top and bottom of the cell, effectively creating walls. Selectivities at the bottom wall (substrate) are set with a Flory-like parameter, $\chi_w = (\chi_{wA} - \chi_{wB})/2$, where χ_{wA} and χ_{wB} describe interactions between the substrate and blocks A and B, respectively. Here we take $\chi_{wB} = 0$, but test two different substrate selectivities for the A-attractive stripes, $\chi_{wA}N = -2.5$ and $\chi_{wA}N = -5.0$. The top wall (air) interacts neutrally with both monomer species, so $\chi_w = 0$ is applied on that surface, as well as on the neutral substrate strips. The geometry of our simulation cell is summarized in Figure 3.19.

3.3.2 Unconfined 2D bulk films

As a preliminary estimate, we use 2D SCFT simulations seeded from isolated dislocation-pair defects (DP) and perfect lamellae (PL) as shown in Figure 3.18. The monomer species forming T-junctions is defined as the A-(segment) block. Bulk morphologies (in periodic boundary conditions with no wall confinement) are prepared, corresponding to a 3D system invariant in the z-direction. To evaluate the formation energies of defects relative to perfect lamellae ($\Delta F = F_{DP} - F_{PL}$, where F_{DP} and F_{PL} are the extensive free energies of DP defects and perfect lamellae respectively) for later comparison with 3D simulations, we assume the z-invariant film modeled by the 2D simulations has a thickness of 4 R_g.

We find the dislocation-pair defect to be stable over a wide range of film widths L_X. Figure 3.20 shows the DP formation energy δF over a range of film widths at $\chi_N = 25$ for several different added homopolymer conditions. Adding A-homopolymer (homopolymer of the T-junction-forming species) reduces the defect formation energy, while adding B-homopolymer increases the defect for-

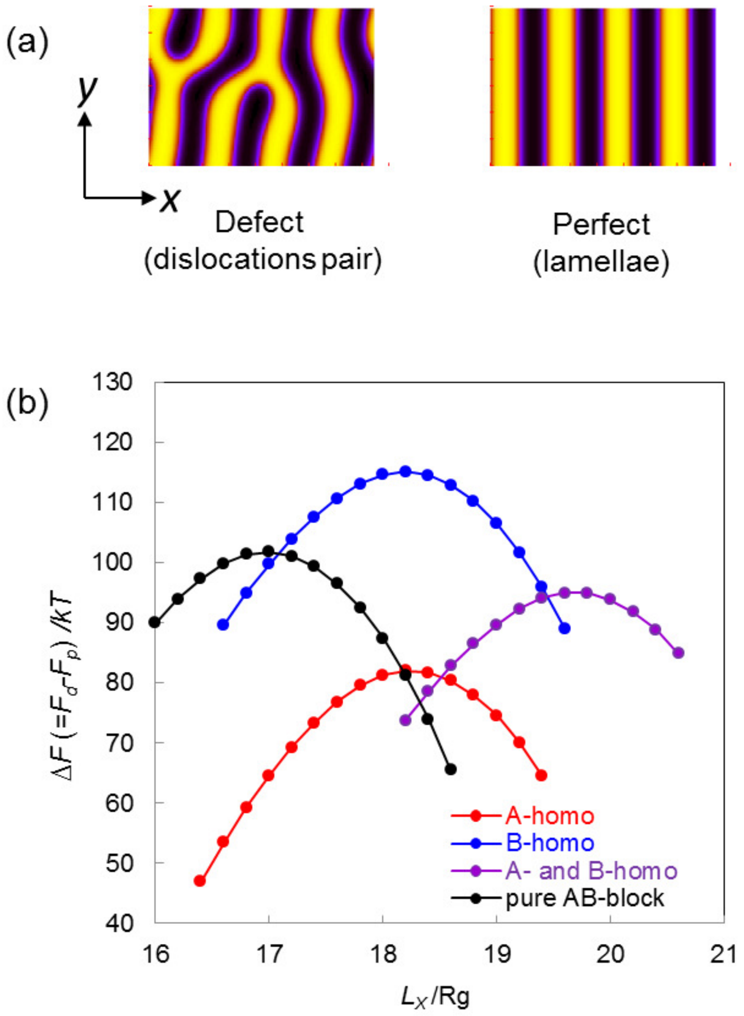

Figure 3.20: (a) Top view of a dislocation-pair defect (DP) and perfect lamellae (PL). (b) Formation energy ΔF of DP defects over a range of channel widths, assuming a z-thickness of 4 R_g. Black: Pure AB diblock. Red: 10% volume fraction of A-homopolymer added. Blue: 10% volume fraction of B-homopolymer added. Purple: 10% volume fraction of A and 10% volume fraction of B-homopolymer both added. In all cases $\chi N = 25$ and the the fractional length α of added homopolymer chains relative to the length of diblock chains is 0.5.

mation energy. This trend is sensible because the dislocation's bridges must cross narrower (wider) B-domains when added A-homopolymer (B-homopolymer) is present. (It is important to note that in a physical system, an "inverse" DP defect where species B forms the T-junctions may be present elsewhere in the melt; for this inverse defect, the changes in ΔF caused by adding A- or B-homopolymer are exactly reversed). When both A- and B-homopolymer are present, the maximum observed ΔF is almost the same as for the pure AB-diblock case.

Figure 3.20 also shows that the system exhibits commensurability widths that maximize the formation energy of the defect structure, as in Section 3.3. This optimal width $L_{X,Opt}$ depends on the presence and species of added homopolymer (in other words, the presence of homopolymer distinctly affects the commensurability width, in agreement with [172–174]). We also find that commensurability width depends on the relative homopolymer chain length α, as seen in the "$L_{X,Opt}$" column of Table 3.1. Increasing α (at constant overall homopolymer volume fraction) also increases $L_{X,Opt}$. Longer A-homopolymer chains tend to gather near the center of A-block domains, while shorter polymer chains distribute themselves more homogeneously within the A-block domains, as noted in [172, 174]. This difference in aggregation behavior results in larger domain sizes for longer added homopolymer chains, increasing $L_{X,Opt}$. When both A- and B- homopolymer are added, the shift in $L_{X,Opt}$ is almost twice as large as when A-homopolymer alone is added, because homopolymer localization occurs near the centers of both A- and B-rich domains.

	α	$L_{X,Opt}/R_g$	ΔF_{max}/kT	1st/kT	2nd/kT	3rd/kT
Pure block	-	17.0	102	10.2	4.5	-
A-homo	0.25	17.8	82	21.0	2.6	-
	0.50	18.2	82	22.0	4.5	0.1
	0.75	18.4	79	22.3	5.9	0.4
B-homo	0.25	17.8	118	5.1	2.2	-
	0.50	18.2	115	7.5	4.8	0.1
	0.75	18.4	111	8.6	5.9	0.3
A- and B-	0.25	18.8	98	15.6	10.5	-
	0.50	19.6	95	19.2	14.6	0.4
	0.75	20.2	87	21.2	17.1	1.6

Table 3.1: Commensurability widths $L_{X,Opt}$, DP formation energies at the commensurability width ΔF_{max}/kT, and heights of the first, second, and third barriers for various homopoymer chain lengths α. For the barriers, dashes indicate that a shoulder, not a barrier, was observed. In all cases the added volume fraction of A and/or B homopolymer is 10% and $\chi N = 25$.

We apply the string method to find kinetic pathways between the metastable DP state and the stable PL configuration. The DP to PL transition is examined at the lamellar commensurability width $L_{X,Opt}$, which we determine by separate prior bulk SCFT calculations. Each string consists of 100∼150 images (successive field configurations along the string), which provides sufficient resolution to trace out the kinetic pathway. As exemplified in Figure 3, all our calculations show a single kinetic pathway in which DP transitions to PL by passing through a state containing a single dislocation defect (SD) and a state containing bridged lamellae (BL). First, connection breaking occurs near one of the DPs T-junctions, and the

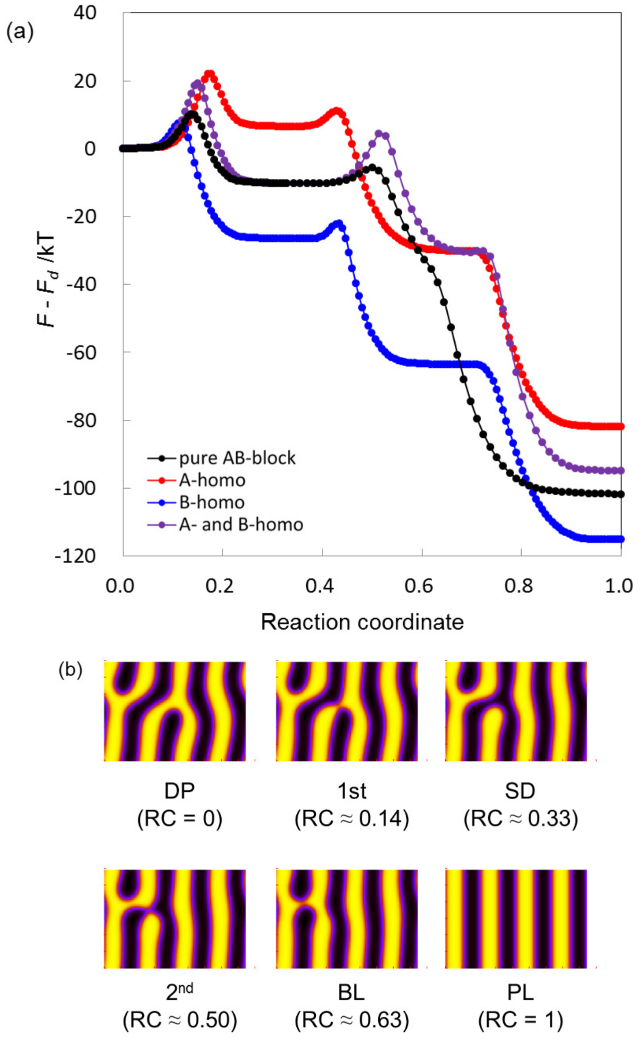

Figure 3.21: (a) Kinetic pathways for the melting of DP defects in the presence of A and/or B homopolymer for the 2D bulk case. Barrier heights are computed assuming a film z-thickness of 4 R_g. In all cases the added volume fraction of A and/or B homopolymer is 10% and $\chi N = 25$. (b) A-segment density profiles along the MEP for a pure AB-diblock melt, showing the various intermediate states: initial DP, the first barrier, single-dislocation (SD), the second barrier, bridged lamellae (BL), and finally perfect lamellae (PL).

system forms a SD as an intermediate metastable morphology. Next, the SD and the end of a nearby broken lamella reconnect to form BL. As a final qualitative step, the bridge part of the BL breaks, and the system transitions to PL (Figure 3.21b). For a pure diblock melt, two barriers and a shoulder are visible on the kinetic pathway between DP and PL (Figure 3.21a). The first barrier corresponds to the transition between DP and SD, the second to the transition between SD and BL, and the shoulder to the transition between BL and PL. We summarize the barrier heights E_b in Table 3.1. For pure symmetric diblock at $\chi N = 25$, the heights of the 1st and 2nd barriers are 10.2 kT and 4.5 kT, respectively. The first barrier is about twice as high as the second one, indicating that the DP basin requires more thermal energy to escape than that of SD, and hence DPs are more difficult to eliminate. Since the BL-PL transition shows no barrier (only a shoulder), the BL state is not metastable and should relax spontaneously. These results agree qualitatively with our previous 2D string method calculations on a grapho-epitaxial setup [116]. Li *et al.* [170] reported a similar quasi-two-dimensional melting mechanism.

For blends of AB-diblock copolymers and homopolymers, as seen in Figure 3.21a, the kinetic pathway reflects the same sequence of morphologies (DP $\rightarrow$ SD $\rightarrow$ BL $\rightarrow$ PL). However, the quantitative nature of the barriers changes markedly. Table 3.1 shows that when α increases from 0.25 to 0.75, the shoulder along the

MEP between the BL and PL states becomes a full-fledged (albeit small) third barrier, indicating that BL is metastable under these conditions. The emergence of this third barrier is observed whether the added homopolymer is of species A, B, or both A and B. For the first and second barriers, the principle trends are as follows: Adding A-homopolymer increases the height of both the first and second barriers relative to the pure diblock case. Adding B-homopolymer reduces the height of the first barrier (relative to the pure diblock case), but increases the height of the second barrier slightly (relative to the pure diblock case) if $\alpha = 0.5$ or 0.75. The presence of A- and B-homopolymer together results in both the first and second barriers being higher than for the pure diblock case. For all added homopolymer compositions (A, B, and A+B), the height of the first and second barriers tends to increase with increasing chain length of added homopolymer α. Again, results are summarized in Table 1.

These trends can be elucidated by considering the aggregation tendencies of the homopolymer additives. As shown in Figure 3.22, homopolymers appear to aggregate anywhere DP, SD, or BL defects form a T-shaped junction. For an A-homopolymer/diblock blend, the presence of addition A-homopolymer in the two T-junctions of the initial DP stabilizes the defect, increasing the first barrier's height relative to the pure diblock case. For a B-homopolymer/diblock blend, the initial DP defect contains no B-rich T-junctions in which homopolymer might

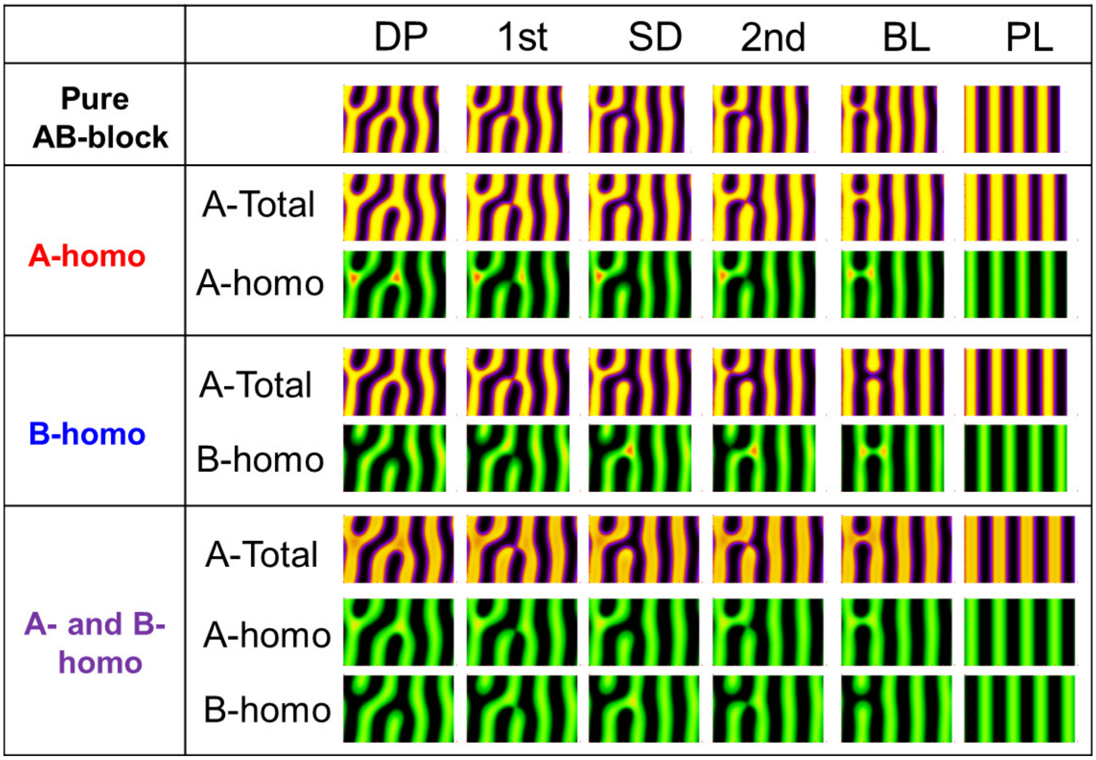

Figure 3.22: A-total and A-homopolymer density profiles along the MEPs for various compositions. The depicted states correspond qualitatively to those shown in Figure3.21b. In all cases $\phi = 10\%$, $\alpha = 0.5$, $\chi N = 25$. Homopolymer tends to aggregate near cores of T-junctions.

preferentially aggregate; therefore, the first barrier's height does not increase, and in fact decreases relative to the pure diblock case. In the SD defect, both species A and species B form T-junctions; therefore, added homopolymer of either species can stabilize the SD defect by localizing in a T-junction core, causing barrier heights to increase.

Although Figure 3.22 only shows the homopolymer density for relative homopolymer chain length $\alpha = 0.5$, we also find that the tendency of homopolymer to aggregate within T-junctions becomes more pronounced with increasing α. This explains why barrier heights increase as α is increased from 0.25 to 0.75. In general, degree of homopolymer aggregation in T-junctions appears positively correlated with barrier height.

The fact that the first barrier is generally higher (lower) when A (B) homopolymer is added can also be explained by considering homopolymer aggregation tendencies. Added A-homopolymer increases the size of A-domains relative to B-domains, making the A-rich bridges of the DP structure more robust. Added B-homopolymer increases the size of B domains (which the A-rich bridges of defect structures must cross), making the A-rich bridges of the DP more fragile.

Our 2D bulk simulations suggest that even a small volume fraction of added homopolymer can significantly affect 1) the stability of defective morphologies and 2) barrier heights along the kinetic pathway to defect elimination. Added B-homopolymer localizing in B-rich domains increases the formation energy of DP and also reduces the kinetic barrier between DP and SD, which is advantageous for the defect melting process. On the other hand, homopolymer localization on cores of T-junctions reinforces stability of the DP defect when A-homopolymer is present, and of the SD defect when added A- and B-homopolymer are simultaneously present. Therefore, avoiding localization of homopolymer in T-junction cores of defect structures should be a high priority in DSA processes.

3.3.3 3D simulations on chemically pre-patterned substrates

We next consider kinetic barriers and transition pathways for a fully 3-dimensional system on a chemically pre-patterned substrate, as described in Section 2. We fix the homopolymer chain length at $\alpha = 0.5$ and the homopolymer volume fraction at $\phi = 0.1$. DP defects are converged from random seeds and found to be metastable.

Figure 3.23 shows the formation energy of DP defects, ΔF, as function of film width L_X for $\chi_{wA}N = -5.0$. For pure AB-diblock copolymer, the maximal ΔF, obtained under near-commensurate conditions for perfect lamellae, is 96 kT. As in the 2D case, adding A-homopolymer reduces the maximal ΔF (to 70 kT), while adding B-homopolymer increases it (to 106 kT). (We note that the effect would be exactly the reverse for the "inverse" DP defect with type B T-junctions.) Upon weakening the attractiveness of the A-wetting substrate stripes from $\chi_{wA}N = -5.0$ to -2.5, each maximal ΔF decreases by about $3 \sim 4$ kT, due to decreased surface pinning of the A-blocks. Commensurability widths for pure AB-diblock are found to be $L_{X,Opt} = 16.8$ R_g for $\chi_{wA}N = -2.5$ and $L_{X,Opt} = 16.9$ R_g for $\chi_{wA}N = -5.0$. Upon adding homopolymer of either species, these shift

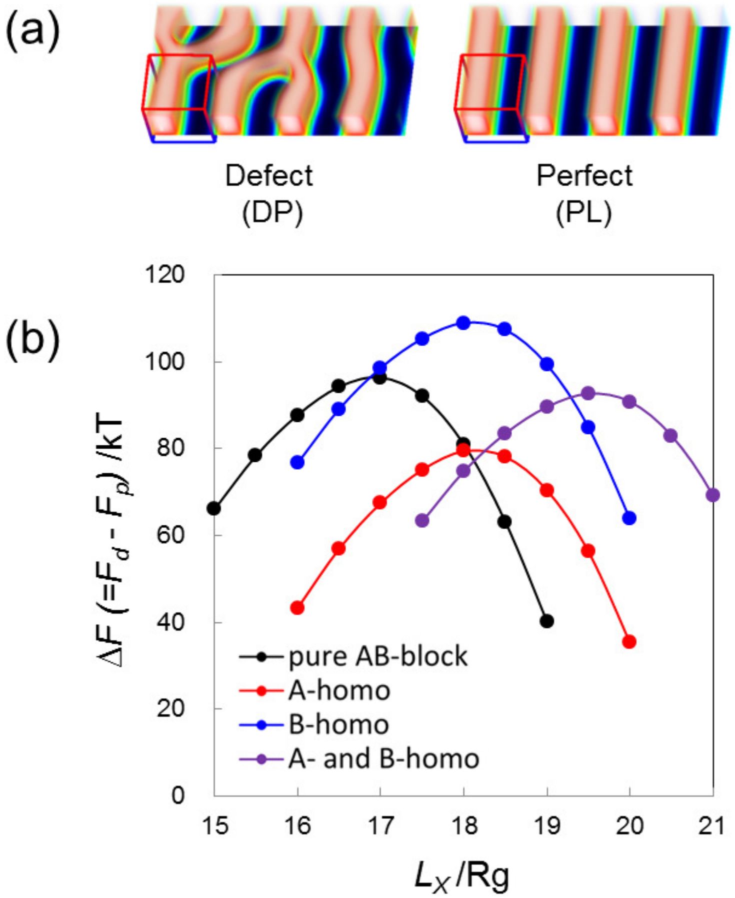

Figure 3.23: (a) 3D DP and PL states converged in the chemo-epitaxial geometry of Figure 3.19. (b) Formation energy ΔF of DP defects in the chemo-epitaxial geometry as a function of L_X for various homopolymer admixture conditions. In all cases $\phi = 10\%$ and the attractiveness of the A-wetting stripe is $\chi_{wA}N = -5.0$.

to $L_{X,Opt} = 18.0\ R_g$ for $\chi_{wA}N = -2.5$ and $L_{X,Opt} = 18.1\ R_g$ for $\chi_{wA}N = -5.0$. Overall, we see that the defect formation energies and commensurate film widths are relatively insensitive to substrate pinning strength for A-attractive stripes with $\chi_{wA}N < -2.5$.

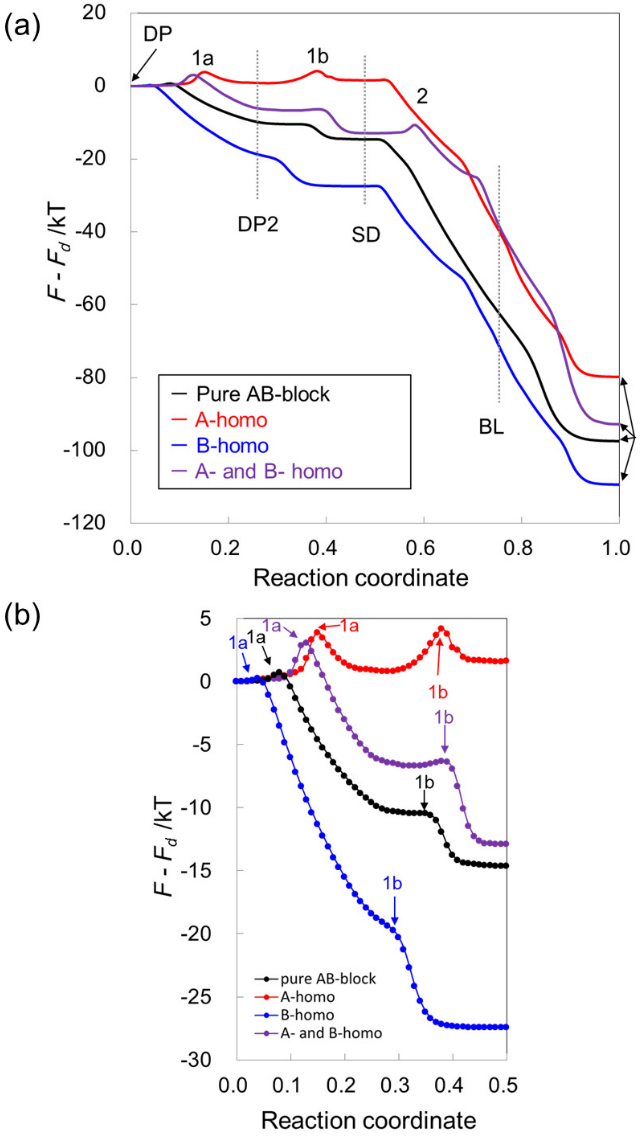

Figure 3.24: (a) Example kinetic pathways found by the string method for the chemo-epitaxial geometry of Figure 3.19 with various homopolymer admixture conditions. In all cases $\phi = 10\%$ and the attractiveness of the A-wetting stripe is $\chi_{wA}N = -5.0$. (b) Enlargement of the kinetic pathway between DP and SD.

We evaluate transition pathways and kinetic barriers at $L_{X,Opt}$ using the string method and SCFT. DP defects transition to PL by way of SD for all tested conditions, similar to the 2D results. However, in the 3D case, an additional shoulder (or barrier, for added A-homopolymer or added A- and B-homopolymer) is observed on the transition pathway between DP and SD (Figure 3.24a). We denote the first barrier 1a and the shoulder or second barrier 1b (Figure 3.24b). Considering the *z*-dependence of the morphology along the kinetic pathway from DP to SD (Figure 3.25), we see that the DPs T-junction connections begin breaking near the bottom surface (substrate). As the transition continues, this break zippers up to the top surface. The substrate clearly facilitates the initial breaking of T-junction connections, reducing the height of the first barrier relative to the 2D bulk case. The second shoulder or barrier, 1b, along the DP to SD pathway is encountered when the system attempts to break the last remaining DP connection at the top surface. The feature 1b is a barrier for added A-homopolymer and for added A- and B- homopolymer, and a shoulder for added B-homopolymer. The subsequent SD-BL transition shows a low kinetic barrier for weak surface pinning; for stronger surface pinning that barrier becomes a shoulder (except if the system contains both A- and B-homopolymer, which yet again acts to stabilize the defect). The final BL-PL transition appears free of barriers, displaying only sloping shoulders for all tested conditions.

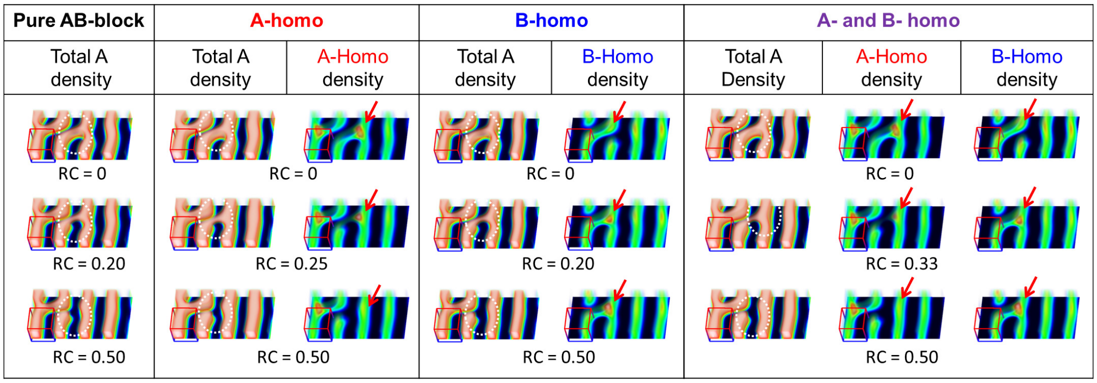

Figure 3.25: Density profiles along the kinetic pathway between DP and SD (corresponding to the MEPs shown in Figure 3.24b). White circles frame regions where connection breaking occurs. Red arrows point out regions of homopolymer localization.

Adding 10% A-homopolymer increases the height of barrier 1a by factor of 5 relative to that for a pure diblock melt, and causes 1b to become a barrier where for pure diblock it was merely a shoulder. Once again, we attribute this to excess A-homopolymer aggregating near the dislocation-pairs T-junction cores (Figure 3.25). Although connection breaking begins easily in the presence of A-pinning substrate domains, two high barriers must still be overcome. Adding 10% B-homopolymer, by contrast, swells the B domains, facilitating connection breaking and reducing the 1a barrier. Adding homopolymer of either species increases the height of the barrier denoted 2, corresponding to the SD to BL transition; however, barrier 2 is much lower than 1a for all conditions, thus its effect on the annealing process is likely negligible.

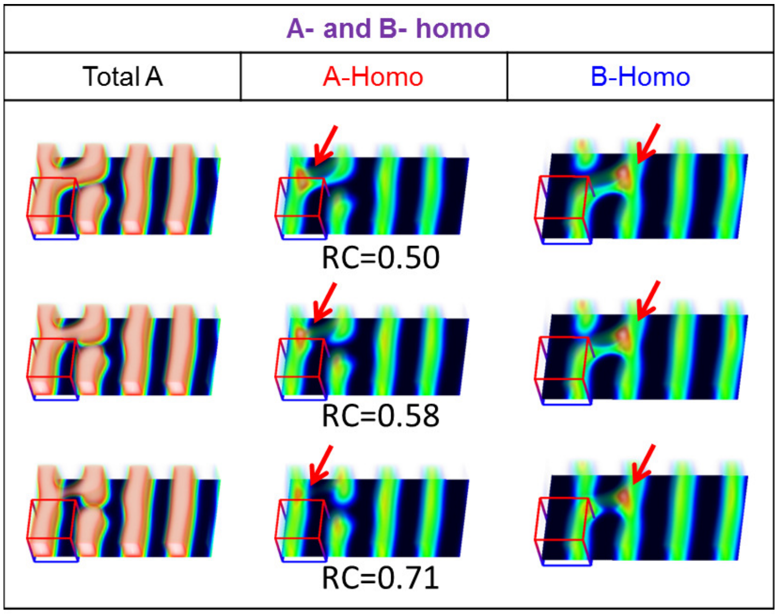

Figure 3.26: Density profiles along the kinetic pathway between SD (at reaction coordinate/string arc length coordinate 0.5) and reaction coordinate 0.71 (corresponding approximately to BL) for the case where both A- and B-homopolymer are present. Red arrows point out regions of homopolymer localization.

When added A- and B-homopolymer are simultaneously present, the height of barrier 1a is 4 times larger than that for the pure AB-diblock melt (but still 30% smaller than when only A-homopolymer is added). Furthermore, barrier 1b's height is also reduced significantly when both homopolymer species are present. On the other hand, the SD defect becomes more stable when added A- and B-homopolymer are simultaneously present, and barrier 2 between SD and BL increases by a factor of 10 relative to when A-homopolymer alone is added. This is because in the SD defect, both species form T-junctions, so both A- and B-homopolymer have available T-junctions in which to localize (Figure 3.26).

When the attractiveness of the A-wetting substrate domains is reduced from $\chi_{wA}N = -5.0$ to $\chi_{wA}N = -2.5$, the barrier heights change (Table 3.2). Also, in general, the highest observed barriers along the 3D paths are significantly smaller than the highest observed barriers for the 2D paths at equivalent homopolymer volume fraction and chain length. It is clear that a substrate pre-patterned according to Figure 3.19 acts to facilitate defect annealing. However, if homopolymer of the species attracted by the pinning domains (in this case A) remains in the system, a higher barrier must be overcome to anneal out DP defects. In living anionic polymerization of PS-b-PMMA copolymer, polystyrene is the species that is polymerized during the first step and can be present as residual homopolymer in the resulting diblock melt. Therefore, our work suggests that PMMA should be the species preferred by the pinning domains of a LiNe chemo-epitaxial prepattern.

Commensurability effects

For the cylinders in grapho-epitaxial confinement studied in Section 3.2, it was determined that channel width had a significant effect on the heights of barriers along the kinetic pathway and on estimated annealing times. Therefore, in this

	$\chi_{wA}N$	$L_{X,Opt}/R_g$	ΔF_{max}/kT	1a/kT	1b/kT	2/kT
Pure block	-5.0	16.8	96	0.75	-	-
	-2.5	16.9	93	1.00	-	0.01
A-homo	-5.0	18.0	79	4.37	3.23	0.04
	-2.5	18.1	77	3.78	4.15	0.25
B-homo	-5.0	18.0	108	0.23	-	-
	-2.5	18.1	106	0.93	-	0.10
A- and B-	-5.0	19.6	93	3.06	0.34	2.26
	-2.5	19.4	90	3.12	0.46	2.16

Table 3.2: Commensurability widths $L_{X,Opt}$, DP formation energies at the commensurability width ΔF_{max}/kT, and heights of barriers 1a, 1b, and 2 along the kinetic pathway between DP and SD for various homopolymer admixture conditions at two different values of the A-wetting substrate domains' A-attractiveness, $\chi_{wA}N = -5.0$ (more strongly attractive) and $\chi_{wA}N = -2.5$ (less strongly attractive). Dashes indicate that a shoulder, not a barrier, was observed. In all cases $\alpha = 0.5$ and $\phi = 10\%$.

section, we evaluate the effect of commensurability on kinetic barriers 1a and 1b between DP and SD defects for the chemo-epitaxial setup. We focus on barriers 1a and 1b because these barriers tend to be the highest along the kinetic pathway and thus are expected to have the most significant effect on the annealing process. As shown in Figure 3.27, the first barriers' height changes non-monotonically with system width, and a minimal barrier height is observed for a particular value of L_X. For a pure diblock melt, the smallest height of barrier 1a is obtained at $L_X = 16.4\ R_g$ (we denote this value as $L_{X,min}$), which is close but not identical to the commensurability width $L_{X,Opt} = 16.8\ R_g$ found in the previous section by maximizing the defect formation energy of DP. Furthermore, the kinetic barrier increases as L_X increases above 16.6 R_g. This L_X dependence of barrier height

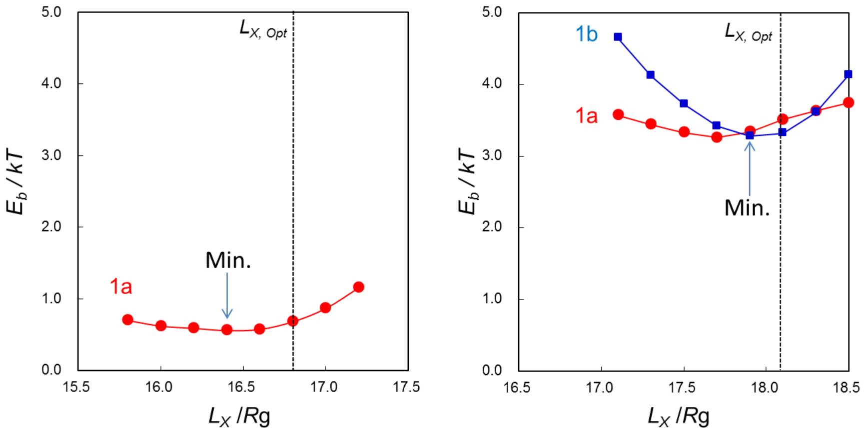

(a) pure AB-block

(b) A-homo

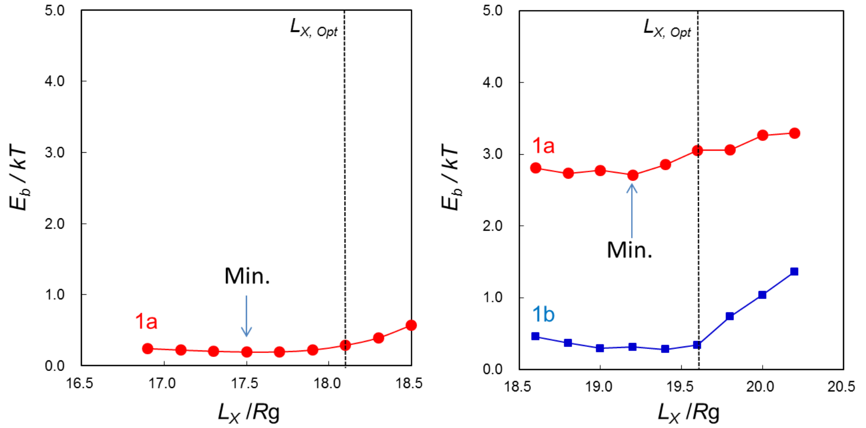

(c) B-homo

(d) A- and B- homo

Figure 3.27: Heights of barriers 1a (red) and 1b (blue) as a function of film width. Notice that for added B-homopolymer (lower left panel) only barrier 1a is present; 1b becomes a shoulder. The vertical dotted line shows the optimized film width $L_{X,Opt}$ at which the formation energy of DP, ΔF, is maximized.

is universal for the range of conditions covered by this study. When the system width is smaller than the commensurability width, lamellae are under compression [116], which acts to accelerate the elimination of DP defects. The second barrier

1b, which is seen for added A-homopolymer and added A-and B-homopolymer, also has minimal height at a smaller L_X than $L_{X,Opt}$. Away from the optimal L_X, however, the height of barrier 1b increases sharply, exceeding that of barrier 1a. For the case where both added A- and B-homopolymer are present, barrier 1b begins to show a pronounced increase when L_X exceeds 19.7 R_g. When added B-homopolymer alone is present, the height of barrier 1b stays roughly constant for $L_X < 17.8$ R_g.

Transition rate calculations for DP melting

Using the minimum energy paths and kinetic barriers identified by the string method, we can estimate reaction rates for transitions between DP and PL. We use the same approach as in our previous study of defect annealing in graphoepitaxy (see Section 3.2.6 or Ref. [143]). Here the DP defect melting process can be represented by the following reaction:

$$DP \Longleftrightarrow DP2 \Longleftrightarrow SD \Longleftrightarrow PL\ , \tag{3.5}$$

where DP, DP2, and SD denote the metastable defects as shown in Figure 7. The first "$\Longleftrightarrow$" corresponds to crossing barrier 1a in either direction, the second corresponds to crossing barrier 1b in either direction, and the third corresponds

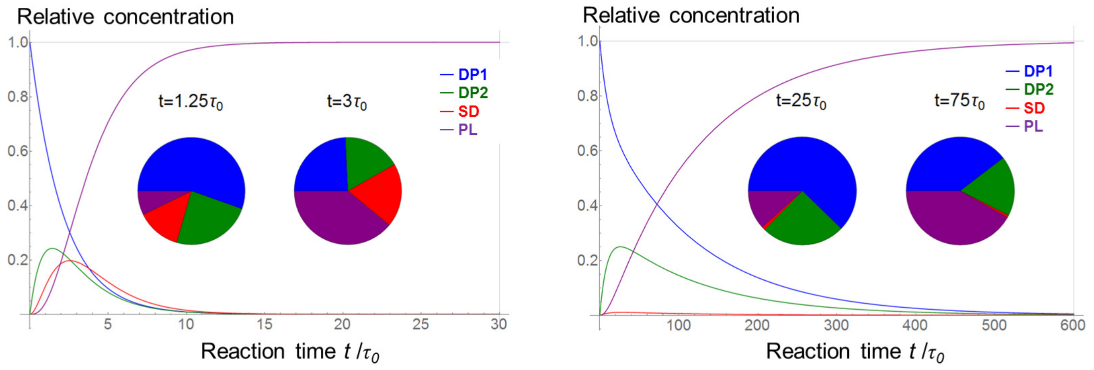

(a) pure AB-block (b) A-homo

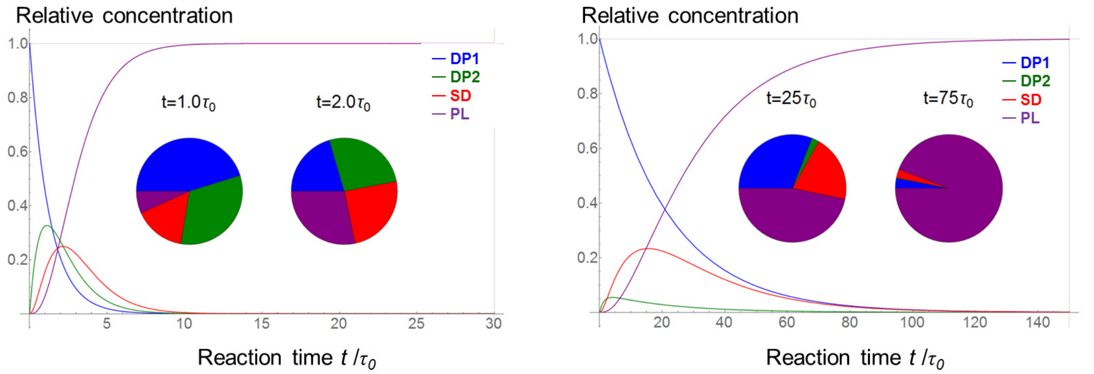

(c) B-homo (d) A- and B-homo

Figure 3.28: Time dependence of relative concentration s of DP, DP2, and SD defects, as well as the defect-free morphology PL, at the optimal channel width $L_{X,Opt}$ for (a) a pure AB-diblock melt, (b) AB-diblock with added A-homopolymer, (c) AB-diblock with added B-homopolymer, and (c) AB-diblock with added A- and B-homopolymer. In all cases $\phi = 10\%$, $\alpha = 0.5$ and $\chi_{wA}N = -5$.

to crossing barrier 2 in either direction. As in Section 3.2.6, we emply a Kramers-like approach in which the kinetic rate $k_{1\to 2}$ for a transition from state 1) to 2) is given by the Arrhenius expression

$$k = \tau_0^{-1} \exp\left[-E_b/kT\right] \ , \tag{3.6}$$

where E_b is the height of the barrier that must be overcome to transition from states 1 to 2 and τ_0 is the time necessary for diffusion of chains parallel to the microdomain interface over a distance comparable to the size of defect [143]. In the case of PS-b-PMMA at a molecular weight corresponding to $\chi N = 25$, for example, $\tau_0 \approx 9s$ [143].

Specifically, we consider the annealing rate of DP morphologies formed on a substrate that is patterned as in Figure 3.19. The barriers summarized in Table 3.2 for the kinetic pathways at $L_{X,Opt}$ (Figure 3.24) are used to calculate the reaction rates. As shown in Figure 3.28, for pure AB-block copolymer (Figure 3.28b) and blends with added B-homopolymer (Figure 3.28c), the annealing time to transition from DP to PL with 99% probability is $15\tau_0$, but when only A-homopolymer is present in the blend, that annealing time ($600\tau_0$) is increased by a factor of 40. When both A- and B-homopolymer are present in the melt (Figure 3.28d), the annealing time ($150\tau_0$) is increased by a factor of approximately 10 relative to the pure AB-block case; however, it is still 4 times smaller than the estimated time of $600\tau_0$ for added A-homopolymer alone.

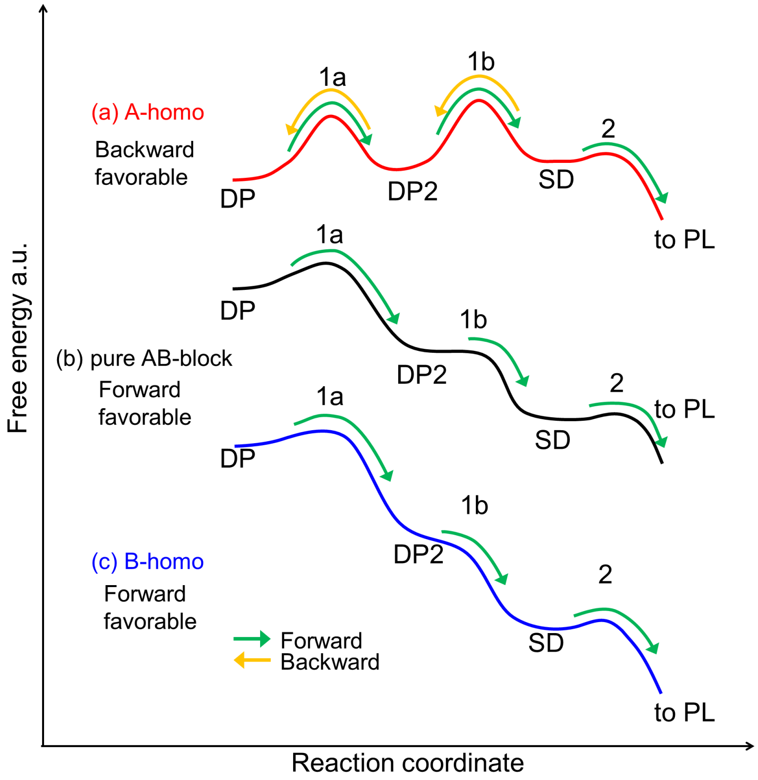

Figure 3.29: Schematic of transitions considered in the annealing calculations for the case of A-homopolymer admixture (a) and A- and B-homopolymer admixture (B). When added A-homopolymer alone is present, barrier 1a and 1b are both significant; in fact, if the system lies in the DP2 basin, the reverse transition from DP2 back to DP is more likely than the forward transition from DP2 to SD. When A- and B-homopolymer are both present, barrier 1b becomes relatively small, suppressing this reverse transition and reducing the overall annealing time.

We can clarify the melting mechanism by examining the forward and backward transition rates among the set of metastable states illustrated in Figure 3.29. For an A-homopolymer blend (Figure 3.29, case a), after crossing the kinetic barrier from the initial DP (RC=0) to the metastable DP/SD composite "DP2" (indicated in Figures 3.24a and 3.25 at RC=0.2), the system is more likely to revert from DP2 back to DP than it is to continue forward and transition to SD. In fact, the reaction rate for the DP2 to DP backward transition is greater than the reaction rate for the DP to DP2 forward transition, because DP2 lies at higher energy (closer to the height of barrier 1a). Once the system reaches an SD configuration it can readily anneal to PL; however, the hindered kinetic nature of the DP to SD transition results in long annealing times for the overall DP to PL transformation. On the other hand, for pure AB-diblock and for added B-homopolymer (cases b and c in Figure 3.29), the free energies of the intermediate morphologies decrease in an approximately stepwise manner along the kinetic pathway. The backward reaction rates are negligible compared to the forward reaction rates in this case; backward transitions from DP2 (SD) to DP (DP2) are suppressed and thus the total reaction time is reduced.

As shown in Figure 3.24 and Table 3.2, the barriers 1a and 1b are significantly smaller when added B-homopolymer or pure AB-diblock is present, relative to the cases where added A-homopolymer or both A- and B-homopolymer are present. Therefore, we expect the DP to PL transition to proceed more quickly in the former two cases. The priority should thus be to remove A-homopolymer from the system. However, if A-homopolymer is present in the AB-diblock melt and is impossible to remove from the system, we can reduce the annealing time of DP defects to an extent by adding B-homopolymer.

3.3.4 Conclusion

We use SCFT simulations and the string method to investigate the self-assembly of symmetric diblock copolymer/homopolymer blends for both a quasi-2D bulk system and a fully 3D system on a chemically pre-patterned substrate. In the 2D simulation of a film not subject to chemo-epitaxy, kinetic pathways and barriers for the transition from a dislocation-pair defect (DP) to perfect lamellae (PL) are evaluated at the lamellar commensurability width $L_{X,Opt}$, which is determined by separate SCFT calculations. Starting from DP for a pure diblock melt, the system transitions to PL by way of a single dislocation (SD) and a bridged lamellar (BL) state, in that order. For 10% added homopolymer of either type, we observe two barriers and one shoulder along the kinetic pathway, corresponding to transitions from DP to SD, SD to BL, and BL to PL, respectively. The first barrier (between DP and SD) is the highest along the kinetic pathway for all considered homopolymer species, volume fractions and relative chain lengths. The height of the first barrier increases when homopolymer of the species possessing T-junctions in the DP is added, since the homopolymer tends to localize near the T-junction cores of the dislocation, thereby stabilizing it.

In 3D simulations with wall confinement on a chemically patterned substrate, the initial DP melts and transitions to PL by way of the SD state at $L_{X,Opt}$. Since the system is no longer invariant in the z-direction, the dislocations connections first break near the periodically A-attractive substrate, and that topological change propagates vertically in the film. This vertical "unzipping" leads to barrier heights along the kinetic pathway that are reduced relative to those for the (uniform in z) transformation deduced from the 2D simulations. In the 3D case, when added homopolymer is able to segregate to the cores of a DPs T-junctions, barrier heights increase by a factor of 5 or more. However, if the added homopolymer does not correspond to the species forming T-junctions, and therefore cannot localize in the junctions, additional homopolymer reduces barrier heights.

We investigate the effects of channel width on barrier heights and find that minimal barrier height tends to occur at smaller system widths than $L_{X,Opt}$ for all tested conditions.

We estimate the total DP to PL transition time using a Kramers-like approach, and find that in the presence of 10% added A-homopolymer, the DP to PL transition takes place with 99% probability after an annealing time of $600\tau_0$, where τ_0 is the time scale for segmental diffusion along A-B microdomain interfaces over a distance comparable to the defect size. Adding B-homopolymer to the

AB-block copolymer/A-homopolymer system reduces the likelihood of backwards transitions, cutting this predicted annealing time by a factor of 4.

Our findings suggest that, even though residual homopolymer is expected in some AB-diblock melts synthesized via common living polymerization techniques, defective morphologies can be suppressed by using a substrate patterned with alternating domains that are neutral and attractive to the monomer species not present as residual homopolymer.

3.4 Application to pitch-multiplication in contact holes

A number of recent experimental studies indicate that directed self-assembly is a feasible technology for creating smaller cylinders within larger cylindrical prepatterns [177, 178]. This procedure is viewed as a promising method to create nanoscale contact holes for vertical interconnect access (VIA) in semiconductor wafers.

The GPU string method code I wrote was also used to calculate minimum energy paths and kinetic barriers for defects appearing in generalized rounded (oblong) grapho-epitaxial prepatterns. However, the first author of the study requested that I not reproduce his figures or data, since he plans to include them in his own thesis. Interested readers may consult Iwama *et al.* [179]. SCFT studies of the most commonly encountered defects in cylindrical, oblong, rectangular, and peanut-shaped ("egg-box") confinement with various wetting conditions can also be found in [176, 180–182]. The effects of thermal fluctuations on the placement of self-assembled cylinders are explored in [183–185].

Chapter 4

Truncation-based energy weighting string method

Reproduced in part with permission from M. Carilli, K. T. Delaney, and G. H. Fredrickson, "Truncation-based energy weighting string method for efficiently resolving small energy barriers," *The Journal of Chemical Physics* **143**, 054105 (2015). Copyright 2015 AIP Publishing LLC.

In recent years, the zero-temperature string method has proven successful in finding and characterizing minimum energy paths for a wide variety of systems [115, 116, 143, 186–188]. However, it possesses two related drawbacks. First, if the system contains only one barrier region, and that region is small with respect to the configurational "distance" between the locally stable wells (in a sense we will clarify in Secs. 4.2.1 and 4.2.2), many images will be wasted tracing out the uninteresting path to the lowest-lying configuration of one well or the other and relatively few will reside within the barrier region, resulting in poor resolution of the barrier. For high-dimensional systems like polymer field theories where each image carries a heavy computational cost, it is essential to focus as many images as possible near the barrier. Second, for nucleation problems (in which the barrier region is most important) many later images correspond to the nucleus growing towards the edge of the computational domain, where unphysical confinement effects take hold. In fact, it is conventional to discard the later section of the string when investigating nucleation problems [115, 187]. Energy weighting alleviates these two difficulties somewhat, but conventional energy weighting schemes (as defined in Section 2.2) still require significant computational effort to relax images that will ultimately be discarded.

In this work we demonstrate “truncation-based energy weighting” (TBEW), a new energy weighting scheme that fully solves both problems by focusing all images within the barrier region. The string can still be guided to explore a transition between two specific locally stable states based on how it is initialized. We demonstrate application of the scheme to a 2-dimensional illustrative test case as well as a high-dimensional problem involving the disorder-to-lamellar transition of the renormalized Brazovskii model [104, 105, 112]. We also investigate the new scheme’s convergence, and verify that its convergence characteristics match those of conventional energy weighting schemes.

4.1 Truncation-based energy weighting

For a string using conventional energy weighting as described in 2.2.1, once converged, the endpoint ϕ_1 will lie at the local minimum A and the opposite endpoint ϕ_N will lie at the local minimum B, while the intervening images trace out an MEP between them. Truncation-based energy weighting (TBEW) modifies this by refocusing all images within some region of interest during every iteration of Step 2; the string does not trace out the full well-to-well MEP but rather the portion of it that is deemed most important to resolve.

For barrier-crossing problems, the most sensible choice is to pick an energy cutoff E_C, and confine all images to the region $V(\phi_i) \geq E_C$. Of course, one must choose E_C less than the barrier height. A good initial guess for E_C is the energy of whichever well, A or B, is relatively metastable.

The sequence of initialized images must span the barrier, e.g., ϕ_1 must lie in the basin of attraction of A and ϕ_N must lie in the basin of attraction of B.

However, it is not essential that the initialized images all satisfy $V(\phi_i) \geq E_C$, as that criterion will soon be enforced by the evolution algorithm.

4.1.1 Algorithm

Step 1: Independently evolve each image.

This step is performed identically to Step 1 of a string method using conventional energy weighting, as in 2.2.1.

Step 2: Interpolate, determine truncation points, and reparametrize.

The core idea of TBEW is to change the reparametrization step such that all images are redistributed only in that portion of the string near the barrier with energy $V(\phi(\alpha)) \geq E_C$. In the following discussion we use the term "left" ("right") to denote the portion the string in the basin of attraction of A (B).

The reparametrization step of TBEW is carried out by first constructing the smooth interpolated curve $\phi(\alpha)$ as in Step 2 of the previous section. Next, we look for the nearest images to the left and right of the barrier whose energies fall below E_C. If none can be found (in other words if all images possess energies $\geq E_C$), then all images are redistributed evenly along α as in Step 2 of the previous section. If one or more images are found with $E < E_C$, we locate the nearest pair of images on each side (left and right if necessary) of the barrier that straddle

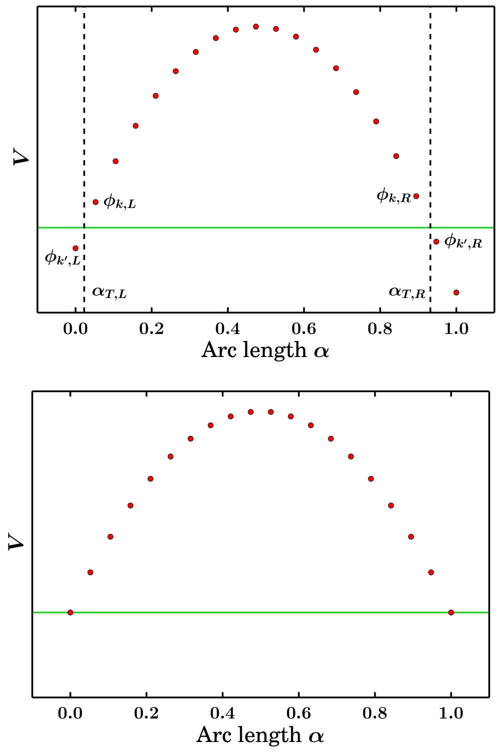

Figure 4.1: Step 2 of TBEW represented schematically. Upper panel: String before truncation and redistribution. Vertical dashed lines are drawn at the α-values at which the string is to be truncated. Lower panel: String after truncation and redistribution.

E_C. Figure 4.1, upper panel, shows an example in which the left and right pairs are denoted $\phi_{k,L}, \phi_{k',L}$ and $\phi_{k,R}, \phi_{k',R}$ respectively (unprimed indices correspond to being nearer to the peak). We then use a suitable root-finding scheme to locate approximately the left and right crossing points α_L and α_R where the interpolated smooth curve $\phi(\alpha)$ intersects $V(\phi(\alpha)) = E_C$, and, instead of redistributing the images evenly between $\alpha = 0$ and $\alpha = 1$, we redistribute them evenly between α_L and α_R. Note that the endpoints are included in this redistribution, placed at α_L and α_R respectively (in conventional EW, by contrast, the endpoints are unaffected by the redistribution, remaining at $\alpha = 0$ and $\alpha = 1$). Finally (after redistribution), we normalize α once more according to its new terminal values. The entire process is illustrated schematically in Figure 4.1.

To find α_L and α_R in practice, we recommend the following one-step secant method for its effectiveness and low computational cost. Once (up to two) pairs of images that straddle E_C have been located, for each pair, compute the approximate derivative $dV/d\alpha$ between each pair as follows:

$$\left.\frac{dV(\phi(\alpha))}{d\alpha}\right|_{\alpha_{k'}} = \frac{V(\phi_k) - V(\phi_{k'})}{\alpha_k - \alpha_{k'}}\,, \tag{4.1}$$

then establish a left or right (according to where the pair lies) truncation point at

$$\alpha_{T,L \text{ or } R} = \alpha_{k'} + (E_C - V(\phi_{k'}))\,/\,\left.\frac{dV}{d\alpha}\right|_{\alpha_{k'}}\,. \tag{4.2}$$

The new endpoints placed at α_L and α_R may still possess energies slightly less than E_C due to inaccuracy of the approximate derivative in Eq. (4.1). If the energy of a putative new endpoint configuration interpolated at α_L or α_R falls below E_C to the extent that string resolution in the barrier region will be impaired, the putative interpolated configuration can be used to perform the second step of a secant method, and obtain a more accurate value of α_L or α_R. However, each secant method step beyond the first requires constructing and evaluating the energy of a new interpolated image, which incurs additional computational cost. For the simulations we present in the following sections, Eqs. (4.1) and (4.2) were used as written above and found to be satisfactory.

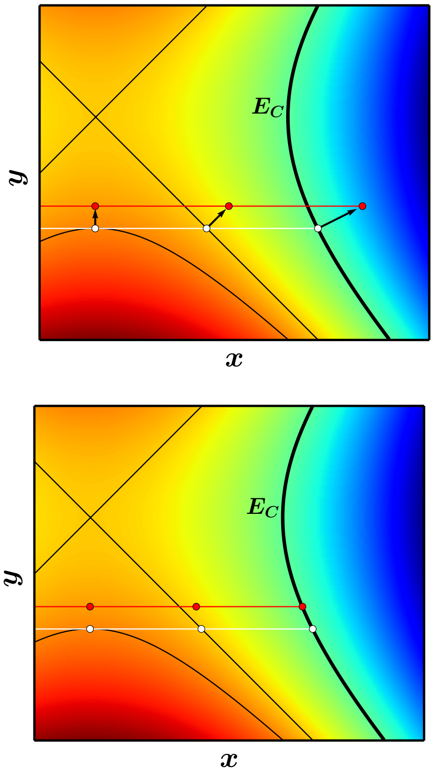

Figure 4.2: Motion of endpoints along E_C in TBEW. Upper panel: The evolution step 1, carried out with unconstrained evolution according to the simplified string method, for a string initially at time t_N (white). Black lines represent equipotential contours; the thick black line represents the cutoff energy E_C. Images evolve along the gradient (normal to the contours). Lower panel: String at t_{N+1} (red) after the truncation and reparametrization step 2. Since the endpoint is created as an interpolation between the rightmost two red images in the upper panel, the endpoint's effective motion is to slide along E_C towards the valley crossing the saddle point.

As the evolution step 1 and reparametrization step 2 of TBEW are iterated, the evolution step is unconstrained (or constrained to be normal to the string) for all images, so endpoints move at least somewhat in the direction of the nearest MEP valley as they relax towards their respective basins of attraction. Since the reparametrization step is independent of the evolution step, the reparametrization step ensures that all images are continually refocused above $V \approx E_C$ in a manner that still allows them to relax towards the nearest MEP valley over time. The result is that the string's endpoints traverse sideways along the contour $V \approx E_C$ until both endpoints converge to the nearest point on the contour $V \approx E_C$ that also lies along an MEP, while the interior images lie along an intervening barrier-region path obeying Eq. (2.25). This motion is illustrated schematically in Figure 4.2.

Note that the repeated refocusing of the images within a particular region means that the endpoints never reach locally stable configurations if those configurations possess energies $< E_C$. In the limit of long time, a periodic state is reached in which endpoints are continually attempting to breach the energy region of interest and being refocused within. However, these movements are infinitesimal, and the movements of interior (non-endpoint) images are similarly small oscillations along the converged path. We revisit this issue in Sec. 4.3. Also, since the path found by TBEW obeys Equation (2.25), but might not place its endpoints at A and B, for the sake of rigor we refer to it as a section of steepest descent path (SDP) rather than MEP.

In the next section, we demonstrate that if a string using TBEW is initialized the same way as a string using conventional EW, the converged section of steepest descent path found by TBEW will lie along the same MEP found by the conventionally energy weighted string. The string using TBEW will simply have all its images focused within the desired energy region (Fig. 4.6).

TBEW may fail in a rough energy landscape, because depending on how the string is initialized, there is a danger that the endpoints will become trapped in spurious wells that do not lie along an MEP between the desired metastable states. However, this is a known shortcoming of conventional EW also (see, *e.g.*, Figure 1 of [76]). Additionally, in such a landscape the MEP may provide a poor description of the physical transition pathway. We expect that any energy landscape smooth enough to be suitable for conventional EW will also be suitable for TBEW.

Choosing the cutoff energy

In general, the choice of E_C should be motivated by some intuition about the potential surface $V(\phi)$. E_C must be less than the barrier height, which is unlikely to be known *a priori*. As stated previously, a good initial guess for E_C

is the energy of whichever well, A or B, is relatively metastable. For nucleation calculations, we find this choice to be effective, as demonstrated in Sec. 4.2.2.

We note that E_C can easily be updated on-the-fly as the calculation progresses, and the estimate of the barrier height relative to the current value of E_C improves. A systematic method for doing so could proceed as follows:

1. Periodically evaluate the resolution of the string according to some error metric, e.g. Eq. 4.4.
2. When the value of this error metric plateaus for the current E_C, estimate the barrier height as the peak of the current string. Increase E_C incrementally towards this peak value, and use the new value of E_C for future reparametrization steps.
3. Repeat 1 and 2 until the value of the error metric for the string drops below some desired global tolerance.

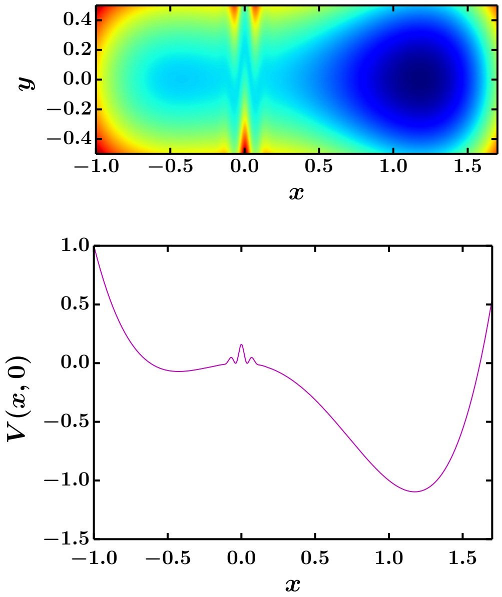

Figure 4.3: Upper panel: 2D potential $V(x, y)$ from Equation (4.3). Lower panel: $V(x, y)$ along $y = 0$ in the x-direction, showing the potential's large-scale double-well structure. Ripples around $x = 0$ arise as the line $y = 0$ cuts directly across the barrier region without attempting to navigate the twisting MEP.

4.2 Comparison of TBEW to conventional energy weighting

4.2.1 2D example

To illustrate the utility of truncation-based energy weighting, we apply the string method using both conventional energy weighting and TBEW to a 2D

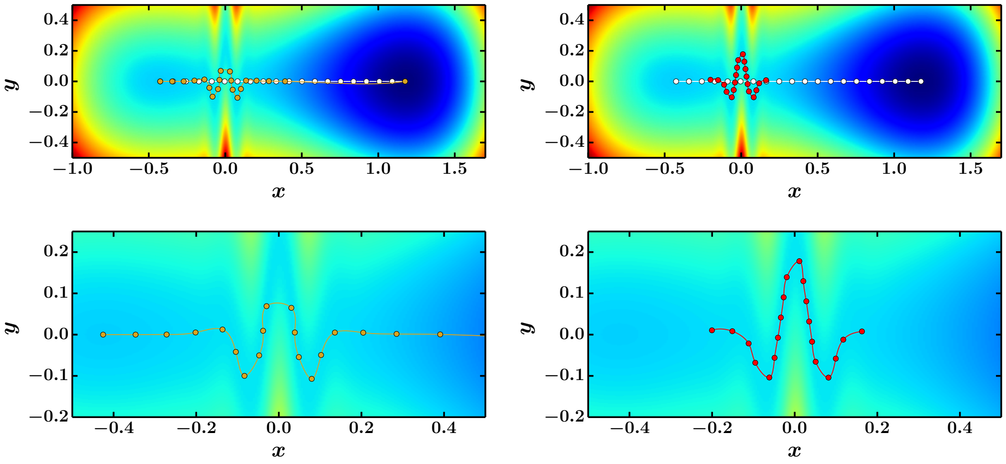

Figure 4.4: Upper row: Initialized strings (white) and converged strings on $V(x, y)$ for conventional (left, gold) and truncation-based (right, red) energy weighting, each with $N = 20$ images. Points represent images. Lines represent the continuous curves $\phi(\alpha) = (x(\alpha), y(\alpha))$, as interpolated in the configuration space (x, y), that serve as an estimate of the MEP (or SDP segment in the case of TBEW). The curve $\phi(\alpha)$ is constructed in each case by drawing a parametric cubic spline through the images. $W(E_i) = \exp(4E_i)$ is used for conventional EW, and $E_C = -0.03$ is used for TBEW. The conventionally-weighted string, once converged, leaves 12 images above $E_C = -0.03$. The TBEW string confines all 20 points within this high-energy region, and traces out a more accurate estimate of the barrier structure. Lower row: Zoom of barrier peak area for original (left) and truncated (right) methods.

energy landscape with potential

$$V(x, y) = -x^2 - x^3 + x^4 + \left(a\left[y - b e^{-(cx)^2}\cos\left(dx\right)\right]\right)^2 \tag{4.3}$$

$V(x, y)$ for $(a, b, c, d) = (2, 0.2, 10, 40)$ is shown in Figure 4.3. It exhibits a double-well structure in the x direction and a locally undulating trough in the y direction.

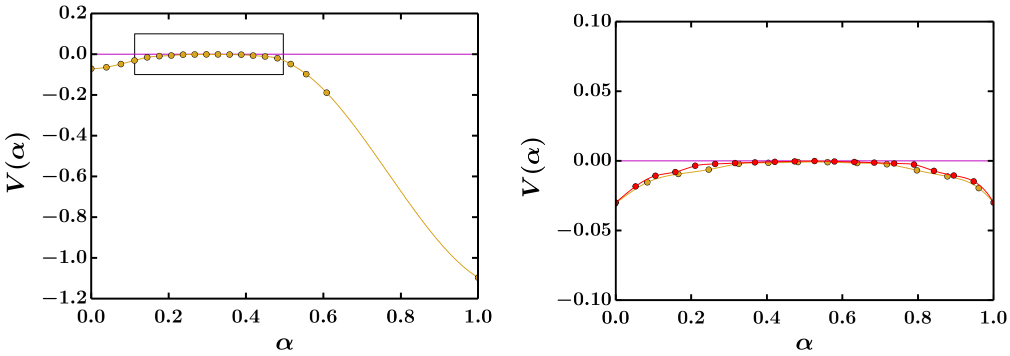

Figure 4.5: $V(\alpha)$ versus α for conventional EW (left, gold) and TBEW (right, red) for the strings in Fig. 4.4. The actual energy of the barrier peak, $V = 0$, is underlaid for reference. The region of the conventionally-weighted string corresponding to the domain of the truncated string ($E_C > -0.03$) is boxed in the left graphic and rescaled and underlaid for comparison in the right graphic. Points represent energy of images. Continuous curves are created via a 1D spline between points.

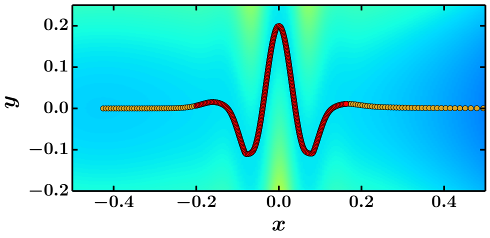

Figure 4.6: Zoom of barrier region showing converged pathways found by well-resolved ($N = 300$) strings. Red: SDP in the vicinity of the barrier found by truncation-based energy weighting with $E_C = -0.03$. Gold: MEP found by conventional energy weighting with $W(E_i) = \exp(4E_i)$. The MEP in the vicinity of the barrier found by TBEW perfectly overlays the corresponding portion of the MEP found by conventional EW, even though the end points of the string subject to truncation do not lie in locally stable configurations.

To escape the metastable well on the left, a system following the MEP on this potential must negotiate the gentle but twisting barrier centered around $x = 0$.

Once the barrier has been crossed, the remainder of the MEP leading to the stable well on the right is straightforward and uninteresting. To compute, *e.g.*, the rate of systems escaping from the well at negative x, the barrier region is the most important portion of the MEP to resolve. We would like our choice of energy weighting to place as many images near the barrier as possible. However, the barrier region only occupies perhaps a third of the (unweighted) arc length associated with the full well-to-well MEP.

Figure 4.4 shows the results of the calculations for conventional energy weighting and TBEW in a challenging case: both strings have few ($N = 20$) images. Figure 4.5 shows the energy $V(\alpha)$ along the corresponding MEP or SDP segment. For conventional EW, we employ an aggressive energy weighting scheme $W(E_i) = \exp(4E_i)$. At each timestep V_{min} is set equal to the energy of the lowest-energy image along the string minus some infinitesimal value in case two neighboring images both have the lowest energy. (V_{min} is determined this way for conventional EW schemes used in all our examples that follow.) Many images of the string using conventional EW fall outside the barrier region and are effectively wasted. By contrast, the string using TBEW focuses all images within the barrier region and achieves superior barrier resolution with the same number of total images.

In Figure 4.6, we confirm that the SDP segment in the barrier region found by TBEW matches the corresponding section of the MEP found by conventional EW when the strings employing each scheme are both well-resolved. Both strings contain the same number of images, $N = 300$, but the string using TBEW (red) succeeds in focusing all its images within the twisting barrier region.

In principle it is possible, with an even more aggressive conventional EW scheme, to focus all images (aside from the 2 endpoints) into the desired barrier region, but finding a scheme that places enough images in the barrier region can be an iterative process dependent on both the underlying potential and the number of images used. The chief virtue of truncation-based energy weighting is convenience: If one possesses an educated guess *a priori* of an energy value below which images become physically uninteresting, truncation-based energy weighting constitutes a drop-in solution that immediately guarantees uniform coverage of the region of interest with no images, not even the endpoints, falling (more than infinitesimally) outside. Such an energy value is often possessed in practice, *e.g.*, for nucleation calculations where the energy of the metastable state is known. Moreover, conventional EW gives *weighted* coverage of the *entire* well-to-well MEP, while TBEW gives *uniform* coverage of a *selected* barrier-region segment of SDP.

With this result in hand we can clarify TBEW's domain of usefulness: when the arc length required to resolve the full MEP from A to B is significantly greater than the arc length of the MEP within the barrier region, the MEP away from the barrier is unphysical or uninteresting, and one possesses an estimate of an energy value below which images are uninteresting.

4.2.2 High-dimensional example: Disorder → lamellar transition of the renormalized Brazovskii model

In the previous 2D example, it was clear by construction that the barrier region was the only portion of the MEP requiring detailed attention, and that the tails to one or both sides could be safely discarded. We now present a high-dimensional physical problem, nucleation of the lamellar phase from the disordered phase of the renormalized Landau-Brazovskii model, which exemplifies those traits, and for which truncation-based energy weighting also outperforms conventional energy weighting. We consider (2.107) with $(\xi, q_0, \tau_R, u_R, w) = (3.0425, 1.0, 0.5135, -0.975, 1.0)$, a region of parameter space where disorder is metastable and lamellae are stable.

We seek a nucleus large enough to exhibit nontrivial structure, and require a simulation cell with sufficient resolution to capture the nucleus' internal features as well as sufficient size to contain the nucleus without compressing it (∼2 times the size of the nucleus itself as estimated in Ref. [187]). We also require sufficient images to resolve the barrier peak. Satisfying all three criteria simultaneously proves computationally challenging with conventional energy weighting, particularly in 3D problems larger than the 2D nucleation calculations reported here.

Figure 4.7 shows the results of a conventionally energy weighted calculation with $N = 50$ images. We find that the vast majority of images are consumed tracing out growth in an unphysical regime where the nucleus already impinges on the cell boundary. These images are a necessary evil with conventional EW because the calculation will not converge until ϕ_N reaches the lowest-energy configuration within its basin of attraction, in this case a fully lamellar simulation cell. In general, when performing nucleation calculations with conventional EW, one can only hope enough images remain in the barrier region to estimate the peak reliably, and that the unphysical tail does not disrupt the barrier-region MEP estimate.

Figures 4.8 shows the results of a TBEW calculation with $N = 25$ images. All images are concentrated within the barrier region, and all images of its SDP

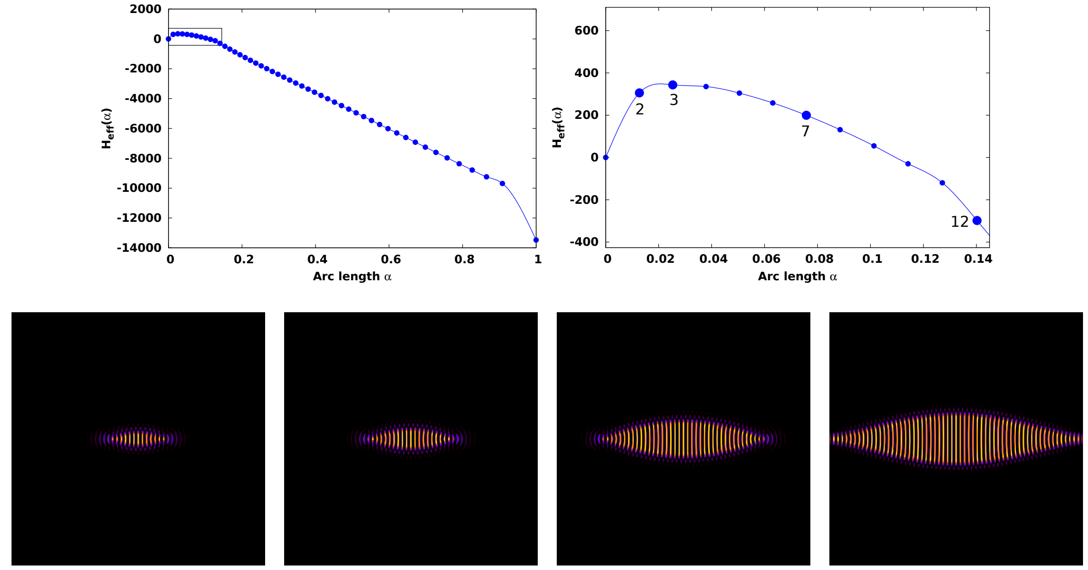

2 3 7 12

Figure 4.7: Upper left: Extensive $H_{eff}(\alpha)$ along the converged string for conventional EW with $W(E_i) = E_i$ and $N = 50$ images. Points represent (effective free) energy of images. Continous curves are constructed with a 1D cubic spline between energy values. A spurious bump appears between images 2 and 3 due to poor resolution. Upper right: Zoom of barrier region. Four images are emphasized, and their field configurations displayed in the lower row, to show the growth of the nucleus along the arc length coordinate α. By image 12, the nucleus has already reached the edges of the simulation cell, indicating that it and all 38 subsequent images are unphysical and a waste of computational effort.

segment lie along an MEP for a lamellar nucleus growing into a disordered environment, unaltered by confinement effects. Thus, no computational effort is wasted. The critical nucleus (Fig. 4.9) and barrier height are captured accurately. The far endpoint of the string does not relax to the fully lamellar state, but remains within the lamellar state's basin of attraction, which is sufficient to maintain "tension" and keep the string spanning the barrier.

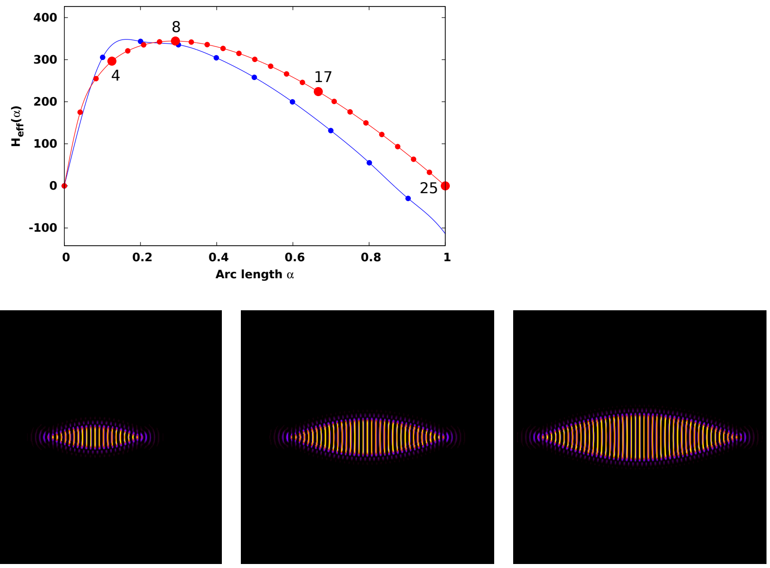

4 8 17 25

Figure 4.8: Upper panel: Extensive $H_{eff}(\alpha)$ along the converged string for TBEW with $N = 25$ images and $E_C = 0$ (red). The corresponding barrier region of Fig. 4.7 is shown and scaled to the same total (non-normalized) arc length for comparison (blue). As in Fig. 4.7, four images are emphasized, and their field configurations displayed in the lower row, to show growth of the nucleus along the arc length coordinate α. None of the TBEW string's images, even the endpoint ϕ_N, impinge on the cell boundary.

Due to the smaller number of images required, the TBEW string converges more quickly in wall time. The TBEW string converges to a steady state in 6 hours on an NVIDIA M2075 GPU, while the barrier region of the string using conventional EW is nearly converged only after 14 hours on identical hardware. Unphysical images in the tail of the conventionally energy weighted string continue to move long after the observed barrier peak settles to its final value, causing images in the barrier region to shift along the interpolated MEP (although the peak does not change).

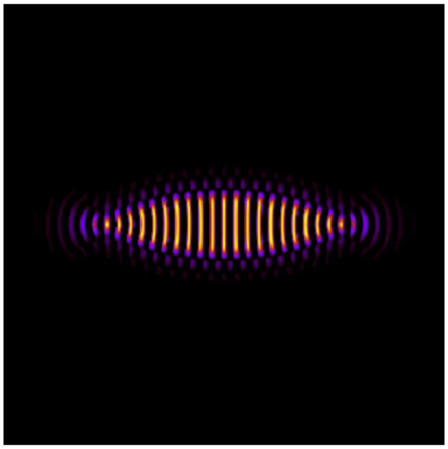

Figure 4.9: Zoomed-in view of the critical nucleus (barrier peak) obtained from the TBEW string in Figure 4.8. (For plotting purposes, negative values of $\bar{\phi}$ are cut off at zero to improve contrast.)

Figure 4.9 shows a closeup view of the critical nucleus (barrier peak) obtained using TBEW. The needlelike shape and "cupping" near the ends indicate strong preference for a lamellar-disorder interface normal to lamellar planes, in accord with the observations of Chastek [17], Milner [14], Balsara [15], and coworkers. The depicted 2D result may not be identical to the result of 3D calculation, although it is qualitatively similar. To our knowledge this represents the first string method calculation of a critical nucleus for the disorder-to-lamellar transition of the Brazovskii model.

To compute the minimum energy paths shown in Figures 4.7 and 4.8, and the critical nucleus shown in Figure 4.9, we use a 2-dimensional simulation cell with length and width equal to 60 lamellar periods, 640 x 640 plane wave resolution, and periodic boundary conditions. The conventional EW scheme employs $W(E_i) = E_i$ and the TBEW scheme employs $E_C = 0$. Images are initialized by embedding progressively larger circular cuts of a lamellar phase within the disordered phase. During initialization, we perform minor adjustments to the field values near the perimeter of each circular cut to ensure that the volume average of $\bar{\phi}$ is zero for each image. Gradient descent with an added Laplacian to conserve the volume average of $\bar{\phi}$ is used to relax each image during update steps, as in Ref. [128]. However, Ref. [128] treats derivatives using finite differences in real space, while we treat derivatives in Fourier space and employ a semi-implicit update scheme for improved stability.

4.3 Notes on convergence

For TBEW, either or both of the endpoints may fail to reach a locally stable configuration in the limit of long time. Rather, the endpoints continuously attempt to evolve towards the lowest-lying state of their respective basins of attraction, only to be truncated and compressed back into the barrier region if their energies decrease below E_C. It is therefore important to establish that, once this time-periodic state is attained, the images do in fact lie along an SDP in sense

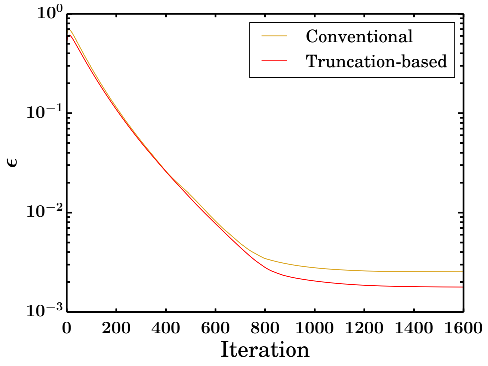

Figure 4.10: Evolution over time (number of iterations of Steps 1 and 2 of the string method) of the SDP accuracy criterion ϵ, Eq. (4.4), for conventional and truncation-based EW on the 2D potential from Sec. 4.2.1 with $N = 300$ for both.

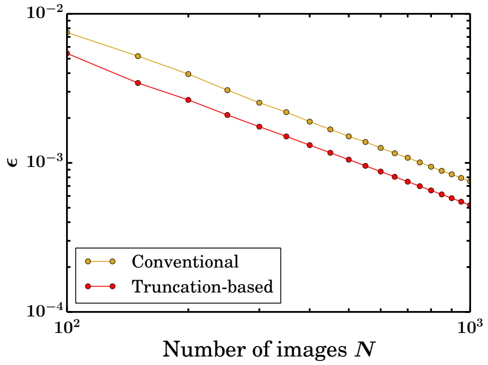

Figure 4.11: Scaling of converged ϵ value with number of images is linear with slope ≈ -1 on a log-log plot for both methods; in other words converged $\epsilon \sim N^{-1}$. When computing ϵ via Eq. (4.4) we calculate the tangent vectors using an upwinding scheme. This upwinding scheme is the dominant source of error, as discussed in Ref. [60].

of Equation (2.25), and their periodic motion simply corresponds to sliding back and forth along the path. To this end, we define the following criterion to assess how well a given string obeys Eq. (2.25):

$$\epsilon = \frac{1}{N_B} \sum_{i=1}^{N_B} \left| [\nabla V(\phi_i)]^{\perp} \right| \ . \tag{4.4}$$

We test this criterion on the 2D potential from Section 4.2.1, using $N = 300$ images for both conventional EW and TBEW. To ensure the comparison is of equivalent quantities, we average over only the N_B images that fall within the barrier region $E \geq E_C$ (TBEW endpoints that occasionally fall infinitesimally below E_C, as described in Section 4.1.1, are also included). For TBEW, $N_B = N$, and for conventional EW, $N_B \leq N - 2$ by the end of the calculation.

Results are displayed in Figures 4.10 and 4.11. Fig. 4.10 shows that both energy weighting schemes exhibit an almost identical (roughly exponential) convergence rate, reaching converged values in the vicinity of $\epsilon = 10^{-3}$. TBEW achieves lower converged error by focusing more images in the problematic twisting region. Fig. 4.11 shows that both schemes exhibit the same linear scaling of the converged error value with the number of images. Evidently, the convergence properties of TBEW match those of conventional EW.

Although the endpoints do not reach stable states in TBEW, the truncated string's interpolated smooth curve $\phi(\alpha)$ approximates the MEP in the vicinity of the barrier peak more accurately than that of the string using conventional EW with the same number of images. All other aspects inherit the accuracy scaling of conventional EW: the interpolation's error scales with the number of images, N, as N^{-4} for cubic splines, and timestepping accuracy scales with Δt according to the chosen ODE or PDE solver.

4.4 Similarities to the fixed length string method

We note that TBEW presents certain similarities to the fixed arc length string method introduced in Ref. [75]. Backofen and Voigt study nucleation in a phase-field model and introduce a string method that constrains the string to certain total arc length. Their method redistributes all images within this fixed arc length interval at each timestep if the string attempts to elongate. As with TBEW, at least one endpoint does not evolve to a stationary state, and all images are focused near a barrier region. However, the fixed length method requires a preliminary coarse unweighted string calculation of the full well-to-well MEP to estimate the arc length necessary to resolve the barrier region. TBEW, by contrast, requires only a single calculation, and focuses the string within the relevant energy region in a manner unaffected by the arc length of the string changing as it evolves.

4.5 Conclusions

We present a useful truncation-based energy weighting (TBEW) scheme for the zero-temperature string method. It possesses two advantages over conventional energy weighting:

1. TBEW forces all images to remain near the barrier peak, and provides uniform coverage of a selected barrier region. It requires only an estimate of an energy value below which images are physically uninteresting, and we have found it more convenient to use in practice than conventional EW, which can require iteratively deciding upon some problem-dependent weighting function. TBEW is especially advantageous for barriers that occupy relatively little arc length in the system's configuration space.
2. For nucleation problems, conventional EW requires that later images traverse unphysical confinement effects as the nucleus grows to fill the simulation cell. TBEW avoids this issue entirely.

We demonstrate TBEW on a 2D example potential as well as a high-dimensional field-theoretic representation of nucleation in the renormalized Brazovskii model. In both cases, TBEW outperforms conventional energy weighting in resolving the barrier.

For a string using conventional EW, the endpoints evolve to locally stable configurations. For a string using TBEW, this may not be the case. We verify that the rate of convergence, degree of converged error, and scaling of converged error with number of images for a string using TBEW match or are superior to those for a string using conventional EW, even when the TBEW string's endpoints fail to reach locally stable configurations in the limit of long time.

Truncation-based energy weighting is straightforward to implement alongside an existing realization of the string method. Its added computational cost entails only a check on each image's energy, and the cost of determining truncation points, which is negligible if the method recommended by Equations (4.1) and (4.2) is employed.

Chapter 5

Nucleation of lamellae from disorder in the Brazovskii model

> Reproduced in part with permission from M. Carilli, K. T. Delaney, and G. H. Fredrickson, “Nucleation of the lamellar phase from the disordered phase of the fluctuating Landau-Brazovskii model,” *In preparation.*

5.1 Previous work

The disorder→lamellar (dis→lam) transition of a melt of symmetric diblock copolymers is known to be a fluctuation-induced first-order phase transition. Commonly used workhorse models like the Leibler model [12] and self-consistent field theory [87, 189] predict the transition to be second-order at a mean-field level. This second-order character does not admit the existence of a metastable disordered phase, and predicts that the disordered phase transitions immediately to the lamellar phase via spinodal decomposition as soon as the phase boundary (also referred to subsequently as the "order-disorder transition" or ODT) is crossed. The influence of fluctuations causes the transition to instead become weakly first-order. The onset of the ordered phase is suppressed by fluctuations, taking place at a lower temperature than predicted by mean field theory; also, for shallow quenches to temperatures below the ODT, the disordered phase may be metastable, and a free energy barrier must be crossed for the system to form a lamellar phase. This interesting behavior has been the subject of extensive analytic, experimental, and computational research.

Analytic investigation of this transition can be traced back the work of Brazovskii [105], who identified a Landau-type field theory with periodic ordered phases whose ODT had fluctuation-induced first-order character. Fredrickson and Helfand [104] (FRH) showed that the Leibler model (describing diblock copolymers in the weak-inhomogeneity limit near the ODT) could be mapped to the Brazovskii model. They applied Brazovskii's analysis to this mapped model and predicted that the dis→lam transition was weakly first-order. They also derived a quantitative estimate for the ODT's shift away from its mean-field value. Fredrickson and Binder [112] (FRB) constructed a renormalized effective field theory for the mapped model that incorporated the effects of fluctuations at a mean-field level; their renormalized theory also showed that dis→lam transition was weakly first-order. Hohenberg and Swift [16] investigated nucleation of the lamellar phase

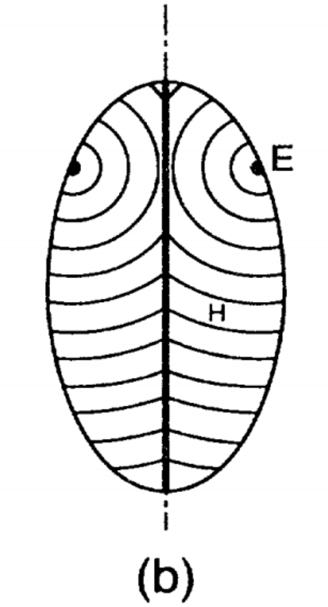

Figure 5.1: Cutaway view of an ellipsoidal nucleus containing a focal conic defect, as predicted by Hohenberg and Swift. The defect structure tries to ensure that lamellar planes are normal to the lamellar-disorder interface as much as possible, because a configuration with lamellar planes parallel to the interface has higher surface tension. Figure adapted from [16].

from the disordered phase using a renormalization-group analysis; they verified the weakly first-order nature of the transition. They also predicted the surface tension between disordered and lamellar phases to be highly anisotropic, favoring interfaces normal to lamellar planes and leading to ellipsoidal critical nuclei or, potentially, to nuclei containing focal conic defects (Figure 5.1). A similar surface tension anisotropy was predicted by Milner and Morse [14].

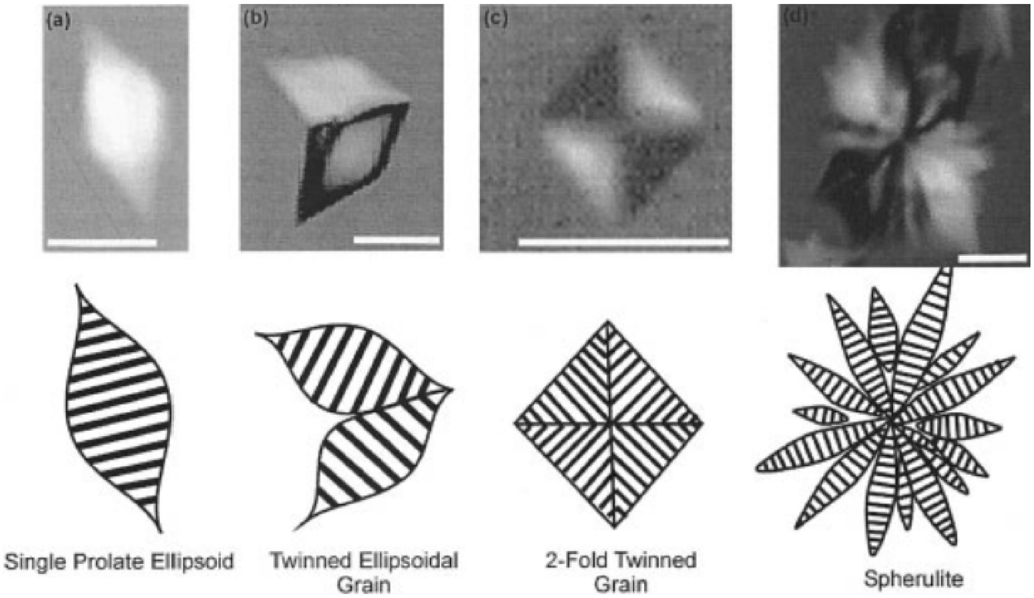

Figure 5.2: Defect-containing nuclei observed by Chastek *et al.* Figure adapted from [17].

Important experimental investigations include the work of Bates *et al.*, who first verified the first-order character of the dis→lam transition [13, 190–192]; a more recent verification for short diblock copolymers was presented by Lee *et al.* [193]. Their work [192] and several subsequent experiments [194–197] presented evidence that the dis→lam transition for a quenched disordered phase occurred via nucleation and growth of anisotropic, roughly ellipsoidal ordered grains. Balsara *et al.* [15], using the surface tension derived by Milner and Morse and an analytic Wulff construction [198, 199], predicted that these grains would have an aspect ratio (length/width) of roughly 2.37. He then experimentally observed the formation of lamellar grains from a disordered diblock melt, finding average aspect ratios of roughly 2.0 for short annealing times and 1.5 for longer annealing times. However, a broad range of droplet shapes and aspect ratios were observed. Chastek *et al.* [17] prepared a metastable solution of diblock copolymer and observed the formation of anisotropic ellipsoidal grains along with variety of other interesting structures, including twinned ellipsoids, 2-fold twinned grains, and spherulites (Figure 5.2). Other recent experiments have demonstrated the formation of anisotropic ordered grains in emulsions containing droplets of diblock copolymer [200, 201].

From a computational perspective, the dis→lam transition has been investigated using a wide variety of simulation techniques, including SCFT with complex Langevin dynamics [94, 202–204], SCFT with partial saddle point Monte Carlo [205], lattice Monte Carlo [206, 207], off-lattice Monte Carlo [164, 208, 209], single-chain-in-mean-field simulations [210], dissipative particle dynamics [211–213], and molecular dynamics [111, 214]. The qualitative consensus is that as long as the simulation incorporates fluctuations in some way, the dis→lam transition appears first-order, and takes place at a lower temperature than that predicted by mean field theory.

Other important studies of the Landau-Brazovskii model specifically include the work of Wickham, Shi, and Wang [198], who used the model to investigate the cylinder→lamellar transition of a diblock copolymer melt. They devised a single-mode approximation analysis that enabled them to predict surface tension anisotropy, critical nucleus shape, and critical nucleus size, finding flattened, lens-shaped critical nuclei. Wright and Wickham [128] and Spencer and Wickham [215] simulated the growth of lamellar nuclei from a metastable cylinder phase, again finding that the system favored flattened ellipsoidal nuclei, whose sizes showed good agreement with the single mode approximation. Spencer also found that nuclei grew with different velocities along different axes such that the overall shape of the growing nucleus was preserved. Spencer [216] simulated the disorder→body-centered-cubic (BCC) transition with explicit fluctuations, finding that fluctuations caused an intermediate disordered micelle morphology to form between the disordered and BCC phases. Shi [217] constructed a mean-field phase diagram that considered all of the model's accessible Fourier modes, using Gaussian fluctuation theory to locate order-order spinodals. Lin *et al.* [187] used the string method to find energy barriers for the lamellar→sphere and cylinder→sphere transition of the Brazovskii model. Hashimoto *et al.* [196] performed exploratory 2-dimensional Langevin simulations of the Fredrickson and Binder's renormalized Brazovskii model, and observed the formation of elliptic nuclei, but made no systematic attempt to quantify this result. Gross *et al.* [106] simulated the fluctuating Landau-Brazovskii model near the dis→lam ODT for a wide range of relative noise strengths, finding that the Fredrickson-Helfand analysis made good quantitative predictions for the renormalized structure factor. They observed disordered phases that did not appear to be metastable: For all tested quenches deep enough that the lamellar phase was stable, a system initialized in the disordered phase would spontaneously (albeit slowly) develop ordered domains that eventually consumed the simulation cell. However, their simulation parameters were not connected to the physical parameters of a diblock melt, and they admitted the possibility of a metastable disordered phase at different parameters. (Also, in the calculations we present here, the window in which we observe metastable disorder is relatively narrow, and can only be isolated by a fine, gradual variation of the quench depth. It is possible that Gross' calculations used quench depth steps that were too large, and jumped over the narrow window.)

Despite all this attention, to our knowledge no systematic computational attempt has been made to clarify the specific mechanism of the dis→lam transition for diblock copolymers. An interesting recent study by Medapuram *et al.* [111] used well-tempered metadynamics and a 1-dimensional global order parameter to extract a free energy barrier between a metastable disordered phase and a stable lamellar phase in molecular dynamics simulations; however, this calculation did not provide insight as to how the transition physically took place. In this work, we use the string method applied to the renormalized Brazovksii model of

Fredrickson and Binder (FRB) to predict the critical nuclei for this transition, and conduct a thorough search for several predicted and observed defect structures. We use parameters explicitly connected to those of an experimentally accessible diblock copolymer melt. For defect-free nuclei, we find good agreement with the results of a single-mode analysis similar to that of [198]. We evaluate our results by simulating the bare Brazovksii model with explicit fluctuations, finding that the FRB model makes reasonable predictions for both the renormalized structure factor and the renormalized ODT. However, the critical nucleus size depends sharply on proximity to the ODT, so even moderate errors in the predicted ODT lead to large errors in predicted critical nucleus size. We conclude that the FRB model is a poor tool to study the dis→lam transition at experimentally accessible parameters, and recommend several directions for future study.

5.2 Predicting critical nucleus size and shape

We seek a window of parameter space where the critical nucleus is big enough to demonstrate interesting structure (including defects, potentially) but small enough that the string method can feasibly be applied (bearing in mind that according to [187], the simulation cell should be at least twice the size of the critical nucleus to avoid artificial compression effects). To find this window, it is useful to develop an approximate analytic prediction of the critical nucleus size. This can be accomplished using classical nucleation theory (CNT), as outlined in Section 2.1.4, following the procedure of Ref. [198]. Three ingredients are required: an estimate of the difference in free energy densities of lamellar and disordered phases $\Delta f = f_{DIS} - f_{LAM}$, an estimate of the (orientation-dependent) surface tension for a planar interface between coexisting lamellar and disordered phases σ, and an estimate of the nucleus shape. The first two can be estimated within the single-mode approximation, and the shape can be found from a Wulff construction. The analysis relies on several approximations, including that the nucleus is large enough for its free energy to be written as the sum of bulk and interfacial terms. Again, the intended purpose of this analysis is only to locate a promising window of parameter space, but we find that the single-mode analysis makes good predictions for the size, shape, and free energy of critical nuclei found by the string method, even outside the regime where those approximations are rigorously valid.

We begin with the renormalized FRB free energy functional, with intensive free energy

$$f = \frac{\beta H_{eff}}{V} = \frac{1}{V}\int d\mathbf{r}\left\{\frac{e}{2}\left[(\nabla^2 + q_0^2)\bar{\phi}\right]^2 + \frac{\tau_R}{2}\bar{\phi}^2 + \frac{u_R}{4!}\bar{\phi}^4 + \frac{w_R}{6!}\bar{\phi}^2\right\} \quad . \tag{5.1}$$

The first step is to find $\Delta f = f_{DIS} - f_{LAM}$. $f_{DIS} = 0$, and f_{LAM} is given according to (2.109) by

$$f_{LAM} = \tau_R A^2 + \frac{u_R}{4} A^4 + \frac{w_R}{36} A^6 \quad , \quad A^2 = -3\bar{u}_R + \sqrt{3}\sqrt{3\bar{u}_R^2 - 4\bar{\tau}_R} \tag{5.2}$$

where $\bar{e} \equiv e/w_R$, $\bar{\tau}_R \equiv \tau_R/w_R$, $\bar{u}_R \equiv u_R/w_R$.

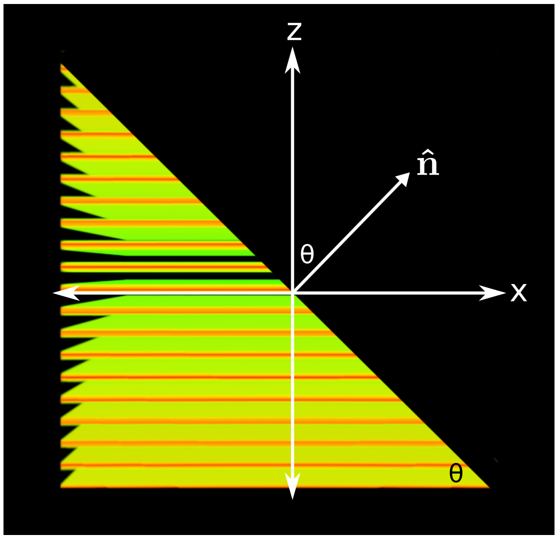

Figure 5.3: Slice geometry for single-mode analysis, viewed along the y-axis. Lamellae are parallel to the xy-plane.

The next step is to determine the free energy per unit area of a planar lamellar-disorder interface (this assumes critical nuclei are large enough that the interface is locally roughly planar). We consider lamellar planes parallel to the xy plane and an interface with unit normal $\hat{\mathbf{n}}$ passing through the origin, as in Figure 5.3. σ will depend on the slice angle θ. Because the lamellae have cylindrical symmetry about the z-axis, we may assume $\hat{n}_y = 0$ so that $\hat{\mathbf{n}} = (\sin\theta, 0, \cos\theta)$. Within the single-mode approximation, the interface-containing configuration is

$$\bar{\phi}(\mathbf{r}) = 2\,a(\mathbf{r}\cdot\hat{\mathbf{n}})\cos(q_0\,\hat{\mathbf{z}}\cdot\mathbf{r}) = 2\,a(s)\cos(q_0\,\hat{\mathbf{z}}\cdot\mathbf{r}) \tag{5.3}$$

where $a(s)$ is a modulating function that varies from 1 at $-\infty$ to 0 at $+\infty$ and $s = \mathbf{r}\cdot\hat{\mathbf{n}}$ is the distance from the interface. Let f_i represent the intensive free energy of the interface-containing configuration. Plugging (5.3) into (5.1) and averaging over one lamellar period (which assumes that a varies slowly on the scale of one lamellar period) we find after some algebra

$$f_i = \frac{1}{V}\int d\mathbf{r}\left\{e\,(\nabla^2 a)^2 + 4\,e\,q_0^2\,(\hat{\mathbf{z}}\cdot\nabla a)^2 + \tau_R\,a^2 + \frac{u_R}{4}a^4 + \frac{w_R}{36}a^6\right\}\ . \tag{5.4}$$

However, a depends only on the distance from the interface $s = \mathbf{r}\cdot\hat{\mathbf{n}}$. Following [198], the interfacial free energy per unit area $\tilde{f}_i$ for a planar interface with unit normal $\hat{\mathbf{n}}$ is then

$$\begin{aligned}\tilde{f}_i &= \int ds\left\{e\,a''(s)^2 + 4\,e\,q_0^2\,(\hat{\mathbf{z}}\cdot\hat{\mathbf{n}})^2 a'(s)^2 + \tau_R\,a(s)^2 + \frac{u_R}{4}a(s)^4 + \frac{w_R}{36}a(s)^6\right\}\\ &= w_R\int ds\left\{\bar{e}\,(a'')^2 + 4\,\bar{e}\,q_0^2\,\cos^2\theta\,(a')^2 + \bar{\tau}_R\,a^2 + \frac{\bar{u}_R}{4}a^4 + \frac{1}{36}a^6\right\}\end{aligned} \tag{5.5}$$

According to [198], we make two final approximations: First, to find σ for a given set of parameters (τ_R, u_R, w_R), we calculate $\tilde{f}_i$ *at coexistence* where $f_{LAM} = f_{DIS} = 0$ (in other words at the renormalized model's ODT), and assume that σ near the ODT can be approximated by σ at the ODT. For a given τ_R, the condition for the ODT is $\bar{\tau}_R/\bar{u}_R^2 = 9/16$, and the preferred amplitude at the ODT is $A_{ODT}^2 = -3\bar{u}_R + \sqrt{3}\sqrt{3\bar{u}_R^2 - 4\bar{\tau}_R} = |\bar{u}_R|(3 + \sqrt{9 - 12 \cdot 9/16}) \equiv |\bar{u}_R|\tilde{A}^2$ (since $\bar{u}_R < 0$). Also, this means that the excess free energy due to the interface's presence is $\tilde{f}_i - f_{DIS} = \tilde{f}_i$. Second, we assume a variational ansatz for $a(s)$:

$$a(s) = \frac{A_{ODT}}{2}\left[1 - h\left(\frac{s}{w}\right)\right] = \frac{\tilde{A}\sqrt{|\bar{u}_R|}}{2}\left[1 - h\left(\frac{s}{w}\right)\right] \tag{5.6}$$

where $h(u) = \tanh u$ and w sets the length scale of the interface (w is not to be confused with w_R, which is a parameter of the renormalized model). To find $\sigma(\theta)$ we plug (5.6) into (5.5), then minimize with respect to w.

$$\begin{aligned}
\tilde{f}_i = w_R \int ds \Bigg\{ &\bar{e}\,\frac{|\bar{u}_R|\tilde{A}^2}{4}\frac{h''(s/w)^2}{w^4} + 4\,\bar{e}\,q_0^2\,\cos^2\theta\,\frac{|\bar{u}_R|\tilde{A}^2}{4}\frac{h'(s/w)^2}{w} + \qquad (5.7)\\
&\bar{\tau}_R\,\frac{|\bar{u}_R|\tilde{A}^2}{4}\left[1 - h\left(\frac{s}{w}\right)\right]^2 + \frac{\bar{u}_R}{4}\frac{|\bar{u}_R|^2\tilde{A}^4}{4}\left[1 - h\left(\frac{s}{w}\right)\right]^4 + \frac{1}{36}\frac{|\bar{u}_R|^3\tilde{A}^6}{4}\left[1 - h\left(\frac{s}{w}\right)\right]^6 \Bigg\}\\
= w_R \Bigg[&e\,|\bar{u}_R|\frac{\tilde{A}^2}{4}\cdot\frac{1}{w^3}\int h''(u)^2\,du + \bar{e}\,q_0^2\cos^2\theta\,|\bar{u}_R|\tilde{A}^2\cdot\frac{1}{w}\int h'(u)^2\,du \qquad (5.8)\\
&+ w\int du\left\{\bar{\tau}_R\,\frac{|\bar{u}_R|\tilde{A}^2}{4}[1 - h(u)]^2 + \frac{\bar{u}_R}{4}\frac{|\bar{u}_R|^2\tilde{A}^4}{16}[1 - h(u)]^4 + \frac{1}{36}\frac{|\bar{u}_R|^3\tilde{A}^6}{64}[1 - h(u)]^6\right\}\Bigg]
\end{aligned}$$

Recalling that we are working at coexistence so that $\bar{\tau}_R/\bar{u}_R^2 = 9/16$, and that $\bar{u}_R < 0$ so that $|\bar{u}_R| = -\bar{u}_R$, (5.7) can be rewritten

$$\begin{aligned}
\tilde{f}_i &= w_R\Bigg[-\frac{\bar{e}\,\bar{u}_R}{w^3}\,g_1 - \frac{\bar{e}\,q_0^2\,\bar{u}_R}{w}\,g_2 + w\,\bar{u}_R^3\,g_3\Bigg] \qquad \text{, where} \qquad (5.9)\\
g_1 &= \frac{\tilde{A}^2}{4}\int_{-\infty}^{\infty} h''(u)^2\,du \ , \quad g_2 = \tilde{A}^2\cos^2\theta\int_{-\infty}^{\infty} h'(u)^2\,du \ ,\\
g_3 &= \int_{-\infty}^{\infty} du\,\Bigg\{-\frac{9}{16}\frac{\tilde{A}^2}{4}[1-h(u)]^2 + \frac{\tilde{A}^4}{64}[1-h(u)]^4 - \frac{1}{36}\frac{\tilde{A}^6}{64}[1-h(u)]^6\Bigg\}
\end{aligned}$$

Plugging in $h(u) = \tanh u$ and $\tilde{A}^2 = (3+\sqrt{9-12\cdot 9/16}) = 9/2$, we find

$$g_1 = \frac{1}{4}\cdot\frac{9}{2}\cdot\frac{16}{15} = \frac{6}{5} \ , \quad g_2 = \frac{9}{2}\cos^2\theta\cdot\frac{4}{3} = 6\cos^2\theta \ , \quad g_3 = -\frac{621}{1280} \ . \tag{5.10}$$

To find the optimal interfacial width w^* within the tanh ansatz for $a(s)$ we minimize (5.9) with respect to w. The result is

$$(w^*)^2 = \frac{-\bar{e}\,q_0^2\,g_2 - \sqrt{\bar{e}^2\,q_0^4\,g_2^2 - 12\,\bar{e}\,\bar{u}_R^2\,g_1\,g_3}}{2\,\bar{u}_R^2\,g_3} \tag{5.11}$$

The approximate surface tension is $\tilde{f}_i$ evaluated at the optimal width w^*.

$$\sigma(\theta) = w_R\Bigg[-\frac{\bar{e}\,\bar{u}_R}{(w^*)^3}\,g_1 - \frac{\bar{e}\,q_0^2\,\bar{u}_R}{w^*}\,g_2 + w^*\,\bar{u}_R^3\,g_3\Bigg] \tag{5.12}$$

The θ dependence is carried by $g_2 = 6\cos^2\theta$. Since $u_R < 0$ and $w_R > 0$, it appears σ has a maximum at $\theta = 0$ and a minimum at $\theta = \pi/2$, indicating that interfaces parallel to lamellar planes are energetically unfavorable and interfaces normal to lamellar planes are favorable (Fig. 5.4).

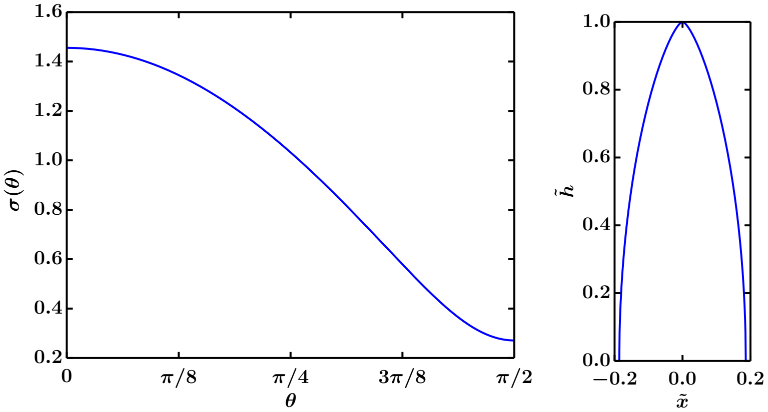

Figure 5.4: Left panel: $\sigma(\theta)$ at $\tau = -3.0$, $\bar{N} = 10^4$ (for which $(\tau_R, u_R, w_R) = (0.332, -0.709, 0.704)$). σ is maximal at $\theta = 0$ and minimal at $\theta = \pi/2$, indicating that the system prefers interfaces normal to lamellar planes. Right panel: Predicted interfacial profile in the xz-plane $\tilde{h}(\tilde{x})$ for a droplet at these parameters. Lamellae are parallel to the x-axis. The droplet is highly anisotropic to minimize area of interfaces parallel to lamellae.

The next step of the single-mode analysis is to determine the droplet shape using a Wulff construction applied to $\sigma(\theta)$. The Wulff construction minimizes the surface free energy of a droplet subject to a constraint of constant volume. Details can be found in [199]. The essential result, as described in [198], is the following: Let the droplet be characterized by its height above the xy-plane $h(\mathbf{x}_\perp)$,

$\mathbf{x}_\perp = (x, y)$. The optimal height is given by

$$\tilde{h}(\tilde{\mathbf{x}}_\perp) = [\tilde{g}(\mathbf{m}) + \mathbf{m} \cdot \tilde{\mathbf{x}}_\perp]_{\min \mathbf{m}} \ \text{, where} \tag{5.13}$$
$$\tilde{h} = \frac{h}{L}, \ \ \tilde{\mathbf{x}}_\perp = \frac{\mathbf{x}_\perp}{L}, \ \ \mathbf{m} = \nabla_\perp h_0, \ \ \tilde{g}(\mathbf{m}) = (1 + \mathbf{m})^{1/2} \frac{\sigma[\theta(\mathbf{m})]}{\sigma_{\max}} \ .$$

$\sigma_{\max} = \sigma(\pi/2)$ is the maximum surface tension, and L is a length scale set by the volume of the droplet. $\mathbf{m}$, the slope of the nucleus, is a variable to be minimized over. The lamellar nucleus has cylindrical symmetry, so it is sufficient to find $h(x)$ in the $y = 0$ plane and rotate about the z-axis. In the $y = 0$ plane, $\mathbf{m} = \nabla_\perp h = \left(\frac{dh}{dx}, 0\right) = (m_x, 0)$ and $g_2 = 6 \cos^2(\arctan m_x) = 1/(1 + m_x^2)$, so $\sigma[\theta(\mathbf{m})]$ is expressed in terms of m_x alone. Minimization of (5.13) over m_x is performed numerically; working directly with $\tilde{\mathbf{x}}_\perp$ and $\tilde{h}$ yields a droplet shape where the half-length $\tilde{l}/2$ along the droplet's long axis is 1 (Fig. 5.4). The aspect ratio of the nucleus is $\sigma(\pi/2)/\sigma(0)$, so the half-width $\tilde{d}/2$ of this droplet along the x-axis is $\sigma(\pi/2)/\sigma(0)$.

Finally, using $\sigma(\theta)$ and the droplet shape, we can compute the critical nucleus size using CNT. The droplet shape $\tilde{h}(\tilde{x})$ found via the Wulff construction is the optimal nucleus shape in units where $l/2 = 1$. First, we compute the surface energy $\tilde{S}_1$ for a nucleus of half-length 1 using $\sigma(\theta)$ and an integral over the droplet's surface (which in practice is discretized as a Riemann sum):

$$S_1 = 2 \int_0^{\tilde{d}/2} 2\pi\, \tilde{x}\, \sigma[\theta(\tilde{h}'(\tilde{x}))]\, \sqrt{1 + \tilde{h}'(\tilde{x})^2}\, d\tilde{x} \tag{5.14}$$

We also compute the volume V_1 for the nucleus of half-length 1 with a Riemann sum:

$$V_1 = 2 \int_0^{\tilde{d}/2} 2\pi\, \tilde{x}\, \tilde{h}(\tilde{x})\, d\tilde{x} \tag{5.15}$$

The surface energy and volume for a nucleus of half-length $l/2$ in model units are then $S_1\,(l/2)^2$ and $V_1\,(l/2)^3$, respectively, as shown in [198]. The total extensive free energy of the nucleus is given by CNT (2.21) as

$$\beta F_n(l) = -V_1\, \Delta f\, (l/2)^3 + S_1\, (l/2)^2 \quad . \tag{5.16}$$

Although S_1 in the preceding analysis is computed at the lamellar-disorder phase boundary and assumed not to vary significantly (that is, held fixed) for parameters away from the phase boundary, Δf in the above expression is allowed to vary, and is computed directly in terms of τ_R, u_R, w_R according to (5.2). Maximizing (5.16) with respect to $l/2$ yields the half-length for the critical nucleus at a given set of renormalized parameters τ_R, u_R, w_R:

$$l_{crit}/2 = \frac{2S_1}{3V_1\,\Delta f} \tag{5.17}$$

The free energy of the critical nucleus is then $\beta F_n(l_{crit})$.

To expose the connection to parameters of a diblock melt, our later results are presented in terms of the bare τ, or equivalently, in terms of χN, which is linearly related to the bare τ. To estimate the critical nucleus size and free energy at a given bare τ, first we compute renormalized parameters τ_R, u_R, w_R at τ (assuming $\bar{N} = 10^4$) using (2.108), then follow the above analysis ending at (5.17).

Figure 5.9 shows the long-axis length l, width d, and extensive free energy βF of critical nuclei as obtained from the single-mode analysis, along with those quantities as extracted from critical nuclei obtained by the string method. Good agreement is observed even for relatively small nuclei, for which the assumptions of the single mode analysis are not strictly valid.

To aid physical intuition, the length and width are presented in units of lamellar periods. However, (5.17) gives a result in model units, in which a lamellar period has length $2\pi/q_0$. Therefore , to present the results in Figure 5.9, we divide l_{crit} from (5.17) by $2\pi/q_0$.

5.3 String calculations on the renormalized model

5.3.1 Defect-free nuclei

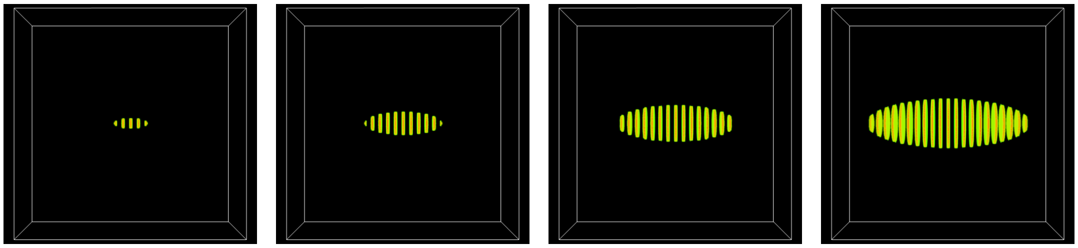

Figure 5.5: Initialization method used to search for defect-free critical nuclei.

In the bare Landau-Brazovskii model, the dis→lam transition is second-order at the mean-field level, therefore there is no region of metastable disorder and no energy barrier for the dis→lam transition. Since the zero-temperature string method is a mean-field technique, it cannot find barriers or critical nuclei for this transition in the bare model. In the renormalized Brazovskii model of Fredrickson and Binder, however, the dis→lam transition is first-order; a metastable region of disorder exists and the zero-temperature string method can be applied. The single-mode analysis suggests that for $\bar{N} = 10^4$, $\tau \leq -3.0$ is a feasible regime in which to find critical nuclei that are large enough to exhibit interesting structure but small enough to tackle with the string method.

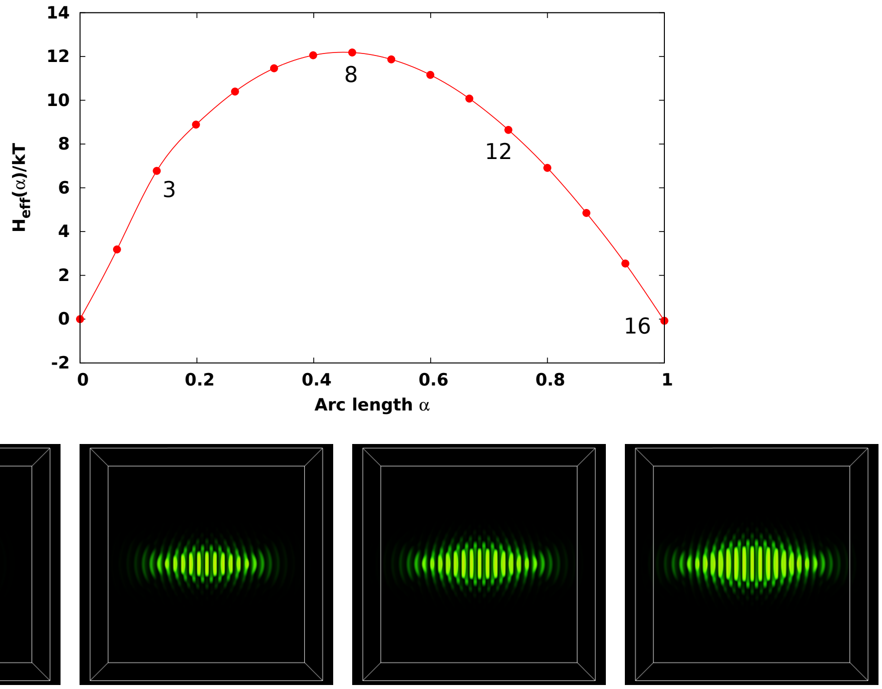

3 8 12 16

Figure 5.6: Converged MEP for the string initialized with concentric ellipses (Figure 5.5) at $\tau = -3.0$. Upper panel: $H_{eff}(\alpha)/kT$ along the converged pathway. Selected images along the string are labelled and shown in the lower row.

We begin by searching for defect-free nuclei in the renormalized model. Images are initialized as concentric ellipses with aspect ratios of $d/l = 0.3$ (Fig. 5.5). Anticipating the anisotropy of converged critical nuclei this way significantly reduces the string method's convergence time. To economize on the number of required images, we use truncation-based energy weighting with $E_C = 0$, which focuses all images within the barrier region. Strings with $N = 16$ images are used. Smaller numbers of images (down to $N = 10$) were also tested; this was found to have negligible effect on the converged barrier. It should be emphasized that without

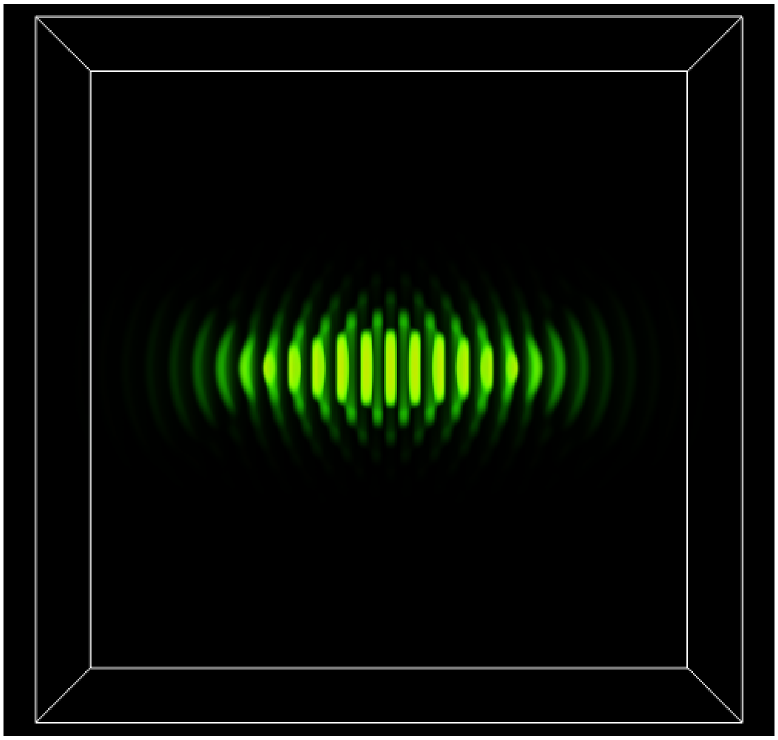

Figure 5.7: Zoomed-in view of the critical nucleus at $\tau = -3.0$, corresponding to the image labelled 8 in Figure 5.6.

either truncation-based energy weighting or a technique like the fixed arc length string method [75], a computationally intractable number of images would be required to resolve the barrier region, even with an aggressive conventional energy weighting scheme. We use simulation cells of size $28 \times 28 \times 10$ lamellar periods with a resolution of $196 \times 196 \times 70$ (7 grid points per lamellar period), which is sufficient to capture the free energy accurately (≈ 7 grid points per period was also used in [215]).

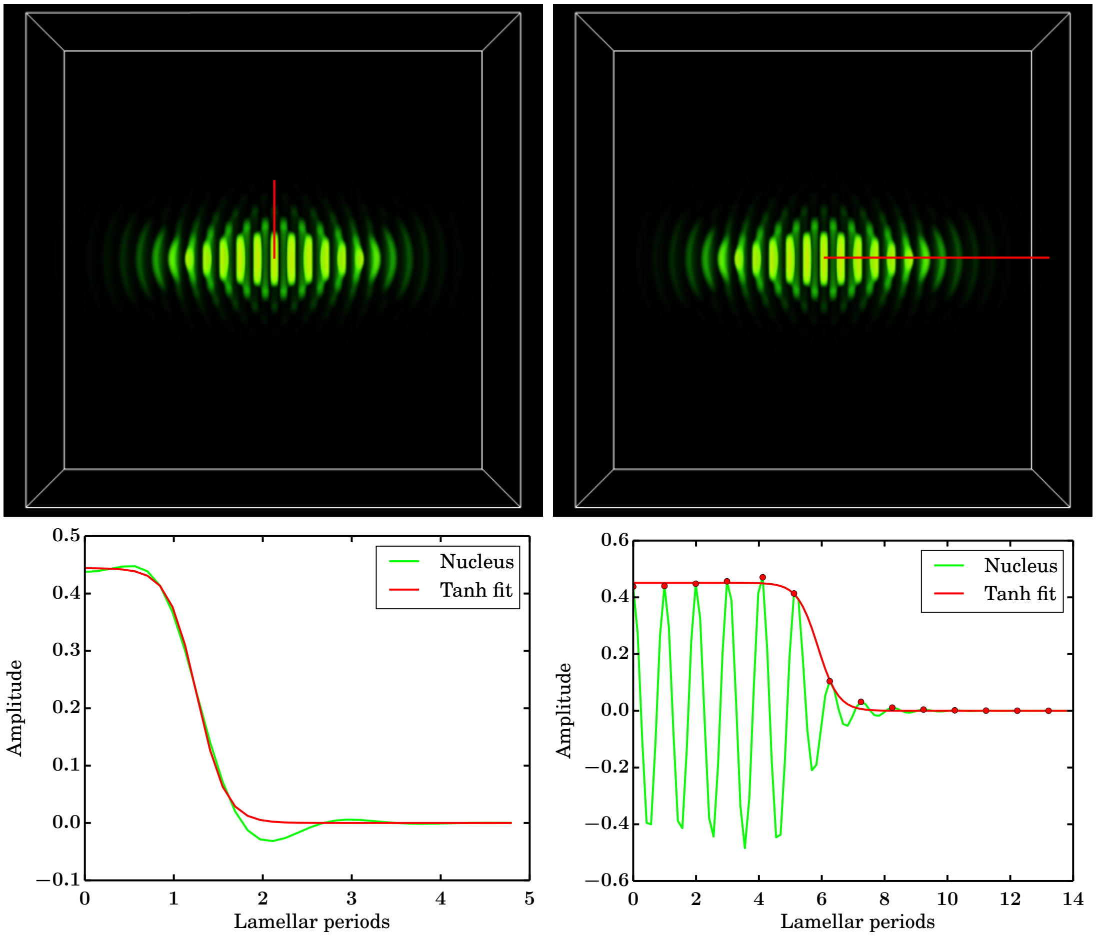

Figure 5.8: Left panels: Fitting method used to extract width of defect-free nuclei. A function of the form $A \tanh\left[\frac{x-d/2}{w_r}\right]$ is fitted to the nucleus' amplitude across the central lamella (red slice in upper panel) to extract the lateral half-width $d/2$ and the interfacial width w_r (A is also left free as a fit parameter). Right panels: Fitting method used to extract length of defect-free nuclei. A function of the form $A \tanh\left[\frac{x-l/2}{w_l}\right]$ is fitted to the nucleus' amplitude peaks (red dots) along its long axis (red slice, upper panel) to extract the half-length $l/2$ and the interfacial width w_l.

We converge defect-free MEPs for $\tau = -3.2$, -3.15, -3.1, -3.15, and -3.0 (in the region suggested by the single mode analysis). The result for $\tau = -3.0$ is shown

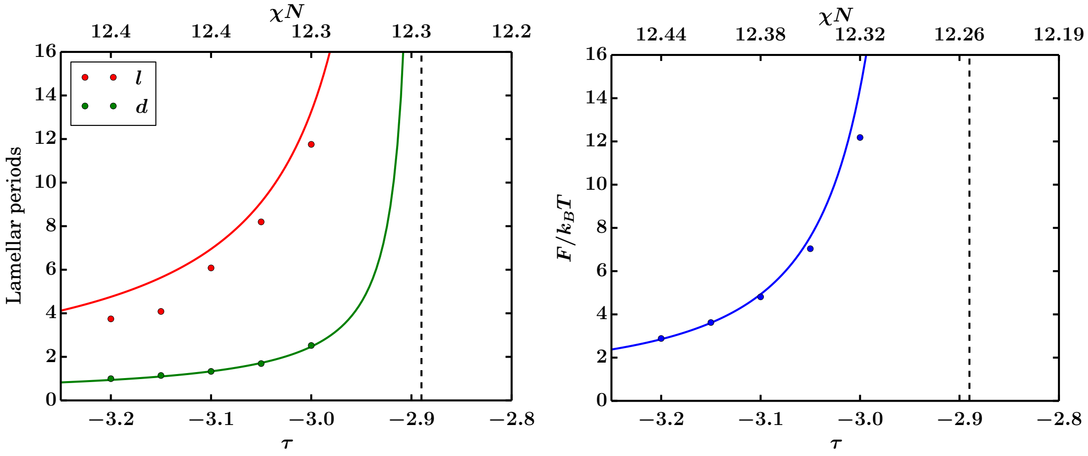

Figure 5.9: Left panel: Comparison of the major-axis lengths (l) and minor-axis diameters (d) extracted by the fitting procedure, alongside the predictions of the single mode approximation (continuous curves). Right panel: free energies of critical nuclei obtained by the string method (dots), alongside the prediction of the single mode analysis (continuous curve). The single mode analysis' predictions are surprisingly accurate even for small nuclei, where its underlyings approximations are not valid. The vertical dotted line at $\tau = -2.89$ is the ODT predicted for the FRB model with $\bar{N} = 10^4$.

in Figure 5.6. A zoom of the corresponding critical nucleus (Image 8) is shown in Figure 5.7. The nucleus appears highly anisotropic, as expected, displaying diffuse “caps” at the long-axis endpoints.

We apply a fitting procedure to extract trends of nucleus size and shape with varying τ. For quantitative comparison with the single-mode analysis, the fit function also assumes the lamellar structure is modulated by a tanh function with characteristic width along the long axis and radial (minor) axis, as shown in Figure 5.8. Results of the fitting procedure, along with free energies of critical nuclei and corresponding quantities computed by the single mode analysis, are shown in Figure 5.9.

5.3.2 A search for nuclei containing defects

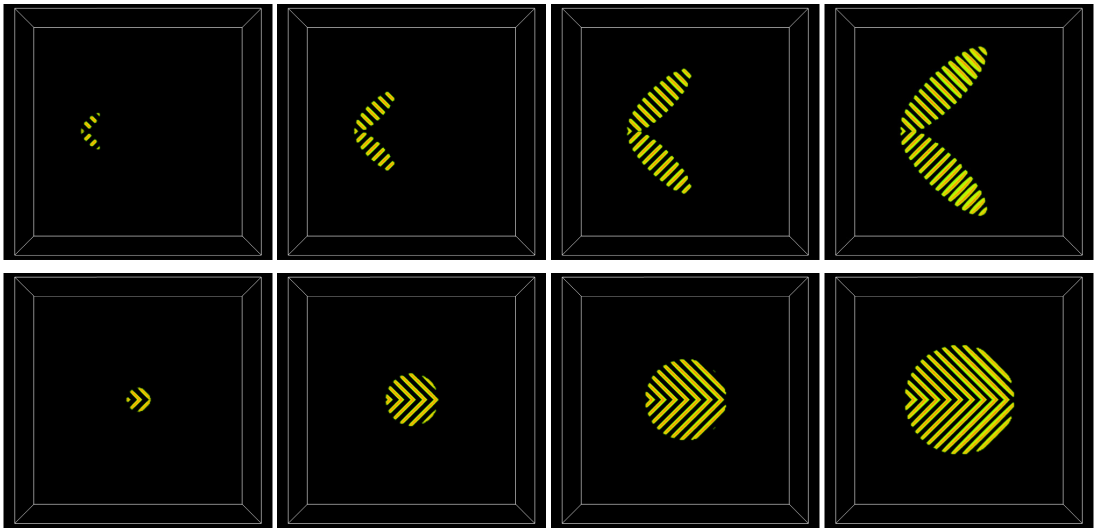

Figure 5.10: Selected images along the strings initialized to search for twinned nuclei, or nuclei containing grain boundaries. The upper row depicts twinned nuclei initialized as ellipsoids with gradually increasing size from a fixed join point in space; we also tested a method where the join point gradually moved outward from the center of the simulation cell as the ellipsoids' size increased (not shown). For each of the three methods, we test strings initialized at seven different slice angles: $\theta = \pi/16$, $\pi/8$, $3\pi/16$, $\pi/4$, $5\pi/16$, $3\pi/8$, and $\pi/2$ (11.25°, 22.5°, 45°, 56.25°, 67.5°, 78.75°, and 90°). The examples above are for $\theta = \pi/4$ (90°).

Having located a regime where relatively large critical nuclei can be found using the string method, we proceed to conduct a comprehensive search for various predicted and experimentally observed defect structures. Leveraging the fact that

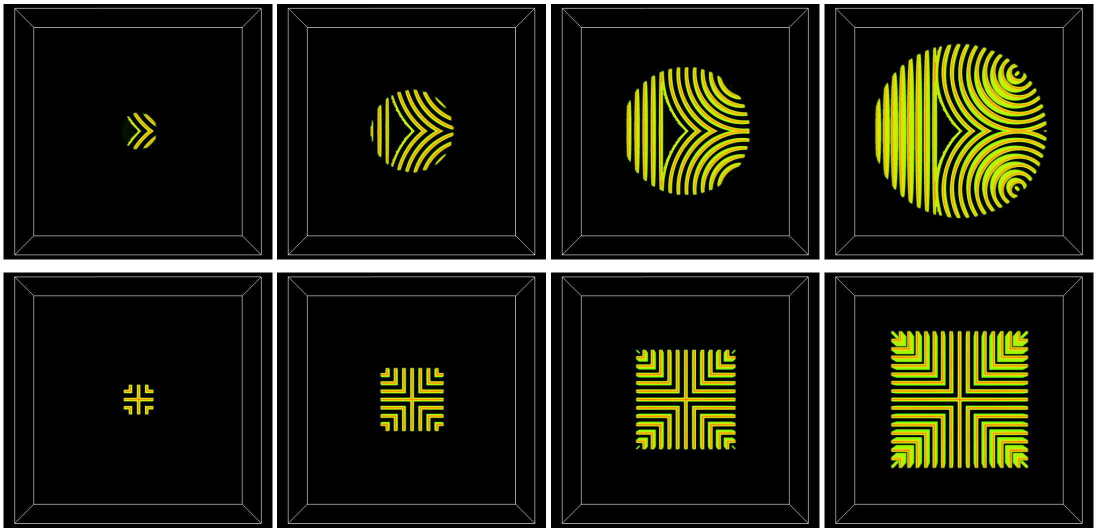

Figure 5.11: Selected images along the strings initialized to search for nuclei containing focal conic defect pairs (upper row) and 4-fold twinned nuclei (lower row). For the focal conic defect pairs, the displayed initialization pathway corresponds to placing the defect core at $r = 10$ lamellar periods from the center of the initialized area; we also test pathways with $r = 8$, $r = 6$, and $r = 4$. For the 4-fold twinned nuclei, we test 4 initialization pathways, in which the initialized rectangular prisms have depth to width ratios of 0.4 (shown), 0.6, 0.8, and 1.0 (cubes). The simulation cell is adjusted to compensate: $28 \times 28 \times 12$ lamellar periods for 0.4, $24 \times 24 \times 20$ for 0.6 and 0.8, and $22 \times 22 \times 22$ for 1.0.

the string method converges to a local MEP dependent on its initialization, we search for MEPs with defect-containing critical nuclei by initializing strings with structures similar to the expected defects. Anticipating that only large critical nuclei will successfully retain defects, we concentrate our efforts on $\tau = -3.0$.

We test a library of initialization methods with various seeded defect structures, including twinned nuclei at various angles and nuclei with grain boundaries at various angles as observed in [17] (Fig. 5.10), nuclei containing 4-fold twinned nuclei as observed in [17] (Fig. 5.10, lower row), and nuclei containing focal conic defects similar to those predicted by [16]. In all cases $N = 16$ images and truncation-based energy weighting with $E_C = 0$ are used. For all but the 4-fold twinned nuclei, a simulation cell of dimension 28 × 28 × 10 lamellar periods is used. Dimensions for the 4-fold twinned simulation cells are given in Figure 5.11.

None of the tested initialization methods result in a stable MEP with morphologies containing defect structures. Ultimately, all seeded initialized pathways find their way back to an MEP whose barrier state is a defect-free nucleus. However, one interesting effect is observed for the twinned nuclei. If twinned nuclei are initialized at a relative angle $\geq\approx 78.75°$, the string finds a long-lived intermediate-time path showing twinned nuclei. At first this appears to be a stable MEP, but it turns out to be stabilized by symmetry; eventually, the system spontaneously chooses to grow along one twinned lobe, as shown in Figure 5.12. For twinned nuclei initialized with a relative angle $\leq\approx 67.5°$, a long-lived symmetry-stabilized path is not observed during the string's convergence; instead, the two lobes zipper together in a gradual, continuous motion as the calcuation proceeds, resulting in a converged defect-free nucleus lying somewhere between the two lobes (Figure 5.13).

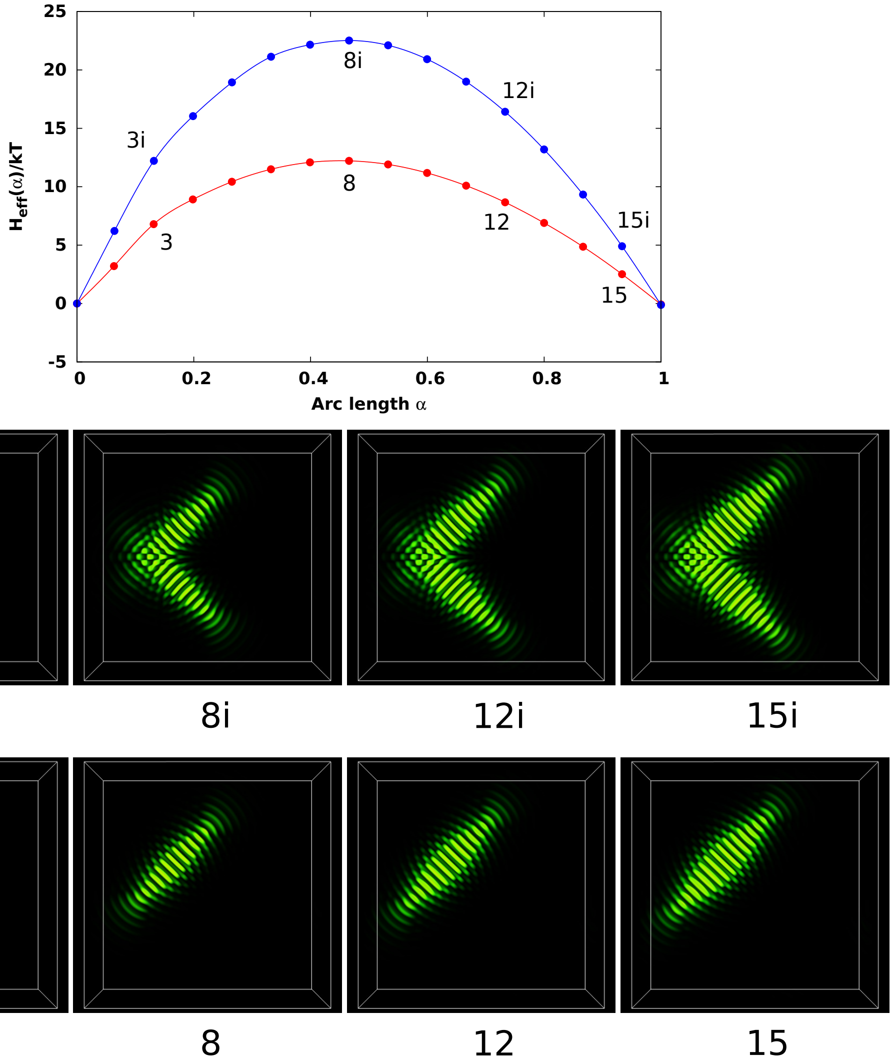

Figure 5.12: Converged and intermediate-time MEPs for the string initialized with twinned ellipses growing from a fixed join point (Figure 5.10, upper row) with join angle $\theta = 90°$ at $\tau = -3.0$. Upper panel: $H_{eff}(\alpha)/kT$ along the converged MEP (red) and long-lived symmetry-stabilized intermediate path (blue). Selected images along each string are shown in the lower two rows. The nuclei along the converged pathway are tilted because the system spontaneously chooses one of the twinned lobes along which to grow; the other lobe shrinks and is absorbed. The nuclei are defect-free, and the energy barrier is essentially identical to that of Figure 5.6.

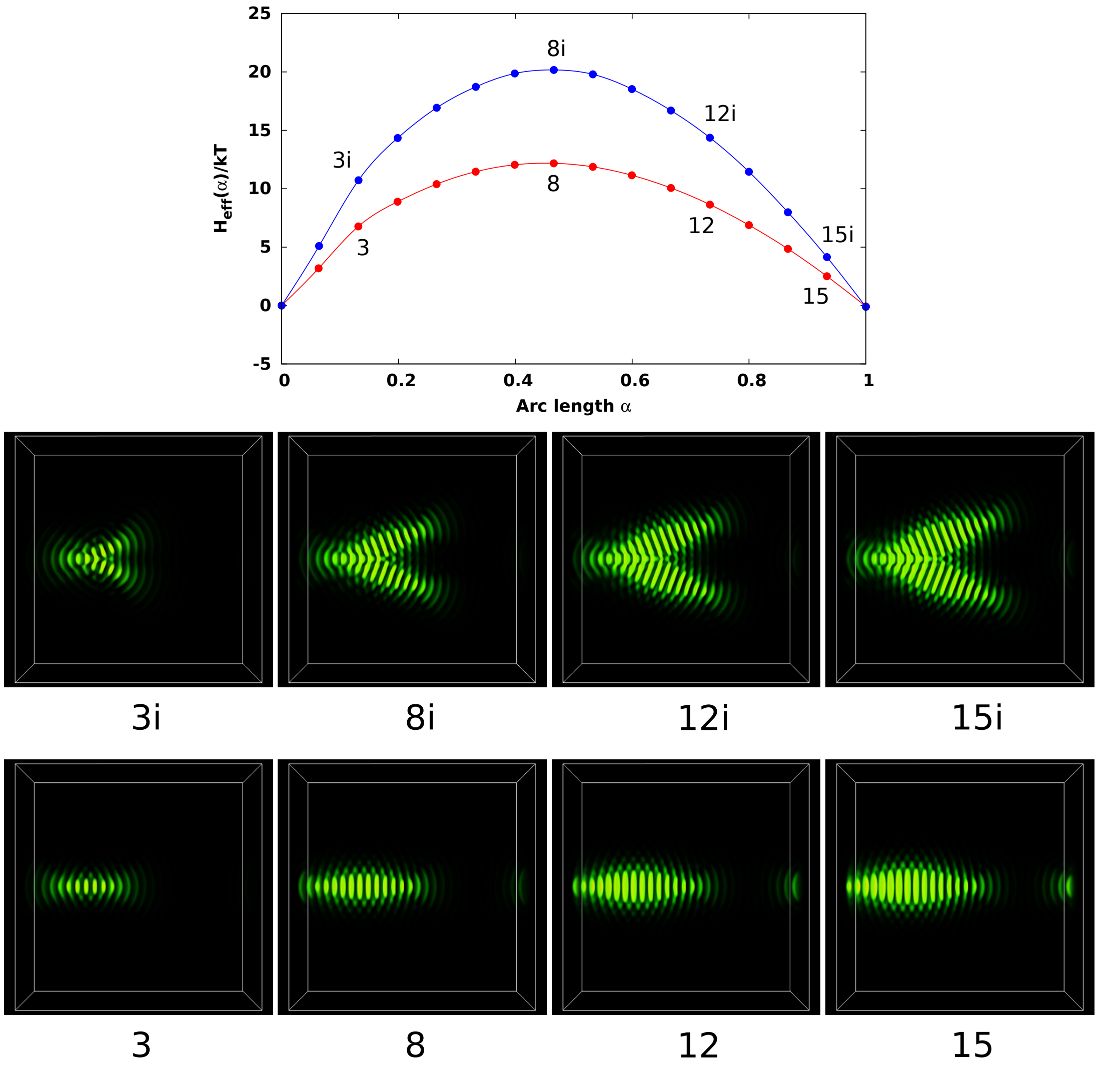

Figure 5.13: Converged and intermediate-time MEPs for the string initialized with twinned ellipses growing from a fixed join point (Figure 5.10, upper row) with join angle $\theta = 56.25°$ at $\tau = -3.0$. Upper panel: $H_{eff}(\alpha)/kT$ along the converged MEP (red) and along the string at an intermediate point during the calculation (blue). Selected images along each string are shown in the lower row. For this join angle, a long-lived symmetry-stabilized string is not observed. Instead, the two lobes deform continuously into a single lobe through a scissor-like motion as the calculation proceeds. Once again, nuclei along the converged string are defect-free, and the energy barrier is essentially identical to that of Figure 5.6.

5.4 Exploring the fluctuating bare model

We would like to evaluate how well critical nuclei obtained from a mean-field string method treatment of the renormalized FRB model (2.107) predict critical nuclei in the bare Brazovskii model (2.106) with explicit fluctuations. As a preliminary step, we perform a general evaluation of the FRB model's predictions.

5.4.1 Structure factor and renormalized τ

First, we test the ability of the FRB model to predict the renormalized structure factor of the fluctuating bare model in the disodered phase near the ODT at $\bar{N} = 10^4$. We run Langevin trajectories on the bare model with $\bar{N}$ scaled out (2.106). For our chosen Fourier transform convention (2.114), the FRB one-loop Hartree approximation predicts [104]

$$\langle \phi_s(\mathbf{k}) \phi_s(\mathbf{k}') \rangle = \frac{\delta_{\mathbf{k},-\mathbf{k}'}}{V \bar{N}^{1/2} (\tau_R + e(q^2 - q_0^2)^2)} \tag{5.18}$$

where τ_R is given by (2.108) and V is the system volume in model units. From (5.18) we see that for $|\mathbf{k}| = q_0$, $\tau_R = \frac{1}{V \bar{N}^{1/2} \langle \phi_s(\mathbf{k}) \phi_s(-\mathbf{k}) \rangle}$. Therefore, to extract an effective renormalized τ from numerical simulations, at each sampling step we compute the structure factor $\phi_s(\mathbf{k}) \phi_s(-\mathbf{k})$ and perform a circular average over all modes with $|\mathbf{k}| = q_0$ to compute $S(q_0) \equiv V \bar{N}^{1/2} \langle \phi_s(\mathbf{k}) \phi_s(-\mathbf{k}) \rangle_C$, where $\langle\rangle_C$

represents the circular average. $S(q_0)$ is recorded over samples in a long Langevin trajectory (see Fig. 5.14 text). The effective τ_R is computed as $\langle 1/S(q_0)\rangle$, where $\langle\rangle$ represents the time-average. Results are plotted in Figure 5.14.

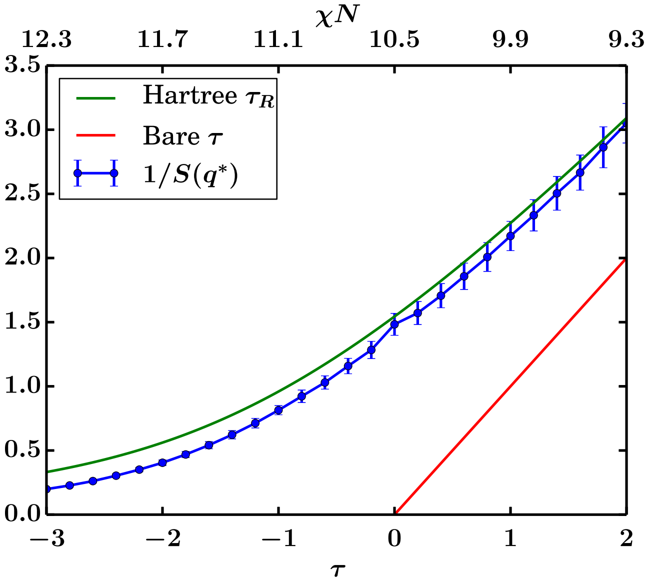

Figure 5.14: Renormalized value of τ as calculated from the one-loop Hartree approximation (green) and extracted from fluctuating 3D simulations of the disordered phase (blue) by averaging $1/S(q_0)$ over the shell of modes in k space with magnitude k^*. Error bars show the standard deviation of the raw data (not the standard error of the mean) to show the relative spread of the raw data. The Hartree approximation agrees relatively well with simulation data at higher τ/lower χN (deeper within the disordered phase); this relative agreement worsens as the system is quenched more deeply below the mean-field ODT ($\tau = 0$). The FRB model predicts that lamellae rather than disorder will be favored for $\tau < -2.89$; however, the disordered phase is observed to survive for quenches down to $\tau \approx -4$ (see Fig. 5.15). All data was collected in a simulation cell of size $12 \times 12 \times 12$ lamellar periods with resolution $84 \times 84 \times 84$ grid points. The average is computed over a Langevin trajectory of length $250,000$ timesteps, with samples taken every 1000 timesteps.

5.4.2 The ODT in the fluctuating bare model

Next, we search for the ODT in the fluctuating bare model at $\bar{N} = 10^4$, and verify that a window of metastable disorder exists. We estimate the ODT as the point where a system initially in the lamellar phase spontaneously collapses to the disordered phase, as in Ref. [204]. We also search for the point where a system initially in the disordered phase spontaneously develops lamellar order. To quantify the system's lamellar order, we introduce a global orientational persistence order parameter Φ inspired by [218]. We construct Φ from an instantaneous field configuration ϕ as follows: First, smooth ϕ by subjecting it to a low-pass filter in Fourier space to zero out all modes with wavelength > 0.5 in model units. The value of 0.5 corresponds to 0.38 lamellar periods and was somewhat arbitrarily selected; any cutoff wavelength $\leq\approx 0.5$ lamellar periods should work. Next, we take Φ in real space and construct a local director field describing the orientation of domains:

$$\hat{\mathbf{d}}(\mathbf{r}) = \frac{\nabla\phi(\mathbf{r})}{|\nabla\phi(\mathbf{r})|} \tag{5.19}$$

From $\hat{\mathbf{d}}(\mathbf{r})$, we construct a local nematic order tensor

$$Q_{ij}(\mathbf{r}) = \hat{d}_i(\mathbf{r})\hat{d}_j(\mathbf{r}) - D^{-1}\delta_{ij} \quad . \tag{5.20}$$

D is the dimensionality of the system; in this case $D = 3$. From Q_{ij} we construct the orientational persistence correlation function

$$g(\mathbf{r}) = \int d\mathbf{r}' \left[Q_{ij}(\mathbf{r}') : Q_{ij}(\mathbf{r}' + \mathbf{r})\right] \tag{5.21}$$

Finally the instantaneous value of Φ is computed as the spatial average of $g(\mathbf{r})$:

$$\Phi = \frac{1}{V} \int d\mathbf{r}\, g(\mathbf{r}) \tag{5.22}$$

A system with perfect lamellar order will have $\Phi = 1.0$. For fluctuating lamellar systems, Φ tends to be in the range $0.1 - 0.4$. Disordered systems tend to have $\Phi \leq 10^{-3}$. Φ is relatively expensive to compute, so when conducting Langevin simulations, Φ is sampled once every 1000 timesteps.

Figure 5.15 shows the results of a hysteresis sweep tracking Φ as the system is warmed from a cold start in the lamellar phase (green) and cooled from a hot start in the disordered phase (red). For system configurations with 7 grid points per period (A and C), $\Delta t = 5 \times 10^{-5}$ is used and Φ is averaged over 100,000 Langevin timesteps. For configuration B, with 10 grid points per period, $\Delta t = 2 \times 10^{-5}$ and Φ is averaged over 250,000 timesteps. In all cases ϕ is sampled every 1000 timesteps. We identify a hysteresis window where the disordered phase appears

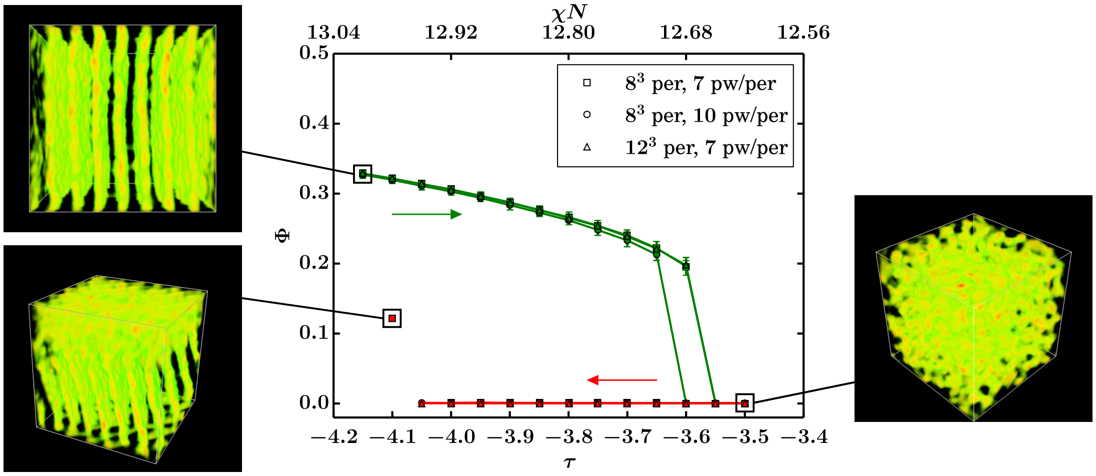

Figure 5.15: Hysteresis of the lamellar persistence order parameter Φ when the system is warmed from a cold start in the lamellar phase (green) and cooled from a hot start in the disordered phase (red). For the warming trajectories (green) the system is initialized as a perfect lamellar phase at $\tau = -4.15$ and allowed to thermalize; a thermal average of Φ is then taken. The final instantaneous configuration at $\tau = -4.15$ is then used as the initial configuration at $\tau = -4.1$, and the process continues in the direction of the green arrow (this chaining of calculations saves thermalization time). The cooling trajectories (red) are initialized as a disordered phase at $\tau = -3.5$, and calculations are chained in the opposite direction (red arrow). Error bars represent the standard deviation of the thermal average of Φ. Three system configurations are tested: a simulation cell of size 8x8x8 lamellar periods with 7 grid points or plane waves (pw) per lamellar period (squares, case "A"), an 8x8x8 cell with 10 pw/per (circles, case "B"), and a 12x12x12 cell with 7 pw/per (triangles, case "C"). A and C show collapse of the lamellar phase at $\tau \approx -3.55$; B shows this collapse at $\tau \approx -3.6$. For cases B and C, the cooling disordered phases jump to highly defective lamellar morphologies around $\tau \approx -4.1$. For case A this transition is observed at $\tau \approx -4.05$. The defective morphologies display very slow annealing kinetics; as a result their thermally averaged Φ values are not shown, but as an example we show an instantaneous snapshot of a defective lamellar morphology for case A (left, lower image) with its accompanying Φ value. We do not observe that any of the defective lamellar morphologies manage to recover a defect-free lamellar morphology on the timescale of the simulation. Examples of instantaneous snapshots of the disordered phase (right image) and lamellar phase (left, upper image) for case A are also shown.

$\bar{N}$	FRB	FRH	Observed
10^4	1.755	1.903	2.18 ± 0.03
10^6	0.378	0.410	0.44 ± 0.015
10^8	0.0815	0.0883	0.091 ± 0.003

Table 5.1: $\Delta\chi N_{ODT}$ predicted by the Fredrickson and Binder effective field theory (FRB), predicted by the Fredrickson and Helfand analysis (FRH), and approximated from simulations by the observed collapse of the lamellar phase (Observed). The ± errors are the range over which collapse of the lamellar phase is observed for different tested system configurations.

metastable, qualitatively similar to Fig. 6 of Ref. [205] (we attribute the improved sharpness of our observed transition to our larger system size).

$\bar{N} = 10^4$ is generally considered the lower limit of approximate validity of the FRB and FRH models, both of which are based on the one-loop Hartree approximation. Although our search for critical nuclei is focused on $\bar{N} = 10^4$, we also search for the ODT using a similar procedure at $\bar{N} = 10^6$ and $\bar{N} = 10^8$, to see if relative agreement with the FRB and FRH predictions improves. For $\bar{N}$ approaching 10^{10}, the FRH model should be rigorously accurate. At each $\bar{N}$ value, we test several different system configurations of size $\geq 8^3$ lamellar periods and resolution ≥ 6 grid points per lamellar period, and for each configuration, we perform a hysteresis sweep as in Figure 5.15. All tested configurations show similar windows of metastable disorder, and collapse of the lamellar phase in a small range of bare τ (or equivalently, χN) values.

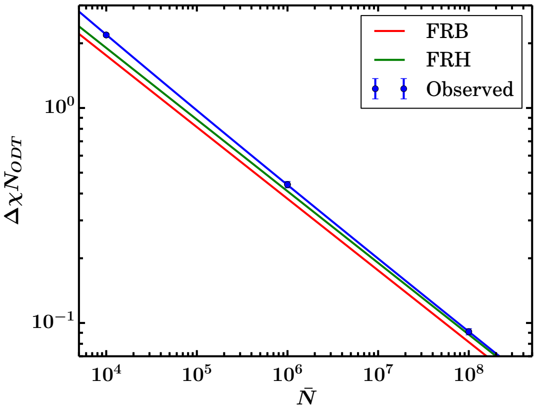

Figure 5.16: Observed $\Delta\chi N_{ODT}$ along with the predictions of FRB and FRH. For large $\bar{N}$, the FRH result should become increasingly accurate. To quantify deviation from the FRH result, we fit the observed data with a function of the form $10.495 + 41.0\bar{N}^{-1/3} + a\bar{N}^b$, and find $\Delta\chi N_{ODT} \approx 10.495 + 41.0\bar{N}^{-1/3} + 30.0\bar{N}^{-0.503}$. Since $-.503 < -1/3$, agreement with the FRH prediction does improve with increasing $\bar{N}$.

Observed values of $\Delta\chi N_{ODT} \equiv \chi N_{ODT} - 10.495$ are tabulated in Table 5.1 and plotted in Figure 5.16. It appears that the relative accuracy of the FRB model's predicted ODT improves with increasing $\bar{N}$, as expected.

5.4.3 Failure of the renormalized model to accurately capture critical nuclei

χN_{ODT} (or equivalently, τ_{ODT}) predicted by the FRB model only differs from the observed value by roughly 20% at $\bar{N} = 10^4$. However, the FRB model only predicts appreciably-sized critical nuclei for $\tau \geq\approx -3.2$ (Figure 5.9). Given the sharp dependence of predicted critical nucleus size on τ, it is unreasonable to ex-

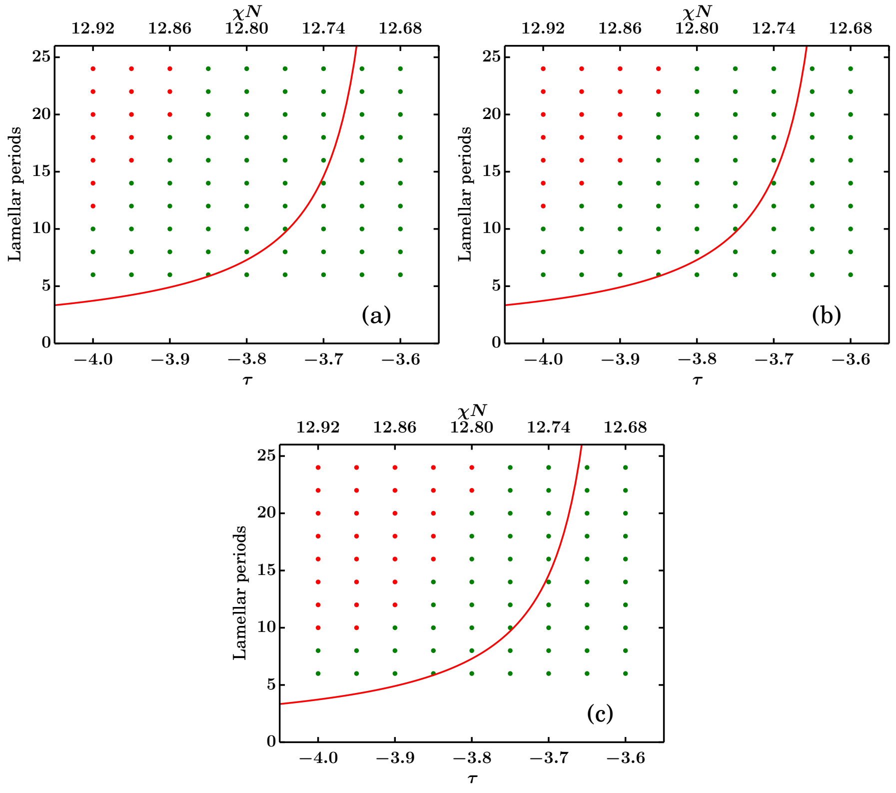

Figure 5.17: Map of where seeded nuclei tend to grow rather than be consumed by disorder at $\bar{N} = 10^4$. Nuclei are seeded as ellipsoids of lamellar structure within disorder. The $y-$axis of each plot indicates the size of seeded nuclei in lamellar periods, measured along the long axis. Three different aspect ratios for the seeded nuclei are tested: length/width = 4 (a), length/width = 3 (b), and length/width = 2 (c). Red indicates that the seeded nucleus grew to consume the simulation cell; green indicates that that the seeded nucleus reverted to disorder. Nuclei seeded with lower aspect ratios, and hence more volume, tend to be more robust. Note that the range of τ values is well outside the range of appreciably-sized nuclei as predicted by the single-mode analysis and string calculations on the renormalized model (Fig. 5.9). As an ad hoc comparison, the continuous red curve is the single-mode analysis prediction for l rigidly shifted by the difference in predicted and observed ODTs. For (a), the simulation cell dimension is $32 \times 12 \times 12$ lamellar periods with resolution $224 \times 84 \times 84$ grid points; for (b) and (c), the cell dimension is $32 \times 16 \times 16$ periods with resolution $224 \times 112 \times 112$ grid points.

pect the nucleus sizes predicted by the FRB model are accurate near the observed ODT of $\tau \approx -3.6$. Note that the range of τ values plotted in Figures 5.9 and 5.15 do not even overlap!

To obtain a coarse estimate of critical nucleus sizes, we seed ellipsoidal nuclei of varying lengths with three different aspect ratios, operating within the observed τ window of Figure 5.15 where disorder is predicted to be metastable. Amplitudes are seeded according to the single-mode prediction (5.2). We run Langevin trajectories on these nuclei to see if they grow or shrink. Results are shown in Figure 5.17. We identify regions where nuclei tend to grow; however, the results bear no relation to the predictions of the single-mode analysis, due to the renormalized model's misjudgment of the ODT. Additionally, fatter nuclei with lower length/width aspect ratios exhibit a larger region of observed growth, indicating that aspect ratios in the range of length/width ≈ 4 to 5 predicted by the renormalized model may not be optimal and that the ideal aspect ratio may actually be closer to the value of 2.37 predicted by Balsara [15]. As a final ad hoc approximation, we also show the prediction of the single-mode analysis shifted to the left by the difference $\Delta\tau = -0.71$ between the predicted ($\tau = -2.89$) and observed ($\tau \approx -3.6$) ODTs.

5.4.4 Attempts to use the string method beyond mean-field theory

The hyperplane sampling method (HSM) and finite temperature string method (FTSM) described in Section 2.2.6 are both advertised to extract free energy barriers from a fluctuating bare Hamiltonian. The HSM requires an existing converged string; the FTSM generalizes this procedure, starting with an initial rough guess sequence of images and iterating over multiple thermal average steps until the string converges to a principle curve. Both require performing constrained thermal averages in the hyperplanes normal to the string at each image. The methods claim to be applicable even for high-dimensional systems, and have in fact been demonstrated for such systems [61, 77]. Additionally, in [78] the converged state of the FTSM is demonstrated to have normal hyperplanes that locally approximate isocommittor surfaces in a high-dimensional energy landscape for the case of isotropic, position-independent diffusion. Our Langevin dynamics on the bare Brazovskii model is a high-dimensional system with isotropic, position-independent diffusion, so I surmised it was a promising use case for both methods. I even created my own custom version of PolyFTS with multi-GPU parallelism to farm out the costly (but independent over images, and therefore trivially parallel) thermal averages in different hyperplanes to multiple GPUs using MPI.

My strategy was to perform sampling in the hyperplane normal to the string at each image by initializing a field in that hyperplane and allowing it to fluctuate, but at each timestep, subtracting off any component of the motion tangent to the string. As guess strings used to define the initial normal hyperplanes and tangent vectors, I tested converged strings from the renormalized model (shifted to lower τ, with amplitude readjusted according the the single-mode approximation), and simply sequences of concentric ellipsoids, as was used to initialize the defect-free renormalized string calculations (Figure 5.5). Unfortunately, I was unable to confine fluctuating images to normal hyperplanes with any reliability. Images seeded in the confined hyperplanes tended to either order or disorder over the course of attempted confined thermal averages, retaining no visible structure of the corresponding image along the string. I cannot rule out that hyperplane sampling is a viable strategy if the initial string is chosen with sufficient care, but it appears to be challenging, and I recommend that other strategies be pursued to extract rates and free energy barriers, as described in Section 6.1.

Chapter 6

Conclusions and outlook

In this thesis, I presented several applications of the zero-temperature string method to novel barrier-crossing problems in polymer field theory, and also performed an in-depth analysis of the dis→lam transition of the renormalized Brazovskii model.

First, I developed an implementation of the string method compatible with self-consistent field theory (SCFT), and wrote a version that leveraged the computational horsepower of state-of-the-art massively parallel computing architectures (NVIDIA graphics processing units). Using my code, collaborators in the Fredrickson group and I were able to identify free energy barriers and transition mechanisms for a wide range of (previously computationally infeasible) defect annealing problems relevant to industrial directed self-assembly (DSA). Our results provide concrete, practical guidance for experimentalists and our semiconductor industry partners in their efforts to stabilize defect-free self-assembled nanoscale structures using copolymer DSA.

Second, I investigated nucleation of the lamellar phase from the disordered phase of the fluctuating Landau-Brazovskii model at parameters connected to those of an experimentally accessible diblock copolymer melt. I used a combination of single-mode analysis and string calculations applied to a renormalized effective free energy functional, and Langevin simulations of the bare Landau-Brazovskii model. While performing string calculations, I observed that the conventionally energy-weighted string method as employed in previous literature was computationally inefficient for large-cell nucleation problems, since many images were wasted tracing out unphysical configurations once the nucleus grew to the edges of the simulation cell. I developed a novel truncation-based energy weighting (TBEW) string method that completely eliminated this inefficiency; using TBEW, I performed a thorough search for a library of predicted and experimentally observed anisotropic critical nuclei and critical nuclei containing exotic defect structures. Stable minimum energy paths were not observed to exist for any of the tested defect-containing nucleation pathways; however, I did find that defect-free critical nuclei exhibited expected anisotropic ellipsoidal structure, in good agreement with the results of the single-mode analysis. To evaluate the predictions of the string method and single-mode analysis, I simulated the bare

Landau-Brazovskii model with explicit fluctuations. I found that the renormalized model made reasonable predictions for various important quantities, including the disordered-phase structure factor and the dis→lam ODT. However, I showed that the critical nucleus size depended rather sharply on proximity to the ODT, and even minor errors in the predicted ODT led to large errors in predicted nucleus size. I conclude that to avoid this issue, future studies of the dis→lam transition of the Landau-Brazovskii model should work directly with the fluctuating bare model rather than the renormalized model.

6.1 Suggestions for future work on dis→lam nucleation

I attempted to extract free energy barriers along converged strings using the hyperplane sampling technique described in Section 2.2.6, with the ultimate goal of running a finite-temperature string method calculation, but found that inducing the required hyperplane confinement was challenging in the full Cartesian space of the field theory. On this basis I recommend that future studies investigate the dis→lam transition using low- or 1-dimensional spaces of collective variables, which are likely to be better behaved.

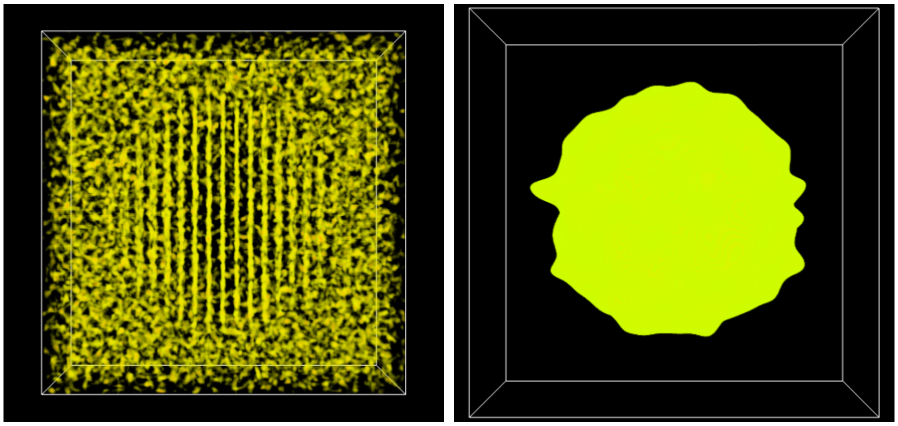

Figure 6.1: A local order parameter capable of distinguishing lamella (of known orientation) from disorder. Left panel: 3D field initialized with an embedded prolate ellipsoid of lamellae and allowed to fluctuate for a short time (the image is shown at reduced opacity for a better view of the embedded structure). Right panel: Q_{xx} of the order parameter Φ, subjected to a low-pass filter to damp out all modes with wavelength less than 2 lamellar periods, then threshholded at a value of 0.3. The "lamellar-like" region is clearly differentiated from the surrounding disorder.

In recent studies of this transition [111, 205], two 1D global order parameters based on the amplitude of the structure factor were shown to distinguish lamellae from disorder. A free energy barrier along the order parameter of Medapuram *et al.* [111] was obtained using metadynamics. It is reasonable to expect a similar metadynamics or umbrella sampling treatment of this order parameter can extract a free energy barrier for the dis→lam transition of the fluctuating Landau-Brazovskii model. However, since these order parameters are global, they are unlikely to represent "good" reaction coordinates. They are unlikely to be good predictors of the committor probability, and collapsing these order parameters onto an effective 1D Smoluchowski equation as described in Section 2.1.3 is unlikely to yield an accurate rate. Therefore, an attempt to extract rates using these parameters should use a rate-finding method less sensitive to reaction coordinate quality (*e. g.*, forward flux sampling or milestoning).

In this thesis, I defined a global parameter Φ capable of distinguishing fluctuating lamellae from disorder. I observed that Φ is effective at differentiating large-scale fluctuating lamellae from disorder, but for small nuclei in large cells Φ does not show sufficient contrast due to its global nature. A better order parameter would be a local parameter capable of differentiating regions of lamellae; the reaction coordinate could be defined as the volume of the largest region of lamellar order present in the system. Such a reaction coordinate would more likely be "good" in the sense of Section 2.1.3. Figure 6.1 demonstrates that a parameter constructed from the Q_{xx} component of Φ effectively identifies regions of lamellar order with known orientation. In principle, this could be used to umbrella sample large seeded nuclei whose bulk rotation will be relatively slow, and for which the free energy contribution stemming from bulk rotation is minimal. Ideally, one would like to construct an anisotropic order parameter that can distinguish lamellae of arbitrary orientation; such an order parameter could be used to umbrella sample spontaneously forming nuclei whose orientation will not be known *a priori*. It may be possible to do so using some clever combination of Q_{xx} and other components of Φ. This merits further investigation.

It should be emphasized that although the dis→lam transition has been studied for 25+ years, extracting free energy barriers from fluctuating models for this transition is a very new and active area of research. Medapuram *et al.*'s result, which to my knowledge is the first such successful calculation, was published this year. The work presented in this thesis will provide valuable guidance to future researchers.

Bibliography

[1] Audus, D. J. Field-Based Simulations of Nanostructured Polyelectrolyte Gels. Ph.D. thesis, University of California, Santa Barbara, 2013.

[2] Bates, F. S.; Fredrickson, G. H. *Physics Today* **1999**, *52*, 32–38.

[3] Segalman, R. A. *Mat. Sci. Eng. R* **2005**, *48*, 191–226.

[4] Stoykovich, M. P.; Nealey, P. F. *Materials Today* **2006**, *9*, 20–29.

[5] Mishra, V.; Fredrickson, G. H.; Kramer, E. J. *ACS Nano* **2012**, *6*, 2629–2641.

[6] Stoykovich, M. P.; Kang, H.; Daoulas, K. C.; Liu, G.; Liu, C.-C.; de Pablo, J. J.; Müller, M.; Nealey, P. F. *ACS Nano* **2007**, *1*, 168–175.

[7] Li, R. R.; Dapkus, P. D.; Thompson, M. E.; Jeong, W. G.; Harrison, C.; Chaikin, P. M.; Register, R. A.; Adamson, D. H. *App. Phys. Lett.* **2000**, *76*, 1689.

[8] Cheng, J. Y.; Ross, C. A.; Chan, V. Z.-H.; Thomas, E. L.; Lammertink, R. G. H.; Vansco, G. J. *Advanced Materials* **2001**, *13*, 1174–1178.

[9] Urbas, A. M.; Maldovan, M.; DeRege, P.; Thomas, E. L. *Advanced Materials* **2002**, *14*, 1850.

[10] Phillip, W. A.; O'Neill, B.; Rodgowin, M.; Hillmyer, M. A.; Cussler, E. L. *ACS Applied Materials & Interfaces* **2010**, *2*, 847–853.

[11] Li, W.; Müller, M. *Annu. Rev. Chem. Biomolecular Eng.* **2015**, *6*, 187–216.

[12] Leibler, L. *Macromolecules* **1980**, *13*, 1602–1617.

[13] Bates, F. S.; Rosedale, J. H.; Fredrickson, G. H.; Glinka, C. J. *Phys. Rev. Lett.* **1988**, *61*, 2229–2232.

[14] Milner, S. T.; Morse, D. C. *Phys. Rev. E* **1996**, *54*, 3793–3810.

[15] Balsara, N. P.; Marques, C. M.; Garetz, B. A.; Newstein, M. C.; Gido, S. P. *Phys. Rev. E* **2002**, *66*, 052802.

[16] Hohenberg, P. C.; Swift, J. B. *Phys. Rev. E* **1995**, *52*, 1828–1845.

[17] Chastek, T. Q.; Lodge, T. P. *J. Polym. Sci. Part B* **2005**, *43*, 405–412.

[18] Peters, B.; Trout, B. L. *J. Chem. Phys.* **2006**, *125*, 054108.

[19] Best, R. B.; Hummer, G. *PNAS* **2005**, *102*, 6732–6737.

[20] Johnson, M. E.; Hummer, G. *J. Phys. Chem B* **2012**, *116*, 8573–8583.

[21] Ermak, D. L.; McCammon, J. A. *J. Chem. Phys.* **1978**, *69*, 1352.

[22] ten Wolde, P. R.; Frenkel, D. *Science* **1997**, *277*, 1975.

[23] Auer, S.; Frenkel, D. *Annu. Rev. Phys. Chem.* **2004**, *55*, 333–361.

[24] Auer, S.; Frenkel, D. *J. Chem. Phys.* **2004**, *120*, 3015–3029.

[25] Beckham, G. T.; Peters, B. *J. Chem. Phys. Letters* **2011**, *2*, 1133–1138.

[26] McQuarrie, D. A. *Statistical Mechanics*; University Science Books, 2000.

[27] Gardiner, C. *Stochastic Methods: A Handbook for the Natural and Social Sciences*; Springer-Verlag, 2009.

[28] Vanden-Eijnden, E. *Lect. Notes Phys.* **2006**, *703*, 453–493.

[29] Kramers, H. A. *Physica* **1940**, *7*, 284–304.

[30] Hänggi, P.; Talkner, P.; Borkovec, M. *Reviews of Modern Physics* **1990**, *62*, 251–341.

[31] Peters, B. *(private communication)*

[32] Langer, J. S. *Annals of Physics* **1967**, *41*, 108–157.

[33] Langer, J. S. *Phys. Rev. Lett.* **1968**, *21*, 973–976.

[34] Langer, J. S. *Annals of Physics* **1969**, *54*, 258–275.

[35] Berezhkovskii, A. M.; Zitserman, V. Y. *Chem. Phys. Lett.* **1989**, *158*, 369.

[36] Knott, B. C.; Molinero, V.; Doherty, M. F.; Peters, B. *J. Am. Chem. Soc.* **2012**, *134*, 19544–19547.

[37] Peters, B. *J. Chem. Phys.* **2009**, *131*, 244103.

[38] Knott, B. C.; Duff, N.; Doherty, M. F.; Peters, B. *J. Chem. Phys.* **2009**, *131*, 224112.

[39] Peters, B.; Bolhuis, P. G.; Mullen, R. G.; Shea, J.-E. *J. Chem. Phys.* **2013**, *138*, 054106.

[40] Bolhuis, P. G.; Chandler, D.; Dellago, C.; Geissler, P. L. *Annu. Rev. Phys. Chem.* **2002**, *53*, 291–318.

[41] Peters, B. *J. Chem. Phys.* **2006**, *125*, 241101.

[42] Berezhkovskii, A. M.; Szabo, A. *J. Chem. Phys.* **2005**, *122*, 014503.

[43] Peters, B.; Beckham, G. T.; Trout, B. L. *J. Chem. Phys.* **2007**, *127*, 034109.

[44] Gibbs, J. W. *Trans. Conn. Acad. Arts Sci.* **1878**, *3*, 108–524.

[45] Becker, R.; Döring, W. *Ann. Phys.* **1935**, *416*, 719–752.

[46] Agarwal, V.; Peters, B. *Adv. Chem. Phys.* **2014**, *155*, 97–159.

[47] Henkelman, G.; Johannesson, G.; Jonsson, H. In *Progress on Theoretical Chemistry and Physics*; Schwartz, S. D., Ed.; Kluwer Academic: Dordrecht, Netherlands, 2000.

[48] Berneche, S.; Roux, B. *Nature* **2001**, *414*, 73–77.

[49] H., W. Umbrella Sampling. 2006; `http://physics.clarku.edu/~hwang/research/umbrella/umbrella_method/umbrella_method.html`.

[50] Barducci, A.; Bonomi, M.; Parrinello, M. *Wiley Interdisciplinary Reviews: Comp. Mol. Sci.* **2011**, *1*, 826–843.

[51] Barducci, A.; Bussi, G.; Parrinello, M. *Phys. Rev. Lett.* **2008**, *100*, 020603.

[52] Laio, A.; Parrinello, M. *PNAS* **2002**, *99*, 12562–12566.

[53] Dellago, C.; Bolhuis, P. G. *Adv. Polym. Sci.* **2008**, 167–233.

[54] Peters, B. *Mol. Sim.* **2010**, *36*, 1265–1281.

[55] van Erp, T. S.; Bolhuis, P. G. *J. Comp. Phys.* **2005**, *205*, 157–181.

[56] Allen, R. J.; Warren, P. B.; ten Wolde, P. R. *Phys. Rev. Lett.* **2005**, *94*, 018104.

[57] Allen, R. J.; Frenkel, D.; ten Wolde, P. R. *J. Chem. Phys.* **2006**, *124*, 194111.

[58] Faradjian, A. K.; Elber, R. *J. Chem. Phys.* **2004**, *120*, 10880.

[59] E, W.; Ren, W.; Vanden-Eijnden, E. *Phys. Rev. B* **2002**, *66*, 052301.

[60] E, W.; Ren, W.; Vanden-Eijnden, E. *J. Chem. Phys.* **2007**, *126*, 164103.

[61] E, W.; Ren, W.; Vanden-Eijnden, E. *J. Phys. Chem. B* **2005**, *109*, 6688–6693.

[62] Freidlin, M. I.; Wentzell, A. D. *Random Perturbations of Dynamical Systems*; Springer-Verlag, 1984.

[63] Peters, B.; Heyden, A.; Bell, A. T.; Chakraborty, A. *J. Chem. Phys.* **2004**, *120*, 7877–7886.

[64] Quapp, W. *J. Chem. Phys.* **2005**, *122*, 174106.

[65] Goodrow, A.; Bell, A. T.; Head-Gordon, M. *J. Chem. Phys.* **2008**, *129*, 174109.

[66] Goodrow, A.; Bell, A. T.; Head-Gordon, M. *J. Chem. Phys.* **2009**, *130*, 244108.

[67] Goodrow, A.; Bell, A. T.; Head-Gordon, M. *Chem. Phys. Letters* **2010**, *484*, 392–398.

[68] Zimmerman, P. M. *J. Chem. Phys.* **2013**, *138*, 184102.

[69] Zimmerman, P. M. *J. Chem. Th. Comp.* **2013**, *9*, 3043–3050.

[70] Zimmerman, P. M. *J. Comp. Chem.* **2015**, *36*, 601–611.

[71] Ren, W.; Vanden-Eijnden, E. *J. Chem. Phys.* **2013**, *138*, 134105.

[72] Behn, A.; Zimmerman, P. M.; Bell, A. T.; Head-Gordon, M. *J. Chem. Phys.* **2011**, *135*, 224108.

[73] Chaffey-Millar, H.; Nikodem, A.; Matveev, A. V.; Küger, S.; Rösch, N. *J. Chem. Th. Comp.* **2012**, *8*, 777–786.

[74] Du, Q.; Zhang, L. *Comm. Math. Sci.* **2009**, *7*, 1039–1051.

[75] Backofen, R.; Voigt, A. *Journal of Physics: Condensed Matter* **2010**, *22*, 364104.

[76] Vanden-Eijnden, E.; Venturoli, M. *J. Chem. Phys.* **2009**, *130*, 194103.

[77] Ren, W.; Vanden-Eijnden, E.; Maragakis, P.; E, W. *J. Chem. Phys.* **2005**, *123*, 134109.

[78] E, W.; Ren, W.; Vanden-Eijnden, E. *Chem. Phys. Lett.* **2005**, *413*, 242–247.

[79] Maragliano, L.; Fischer, A.; Vanden-Eijnden, E.; Ciccotti, G. *J. Chem. Phys.* **2006**, *125*, 024106.

[80] Maragliano, L.; Vanden-Eijnden, E. *Chem. Phys. Lett.* **2007**, *446*, 182–190.

[81] Ovchinnikov, V.; Karplus, M.; Vanden-Eijnden, E. *J. Chem. Phys.* **2011**, *134*, 085103.

[82] Miller, T. F. I.; Vanden-Eijnden, E.; Chandler, D. *PNAS* **2007**, *104*, 14559–14564.

[83] Müller, M.; Sun, D.-W. *Phys. Rev. Lett.* **2013**, *111*, 267801.

[84] Müller, M.; Smirnova, Y. G.; Marelli, G.; Fuhrmans, M.; Shi, A.-C. *Phys. Rev. Lett.* **2012**, *108*, 228103.

[85] Pan, A. C.; Sezer, D.; Roux, B. *J. Phys. Chem. B* **2008**, *112*, 3432–3440.

[86] Müller, M.; de Pablo, J. *Annual Review of Materials Research* **2013**, *43*, 1–34.

[87] Fredrickson, G. H. *The Equilibrium Theory of Inhomogenous Polymers*; Clarendon Press, 2005.

[88] Matsen, M. W. *Self-Consistent Field Theory and Its Applications, in Soft Matter, Vol. 1: Polymer Melts and Mixtures*; Wiley-VCH Verlag GmbH and Co. KGaA, 2005.

[89] Flory, P. J. *Principles of Polymer Chemistry*; Cornell University Press, 1953.

[90] Matsen, M. W. *J. Chem. Phys.* **1997**, *106*, 7781–7791.

[91] Bosse, A. W.; Garcia-Cervera, C. J.; Fredrickson, G. H. *Macromolecules* **2007**, *40*, 9570–9581.

[92] Hur, S.-M.; Garcia-Cervera, C. J.; Kramer, E. J.; Fredrickson, G. H. *Macromolecules* **2009**, *42*, 5861–5872.

[93] Gerlach, U. H. The Method of Steepest Descent and Stationary Phase. 2010; `https://people.math.osu.edu/gerlach.1/math/BVtypset/node128.html`.

[94] Lennon, E. M.; Katsov, K.; Fredrickson, G. H. *Phys. Rev. Lett.* **2008**, *101*, 138302.

[95] Ceniceros, H. D.; Fredrickson, G. H. *Multiscale Model. Sim.* **2004**, *2*, 452–474.

[96] Villet, M.; Fredrickson, G. H. *J. Chem. Phys.* **2010**, *132*, 034109.

[97] Villet, M. C. Advanced Computational Field Theory Methods for Fluctuating Polymer Solutions. Ph.D. thesis, University of California, Santa Barbara, 2012.

[98] Audus, D. J.; Delaney, K. T.; Ceniceros, H. D.; Fredrickson, G. H. *Macromolecules* **2013**, *46*, 8383–8391.

[99] Rasmussen, K. Ø.; Kalosakas, G. *J. Poly. Sci. B: Poly. Phys.* **2002**, *40*, 1777–1783.

[100] Tzeremes, G.; Rasmussen, K. Ø.; Lookman, T.; Saxena, A. *Phys. Rev. E* **2002**, *65*, 041806.

[101] Strang, G. *SIAM J. Numer. Anal.* **1968**, *5*, 506–517.

[102] Bosse, A. W.; Sides, S. W.; Katsov, K.; Garcia-Cervera, C. J.; Fredrickson, G. H. *J. Poly. Sci. Part B: Poly. Phys.* **2006**, *44*, 2495–2511.

[103] Düchs, D.; Ganesan, V.; Fredrickson, G. H.; Schmid, F. *Macromolecules* **2003**, *40*, 9237–9248.

[104] Fredrickson, G. H.; Helfand, E. *J. Chem. Phys.* **1987**, *87*, 697.

[105] Brazovskii, S. A. *JETP* **1975**, *68*, 175–185.

[106] Gross, N. A.; Ignatiev, M.; Chakraborty, B. *Phys. Rev. E* **2000**, *62*, 6116–6125.

[107] Amit, D. J. *Field theory, the renormalization group, and critical phenomena*; World Scientific Publishing Co., 1984.

[108] Swift, J.; Hohenberg, P. C. *Phys. Rev. A* **1977**, *15*, 319–328.

[109] Swift, J.; Leitner, P. *Phys. Rev. B* **1977**, *16*, 4137–4141.

[110] Mukamel, D.; Hornreich, R. M. *J. Phys. C: Solid St. Phys.* **1980**, *13*, 161–171.

[111] Medapuram, P.; Glaser, J.; Morse, D. C. *Macromolecules* **2015**, *48*, 819–839.

[112] Fredrickson, G. H.; Binder, K. *J. Chem. Phys.* **1989**, *91*, 7265.

[113] International Technology Roadmap for Semiconductors. 2013; `http://www.itrs.net`.

[114] Herr, D. J. C. *J. Mater. Res.* **2011**, *26*, 122–139.

[115] Cheng, X.; Lin, L.; E, W.; Zhang, P.; Shi, A.-C. *Phys. Rev. Lett.* **2010**, *104*, 148301.

[116] Takahashi, H.; Laachi, N.; Delaney, K. T.; Hur, S.-M.; Weinheimer, C. J.; Shykind, D.; Fredrickson, G. H. *Macromolecules* **2012**, *45*, 6253–6265.

[117] Laachi, N.; Takahashi, H.; Delaney, K. T.; Hur, S.-M.; Shykind, D.; Weinheimer, C. J.; Fredrickson, G. H. *Proc. of SPIE* **2012**, *8323*, 83230K.

[118] Huang, J.-S. Leaps in Visual Computing. 2015; `http://on-demand.gputechconf.com/gtc/2015/presentation/S5715-Keynote-Jen-Hsun-Huang.pdf`.

[119] Cuda C Programming Guide. 2015; `http://docs.nvidia.com/cuda/cuda-c-programming-guide`.

[120] Harris, M. J. Real-Time Cloud Simulation and Rendering. Ph.D. thesis, University of North Carolina at Chapel Hill, 2003.

[121] OpenACC Home. 2015; `http://www.openacc-standard.org/J`.

[122] OpenCL–The open standard for parallel programming of heterogeneous systems. 2015; `https://www.khronos.org/opencl/`.

[123] Glaser, J.; Nguyen, T. D.; Anderson, J. A.; Lui, P.; Spiga, F.; Millan, J. A.; Morse, D. C.; Glotzer, S. C. *Comp. Phys. Comm.* **2015**, *192*, 97–107.

[124] Niemeyer, K. E.; Sung, C.-J. *J. Supercomput.* **2014**, *67*, 528–564.

[125] Le, H. P.; Cambier, J.-L.; Cole, L. K. *Comp. Phys. Comm.* **2013**, *184*, 596–606.

[126] Beberg, A. L.; Ensign, D. L.; Jayachandran, G.; Khaliq, S.; Pande, V. S. *IEEE International Symposium on Parallel & Distributed Computing 2009* **2009**, 1–8.

[127] Olivares-Amaya, R.; Watson, M. A.; Edgar, R. G.; Vogt, L.; Shao, Y.; Aspuru-Guzik, A. *J. Chem. Theory and Comp.* **2010**, *6*, 135–144.

[128] Wright, I.; Wickham, R. A. *J. Phys. Conf. Ser.* **2010**, *256*, 012008.

[129] Gao, J.; Song, W.; Tang, P.; Yang, Y. *Soft Matter* **2011**, *7*, 5208–5216.

[130] Frigo, M.; Johnson, S. G. FFTW: An adaptive software architecture for the FFT. Proc. 1998 IEEE Intl. Conf. Acoustics Speech and Signal Processing. 1998; pp 1381–1384.

[131] Frigo, M.; Johnson, S. G. *Proceedings of the IEEE* **2005**, *93*, 216–231, Special issue on “Program Generation, Optimization, and Platform Adaptation”.

[132] cuFFT :: CUDA Toolkit Documentation. 2015; `http://docs.nvidia.com/cuda/cufft/#axzz3k2ngiVuu`.

[133] Delaney, K. T.; Fredrickson, G. H. *Comp. Phys. Comm.* **2013**, *184*, 2102–2110.

[134] Harris, M. Optimizing parallel reduction in CUDA. 2007; `https://docs.nvidia.com/cuda/samples/6_Advanced/reduction/doc/reduction.pdf`.

[135] Press, W. H.; Flannery, B. P.; Teukolsky, S. A.; Vetterling, W. T. *Numerical Recipes in C: The Art of Scientific Computing, Second Edition*; Cambridge University Press, 1992.

[136] Izumi, K.; Kim, B.; Laachi, N.; Delaney, K. T.; Carilli, M.; Fredrickson, G. H. *Proc. of SPIE* **2015**, *9423*, 94232C.

[137] Izumi, K.; Kim, B.; Laachi, N.; Delaney, K. T.; Carilli, M.; Fredrickson, G. H. *To be submitted to J. Polym. Sci. B* **2015**,

[138] Ruppel, M.; Pester, C. W.; Langner, K. M.; Sevink, G. J. A.; Schoberth, H. G.; Schmidt, K.; Urban, V. S.; Mays, J. W.; Böker, A. *ACS Nano* **2013**, *7*, 3854–3867.

[139] Angelescu, D. E.; Waller, J. H.; Adamson, D. H.; Deshpande, P.; Chou, S. Y.; Register, R. A.; Chaikin, P. M. *Advanced Materials* **2004**, *16*, 1736–1740.

[140] Pelletier, V.; Adamson, D. H.; Register, R. A.; Chaikin, P. M. *Applied Phys. Lett.* **2007**, *90*, 163105.

[141] Segalman, R. A.; Yokoyama, H.; Kramer, E. J. *Advanced Materials* **2001**, *13*, 1152–1155.

[142] Park, S.-M.; Stoykovich, M. P.; Ruiz, R.; Zhang, Y.; Black, C. T.; Nealey, P. F. *Advanced Materials* **2007**, *19*, 607–611.

[143] Kim, B.; Laachi, N.; Delaney, K. T.; Carilli, M.; Kramer, E. J.; Fredrickson, G. H. *J. Appl. Polym. Sci.* **2014**, *131*, 40790.

[144] Hammond, M. R.; Cochran, E.; Fredrickson, G. H.; Kramer, E. J. *Macromolecules* **2005**, *38*, 6575–6585.

[145] Kim, B.; Laachi, N.; Fredrickson, G. H. *Proc. SPIE* **2013**, *8680*, 868016.

[146] Cheng, J. Y.; Mayes, A. M.; Ross, C. A. *Nature Materials* **1996**, *29*, 823–828.

[147] Matsen, M. W.; Bates, F. S. *Macromolecules* **1996**, *29*, 1091–1098.

[148] Paradiso, S. P.; Delaney, K. T.; Garcia-Cervera, C. J.; Ceniceros, H. D.; Fredrickson, G. H. *ACS Macro Letters* **2014**, *3*, 16–20.

[149] Huang, L.; He, X.; He, T.; Liang, H. *J. Chem. Phys.* **2003**, *119*, 12479.

[150] Hasegawa, R.; Doi, M. *Macromolecules* **1997**, *30*, 3086–3089.

[151] Sevink, G. J. A.; Pinna, M.; Langner, K. M.; Zvelindovsky, A. V. *Soft Matter* **2011**, *7*, 6161–5170.

[152] Anderson, J. A. Phases of polymer systems in solution studied via molecular dynamics. Ph.D. thesis, Iowa State University, 2009.

[153] Kim, S. O.; Solak, H. H.; Stoykovich, M. P.; Ferrier, N. J.; de Pablo, J. J.; Nealey, P. F. *Nature* **2003**, *424*, 411–414.

[154] Stoykovich, M. P.; Müller, M.; Kim, S. O.; Solak, H. H.; Edwards, E. W.; de Pablo, J. J.; Nealey, P. F. *Science* **2005**, *308*, 1442–1446.

[155] Edwards, E. W.; Stoykovich, M. P.; Müller, M.; Solak, H. H.; de Pablo, J. J.; Nealey, P. F. *J. Polym. Sci. B: Polym. Phys.* **2005**, *43*, 3444–3459.

[156] Kim, S. O.; Kim, B. H.; Kim, K.; Koo, C. M.; Stoykovich, M. P.; Nealey, P. F.; Solak, H. H. *Macromolecules* **2006**, *39*, 5466–5470.

[157] Ruiz, R.; Kang, H.; Detcheverry, F. A.; Dobisz, E.; Kercher, D. S.; Albrecht, T. R.; de Pablo, J. J.; Nealey, P. F. *Science* **2008**, *321*, 936–939.

[158] Welander, A. M.; Kang, H.; Stuen, K. O.; Solak, H. H.; Muüller, M.; de Pablo, J. J.; Nealey, P. F. *Macromolecules* **2008**, *41*, 2759–2761.

[159] Liu, C.-C.; Ramirez-Hernandez, A.; Han, E.; Craig, G. S. W.; Tada, Y.; Yoshida, H.; Kang, H.; Ji, S.; Gopalan, P.; de Pablo, J. J.; Nealey, P. F. *Macromolecules* **2013**, *46*, 1415–1424.

[160] Doerk, G. S.; Cheng, J. Y.; Singh, G.; Rettner, C. T.; Pitera, J. W.; Balakrishnan, S.; Arellano, N.; Sanders, D. P. *Nature Communications* **2014**, *5*, 5805.

[161] Izumi, K.; Laachi, N.; Man, X.; Delaney, K. T.; Fredrickson, G. H. *Proc. of SPIE* **2014**, *904922*, 9049.

[162] Gronheid, R. et al. *Proc. of SPIE* **2014**, *904905*, 9049.

[163] Pathangi, H. et al. *Proc. of SPIE* **2015**, *9423*, 94230M.

[164] Detcheverry, F. A.; Pike, D. Q.; Nealey, P. F.; Müller, M.; de Pablo, J. J. *Phys. Rev. Lett.* **2009**, *102*, 197801.

[165] Nagpal, U.; Müller, M.; Nealey, P. F.; de Pablo, J. J. *ACS Macro Letters* **2012**, *1*, 418–422.

[166] Detcheverry, F. A.; Lui, G.; Nealey, P.; de Pablo, J. J. *Macromolecules* **2010**, *43*, 3446–3454.

[167] Detcheverry, F. A.; Nealey, P.; de Pablo, J. J. *Macromolecules* **2010**, *43*, 6495–6504.

[168] Ginzburg, V. V.; Weinhold, J. D.; Hustad, P. D.; Trefonas, P. *J. Photopolym. Sci. Tech.* **2013**, *26*, 817–822.

[169] Ginzburg, V. V.; Weinhold, J. D.; Hustad, P. D.; Trefonas, P.; Kim, B.; Laachi, N.; Fredrickson, G. H. In *Directed Self-Assembly of Block Copolymers for Nano-manufacturing*; Gronheid, R., Nealey, P., Eds.; Woodhead Publishing: Cambridge, MA, 2015.

[170] Li, W.; Nealey, P. F.; de Pablo, J. J.; Müller, M. *Phys. Rev. Lett.* **2014**, *113*, 168301.

[171] Urwin, J. R.; Stearne, J. M. *Macromol. Chem.* **1964**, *78*, 194–203.

[172] Hashimoto, T.; Tanaka, H.; Hasegawa, H. *Macromolecules* **1990**, *23*, 4378–4386.

[173] Tanaka, H.; Hasegawa, H.; Hashimoto, T. *Macromolecules* **1991**, *24*, 240–251.

[174] Matsen, M. W. *Macromolecules* **1995**, *28*, 5765–5773.

[175] Williamson, L.; Kim, J.; Cao, Y.; Lin, G.; Gronheid, R.; Nealey, P. F. *Proc. SPIE* **2015**, *9423*, 942315.

[176] Iwama, T.; Laachi, N.; Delaney, K. T.; Kim, B.; Fredrickson, G. H. *Proc. of SPIE* **2014**, *9049*, 904927.

[177] Seino, Y.; Yonemitsu, H.; Sato, H.; Kanno, M.; Kato, H.; Kobayashi, K.; Kawanishi, A.; Azuma, T.; Muramatsu, M.; Nagahara, S.; Kitano, T.; Toshima, T. *Proc. of SPIE* **2012**, *8323*, 83230Y.

[178] Yi, H.; Bao, X.-Y.; Zhang, J.; Tiberio, R.; Conway, J.; Chang, L.-W.; Mitra, S.; Wong, P. H.-S. *Proc. of SPIE* **2012**, *8323*, 83230W.

[179] Iwama, T.; Laachi, N.; Kim, B.; Carilli, M.; Delaney, K. T.; Fredrickson, G. H. *Macromolecules* **2015**, *48*, 1256–1261.

[180] Iwama, T.; Laachi, N.; Delaney, K. T.; Kim, B.; Hur, S.-M.; Bristol, R.; Shykind, D.; Weinheimer, C. J.; Fredrickson, G. H. *J. Photopolymer Sci. Tech.* **2013**, *26*, 15–20.

[181] Laachi, N.; Iwama, T.; Delaney, K. T.; Shykind, D.; Bristol, R.; Weinheimer, C. J.; Fredrickson, G. H. *J. Photopolymer Sci. Tech.* **2014**, *27*, 21–24.

[182] Laachi, N.; Iwama, T.; Delaney, K. T.; Shykind, D.; Weinheimer, C. J.; Fredrickson, G. H. *J. Polym. Sci. B: Polym. Phys.* **2014**, *53*, 317–326.

[183] Laachi, N.; Iwama, T.; Delaney, K. T.; Kim, B.; Bristol, R.; Shykind, D.; Weinheimer, C. J.; Fredrickson, G. H. *Proc. of SPIE* **2014**, *9049*, 90491M.

[184] Laachi, N.; Iwama, T.; Delaney, K. T.; Kim, B.; Bristol, R.; Shykind, D.; Weinheimer, C. J.; Fredrickson, G. H. *J. Micro/Nanolith. MEMS MOEMS* **2015**, *14*, 013505.

[185] Iwama, T.; Laachi, N.; Delaney, K. T.; Fredrickson, G. H. *J. Micro/Nanolith. MEMS MOEMS* **2015**, *14*, 013501.

[186] E, W.; Ren, W.; Vanden-Eijnden, E. *J. Appl. Phys.* **2003**, *93*, 2275.

[187] Lin, L.; Cheng, X.; E, W.; Shi, A.-C.; Zhang, P. *J. Comput. Phys.* **2010**, *229*, 1797–1809.

[188] Venturoli, M.; Vanden-Eijnden, E.; Ciccotti, G. *J. Math. Chem.* **2008**, *45*, 188–222.

[189] Matsen, M. W. In *Self-Consistent Field Theory and Its Applications*; Gompper, G., Schick, M., Eds.; Wiley-VCH: Weinheim, Germany, 2006.

[190] Bates, F. S.; Rosedale, J. H.; Bair, H. E.; Russell, T. P. *Macromolecules* **1989**, *22*, 2557–2564.

[191] Bates, F. S.; Rosedale, J. H.; Fredrickson, G. H. *J. Chem. Phys.* **1990**, *92*, 6255.

[192] Rosedale, J. H.; Bates, F. S. *Macromolecules* **1990**, *23*, 2329–2338.

[193] Lee, S.; Gillard, T. M.; Bates, F. S. *AIChE Journal* **2013**, *59*, 3502–3513.

[194] Schuler, M.; Stühn, B. *Macromolecules* **1993**, *26*, 112–113.

[195] Hashimoto, T.; Sakamoto, N. *Macromolecules* **1995**, *28*, 4779–4781.

[196] Hashimoto, T.; Sakamoto, N.; Koga, T. *Phys. Rev. E* **1996**, *54*, 5832–5835.

[197] Newstein, M. C.; Garetz, B. A.; Balsara, N. P.; Chang, M. Y.; Dai, H. J. *Macromolecules* **1998**, *31*, 64–76.

[198] Wickham, R. A.; Shi, A.-C.; Wang, Z.-G. *J. Chem. Phys.* **2003**, *118*, 10293.

[199] Chaikin, P. M.; Lubensky, T. C. *Principles of Condensed Matter Physics*; Cambridge University Press: Cambridge, 1995.

[200] Jang, S. G.; Audus, D.; Klinger, D.; Krogstad, D. V.; Kim, B. J.; Cameron, A.; Kim, S.-W.; Delaney, K. T.; Hur, S.-M.; Killops, K. L.; Fredrickson, G. H.; Kramer, E. J.; Hawker, C. J. *JACS* **2013**, *135*, 6649–6657.

[201] Schmidt, B. V. K. J.; Elbert, J.; Scheid, D.; Hawker, C. J.; Klinger, D.; Gallei, M. *ACS Macro Letters* **2015**, *4*, 731–735.

[202] Ganesan, V.; Fredrickson, G. H. *Europhys. Lett.* **2001**, *55*, 814–820.

[203] Fredrickson, G. H.; Ganesan, V.; Drolet, F. *Macromolecules* **2002**, *35*, 16–39.

[204] Alexander-Katz, A.; Fredrickson, G. H. *Macromolecules* **2007**, *40*, 4075–4087.

[205] Stasiak, P.; Matsen, M. W. *Macromolecules* **2013**, *46*, 8037–8045.

[206] Fried, H.; Binder, K. *J. Chem. Phys.* **1991**, *94*, 8349.

[207] Vassiliev, O. N.; Matsen, M. W. *J. Chem. Phys.* **2003**, *118*, 7700–7713.

[208] Zong, J.; Wang, Q. *J. Chem. Phys.* **2013**, *139*, 124907.

[209] Pike, D. Q.; Detcheverry, F. A.; Müller, M.; de Pablo, J. J. *J. Chem. Phys.* **2009**, *131*, 084903.

[210] Müller, M.; Daoulas, K. C. *J. Chem. Phys.* **2008**, *128*, 024903.

[211] Groot, R. D.; J., M. T. *J. Chem. Phys.* **1998**, *108*, 8713.

[212] Sandhu, P.; Zong, J.; Yang, D.; Wang, Q. *J. Chem. Phys.* **1998**, *138*, 194904.

[213] Gavrilov, A. A.; Kudryavtsev, Y. V.; Chertovich, A. V. *J. Chem. Phys.* **2013**, *139*, 224901.

[214] Glaser, J.; Medapuram, P.; Beardsley, T. M.; Matsen, M. W.; Morse, D. C. *Phys. Rev. Lett.* **2014**, *113*, 068302.

[215] Spencer, R. K. W.; Wickham, R. A. *Soft Matter* **2013**, *9*, 3373.

[216] Spencer, R. K. W. Diblock Copolymer Micelle Structure and Dynamics near the by Abstract Diblock Copolymer Micelle Structure and Dynamics near the Order-Disorder Transition. Ph.D. thesis, University of Guelph, 2014.

[217] Shi, A.-C. *J. Phys.: Condens. Matter* **1999**, *11*, 10183–10197.

[218] Qian, H.; Mazenko, G. F. *Phys. Rev. E* **2003**, *67*, 036102.